Department of Chemistry
University College London
University of London

The influence of titanium dioxide surface chemistry on osteogenic stem cell selection

Marcus John Tillotson

Submitted in partial fulfilment of the requirements
for the degree of Doctor of Engineering
at University College London

July 2014

Declaration

'I, Marcus J. Tillotson confirm that the work presented in this thesis is my own. Where information has been derived from other sources, I confirm that this has been indicated in the thesis.'

Abstract

Micro structured, high surface energy titanium (Ti) has been shown to be an effective substrate for osseointegration of an implant with surrounding bone tissue. The aim of this project is to test the hypothesis that the enhanced osteogenic differentiation and function of multipotent stromal cells (MSCs) in response to modified Ti surfaces is caused by a selection event within the population.

The first cell type capable of producing new bone on an implant after placement are the MSCs which circulate in the bloodstream and are recruited to the site of tissue damage. The reservoirs of these cells are heterogeneous in nature, consisting of a mixture of cells with varying differentiation abilities. In order to utilise these cells and to reduce the chance of unwanted events during regenerative therapies, the selection of a subset of cells that is truly multipotent is required. The behaviour of the cells is altered by the modifications to the Ti surfaces and this underpins the differences seen in clinical performance. Stem cells from various tissues have been used to seed modified Ti surfaces in order to analyse these changes in cell behaviour. Combined with subsequent expansion, selected cells could be used for regenerative or bone engineering applications.

The outer atoms of Ti form a stable, passive surface oxide layer that serves as a substrate for the formation of an osseous bond between tissue and fixture. Initial interactions occur between adhesion proteins on bone cell surfaces and the metal oxide layer. I discuss the contribution of van der Waals forces on molecular chemistry at the TiO_2 [110] surface. The nano-roughened, hydrophilic surface of Ti has been attributed to improved biocompatibility. Spectroscopic and computational techniques demonstrate that the UV induced hydrophilic conversion of Ti occurs through surface hydroxyl group reorganisation. This enhances the adsorption effect of peptide adhesion domains. Thus, altered chemical interactions between simple molecules and the crystal surface determines the differential cellular osteogenic response to rough, hydrophilic Ti surfaces, through the increased expression of extra cellular matrix (ECM) adhesion components.

Acknowledgements

University College London; Molecular Modelling and Materials Science Doctoral Training Centre and the division of Biomaterials and Tissue Engineering, UCL Eastman Dental Institute.

Straumann AG (Walderberg) for their role as EngD industrial partners and for providing Titanium discs.

The EPSRC for the research funding of this project.

The UK's HPC Materials Chemistry Consortium, which is funded by EPSRC (EP/L000202). This work made use of HECToR, the UK's national high performance computing service, which is funded by the office of Science and Technology through EPSRC's High End Computing Programme.

I would like to extend my gratefulness to the following individuals whose valuable contributions have made this thesis possible; Dr. Peter Brett, Prof. Nikolaos Donos and Dr. Ricardo Grau-Crespo for their advice, guidance, extensive expertise and companionship.

Contents

List of Figures

List of Tables

List of abbreviations

A	Anatase
AACVD	Aerosol-Assisted Chemical Vapour Deposition
ADSC	Adipose Derived Stem Cell
αMEM	alpha Minimum Essential Medium
AMBER	Assisted Model Building with Energy Refinement
AN	Anionic
APCVD	Atmospheric Pressure Chemical Vapour Deposition
BIC	Bone Implant Contact
CFU	Colony Forming Unit
CGM	Complete Growth Medium
cp	commercially pure Ti
d	day
dex	dexamethasone
DFT	Density Functional Theory
dication-free PBS	Ca^{2+} and Mg^{2+} free Phosphate Buffered Saline
DMEM	Dulbecco's Modified Eagle Medium
DMSO	Dimethyl Sulfoxide
DoS	Density of States
E_{ads}	Adsorption energy
ECM	Extracellular Matrix
EDAX	Energy-dispersive X-ray spectroscopy
EDTA	Ethylenediaminetetraacetic acid
eV	electronvolt
FACS	Fluorescence-Activated Cell Sorting
FBS	Fetal Bovine Serum
FITC	Fluorescein isothiocyanate
FM	Freezing Medium
FWHM	Full Width Half Mean
GAPDH	Glyceraldehyde-3-phosphate dehydrogenase
GGA	Generalised Gradient Approximation
h	hour
HA	Hydroxyapatite
H-bond	Hydrogen Bond
hBMSC	human Bone Marrow-derived Stem Cell
hMSC	human Mesenchymal Stromal Cell

HSC	Hematopoietic Stem Cell
K	degrees Kelvin
LDA	Local Density Approximation
LEED	Low Energy Electron Diffraction
LJ	Lennard-Jones potential
MD	Molecular Dynamics
N	number of donors
n	number of experimental replicates
NVT	constant No. of particles, Volume, Temperature-*canonical* ensemble
O_b	Bridging Oxygen
OM	Osteogenic Media
PAW	Projector Augmented-Wave
PBC	Periodic Boundary Conditions
PBE	Perdew, Burke and Ernzerhof exchange-correlation functional
PDOC	Photocatalytic Decomposition of Organic Contaminants
PhD	Photoelectron Diffraction
PI	Propidium Iodide
PP	Parent Population
P/S	Penicillin Streptomycin
qPCR	quantitative Polymerase Chain Reaction
R	Rutile
R_a	arithmetic mean of the absolute height of all points in a surface profile
RDF	Radial Distribution Function
RGD	arginine-glycine-aspartic acid motif
RT-PCR	Real Time-Polymerase Chain Reaction
SBF	Simulated Body Fluid
SEM	Scanning Electron Microscopy
SLA	Sand blasted, Acid etched surface
SLV	SLActive - hydrophilic modified SLA surface
SMO	Smooth polished Ti
SMOd	hydrophilic modified SMO surface
SP	Selected Population
SPC/E	Simple Point Charge/E
STM	Scanning Tunnelling Microscopy
SXRD	Surface X-ray Diffraction
TCP	Tissue Culture Plastic
TDS	Thermal Desorption Spectra
Ti_{5f}	5- fold coordinated Ti site
Ti_{6f}	6- fold coordinated Ti site
TIP3P	InTermolecular Potential 3P
TPD	Temperature Programmed Desorption
VASP	Vienna Ab initio Simulation Package
vdW-DF	van der Waals Density Functional
UV	Ultra Violet
ZW	Zwitterionic

Table 1: List of abbreviations

Chapter 1

Introduction

1.1 Overview

One of the reasons that research into surface science has been actively pursued is because vastly important chemical reactions, for example those involving the initial response to a biological implant, are carried out on the surface of metal oxides. The dynamics of chemical surface interactions are a very complex affair. The interaction of atoms and molecules with the TiO_2 surface environment are involved in the widely ranging topics of photocatalysis and biological implants (Steinemann, 1998; Thompson and Yates, 2006). This study of how simple molecules interact with a relatively simple crystal surface, provides important first steps towards understanding the elements of molecular chemistry on oxide surfaces. Initial biological interactions occur between adhesion proteins on bone cell surfaces and the metal oxide layer (Pierschbacher and Ruoslahti, 1984). As such, adsorption energies (E_{ads}) are important factors as they can provide a barrier to cell adhesion.

Through the study of the molecular chemistry, theoretically and experimentally, I aim to build a better understanding of the nature of the material that underlies it's performance in regard to cellular responses. Surface topographical modifications of Ti implants strongly influence cell responses. Observations of selective genetic and phenotypic cell responses to

Ti provide suggestions to the processes that occur within heterogeneous MSC populations during this surface induced event.

Titanium and its alloys have long been the material of choice for the repair of damaged or defective bone tissue. They are widely used to manufacture dental and orthopedic implants to repair damage caused by disease, aging and trauma. One of the main goals of surgeons is to reduce the time taken for an implant to become fixed into the bone to allow rapid rehabilitation after surgery. Many surface modifications have been used in an attempt to improve fixation times; physical modifications (roughening), chemical modifications (surface free energy) and coatings. The behaviour of MSCs is altered by the modifications to the Ti surfaces, and these changes in behaviour underpin the differences in clinical performances of the surfaces (Buser et al., 1991). Osteogenic stem cells from various tissues have been used for autologous transplantation to seed titanium constructs used to repair major defects. The extraction of adult stem cells combined with the *in vitro* selection of the osteogenic fraction and then seeding of constructs in bioreactors before implantation may lead to a new treatment modality.

The loss of function of tissues from disease, injury or aging causes serious health problems as well as a tremendous social and economic cost. There is an important incentive for finding techniques that promote consistent, robust bone formation for repair and regeneration. The substitution of tissues such as bone or cartilage can currently be performed with allograft materials but this introduces a risk of infection or graft rejection. Autologous bone grafts have, therefore, been considered for augmenting bone regeneration. This can eliminate immunological rejection and unnecessary pathogen transfer. Unfortunately, autologous transplantation provides a limited volume of bone grafts and is affected by potential donor site morbidity. Artificial implants have limitations too, due to insufficient bonding to bone and allergic reactions that can be caused through material abrasion. This makes the lifespan of the implant finite and can lead to the need for replacement. Many types of metallic implants have been used including gold, stainless steel and, more recently, chromium alloys. Several of these have shown significant drawbacks due to corrosion and the subsequent activated immune response. Titanium was shown in 1952 to have

a biocompatible nature (Steinemann, 1998; Schuler et al., 2006). Professor Per-Ingvar Brönemark of Sweden discovered that titanium fuses to bone (Sullivan, 2001). This property, osseointegration, involves the direct attachment or connection of osseous tissue to a material without any intervening connective tissue. A direct structural and functional connection between living bone and the load bearing surface of the artificial implant is thus formed. Titanium is often considered the 'gold standard' material for repairing damaged bone tissue, for example; titanium stems are widely used in the replacement of hip or knee joints, attachment of metal plates is used for the mending of badly broken bones and ceramic crowns are inserted into sockets for the replacement of missing or damaged teeth.

There is now the possibility of engineering tissue substitutes *in vitro* by seeding multipotent stromal cells or osteoblasts onto titanium constructs. This has provided new strategies for cranial and maxillofacial reconstruction as well as for the restoration of damaged or diseased bone.

1.2 Titanium properties

There are a number of reasons that Ti is considered to be biocompatible. These can be attributed to its tolerability by the body. It has a tendency not to precipitate phosphates and other minerals from bone and it has demonstrated strong interactions with adhesion proteins. Under atmospheric conditions, a $\sim$ 3-7 nm oxide layer spontaneously forms on Ti surfaces. This passive layer a strong, direct effect on the biocompatibility and success of the implant.

Any material that is implanted into the body is considered to be 'foreign' and has the potential to cause chemical, physiological or mechanical insult to living tissue. Electron exchange occurring at the metal surface, following contact with water and tissue fluid, can lead to denaturation of the tissue surrounding the metallic implant. If metal ions become released during the corrosion process they are considered to be toxic to living cells. The tendency for a metal to do this can be measured using its polarisation resistance (figure

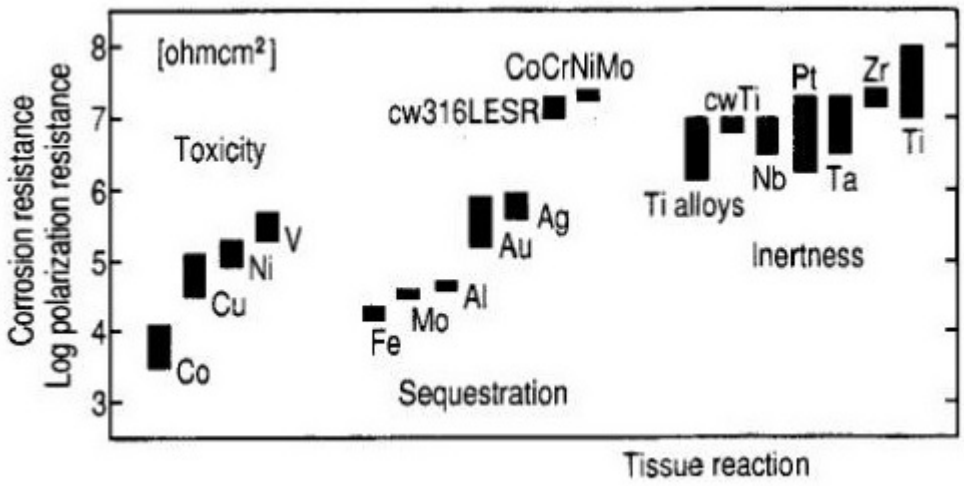

Figure 1.1: Diagram to show tissue reaction for various metallic elements and practical alloys, grouped according to toxicity, sequestration and inertness, against measured polarisation resistance. Corrosion resistance is roughly proportional to the measured log of polarisation resistance. Figure from Steinemann (1998).

1.1). The electron exchange processes that lead to the denaturation of macromolecules occurs most notably in elemental vanadium and copper the least. In addition to polarisation resistance, toxic effects are also observed from stainless steel and colbalt-based alloys (Steinemann, 1998).

Titanium itself is reactive in its elemental state. In air and electrolytes, an oxide layer forms at the surface that is particularly stable and protects from further corrosion. This passive layer imparts the metal with corrosion and ion-leaching resistance. It provides a barrier by encasing the toxic bulk element and enacts as an organic substrate that is recognised by the body's tissue reparative system leading to the attachment of molecules, cells and eventually bone (Liu et al., 2004).

The dense oxide layer formed provides a positive effect by preventing any metal ions from reaching the outer surface and being released into the electrolyte. In this way, the unwanted product of corrosion, the production of free ions, does not occur. The titanium oxide in the very thin surface film exists in an amorphous or glassy state and occludes the availability of electrons in the bulk metal towards the electrolyte or living tissue, thus

concealing the naked Ti surface from the bone into which it is implanted.

There are three polymorphs of titanium dioxide (TiO_2); rutile, anatase and brookite. The most thermodynamically stable structural variant is rutile (R). Surface energy, γ, describes the thermodynamic stability of the surface. For rutile the most thermodynamically stable crystallographic plane is [110] which represents cleavage along the orthorhombic *ab* face diagonal. The surface has an amphoteric nature and the zero point of charge occurs at ∼pH 6. In comparison, the zero point charges of Al_2O_3 and ZrO_2 are ∼pH 9 and ∼pH 2 for SiO_2. Hence, at physiological pH values, the surface of titanium oxide has no charge whereas aluminium oxide and zirconium oxide are negative and quartz (SiO_2) has a positive charge. The zeta potentials between a dispersed layer of natural phosphate minerals, as found in bone, and the stationary layer of fluid have also been measured at the zero point charge. The measurements indicate a stability of the colloid dispersion of body fluids that is in close contact to the Ti surface. This prevents the precipitation of phosphates and other bone minerals out of solution at a pH value that exists in the body. This acts to prevent further leaching of bone minerals and the weakening of the bone structure around the implant (Somasundaran P, 1984).

Strong adhesion occurs between bone and the implant surface. Histological and microscopic examinations further defined osseointegration as the state attained by clinically successful implant devices, characterised by the close apposition of new and reformed bone with (an implanted) fixture; that at the light microscopic level has no intervening connective or fibrous tissue (Branemark, 2005). There are several stages that are considered to occur in sequence during the osseointegration stage. Osteoinduction is the initial event constituting the migration of tissue progenitor cells to the implant surface; and their attachment, proliferation and subsequent differentiation on the substrate. It is followed by osteoconduction, which is the formation of woven bone at the bone-implant interface leading to an osseous union between implant and adjacent tissue. It is further divided to (i) contact osteogenesis, the de novo bone formation on the surface of the implant; and (ii) distance osteogenesis, the formation of bone on the surface of old bone apposing implant.

Small molecules such as water, ions and serum proteins adsorb to the electro-statically

negative surface of the implant; saturating it almost instantaneously. Platelets amass at the implant site and attach to the surface through arginine-glycine-aspartic acid (RGD) motif containing adsorbtion proteins. Surface topography offers a strong substrate for fibrin fibres, formed during the initial platelet cascade, to adhere to. Migrating MSCs are suggested to use these fibres as scaffolds in order to translocate to the surface where they differentiate to an osteoblast phenotype. The newly formed osteoblasts deposit a mineralised matrix on the implant surface (Davies, 2003). Ultrastructural scanning electron microscopic studies (SEM) report that a non-uniformly distributed layer of amorphous material $\sim$ 20-400 nm thick is deposited peripheral to the implant.

A layer of apaptite is found on titania, alumina and hydrated silica implant surfaces when placed in simulated body fluid (SBF) (Li et al., 1994). Hydroxyapatite, $Ca_{10}(PO_4)_6(OH)_2$ (HA), is a major component of bones and teeth where it grows as nano-sized mineral platelets at nucleation sites on a collagen type 1 template. The apaptite platelets are $\sim$ 2-4 nm thick and are arranged in a orderly fashion within and around the collagen fibrils (Almora-Barrios and de Leeuw, 2010). This HA layer supresses the bioreactive nature of an implant and the porous structure encourages bone cell growth.

The structure of a tissue and its interaction cohesion occurs along different length scales - the space between bone and vessels in soft tissues is in the order of mm, the size of cells is in the order of μm and the Debye length, determining the interaction distance of chemical forces, is in the nm range. Fibronectin is one of the main adhesion proteins involved in bone cell attachment, and the RGD tripeptide domain is the focal point where cells attach to the surface of large macromolecules (Pierschbacher and Ruoslahti, 1984). Titanium dioxide, being amphoteric, has four or five reactive groups of acidic and basic character per nm^2 of surface. The volume of an amino acid molecule in the RGD tripeptide is in the region of 0.1 to 0.2 nm^3. For amino acids spread out on the surface, about 4 or 5 molecules will cover an area of 1 nm^2 which matches well with the number of available bonds on the inorganic substrate. Thus, strong interactions can occur between the RGD tripeptide molecules and the surface. A proton is exchanged and electrostatic energy is gained (Boehm, 1971) providing a mechanism for the short range interaction for adhesion-

promoting factors of living tissue to the native oxide of titanium.

The biological factors that determine the contact of the implant to bone and the bonding strength can be influenced through, physical modifications (roughening), chemical modifications (surface free energy), and coatings. The roughening of surfaces (figure 1.2) encourages the entrapment of fibrin protein, adhesion and mechanical stability of implants in host bone.

1.2.1 Titanium surface modifications

Titanium is a possible material for use in clinical implants because bone regeneration can occur on the surface with no evidence of host rejection. Much attention has been made on improving the properties of titanium as a biomaterial. It has been shown that osteoblastic cell adhesion, growth and differentiation are related directly to surface energy and roughness (Wall et al., 2009; Le Guehennec et al., 2008).

Physical modification - roughening

Osteoblasts have been shown to respond more favourably to roughened surfaces than smooth (Brett et al., 2004). Roughened surfaces can be fabricated in various ways to produce defined macro-, micro- and nano-topographies. These include micro-machining, plasma spraying, particle blasting and acid etching.

Surface roughness has been an important factor for establishing reliable bone-anchored implants. Micro-topography is the measure of physical landscape of a surface within the dimensional range of 1-10 μm along a vertical axis from a mean surface plane. Nano-topography is defined as a physico-chemical measure of the geometric landscape of a surface within a spatial dimensional range of 1-100 nm from the mean plane. At this spatial range, physical features influence chemical forces emanating from surface constituent atoms and molecules, which subsequently alter surface energy. The differences in surface roughness between smooth, polished (SMO) and sand blasted, acid etched-roughened Ti (SLA) under

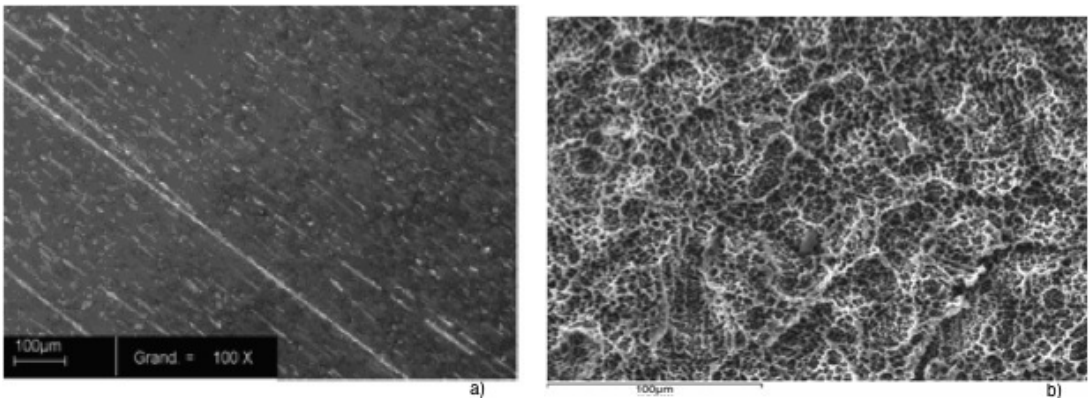

Figure 1.2: SEM micrographs showing the difference in surface roughness of titanium discs (a) smooth polished Ti, SMO has a R_a of 0.03 μm (b) Roughened Ti, SLA has a R_a of 4.12 μm. Images taken at the Eastman Dental Institute.

SEM are shown in figure 1.2. Parallel groves can be seen on the SMO surface as a result of polishing with fine grit silicon carbide grinding paper (figure 1.2a). The plane polished Ti surface has a mean roughness value (R_a; arithmetic mean of the absolute height of all points in a surface profile) of 0.03 μm. The SLA surface (figure 1.2b) shows wide cavities, 20-40 μm in diameter, produced by the Al_2O_3 blasting process. Some surface contamination may exist due to alumina or titanium oxide grit blasting particles. This has been thought by Esposito *et al.* to hamper the osseointegration process (Esposito et al., 1998). Acid etching, in a mixture of HCl and H_2SO_4, produces nanometre-sized topography with a R_a value of 4.12 μm.

In vitro studies have provided a positive correlation between surface roughness and cellular attachment as well as subsequent osteoblast-like cell activity (Rönold et al., 2003). This has been supported using *in vivo* studies, by groups such as Buser *et al.*, who measured the mechanical testing strength of the connection between bone and implant (Buser et al., 1991). Rönold *et al.* suggested that an upper limit exists for the correlation between surface roughness and bone fixation (Rönold et al., 2003). Using an *in vivo* tensile test procedure they found that a R_a of 3.62 μm created by grit blasting gave the optimum functional attachment between bone and implant. It was speculated that a surface with more pits and undercuts, providing a larger surface area, is better for bone cell attachment as seen under SEM (figure 1.3).

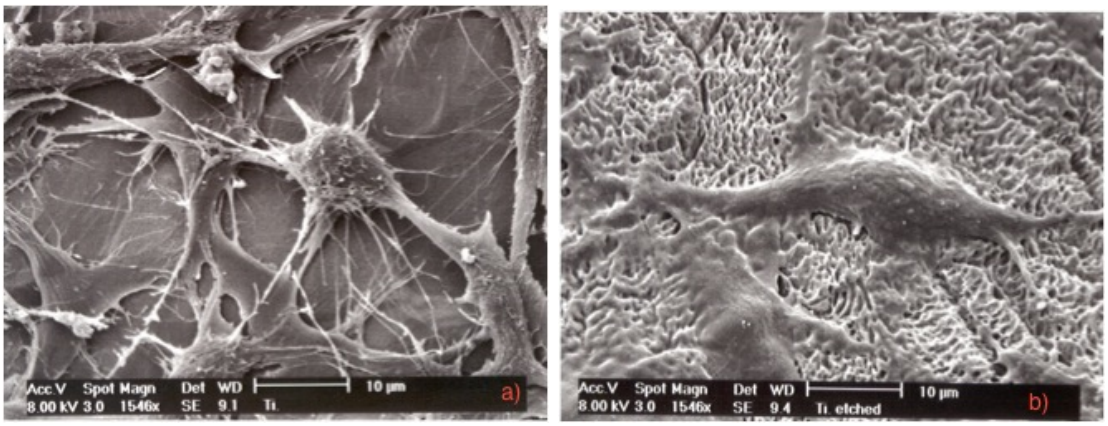

Figure 1.3: SEM of MSC attachment on titanium surfaces; (a) smooth polished Ti, SMO (b) roughened Ti, SLA. The SMO seeded cell has cytoplasmic processes emanating from the periphery. The cell on SLA is relatively more stretched, settling into the roughened surface, compared to the cell on SMO. Thus the SLA surface demonstrates stronger cell attachment. Images from Brett et al. (2004).

Wall *et al.* have shown that initial stem cell differentiation was enhanced by roughened topographies (Wall et al., 2009). This was accompanied by a reduction in cell number early in the culture and increased expression of osteogenic markers. This relates to higher implant survival rates in clinical practice for roughened surfaces compared to polished surfaces.

The biological response of a host is related to the surface topographic characters of an implant at the micro and nano-scales. The roughness of the micro-roughened surface has an influence on the biocompatibility, mechanical characteristics and interlocking effect between the implant and tissue. A roughness ranging from 10 nm to 10 μm influences biocompatibility due to the topography being within the same size range as a biomacromolecule and a cell respectively. A nano-roughness of less than 10 nm at the surface corresponds to defects in the crystal structure. Vacancy defect, such as Schottky defects, result from vacant lattice sites that would be occupied in the crystal structure. Grain boundaries are where the crystallographic direction of the lattice abruptly changes. Step and pit structures result from a stepped surface and random, infrequent hollow channels developing on surface at the atomic scale. These naturally occurring crystallographic defects are in the active region of the molecular scale and significantly affect the surface

energy of biomaterials. This has a further influence on the interface of the implant and the integration with biomolecular material and, ultimately, affects the adhesion, spreading and growth of the cell.

Chemical modifications - surface free energy

Titanium can be modified to have increased surface roughness, but also to have a higher degree of wettability. SLActive (SLV) is a surface produced by Straumann AG, from previously roughened titanium, that is conditioned in a N_2 atmosphere rather than air and immediately preserved in an isotonic saline (NaCl) solution in water. Under these conditions, SLV has a relatively large quantity of hydroxyl ions retained on the surface oxide compared to SLA (Rupp et al., 2006). These hydroxyl ions greatly increase the substrate's surface free energy, rendering it hydrophilic, as assessed by a dynamic water contact angle analysis yielding measurements of 0° for SLV, compared to 138.3 ± 4.2° angles for SLA and 96° angle for SMO surfaces (Buser et al., 2004).

Surface energy, though influenced by topography, is strictly a chemical variable that increases the surface's electrostatic negativity and apolarisation to water, increasing wettability. This parameter is determined by measuring the contact angle between a water droplet and a surface that reflects the ratio of adhesive forces between surface-water and cohesive forces between water-water molecules. The larger the adhesive than cohesive forces, the smaller the contact angle and more 'hydrophilic' a substrate, and vice versa. Wettability and surface energy are key parameters in the adhesion and spreading of osteoblastic cells (Liu et al., 2004). A previous study has suggested that faster healing and greater implant stability was achieved with the SLV implant surface than with conventional, hydrophobic surfaces (Buser et al., 1991). In addition, osteoblastic differentiation was enhanced by the most hydrophilic surface. Wall *et al.* reported a better osteogenic response to SLV compared with the more hydrophobic SLA surface (Wall et al., 2009). This was seen to be related with an increased gene expression of the osteogenic promoter WNT5A amongst others, which is responsible for osteogenic differentiation, in response to this surface.

Chemical modifications - coatings

One of the key advantages of Ti, over other metallic implant materials, is that chemical coatings are not required for the induction of the osteogenic response in MSCs *in vitro* and for *in vivo* osseointegration. Chemical composition has been altered and tested in various scenarios but are shown to be inferior in the long run compared with nude Ti (Schuler et al., 2006).

The native surface can be modified for roughness and with increased hydrophilic properties in order to improve it's biocompatability. In the modified Ti surfaces, the main implant to biological interface occurs via the TiO_2 structure. The mechanisms, for this interaction and those involved in the cell responses to it, are not fully understood.

1.3 Bone

Bone tissue consists of a collagen and calcified mineral based ECM. The ECM can be subdivided into inorganic salts and an organic matrix (Thibodeau and Patton, 2007). The predominant mineral salt is HA, a combination of calcium phosphate $Ca_3(PO_4)_2$ and calcium hydroxide $Ca(OH)_2$, which combines with di-cations and carbonates in the organic matrix. The bone mineral is the basis of the hardness of the skeleton and it resists loads caused by the weight and movement of the body (Sommerfeldt and Rubin, 2001). The organic part is a matrix of collagen fibers primarily composed of type I collagen. The architecture of this composite material ascribes bones their unique hardness and mechanical elasticity to sustain large forces.

Bone is divided into two distinct types based on the architecture of the connective tissue ECM; cortical and cancellous (figure 1.4). Cortical bone is a relatively dense, compact type of osseous and forms the outer part of a bone. The cancellous type occurs as spongy with a 'honey comb' of branching bars, plates and rods called 'trabeculae' (Vassilios et al., 2001). This architecture accommodates a higher level of vascular tissue compared to cortical bone that nourishes bone marrow and it's embedded populations of various stem

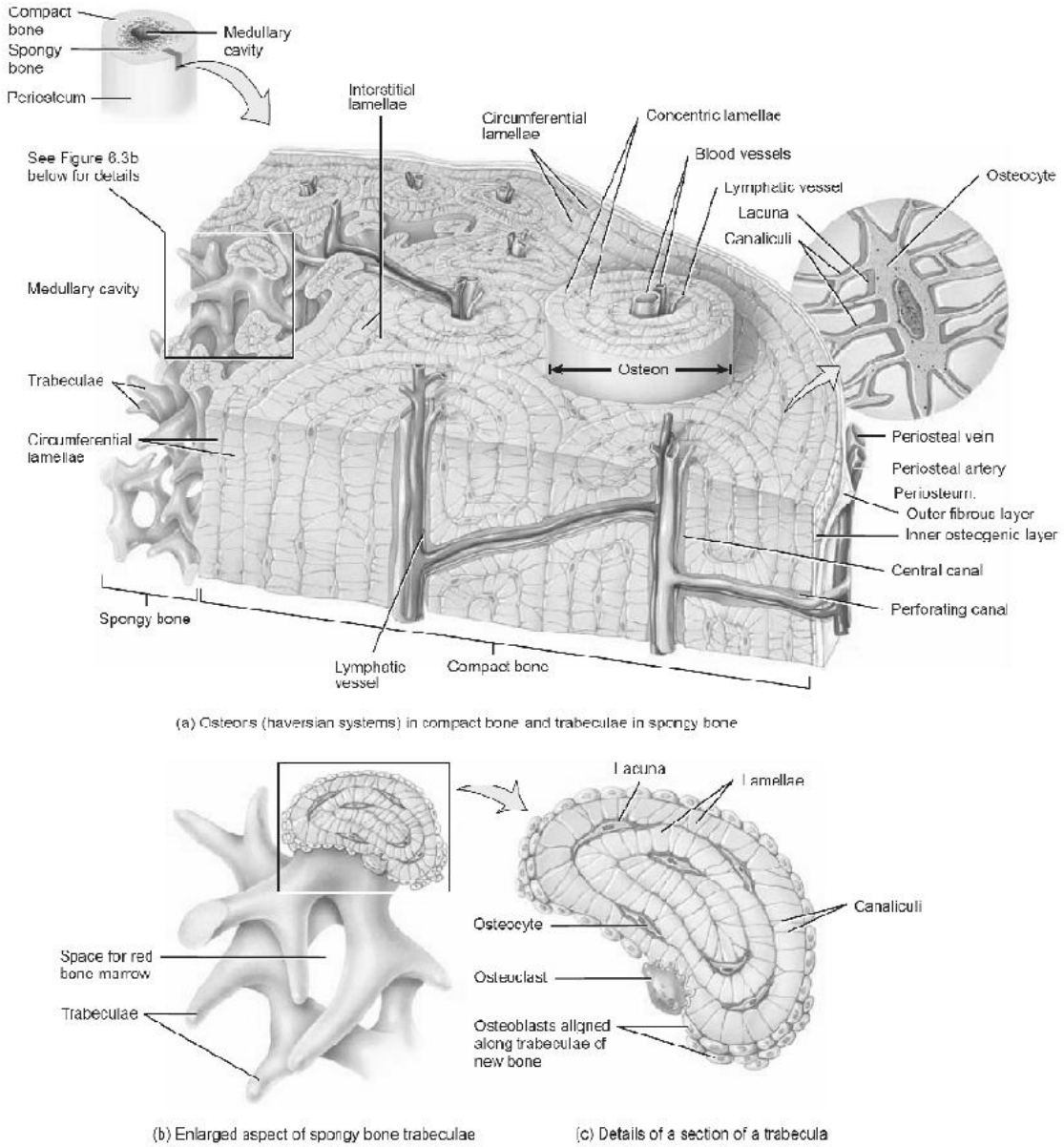

Figure 1.4: Microscopic structure of a diaphysis segment of bone showing a cross section along the transverse and sagittal planes.
(a) The axis from right to left shows a membrane that covers the outer surface, the periosteum, followed by compact cortical bone and the trabeulae structures of spongy bone. Within cortical bone are osteons, composed of the haversian canal, containing resident blood and lymphatic vessels and surrounded by concentric rings of lamellae. Spaces between lamellae are either lacunae (osteocyte sites) or emanating canaliculi, indicated in the magnified representation on the upper right hand side.
(b & c) Magnified views of the cross section of a trabecula indicating the irregular arrangement of lamellae. Figure (c) also depicts osteoblastic and osteoclastic activity on the periphery. Figure from Tortora and Derrickson (2009).

cells (Tortora and Derrickson, 2009).

There are three major bone cell types; osteoblasts, osteocytes and osteoclasts that are all involved in the remodelling process of bone (Thibodeau and Patton, 2007). Osteoblasts are derived from osteoprogenitor cells (MSCs) and take on the task of ECM formation. The osteoblasts secrete collagen and other proteins which are gradually mineralised. With ECM formation there is an increase in resistance of mass-transfer to the secreting cells. The osteoblasts buried within the mineralised matrix differentiate into osteocytes. These terminally differentiated osteocytes now obtain mass-transport via compression-derived, fluid convection through much smaller channels, the lacuno-canaliculi (lacunae: approximately 5 μm radius: canaliculi: approximately 200 nm radius). Despite the reduced porosity, the fluid flow in the lacuno-canaliculi remains significant to carry out mass-transport of signaling molecules, nutrients to, and wastes from, the osteocytes due to stronger induced fluid compression effects. In addition, this generates an important mechanical stimulus in the mineralised matrix. The osteocytes act as mechanosensory cells by producing signaling molecules in the bone tissue in response to load induced strains. Osteoclasts, which are the third type of bone cells, are derived from hematopoietic stem cells (HSCs) and their main function is to direct new bone formation by degrading the old mineral matrix (Schwartz et al., 1999b).

1.4 Multipotent Stromal Cell characteristics

Multipotent Stromal Cells (MSCs) can be defined as lineage unspecified, functionally undifferentiated, mononuclear cells that are capable of differentiating into the constituting cell types *in vivo* while being able to home in to other tissues to participate in extraparental tissue repairs (Loeffler and Roeder, 2002). These have the appearance of fibroblastic trigonal cells in culture (figure 1.5) (Pittenger et al., 1999). MSCs are functionally associated with tissue regeneration and repair (Caplin, 2008). These are the primary cells recruited to repair damaged bone and are responsible for the tissue regeneration that occurs very early at the bone-implant interface, by differentiating to form osteoblasts

Figure 1.5: Confocal image of MSCs on TiO_2 coated glass. Actin filaments are stained in green using phalloidin and the nucleus in red using propidium iodide (PI). The cell at lower left is in the process of cell division. The cell at upper right represents a large spindle or flattened like cell, named a mature marrow stromal cell (Colter, 2000; Colter et al., 2001). The smooth surface used here encourages cellular spreading. Cells seeded on uncoated glass surfaces showed a similar patten of cellular spreading and actin filament arrangement. Roughened surfaces are reported to elicit actin filament reorganisations (Miron et al., 2010). Magnification x400. Scale bar represents 50 μm.

that establish osseointegration through the deposition of the first calcified tissue onto the implant surface (Cuomo et al., 2009; Davies, 2003).

For these cells to be used effectively in the tissue engineering process, it is generally accepted that they need to be differentiated into the desired lineage before they are introduced into patients. There are concerns that clinical use of undifferentiated stem cells may lead to uncontrolled proliferation in the formation of cancerous tissue (Davies, 1998). There has been great interest in the exploitation of MSCs and their expanded progeny as therapeutic agents for tissue regeneration and repair.

The study of MSCs in their native environment has been hindered by the inability to identify them *in situ*. Nonetheless, rare cell populations in the bone marrow that are highly enriched in MSC activity have been isolated and studied *in vitro*. The MSCs are mainly identifiable by their *in vitro* properties; in particular, their distinct characteristic to strongly attach to tissue culture plastic (TCP). These cells are generally regarded as TCP adherent mononuclear cells. They are negative for HSC markers, are highly replicative forming single cell derived clonal colonies, and are multipotent - able to differentiate to osteoblastic, adipocytic and chondrocytic like cells *in vitro* when induced with appropriate stimulants (Lazennec and Jorgensen, 2008). In the bone marrow, MSCs enter differentiation pathways to replenish mature, osteoblasts, adipocytes and hemosupportive stroma. Recent studies have shown that bone marrow-residing nesting MSCs are innervated by sympathetic nervous system fibers and mediate neural control of hematopoiesis.

Multipotent stromal cells can be found in many different tissues; bone marrow, muscle and adipose. They are thought to be a heterogeneous population of multipotent cells that form part of a supporting reticular network thought to regulate HSC differentiation, and are functionally implicated in the homeostatic repair of mesoderm tissues (Lazennec and Jorgensen, 2008). The heterogeneous nature of MSCs infers that a TCP adherent bone marrow isolate is a population of different cell types that vary in lineage commitment and differentiation potentials. This population is proposed to contain a small proportion of the extremely rare true somatic adult stem cells, combined with a larger proportion of early stem derived progenitor cells of mesoderm tissues and their somewhat committed

precursors (Benayahu, 2007).

The cell source used for tissue engineering should be expanded *in vitro* when cultured in two-dimensional monolayers of adherent cells in specialised medium. They should also have the capacity to differentiate in a manner that can be reproducibly controlled. The type and maturity of the cells substantially influences the robustness and the nature of the regenerative response.

1.4.1 Bone marrow derived MSCs

MSCs were originally found to reside in the stromal adherent fraction of bone marrow, where they sustain the homeostatic turnover of non-hematopoietic stromal cells, regulate HSC maintenance and might contribute to vascular stability. Bone marrow derived cells are the most widely studied source of MSCs. There are two main stem cell populations with distinct progenies that have been identified within bone marrow. These are the HSCs and the MSCs. The MSCs were first termed CFU-Fs because of their ability to generate single cell-derived colonies, in analogy to their hematopoietic counterparts. MSCs from almost all embryonic and postnatal tissues can be expanded *in vitro* to generate cell cultures that conserve trilineage potential. The HSCs include all lymphoid and myeloid lineages that finally produce blood circulating cells and organ resident cells of the immune response. They are tightly regulated by the bone marrow microenvironment in terms of renewal and differentiation (Park et al., 2007). MSCs are rare in bone marrow representing $\sim$1 in 10,000 nucleated cells. The MSC fraction is characterised by the ability of the cells to adhere to plastic. MSCs isolated from adult human bone marrow are the obvious choice for bone tissue engineering as these cells have high potential for osteogenic differentiation, although other cell sources may be relatively easier to procure. They are also able to be expanded greatly in culture to levels of cell numbers that are therapeutically useful, whilst retaining their growth and multilineage potential due to the self renewing nature of the undifferentiated cells. MSCs can be expanded *in vitro* to generate mesenchymal stromal cultures, which under appropriate conditions, can differentiate into adipocytes, chrondrocytes and osteoblasts.

The osteogenic differentiation of MSCs can be initiated *in vitro* by dexamthasone (dex), L-ascorbic acid and inorganic phosphate (Muraglia et al., 2000). During osteogenic differentiation several genes are up regulated such as Alkaline phosphatase (ALP), Collagen 1A1 (Col1A1), Osteopontin (OP) and Bone sialoprotein (BSP) (Marie and Fromigue, 2006). Runt-related transcription factor 2 (Runx2), has also been identified as a transcription factor involved in osteogenic differentiation, and some factors such as Sox9 are down regulated at the point of osteogenic determination (Jonason et al., 2009). Runx2 controls various signaling pathways that are used to control the expression of many genes such as the late osteogenic marker, OP (Weiss et al., 1986). OP is a human gene product that functions as an extracellular, structural glycoprotein in the organic component of bone. Type 1 collagen is the major protein component in bone tissue. It provides a template for mineral deposition. Procollagen is its soluble precursor molecule and comprises two pro-α1 and one pro-α2 chains that are encoded by Col1A1 and Collagen 1A2 (Col1A2) genes (Van der Dolder and Jansen, 2007).

The study of the MSC has identified the lack of a singular discriminative marker. The present set of markers may represent an overlapping repertoire of proteins between three theoretical sub-populations of an adherent isolate, while ignoring the heterogeneity such as the transcription and post translational modification of important lineage determining regulators. Attempts at characterizing the cell type on the basis of a consensus of cell surface expressed molecular markers has revealed three categories of proteins that differentiate MSCs from cells of a similar *in vitro* profile. These categories include positive, negative and variable surface markers on hMSCs. Stro-1 is a candidate for an MSC-related cell surface marker. For example, Fukiage *et al.* showed that a fraction of hBMSCs with the anti-Stro-1 antibody was shown to be rich in MSC-like cells (Fukiage et al., 2008). Mienel *et al.* reported that the MSC nature of the cells can also be determined on the basis of the expression of CD105/endoglin (a marker of MSCs, formerly known as SH2) and CD71 (a receptor expressed in the proliferating cells) as well as the lack of expression of CD31 and CD34 (markers of cells that are of endothelial or hematopoietic origin) (Meinel et al., 2004). Fukiage *et al.* found CD106 to be a reliable indicator for osteogenic differentiation potential of MSCs (Fukiage et al., 2008). A cell type that has been recently hypothesized

as being 'parental in lineage to MSCs is the Perivascular cell, or Pericyte. This cell occurs the outer lining on endothelial cells in capillaries and micro vessels and is regarded as a vasculature resident predecessor of true mesenchymal stem cells (Crisan, 2008). Pericytes have been isolated on the cell surface expression of $CD146^+$ and $CD34^-$ from human adult tissues, and have shown to be capable of clonogenic self renewal, forming single cell derived colonies, and undergoing osteogenic, adipogenic, chondrogenic and myogenic lineage differentiation *in vitro* (Crisan, 2008). This proposition implies that MSC may be part of a regenerative system that, like the many systemic organisations (immune and nervous systems etc), is engaged in replacement of tissue to recuperate loss of organ function; albeit to a limited extent.

Alkaline phosphatase, ALP, activity is an important marker of early osteogenic differentiation, bone formation and matrix mineralisation. It indicates the commitment of mesenchymal stem cells towards the osteogenic phenotype (Lian and Stein, 1993). The synthesis of ECM components such as osteocalacin and type-1 collagen can also provide evidence of the ability of cells to exhibit an osteoblastic phenotype as does any observed deposits of calcified matrix *in vitro.* An increase in the expression of osteogenic markers SPP1 (secreted phospoprotein1), Runx2 and iBSP (integrin binding sialoprotein) as well as the osteogenic promoter, WNT5A may be used to indicate an osteogenic response (Wall et al., 2009).

1.4.2 Adipose-derived stem cells

Adult adipose-derived stem cells (ADSCs) have generated much interest, given reports suggesting that they harbour significant differentiation capability and undergo skeletal (Tapp et al., 2009), endothelial (Brzoska et al., 2005), myogenic (Rodriguez et al., 2006) and even neuronal differentiation (Jang et al., 2010).

They are potentially an ideal cell source, not only because abdominal fat is relatively abundant but also because its harvest is minimally invasive and a much less traumatic procedure than bone marrow harvest. Hence, it is much better suited, particularly in

pediatric patients where the size of defects may be greater than the amount of autologous bone available. ADSC transplants have provided effective treatment options for soft tissue defects, and non-healing wounds (Kim et al., 2011). ADSCs are thought, here to support the regeneration of tissues through their ability to secrete angiogenic growth factors such as vascular endothelial growth factor (VEGF) which promotes neo-vascularisation of new tissues (Salgado et al., 2010). ADSCs have been shown to be particularly useful in aesthetic surgery (Eremia and Newman, 2000). Current clinical therapies involving ADSCs have also shown promising results for bone regeneration. In a study by Lendeckel *et al.*, ADSCs have been combined with milled autologous cancellous bone and fibrin glue to repair a large calvarial defect (Lendeckel et al., 2004). This resulted in new bone formation and near complete osssification of the preoperative defect at three months. However, it is difficult to assess the degree of the therapeutic effect of ADSCs, as multiple concomitant treatments were used in this study. More recently, Thesleff *et al.* transplanted ADSCs seeded in β-tricalcium phosphate (β-TCP) granules to successfully repair calvarial defects (65-90 mm x 37-75 mm) in patients without the use of autologous bone grafting (Thesleff et al., 2011). This suggests that ADSCs alone are capable of ossifing defects without the use of exogenous growth factors. In this way, they may provide a relatively simple method of autologous bony reconstruction with little donor site morbidity.

Adipose tissue derived stem cells have shown a differential potential similar to other MSCs with the additional advantage that they typically provide a higher yield on isolation and a greater proliferative rate in culture compared to BMSCs *in vitro* (Higuchi et al., 2011). Most ADSCs express markers of tissue specific commitment / differentiation, while maintaining a proliferative, undifferentiated morphology. Exposure to chrondrogenic, osteogenic, adipogenic or neurogenic conditions have resulted in morphological differentiation and tissue-specific marker upregulation. These findings suggest that the ADSC 'lineage mixed' phenotype underlies their significant plasticity. ADSCs have proven to be favourable candidates based on their osteogenic capacity *in vitro*. Selective ADSC osteogenic differentiation has been observed in a study by Guasti *et al.*, however, chrondrogenic induction was always found to result in both cartilage and bone formation in commercial chrondrogenic media (Guasti et al., 2012).

1.4.3 Stem cells isolated from other mesenchymal tissues

Muscle tissue contains several different cell types. Most research, such as by Qu-Petersen *et al.*, focused on the isolation of a myogenic population from muscle to use in regeneration applications to treat diseases such as muscular dystrophy (Qu-Petersen et al., 2002). One isolated population, which was named muscle-derived stem cells (MDSCs), showed an increase in the expression of neuronal and endothelial markers. When it was discovered that muscle tissue contains cells that are not restricted to the myogenic lineage, attempts were made to isolate other MDC-derived subpopulations. Two markers that have been used are CD56, which has been used as a satellite cell marker and $\alpha 7$, which has been used as a mayoblast marker (Mackey et al., 2009; Ozeki et al., 2006). It was concluded that the MDCs^{CD56+} population consisted of cells that were committed to the myogenic lineage. The cells that were lacking CD56 had higher plasticity, with the ability to express osteogenic and adipogenic genes when stimulated accordingly.

Dental pulp tissue has been shown to comprise of mesenchymal cells that are derived from the neural crest. Some of these cells possess multiple differentiation properties and have been termed dental pulp stem cells (DPSCs). hDPSCs play a role in the regeneration process of tissues after injury. As such, their isolation and recruitment present strategies for regeneration and tissue engineering applications (Sloan and Waddington, 2009).

Researchers have also isolated stem cell-like populations from other tissues, for example from neonatal foreskin (Jones and Watt, 1993), cartilage (Dowthwaite et al., 2004) and oral mucosa (Davies et al., 2010). All these methods have used the cell's adhesion properties to fibronectin to isolate stem cell-like populations.

1.5 Stem cell expansion for regenerative purposes

As an application in regenerative medicine, stem cell selection by modified titanium and their subsequent expansion could be used for autologous transplantation at an implant site in order to aid regeneration and improve healing time.

It is necessary to increase the limited number of stem cells harvested from a single patient to be used in an autologous transplantation. Human MSCs are the cells of choice for a number of reasons. Firstly, MSCs are self-renewable, multipotent progenitor cells with the capacity to differentiate into several distinct mesenchymal lineages, including bone, cartilage, adipose, tendon and muscle tissue (Park et al., 2007). Osteogenic differentiation of MSCs results in the formation of osteoblast cells required for bone growth. They are the primary cells to be recruited to the site of an injury and initiate the healing process through the production of calcified tissue (Thibodeau and Patton, 2007). In this way, MSCs are thought to be the reason why bone can heal itself without scaring (Sommerfeldt and Rubin, 2001). Using adult stem cells in tissue engineering applications also has an advantage since MSC populations expand much more readily than mature cell types (Alhadlaq and Mao, 2005). For example, osteoblasts can only be obtained in small numbers and posses low proliferation capacity *ex vivo* whereas, theoretically unlimited numbers of MSCs can be obtained.

MSCs can be pre-differentiated on applicable scaffolds by addition of osteogenic differentiation factors, such as; BMPs (bone morphogenetic protein); or combinations of dexamethasone, β-glycerol phosphate and ascorbic acid, and then implanted *in vivo*. However, Ti surfaces have a degree of osteogenic stimulation and might be used to select a population of cells from the MSC population that are pre-determined to differentiate along the osteogenic lineage. This could reduce the need for the use of chemical osteogenic factors.

The first step is the proliferation of cells in order to establish a sufficient number of primary undifferentiated cells to take forward to tissue culture. Expansion from a small number of cells resulting from the selection procedure, by many orders of magnitude, is then required. These cells could be seeded onto either a 3D microporous scaffold or onto a 2D surface, such as in the case of a plate Ti implant.

A final approach that might be of use is in the preparation of tissue constructs. Using the methods above to achieve a good distribution of osteoblastic cells and mineral matrix deposition could be followed by implantation into the host at a site distant from the final site of implant. This would allow the construct to develop a capillary system under the

natural environment *in vivo* before final implantation into the site of need. This is a process that has been successfully been used by Warnke *et al.* in the reconstruction of a mandible in a patient after surgery to remove a large tumour (Warnke et al., 2004). The approach utilised a multi-step procedure in which harvested stem cells were combined with different growth factors (bone morphogenic proteins BMP-2 and BMP-7) in a Ti scaffold, which were then re-implanted into a patient's muscle tissue to allow for ectopic bone formation. Following a seven to nine month period after implantation, the titanium-enclosed ectopic bone was transplanted with the surrounding muscle to fill the bone defect. This technique provided excellent functional and aesthetic results, although it is fairly complex and requires several steps over a period of several months. A procedure proposed by Sandor *et al.*, involves a one-step surgical process where harvested cells are placed on a scaffold of β-TCP with BMP-2 and then added to a molded Ti mesh in order to fill a mandible defect (Sandor et al., 2013). This allows for *in situ* bone formation and circumvents the need for ectopic bone development and a second surgical site. While this technique has produced favourable clinical outcomes with histologic signs of bone formation after transplant, the mechanisms behind osteogenic transformation need to be more fully understood before a comparison into the efficacy of different cell based treatments can be made.

1.6 Computational materials science

During the last 20 years there has been a dramatic explosion in the application of computational chemistry techniques to a vast range of different chemical problems, including biomaterials science. Indeed, possibly more so than any other field of material chemistry, computational methods have proven to be a very successful tool in understanding, with atomic detail, key aspects of surface science and can be considered a powerful complement to experimental work.

Computational methods allow us to calculate the geometries and properties of chemical systems at a molecular level. Further analysis of these calculated properties allows us to

determine bond and reaction energies, reaction pathways and thermodynamic properties. More importantly, they provide a means to study systems under conditions that are difficult to probe in the laboratory and allow us to study properties that are often impossible to analyse experimentally. Here I will present a very general discussion of two methods that are employed for electronic / atomistic modelling in this research; namely Density Functional Theory (DFT) and Molecular Dynamics (MD).

1.6.1 Density Functional Theory

Electronic structure methods apply the laws of quantum mechanics in an attempt to solve the Schödinger equation, which can only be solved for the simplest atom and molecule: the hydrogen atom and H_2^+. Therefore, to solve the equation for other systems requires approximations.

The density functional theory enables the properties of a system to be solved in terms of electron probability densities ρ, rather than the wavefunction Ψ i.e. the electron density of a system contains the same information as the multi-electron wave function and is defined as:

$$\rho(\mathbf{r}) = \sum_{i=1}^{N} |\Psi_i|^2 \tag{1.1}$$

where, $\rho(\mathbf{r})$ denotes the total electron density at a particular point $\mathbf{r}$ in space.

The DFT is based on a theorem by Hohenberg and Kohn (Hohenberg and Kohn, 1964) which defines energy as a function of the electron density:

$$E[\rho(\mathbf{r})] = \int V(\mathbf{r})\rho(\mathbf{r})dr + F[\rho(\mathbf{r})] \tag{1.2}$$

where, $V(\mathbf{r})$ is the external potential and $F[\rho(\mathbf{r})]$ is the universal functional, which refers to the sum of the kinetic electron interactions, the electron - electron Coulombic, exchange

and correlation energies. However, due to the difficulty of knowing the electron - electron term, DFT only became workable through a method developed by Kohn and Sham (1965).

The Kohn-Sham (KS) method introduced a fictitious system of non-interacting electrons that has the same density as the real system (Kohn and Sham, 1965).

$$E[\rho(\mathbf{r})] = T_{ni}[\rho(\mathbf{r})] + V_{ne}[\rho(\mathbf{r})] + V_{ee}[\rho(\mathbf{r})] + E_{xc}[\rho(\mathbf{r})] \tag{1.3}$$

where, $T_{ni}\left[\rho(\mathbf{r})\right]$ refers to the kinetic energy of the non - interacting electrons, $V_{ne}\left[\rho(\mathbf{r})\right]$ is the nuclear - electron potential, $V_{ee}\left[\rho(\mathbf{r})\right]$ is the electron - electron repulsion, and $E_{xc}\left[\rho(\mathbf{r})\right]$ is the exchange-correlation.

The KS equations are solved iteratively in a self-consistent manner. Initially, a set of trial coefficients is formulated. By using an approximate form (which remains fixed during all iterations) for the functional $E_{xc}\left[\rho\right]$, we next compute υ_{xc} as a function of $\mathbf{r}$. The set of KS equations are then solved to obtain an initial set of orbitals. This set of orbitals is then used to compute an improved density $\rho(\mathbf{r})$ and the process is repeated until the density and exchange-correlation energy have converged to within tolerance. The electronic energy is then computed from $E = f\left[\rho(\mathbf{r})\right]$.

The functional $E_{xc}\left[\rho(\mathbf{r})\right]$ is called the 'exchange-correlation functional' and accounts for the exchange energy from the antisymmetry of the wavefunction and the correlation of the movement of electrons.

In the simplest approximation, known as the local density approximation (LDA), the exchange-correlation energy term is calculated from a *locally* homogeneous electronic gas configuration (jellium). The LDA is separated into an exchange and a correlation term and is written as:

$$E_{xc}^{LDA}[\rho_\alpha(\mathbf{r}), \rho_\beta(\mathbf{r})] = \int d^3\mathbf{r}\rho(\mathbf{r})\varepsilon_{xc}^{LDA}(\rho_\alpha(\mathbf{r}), \rho_\beta(\mathbf{r})) \tag{1.4}$$

An improvement on the LDA description of the exchange-correlation energy can be made by incorporating a functional that is dependent on the gradient of spin densities. The so called the generalised gradient approximation (GGA) is written as:

$$E_{xc}^{GGA}[\rho_\alpha(\mathbf{r}), \rho_\beta(\mathbf{r})] = \int d^3\mathbf{r} f(\rho_\alpha(\mathbf{r}), \rho_\beta(\mathbf{r}), \bigtriangledown\rho_\alpha(\mathbf{r}), \bigtriangledown\rho_\alpha(\mathbf{r})) \tag{1.5}$$

where, f is a suitable chosen function with adjustable parameters that enable it to be fitted to experimental data. Within GGA, the gradients also incorporate information about the density in the vicinity of $\mathbf{r}$. A very common exchange functional was formulated by Perdew, Burke *et al.* and is referred to as PBE (Perdew et al., 1996). It has been known from calculations to significantly improve binding energies and atomic energies over LDA. As a result, it has improved bond lengths and angles. It provides a small improvement in the band gap of semiconductors and insulators, but it is still too narrow due to the electron self-interaction problem.

DFT + U

A very important limitation is that the exchange contribution given by a density functional does not cancel the Coulomb interaction of the electron with itself. This results in the unphysical description of electron self-interaction. One of the consequences is to produce an artificially delocalised electron density and greater overlap to exist between orbitals. The effect is most notable in systems where electrons tend to be very localised and strongly interacting, as in transition metal oxides (TMO). As a result, the covalent character in the bonding of ionic and semi-ionic compounds is typically exaggerated. Band gaps are underestimated leading to the prediction of delocalised metallic states over the real localised state in semi-conductors.

One method that attempts to overcome the self-interaction limitation is the DFT+U method. By the inclusion of a Hubbard Hamiltonian (Hubbard, 1963), a penalty energy to the hydridisation of the d orbitals is introduced:

$$E_{DFT+U} = E_{DFT} + \frac{(U-I)}{2} \sum_{\sigma} Tr[\rho^{\sigma} - \rho^{\sigma}\rho^{\sigma}] \tag{1.6}$$

where, U is a spherically averaged Hubbard parameter describing the energy increase for placing an extra electron on a particular site. This formalisation was developed by Dudarev, Boton *et al.* and implemented in the Vienna Ab initio Simulation Programme (VASP) code used in this thesis (Dudarev et al., 1998). A value of $U = 3$ or 4 for TiO_2 offers a good compromise to restore the correct magnitude of the Coulomb repulsion and the correct insulator property is predicted.

The van der Waals density function

Another important limitation results from the local character of the functional which prevents a correct description of dispersion interactions (London or van der Waals (vdW) forces). The origin of the vdW force is in the correlation of the electronic movement of distant atoms. The PBE GGA functional only describes the short-range part of the vdW interactions, while at large inter-nuclear separations it produces an exponentially decaying attraction instead of the correct $-C/R^6$ trend. Various alternative functionals have been proposed to better describe non-local interactions, such as optB88-vdW, whose approach is compared and contrasted with PBE in the VASP code used in this thesis. This procedure has some advantages, such as an improved description of the weak interactions involved in molecular-surface adsorptions.

1.6.2 Modelling solvation - Molecular Dynamics

All biological systems are dependent on water as a solvent for crucial molecular process to occur. Therefore it was important to simulate molecular-surface interactions in an aqueous environment. Modelling solvation is a challenging issue in computational chemistry. The origin of the complexity of the problem is from the large number of dynamical interactions of the solvent molecules with the molecular system being investigated. There are several

approaches for modelling solvation (Tomasi et al., 2005). The method used here involved surrounding the surface with a large number of solvent molecules which are treated using interatomic potentials and the properties of the system calculated using molecular mechanics.

The equations of motion

For the case of a particle moving under the influence of a force $\vec{F}(\vec{r})$:

$$m\frac{d^2\vec{r}}{dt^2} = \vec{F}(\vec{r}) \tag{1.7}$$

the classical equations of motion are:

$$\frac{d\vec{r}(t)}{dt} = \frac{\vec{p}(t)}{m} \tag{1.8}$$

$$\frac{d\vec{p}(t)}{dt} = F(\vec{r}) \tag{1.9}$$

where, $\vec{p}(t) = m\vec{v}(t)$ is the particle's momentum. The integration of the equations (1.8 & 1.9) will define the trajectory of the particle subject to an external force-field $\vec{F}(\vec{r})$. This provides a value of the position $\vec{r}(t)$ and momentum $\vec{p}(t)$ at each instant in time. In a system of N interacting particles, the force acting on each particle will change whenever the particle changes its position or whenever any other particles that interact with it changes position. This produces a set of N coupled Newton's equations. In an MD simulation the calculations are broken down into a series of very short time steps Δt (typically 10^{-15} sec). At each step the forces on the atoms are computed and combined with the current positions and velocities to generate new positions and velocities at the end of each short time interval. The force acting on each atom is assumed to be constant during each interval. The atoms are then moved to the new positions, and an updated set of forces

acting on each one is computed. In this way the MD simulation generates a dynamical trajectory that describes the time evolution of the dynamic variables $\vec{p}_i$ and $\vec{r}_i$ for each particle on a time grid.

Conservation of the total energy

The total energy of a system is the sum of the kinetic and potential energy:

$$E = K + V \tag{1.10}$$

This energy conservation law applies whether or not an external potential exists. For the case of a single particle moving in one dimension, the total energy of the particle is given by:

$$E = \frac{1}{2}\frac{p^2}{m} + V(r) \tag{1.11}$$

By differentiating this expression with respect to time we obtain:

$$\frac{dE}{dt} = \frac{d}{dt}\left[\frac{1}{2}\frac{p^2}{m} + V(r)\right] = \frac{1}{2}\frac{2}{m}p\frac{dp}{dt} + \frac{dV(r)}{dt} = \frac{p}{m}\frac{dp}{dt} + \frac{d}{dr}V(r)\frac{dr}{dt} = \frac{p}{m}\left(\frac{dp}{dt} - F\right) = 0 \tag{1.12}$$

This proves that the total derivative $\frac{dE}{dt}$ is zero, i.e that the total energy is a constant of motion. The property of conservation of the total energy is important to establish a link between molecular dynamics and statistical mechanics.

Statistical mechanics

Statistical mechanics relates the macroscopic properties of a system to the microscopic details of such a system. It is based on the Gibbs' *ensemble* concept which is a collection of all possible systems which have different microscopic configurations but an identical thermodynamic state. The thermodynamic state of a system is defined by the parameters of temperature T, pressure P and the number of particles N. The many individual microscopic configurations of a very large system leads to the same macroscopic properties. The *Canonical* ensemble (NVT) was used in this study. This is a collection of all systems whose thermodynamic state is characterised by a fixed number of atoms, N, a fixed volume, V, and a fixed temperature, T.

Modelling the physical system

The main ingredient of a simulation is the model for the physical system. For MD this corresponds to the choice of the *potential energy*. This is a function $V(\vec{r}_1,\vec{r}_2,\ldots,\vec{r}_N)$ of the positions of the nuclei, representing the potential energy of the system when the atoms are arranged in that specific configuration.

Forces are then derived as the gradients of the potential with respect to atomic displacements:

$$\vec{F}_i = -\bigtriangledown_{\vec{r}_i} V(\vec{r}_1,\vec{r}_2,\ldots,\vec{r}_N) \tag{1.13}$$

For the case of a system containing N atoms, the potential energy can be divided into terms depending on the coordinates of individual atoms, pairs, triples, etc.:

$$V(\vec{r}_1,\vec{r}_2,\ldots,\vec{r}_N) = \sum_i^N \upsilon_1(\vec{r}_i) + \sum_i^N \sum_{j=i+1}^N \upsilon_2(\vec{r}_i,\vec{r}_j) + \sum_i^N \sum_{j=i+1}^N \sum_{k=j+1}^N \upsilon_3(\vec{r}_i,\vec{r}_j,\vec{r}_k) + \ldots \tag{1.14}$$

where, the first term in equation 1.14 represents the effect of the external field of the system. The remaining terms represent particle interaction. The second term $\upsilon_2(\vec{r}_i, \vec{r}_j)$ is the pair potential.

The Lennard-Jones potential

One of the pair potentials used is the Lennard-Jones (LJ) 12-6 potential:

$$U(r_{ij}) = 4\epsilon\left[\left(\frac{\sigma}{r_{ij}}\right)^{12} - \left(\frac{\sigma}{r_{ij}}\right)^{6}\right] \tag{1.15}$$

which represents the interaction potential for a pair of atoms. The potential has an attractive tail at large r, it is strongly repulsive at shorter distances, passing through 0 at $r = \sigma$ and increasing steeply as r is decreased further . The term $1/r^{12}$ dominates at short distance. It models the repulsion between atoms when they are brought very close to each other. Its physical origin is from the Pauli exclusion principle. When the electronic clouds of electrons start to overlap, the energy of the system increases abruptly.

The term $1/r^6$ dominates at large distance and is the attractive part of the atomic interaction. This term originates from the van der Waals dispersion forces.

The LJ potential has an infinite range. In practical application, however, a *cut-off* radius R_c is established. Interactions between atoms that are separated by more than R_c are disregarded. This vdW cut off results in enormous saving of computational resources, because the number of atomic pairs increases with the square of r.

Periodic boundary conditions

When using periodic boundary conditions (PBC) the simulation box is replicated to infinity by rigid translation in all Cartesian directions. Without the application of PBC, the simulation would only contain a cluster of atoms. No matter how large the simulated

system is, the number of atoms it contains would be negligible compared to the number of atoms in a macroscopic piece of matter (of the order of 10^{23}). The ratio between the number of surface atoms and the total number of atoms would be much larger than in reality, causing surface effects to be much more important than what they should.

An additional cut off radius r_{cut} is applied when calculating the force between two atoms. This is known as the *minimum image convention* and is chosen so that r_{cut} is not greater than half of the width of the simulation cell, i.e. $L_{box} > 2r_{cut}$. The r_{cut} prevents an atom from interacting an equivalent atom in the neighbouring cell (which is an image of the simulation cell created by applying PBC).

Integration algorithms

The integration algorithm is required to integrate the equation of motions of the interacting particles and follow their trajectories. Time integration algorithms are based on the *finite difference methods*, where time is discreted on a finite grid, with the *time step* Δt being the distance between consecutive points on the grid. The integration scheme gives the same quantities at a later time $t + \Delta t$. By iterating the procedure, the time evolution of a system can be followed for a certain period of time. The integration method used was the velocity Verlet scheme.

Choice of timestep

It is important to determine the most appropriate time step in a MD simulation. If it is too small the trajectory will cover only a limited proportion of the phase space; if it is too large instabilities may arise in the integration algorithm due to high energy overlaps between atoms.

As a general rule, the timestep should be approximately one tenth of the time of the shortest period of motion. In a flexible molecule, the highest frequency of vibration are due to bond stretches, especially those associated with bonds to H atoms. A C-H bond

vibrates with a repeat period of $\sim$ 10 fs, and therefore $\Delta t \sim 1$ fs is required.

Starting a simulation

Running a MD simulations requires three steps:

- Establish an initial configuration of the system
- Equilibration phase; letting the system reach equilibrium
- Production phase; accumulate the quantities of interest

The purpose of the equilibration phase is to bring the system to equilibrium from the starting configuration. The properties used to characterise whether equilibrium has been reached include the kinetic, potential and total energies at defined conditions of temperature and pressure. In the microcanonical ensemble the kinetic and potential energies would be expected to fluctuate but the total energy should remain constant.

When the system has reached equilibration then production phase can commence. Various properties are routinely calculated and stored for subsequent analysis and processing. A visual inspection of the time evolution of the system was possible by using the visualiser software programs; Materials Studio and VMD. For quantitative information data must be extracted by processing atomic coordinates and velocities.

Radial distribution functions

Radial distribution functions (RDFs) represent a property to characterise the structure of a system, particularly liquids. The RDF $g_{\alpha\beta}(r)$ gives the probability of finding an atom of type β at a distance r from atom type α, relative to the probability expected for a completely random distribution at the same density. For two non-equivalent species ($\alpha \neq \beta$) the RDF is described in equation 1.16.

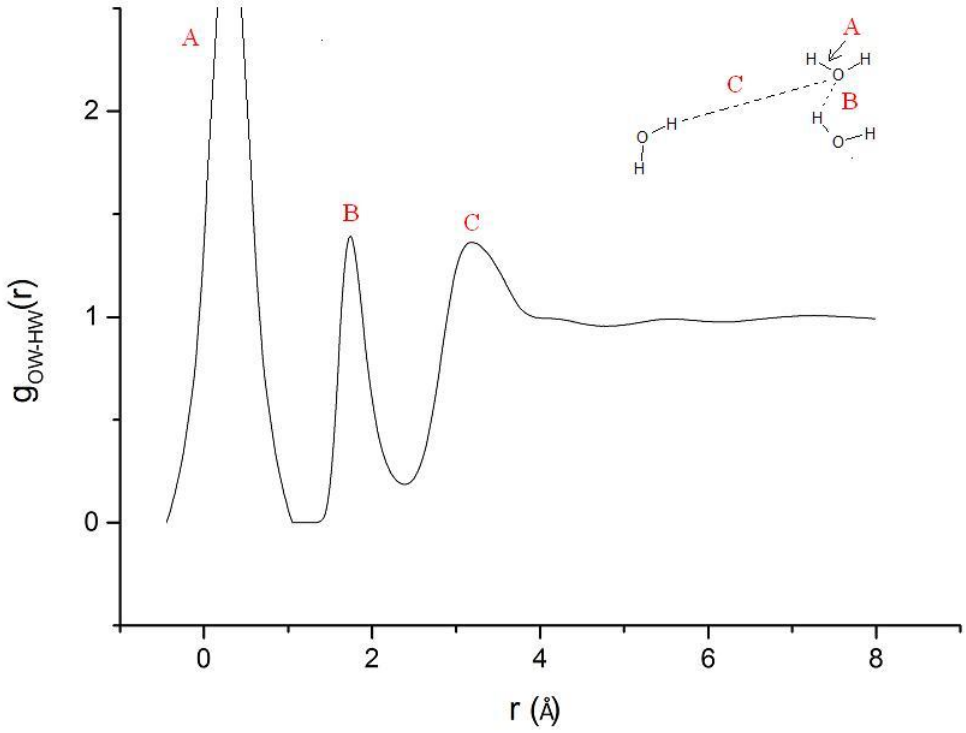

Figure 1.6: RDF of the O-H pair of water

$$g_{\alpha\beta}(r) = \left\langle \sum_{\alpha=1}^{N_\alpha} \sum_{\beta=1}^{N_\beta} \delta(\vec{r} - r_{\alpha\beta}^{\rightarrow}) \right\rangle \tag{1.16}$$

Figure 1.6 shows the RDF of the O-H pair obtained from a simulation of liquid water. The peak labelled A corresponds to the intermolecular O-H bond, the peak B defines the average position of the O$\cdots$H-OH hydrogen bonding distance. Peak C is associated with the hydrogen atoms in the second coordination shell of each O atom. At long distances $g_{\alpha\beta}(r)$ tends to the ideal gas value, $g_{\alpha\beta}(r) = 1$ indicating that there is no long range order.

1.7 Project aims and objectives

Hypothesis

The material based surface interactions of modified Ti are responsible for the selection of an osteogenic subpopulation from human mesenchymal stromal cells (hMSCs).

The main observation that leads to this proposed hypothesis:
The differential effects of modified Ti surfaces have been demonstrated in numerous studies to affect the osteogenic process. *In vitro* evidence has indicated differences in the capacity of each surface with a suggested order of SLV (rough-hydrophilic), SLA (rough-hydrophobic), SMO (smooth polished surface), TCP (tissue culture plastic) in terms of their ability to support and promote osteogenic activity (Miron et al., 2010; Wall et al., 2009; Mendonca et al., 2008).

Secondly, a wide range of potential cell types, including various stem cell lineages have been suggested as potential candidates for *in vitro* selection and expansion for regenerative purposes.

Aims

The aims were; (i) to gain a greater understanding of the surface chemistry of modified TiO_2 in regard to tissue implants, (ii) to asses the potential of osteogenic selection by different Ti substrates, (iii) to compare the osteogenic responses of stem cell populations isolated from different mesenchymal tissues.

Objectives

The objectives of this project were:

1. To develop a molecular model of the TiO_2 surface that enables the development of an understanding of organic molecular interactions, including the cellular adsorption tripeptide, RGD.

2. To confirm the mechanism of the hydrophilic conversion of TiO_2 by UV light using spectroscopic and computational modelling techniques.

3. Form an understanding of stem cell osteogenic responses in order to determine which tissue-derived MSCs are the most effective for osteogenic selection by modified Ti.

4. Form an understanding of osteogenic stem cell selection through a comparison of expressed osteogenic markers, cellular mineralisation differences and osteoblastic protein secretion in populations exposed to modified Ti.

Chapter 2

Materials and methods

2.1 List of chemicals & supplies

Product	**Company**	**Cat. no.#**
β-glycerophosphate	Calbiochem	35675
AlamarBlue	AbD Serotec	BUF012B
Alizarin Red S	Sigma-Aldrich	A5533
Cetylpyridium Chloride	Sigma-Aldrich	C0732
Crystal violet	Sigma-Aldrich	548-62-9
Dexamethasone	Sigma-Aldrich	D2915
Dimethyl sulfoxide	Sigma-Aldrich	472301
Ethanol, molecular grade	Sigma-Aldrich	51976
HCl	BDH Lab. supplies	20252.420
Iso-propyl alcohol	Acros Organics	327270010
L-ascorbic acid 2-phosphate	Sigma-Aldrich	A8960
NaOH	BDH Lab. supplies	10252
Paraformaldehyde	Sigma-Aldrich	158127
PBS Ca^{2+} Mg^{2+} free	PAA	H15-002
Penicillin/Streptomycin	PAA	P11-010
Phalloidin	Sigma-Aldrich	P5282
Sodium Phosphate	Sigma-Aldrich	342483
Taqman Universal PCR master mix	Applied Biosystems	4364340
Triton-X	Sigma-Aldrich	101586B
Trypan Blue	Sigma-Aldrich	T8154
Trypsin	PAA	L11-004
Water - RNAse/DNAse free	5 prime	2900136

Table 2.1: List of chemicals

Product	**Company**	**Cat. no.#**
Live / Dead cell staining detection kit	BD Biosciences	556547
High capacity cDNA Reverse Transcription kit	Applied Biosystems	4368813
RNeasy mini kit	Quigen	74104
Sircol Red Collagen Assay	Biocolor	S1000
- Acetic acid	Sigma-Aldrich	320099
- Porcine pepsin	Sigma-Aldrich	P9859
QuantiChrom Calcium Assay	Universal Biologicals UK	DICA-500
Taqman Array Fast Plates	Applied Biosystems	1908085
- Taqman Fast Universal PCR Master Mix	Applied Biosystems	4357649

Table 2.2: List of assay kits and associated chemicals

2.2 Methodology

Molecular modelling was carried on a crystalline solid rutile [110] structure with translational periodicity for an unit cell comprising 64 Ti atoms and 128 O atoms. The Vienna ab-initio simulations programme (VASP) (version 5.2.12-gamma) and DL_POLY_2 (classic) programs were used for density functional theory (DFT) and molecular dynamics (MD) methods respectively. A slab-gap model was created with a 15 Å vacuum gap. For MD simulations, 150 water molecules were added to the vacuum gap, with the liquid state starting from a configuration that corresponds to a solid lattice. Water was described using the simple point charge (SPC/E) and intermolecular potential (TIP3P) models. Organic molecular interactions were described using assisted model building with energy refinement (AMBER) potentials. Equilibration was achieved in the canonical (NVT, N=moles, V=volume, T=temperature) ensemble, to zero K, for 40 ps. The production phase typically lasted for 100 ps. Both phases were performed with a timestep of 0.0001 ps. For DFT, the VASP code was modified for the van der Waals density functional (vdW-DF), using projector augmented-wave (PAW) potentials, 400 eV cut off energy and results were compared to those obtained using the Perdew, Burke and Ernzerhof (PBE) exchange-correlation functional. Simulations were performed on the UK high performance computer, HECToR and the UCL chemistry ib-server utilising between 4 and 96 cores.

Experimental investigations were conducted in a two dimensional cell culture model con-

sisting of cells suspended in a liquid medium, placed under the influence of gravity onto a substrate, immobilised in a sterile culture vessel. The experimental substrates were tissue culture plastic (TCP), smooth polished cp Ti (SMO), smooth Ti modified by UV irradiation to confer hydrophilic properties (SMOd), hydrophobic sand-blasted acid-etched Ti (SLA) and hydrophilic SLA (SLV). The TCP was used as the control substrate for material type dependent effects on cell responses. This was because it is the prime reference for comparison, as aspects of bone development in human cells have been largely conducted on TCP. The SMO surface was used as a reference control for the Ti modification's influence on cellular responses.

2.3 Modified Titanium surfaces

2.3.1 Preparation

Titanium (Ti) discs fabricated with the modified implant topographies were manufactured and provided by Institut Straumann AG (Walderberg, Switzerland). The implant surface-reproduced discs were of 1.8 cm^2 surface area (15 mm diameter) designed for use in 1.96 cm^2 24-well tissue culture treated plates. A detailed description of the manufacturing methods and characterization of the three Straumann surface preparations, SMO, SLA and SLActive, is provided in (Rupp et al., 2006). In brief, the Ti discs were punched out from sheets of commercially pure Ti (cpTi; Grade III). The crude discs were polished to a mirror on one side with SiO_2 grinding paper of grit size 15-600 μm diameter. These discs were further treated with diamond paste in oil and finally with a SiO_2 suspension to obtain a fine surface; measured to have a Ra value of 0.6 μm. The SLA discs were prepared by blasting SMO surfaces with large alumina particles (average size 250 μm diameter) and then acid-etching in a hot solution of HCl / H_2SO_4 followed by several rinses in de-ionised water. The SLV surfaces were produced with the SLA protocol, with the exception of the final rinse being performed under nitrogen protection; thus disallowing contamination of the surface with atmospheric oxygen and organic chemical moieties, and increasing surface energy. The SLV discs were supplied sealed in glass tubes immersed in isotonic NaCl at

pH 4-6. The average Ra value of SLA and SLV is ~ 4.5 μm.

Energy-dispersive X-ray spectroscopy (EDAX) elemental analysis was used to investigate the chemical characterisation of the cp titanium discs (figure B.1). They were found to consist of high purity titanium with traces of Hafnium and Cerium. Some sodium impurities were found on the surface of SLV due to its storage in saline solution after processing.

2.3.2 Passivation

The SMO and SLA discs were passivated prior to experimentation in order to clean the surface and reduce the effect of external environmental factors. The process of passivation works in two main ways. By thickening the protective outer oxide layer it prevents further corrosion and reduces the potential release of Ti ions from the surface into the surrounding solution. In addition, the process removes excess hydrocarbon buildup on the Ti surface. This was performed by washing discs in a 10 % (v/v) solution of 1 M Nitric Acid in distilled water followed by washing in de-ionised water. Discs were air-dried in a sterile environment under ultra-violet irradiation for 1 hour on each side prior to use. The SLV discs were supplied submerged in saline in sterile glass tubes containing an inert nitrogen atmosphere. They were washed in complete growth media prior to cell seeding. This removed excess sodium and chloride ion contamination. It also ensured the Ti discs were kept submerged in a liquid medium through the course of the experimental setup. This prevents any gradual loss of hydrophilic properties which occurs due to exposure to atmospheric oxygen.

2.4 Cell culture

This project entailed the culture of two different types of human cells. These were primary human bone marrow-derived stromal cells (hBMSCs) and human adipose-derived stem cells (hADSCs). The aspects of cell culture are explained in the following sub-sections.

Equipment	Manufacturer	Application
Laminar Flow Cabinet	NUAIRE Class II	Confined clean work environment; pre-cleaned with 70 % ethanol spray and propanol wipes prior to every use
Incubator	Nuaire NU-5500 DH AutoFlow CO_2 Incubator	Set at 5 % CO_2 and 37 °C for cell incubation; cleaned every fortnight with bleaches.
Cryogenic cell storage	Thermo Scientific	Liquid nitrogen containing chamber with removable lid and six vertical racks, each capable of containing 5 x 96 sample cryo-boxes. Re-stocked with liquid nitrogen every fortnight.
Water bath	ETI 800 series	Weekly cleaned 50 L chamber with adjustable thermostat, set at 37 °C.
Inverted microscope	Olympus CXK31	Standard device with fixed binocular observation tube and 4, 10, 40 and 100x magnification objective lenses.
Hemocytometer with trypan blue	Sigma	Standard 9x (1 x 1 mm) grid with cover slip.
Centrifuge	Different	Tissue culture purposed large centrifuge. Microcentrifuge for smaller samples.
Pipettes	Qiagen	Calibrated pipette 'gun' and 1000, 200, 20 and 10 μL micropipettes.

Table 2.3: Cell-culture environment

2.4.1 Environment and consumables

Cell culture was used for the maintenance, propagation, experimentation and storage of adherent primary human cells in sterile conditions. This work was conducted in a fully equipped tissue culture laboratory. The macro equipment used for tissue culture is tabulated in table 2.3. Most tissue culture consumables were acquired sterile. Non-sterilised items, including micropipette tips, forceps, were autoclaved and oven dried at 60 °C prior to use.

General consumables used for cell culture are detailed in table 2.4. The flasks and tubes were procured sterile and were disposed of following single use.

Cell culture media and reagents used are tabulated in table 2.5.

Equipment	Manufacturer	Application
Flasks	Fluka	Enclosed polystyrene flasks with a negatively charged inner substratum for cell culture. Three sizes used: 150, 75 and 25 cm^2 flasks. Inner space accessed through an air-permeable screw-able cap.
Plates	Nunc	Treated polystyrene multi-well plates with removable lid. Two types used depending on individual well size: 1.9 cm^2 24-well for cell culture and 0.19 cm^2 96 well for assay analysis.
Test tubes	Nunc	Sterile polystyrene tubes for cell culture purposes. Sizes used: 50, 15 and 1.5 mL.
Microtubes	Nunc	Sterile plastic tubes of 500 and 200 μL.
Cryo-preservation tubes	Nunc	Screw cap sterile plastic vials of 2 mL volume for cryopreserving cells.

Table 2.4: Cell-culture consumables

Instruments and consumables used for the sterilisation of equipment are tabulated in table 2.6.

2.4.2 Practice

A cycle of cell culture constituted of the revival of a cryopreserved cellular specimen, and propagating it in an appropriate medium and vessel for a period of time in humidified conditions. During this period, medium would be replaced twice every week in order to replenish cellular nourishment and remove metabolic waste. Under ideal conditions, cultured cells increased in numbers forming confluent monolayers. These were detached, and either re-propagated (sub-cultured), used in experimentation, or cryopreserved. The details of cell culture practice undertaken are elaborated in the following sub-sections.

2.4.3 Culture media

All liquid reagents and media were pre-warmed in water bath for $\sim$ 30 minutes prior to use. The type of medium used depended on cell type and purpose of culture (i.e. proliferation of cells or differentiation). Complete growth medium (CGM) was composed

Reagent	Manufacturer	Application
Alpha minimal essential medium	Gibco	α**MEM**; L-Glutamine supplemented basal medium for hMSC propagation and growth.
Dulbeccos modified eagles medium	PAA Lab.	**DMEM**; L-Glutamine supplemented high-glucose (10 gL^{-1}) basal medium for hADSC growth.
Dulbeccos modified eagles medium	PAA Lab.	**DMEM**; L-Glutamine supplemented low-glucose (1 gL^{-1}) basal medium for osteogenic inductive medium.
Trypsin/ EDTA	PAA Lab.	A solution of 0.05 % / 0.002 % Trypsin/EDTA in calcium and magnesium free phosphate buffered saline.
Ca^{2+} Mg^{2+} free Phosphate Buffered Saline	PAA Lab.	**Dication-free PBS**; an isotonic solution of NaCl in water used for cell washing, and dilutions.
Fetal Bovine Serum	Gibco	**FBS**; heat inactivated serum sourced from South America, supplemented to basal medium to nourish cells whilst in culture.
Antibiotics	PAA Lab.	A mixture of Penicillin 10 units ml^{-1} and Streptomycin 10 mg ml^{-1} in dication-free PBS.
Dimethyl sulfoxide	Sigma	**DMSO**; used as a cryoprotectant for cryopreserving cells.
Dexamethasone	Sigma	Water soluble glucocorticoid molecule complexed with Cyclodextrin for use in osteogenic differentiation.
β-glycerophosphate	Calbiochem	Water soluble phosphate donor for use in osteogenic differentiation.
Ascorbate-2-phosphate	Fischer	Metabolite used for collagen synthesis in osteogenic differentiation.

Table 2.5: Cell-culture reagents

Equipment	Manufacturer	Application
Alcohols	Various	Industrial methylated spirit at 70 % in water used as a sterilizing spray. Propanol wipes (Azowipes) were applied to clean and sterilise large surfaces.
Autoclave		Pressurised steam sterilizer set at 126 °C for 20 min.
Ultra violet radiation	Steristorm	UV light cabinet with 255 nm wavelength bulb.
Bunsen burner	Various	Portable flame burner used for heat sterilisation of metallic instruments, such as forceps, scalpel blades.

Table 2.6: Sterilisation equipment

by supplementing the appropriate basal medium with 10 % (v/v) fetal bovine serum (FBS) and 1 % (v/v) penicillin / streptomycin antibiotic mix. The hMSCs preferred αMEM and the hADSCs, DMEM high glucose (10 gL^{-1}) as basal media. This was established by previous collaborators' work in the use of these cell types (data not shown). Osteogenic inductive medium (OM) was similar for both cell types; comprising of Dulbeccos Modified Eagles Medium low glucose (1 gL^{-1}) supplemented with 10 % (v/v) FBS, 1 % antibiotics, 10 nM dexamethasone; 10 mM β-glycerolphosphate; and 50 μM ascrobate-2-phosphate. The volumes of medium used per culture vessel substrate area are tabulated in table 2-5. Freezing media (FM) was prepared for the cryopreservation of cell samples. This comprised of CGM supplemented with 30 % FBS and 10 % (v/v) dimethyl sulphoxide (DMSO) as a cryoprotectant. This reduces ice formation and thus prevents cell death during the freezing process to -196 °C in liquid nitrogen.

2.4.4 Cell revival

Cell samples were cryogenically stored in cryovials submerged in liquid nitrogen. These cells were revived quickly, to prevent harmful cellular penetration by DMSO. A cryovial was half immersed in 37 °C water until thawed and the contents transferred to pre-warmed growth medium in a 15 mL tube. The number of cells in suspension was determined by hemocytometer. 10 μL of cell suspension was combined with 10 μL trypan blue and the total number of non-stained cells was counted in the four corners of the 1 mm^2 boxes within the 9 boxed-grid. An average count was used in the formulas below to estimate the

quantity of cells in suspension:

Estimated cell concentration: C (cells/mL) = A (cells) x D_f x 10^4 mL^{-3}

(2.1)

Estimated total cell number: C_n (cells) = C x V_f

(2.2)

where, C = cell concentration. A = average cell count from 4 x $1mm^2$ boxes of hemocytometer. D_f = dilution factor (=2 from equal volume of trypan blue). C_n = total cell number.

2.4.5 Sub-culture

Cellular detachment from a substrate was carried out with a Trypsin/EDTA solution. This was performed by twice washing cells with dication-free PBS and incubating the monolayer with Trypsin/EDTA solution at the proportion of 1 mL reagent per 25 cm^2 of substrate area in 37 °C, humidified conditions for 5 min. The detached cell suspension was added to an equal volume of CGM to deactivate the trypsin and then pelleted at 1000 x g for 5 min. After centrifugation the media containing trypsin was aspirated off and the pellet re-suspended in a known volume of CGM. Cells were counted using a hemocytometer as described previously. A known number of cells were added to culture vessels containing pre-warmed medium. This initial seeding density differed according to the experiment being performed with differentiation and gene expression protocols requiring a higher density of cells. The volume of inoculate was calculated with the arithmetic formula:

$$V_i \text{ x } C_i = V_f \text{ x } C_f, \text{ if } N_i = N_f \tag{2.3}$$

where, V = volume of suspension, C = concentration of suspension, N = number of cells, i = initial and f = final.

Cultures were incubated at 37 °C in humidified conditions, 5 % CO_2 with bi-weekly medium changes until attaining a $\sim$ 80 percent confluence.

2.4.6 Cryopreservation

Pelleted, detached cells were suspended at a density of 0.5 - 1 x 10^6 cells mL^{-1} in freezing media. An aliquot of 1 mL of suspension was added to individually marked cryovials, which were capped and slow frozen to −80 °C at a rate of 1 °C min^{-1} using a portable freezing container with glycerol. Vials were stored for 24 hours at −80 °C before being transferred to cryogenic liquid nitrogen tanks.

2.4.7 Culture of mesenchymal stromal cells

Human mesenchymal stromal ells (hMSCs) from three unrelated donors (N = 3, Caucasian, male: 20-30 year age group) were obtained from the Institute for Regenerative Medicine, Texas A & M Health Science Center, College of Medicine, USA. These cells were isolated from bone marrow aspirates on their ability to adhere to tissue culture plastic compared to non-adherent hematopoietic adult stem cells. The MSCs had been pre-characterised for colony forming units, osteogenic, chrondrogenic and adipogenic differentiation and the expression of stromal cell surface markers by the suppliers. The hMSCs were cultured according to the parameters suggested in previous publications (Colter et al., 2001; Sekiya

et al., 2002). Cells were expanded at low density (100 cells cm^{-2}) in CGM in a 150 cm^2 Tissue Culture (TC) treated flask (Nunc). On obtaining $\sim$ 80 % confluence, cells were sub-cultured onto 24 well TC plates containing the following surfaces TCP, SMO, SMOd, SLA and SLV Ti at a density of $\sim$ 2.0 x 10^4 cells / well. The populations of cells exposed to Ti are refered to as the selected populations and contain cells that are tested for phenotypical alterations in comparison to the population exposed to TCP. The TCP cells represent the unchanged parent population, identical in composition to the original MSC population. Phenotypic analysis experiments were performed on selected populations and the control parent population cultures that had undergone a maximum of five passages.

2.4.8 Culture of adipose derived stem cells

Human adipose derived stem cells (hADSCs) from three unrelated donors (N = 3, Caucasian, male: 10 - 15 year age group) were provided by the Institute of Child Health (ICH), UCL (London, UK). These cells were isolated from sub-cutaneous fat deposits. Cells were cultured in an identical way to hMSCs described above.

2.5 Microscopy

The conceptually simplest way to analyse the progress of a cell culture sample is by "looking at it".

2.5.1 Light microscopy

An inverted light microscope (Olympus CXK31, MediaCybernetic) was used to visualize cellular confluence and morphology at different stages of culture. Observations were conducted with a x10 ocular lens and x4 and x10 magnification objective lenses.

2.5.2 Confocal microscopy

Fluorescence cell visualisation was used to assess differences in cell cytoskeleton structure in response to different surfaces. Phalloidin is a peptide that binds specifically to F-actin. Staining was performed using an AlexaFluor phalloidin 488 probe. Propidium iodide (PI) was used as a nucleus stain. Cells were washed twice in PBS and fixed in 4 % formaldehyde in PBS for 10 mins at room temperature. 200 μL aliquots were washed twice more in PBS and then the membranes were permeabilised in 0.1 % Triton X-100 for 5 mins. A 1 μg mL^{-1} staining solution of methanolic phalloidin was added to each sample and incubated in the dark for 20 mins. After washing 2x with PBS the samples were counter stained with 1 μg mL^{-1} PI. Cells were visualised by confocal microscopy (Radiance 2100, Bio-Rad) in green and red monochromatic light.

2.6 Colony forming unit analysis

MSCs are a highly proliferative cell type, capable of forming single cell derived colonies when plated at extremely low cell seeding densities. The measure of colony forming ability of a cell population is indicative of the relative proportion of uncommitted / replicative cells and can be used as an indication of stem-like nature. It is evaluated by a colony forming unit (CFU) assay (Colter, Sekiya and Prockop 2001). A typical CFU assay was performed by culturing $\sim$ 100 cells in a T-75 flask for 10 days at 37 °C and 5 % CO_2 with bi-weekly media changes. At 10 days, cultures were fixed and stained in a solution of 3 % Crystal Violet in Methanol, followed by several washes in distilled water and finally air dried.

The comparative parameters that were measured included colony number and mean colony diameter ($\geq$ 2 mm). Images of flasks were taken by camera and analysed using ImagePro software (Alpha Innotech Digital imaging system; UK). Stained colonies were examined and the size distribution determined for each population. Mean diameter was calculated in 2 degree radial increments from the center of each colony. This gave a better indication

of size for irregular shaped colonies. The number of colonies 2 mm or larger in diameter divided by cells plated x 100 was recorded as the % CFU.

2.7 Cell proliferation assays

The AlamarBlue cell viability assay was used to establish cell numbers in experimental settings where hemocytometric measurements were not applicable.

2.7.1 AlamarBlue fluorescent-metabolic substrate

AlamarBlue is dark blue, water soluble solution of a non-fluorescent dye called resazurin. This is a colourimetric indicator that is metabolised in cellular mitochondria to yield a reduced form; a soluble fluorescent red colored dye called resorufin. This can be measured with fluorescence or colorimetric spectrometry. It is a non-destructive assay that due to reportedly null toxicity to cells can be used for the serial analysis of changes in cell numbers of a culture over an indefinite course of time. An AlamarBlue assay was conducted in cells cultured in 24-well plates in 1 mL of culture medium. The oxidized blue dye was added to culture at 10 % the total volume of supernatant (i.e. 100 μL dye per 1 mL medium) and incubated for 4 h in humidified conditions. 100 μL of conditioned culture supernatant was then transferred to an opaque microtitre 96 well plate. Fluorescent excitations were evolved at 530 nm and emissions measured at 590 nm. The conditioned medium was replaced with fresh CGM for further continuation of the cell culture assay. Cell numbers were determined by extrapolating fluorescent values from a standard curve. An example of the AlamarBlue standard curve used to calculate cell numbers is given in figure C.1.

2.8 Gene expression

Gene expression changes were analysed with real time polymerase chain reaction (RT-PCR) using the $2^{-\Delta\Delta Ct}$ method. This method comprised three steps; the extraction of

RNA, reverse transcription to cDNA and Taqman probe based RT-PCR assay of relative levels of expression. Descriptions of individual steps are provided in the following subsections.

2.8.1 RNA extraction and quantification

Total RNA was extracted with the RNeasy Mini kit from Qiagen according to the manufacturers instructions. Adherent cells cultured in a 24 - well TC plate were homogenized in situ with buffer RLT (350 μL per well). Total homogenate was collected in two stages. RNA was then precipitated from the homogenate by mixing with an equal volume of 70 % ethanol in distilled water. The lysate was transferred to RNeasy mini kit RNA columns. The kits employ a silica membrane within the column to which RNA adheres. The membrane captured total RNA was washed in a series of different buffers to remove excess cellular material and finally eluted from the membrane with RNAse-free water (40 μL per column). The integrity and quantity of extracted RNA was evaluated by spectrophotometry. 2 μL samples were placed on a Tecan optical plate and quantified at λ 260 / λ 280 nm absorbance wavelengths. λ 260 nm measures nucleic acid content while λ 280 nm measures protein content.

2.8.2 Reverse transcription

Reverse transcription was performed with first strand synthesis reactions using the High Capacity Reverse Transcription Kit from Applied Biosystems. Each reaction consisted of 10 x RT buffer / 25 x dNTP Mix / 10 x Random Primers / Multiscribe Reverse Transcriptase / nuclease-free water at a volume ratio of 2 : 0.8 : 2 : 1 : 4.2, and 10 ng of RNA diluted in nuclease-free water. This was combined in 1:1 with master mix to make the final cDNA sample volume up to 20 μL. Samples were placed in a thermocycler (PTC-100, Genetic Research Instrumentation Ltd). A 100 ng sample of cDNA was thus prepared which was immediately stored at -80 °C.

2.8.3 Real Time-Polymerase Chain Reaction

The RT-PCR reactions were performed in a 7300 Real Time PCR System from Applied Biosystems. These were undertaken in 20 μL reactions with 2.0 μL of cDNA per reaction; equivalent to 10 ng of RNA. Ct values of markers were normalised to the GAPDH house keeping gene. These ΔCt values of samples were calibrated to the reference ΔCt values of cells in suspension at time zero (T0), to obtain $\Delta\Delta$Ct values of each sample. Relative fold values of expression were calculated arithmetically with the formula, $2^{-\Delta\Delta Ct}$. Fold values were calculated separately for each replicate, which were combined and used to calculate mean (n = 3) and error of samples.

2.8.4 Gene expression array

A qPCR array was custom designed in the format of 2 x 48 genes in a 96 well plate. Taqman RT-PCR genetic probes were procured from AppliedBiosystems (Cat. # 1908085) and used to evaluate global transcriptional changes in genes associated with osteogenic identity. These arrays contain a sequence-specific unlabelled primers and a FAM dye-labeled, Taqman genetic probe, to which a 10 μL 1:1 mix of sample cDNA and Universal PCR master Mix are added, and spun at 1000 rpm to bring the liquid to the bottom of all wells. These plate were run under Fast cycling conditions for two step RT-PCR (AppliedBiosystems 7900 HT) at the UCL Institute of Child Health, London, UK. GAPDH was used as the housekeeping gene. Data was exported in the form of Ct values, which were used to calculate relative fold differences in expression between sampled genes. The gene expression levels were averaged for 3 patients from MSCs and ADSCs (N = 3). A summary of the genes and their functions is given in appendix A.

2.9 Calcium mineralisation assays

The degree of calcium mineralisation is directly related to the degree of osteogenic differentiation. It was assessed by the Alizarin Red S Stain dye elution method and by the

quantitative QuantiChrom Calcium Assay. These are described below.

2.9.1 Alizarin Red S dye semi-quantitative monolayer stain

Alizarin Red S is a red dye in acidic pH that through a chelating process binds matrix deposited Ca^{2+} in a 2:1 molar stoichiometry. Bound dye is eluted in Cetylpyridinium Chloride (CPC) and absorbance of dye measured at 562 nm in a spectrophotometer. The arbitrary units of absorbance where compared with TCP, as the control, to provide a semi-quantitative estimate of Ca^{2+} content between samples. Alizarin Red S stain for matrix deposited calcium was carried out by washing monolayers gently with dication-free PBS, and fixing the monolayer in 10 % formalin for 10-15 min. The monolayer was then stained with a 2 % Alizarin Red S Solution adjusted to pH = 4.1 - 4.3, in deionised water for 10 min followed by x4 washes with water. Samples were then allowed to air dry. Calcium bound dye was eluted by 10 % w/v solution of CPC in 10 mM Sodium Phosphate (Na_3PO_4) Buffer of pH = 7.0. Spectrophotometric absorbance of elutant was measured at 562 nm.

2.9.2 QuantiChrom calorimetric quantification of deposited calcium

Osteogenic responses of hMSCs was assayed with the QuantiChrom Calcium Quantification assay kit (Universal Biologicals UK). This methodology is suitable for the recurring problem of detachment of monolayer in OM. Calcium levels were assayed by homogenizing a monolayer with 500 μL of 1 M HCl in deionised water for 1 h at room temperature and then assaying a 5 μL aliquot of homogenate with 200 μL of 1 x assay reagent in a clear 96-well TC plate (Nunc). Absorbance of samples was measured at 612 nm (Tecan). Calcium concentrations (μg mL^{-1}) were determined by interpolating absorbance values from an 8 point standard curve. An example of the QuantiChrom standard curve used to calculate Ca^{2+} concentration is given in figure C.2.

Product	**Company**	**Cat. no.#**
1° antibodies		
V450 Mouse Anti-Human CD146	BD Biosciences	562136
PE-Cy 5 Mouse Anti-Human CD49d	BD Biosciences	559880
FITC Mouse Anti-Human CD105 (Endoglin)	BD Biosciences	561443
PE Mouse Anti-Human	BD Biosciences	551298
FITC Mouse Anti-Human CD164	BD Biosciences	551297
IgM Mouse Anti-Human Stro-1	R & D Systems	MAB1038
2° antibodies		
FITC Mouse IgG2a, κ Isotope Control	BD Biosciences	554647

Table 2.7: List of antibodies

2.10 Extracellular matrix (ECM) collagen quantification assay

Extracellular matrix collagen was assayed by homogenising a monolayer with 400 μL of cold 0.5 M acetic acid supplemented with 100 μg mL^{-1} porcine pepsin (Sigma-Aldrich). Homogenates from three replicate wells were pooled and concentrated overnight with 200 μL of Isolation and Concentration reagent at near 0 °C. The pooling of samples was required due to the minute amounts of collagen formed by cells in individual wells. Concentrated samples were centrifuged to pellet collagen while the albumen rich supernatant was discarded. Collagen pellets were stained with Sirius red in picric acid and later washed in acid-salt solution to remove unbound dye. Bound stain was eluted with 250 μL of an alkali solution. Absorbance of 200 μL of each sample was measured at 555 nm in a clear 96-well microtitre plate. Total quantities were determined by interpolating absorbance values from a 6 point standard curve (highest point = 45 μg collagen). An example of the Sircol Red standard curve used to calculate total amount of collagen is given in figure C.3.

2.11 Flow cytometry

Fluorescent activated cell sorting (FACS) was used to measure the levels of apoptosis and necrosis within cell populations and to measure the presence of specific cell surface antibody markers. A list of the antibodies used is given in table 2.7.

2.11.1 Apoptosis and Live / Dead cell staining

The amount of apoptosis and necrosis of cells within MSC populations was analysed by staining with Annexin V (FITC) and Propidium Iodide (PI) (PE) (Live / Dead cell staining kit; BD Biosciences). Annexin V is a fluorescent probe which binds to phosphatidylserine (PS) which is normally found on the internal part of the plasma membrane. This affinity can be used in apoptosis measurements since the cell membrane, including the phospholipids, start to lose it's integrity at an early stage of apoptosis. PS is translocated to the outer leaflet of the plasma membrane, thereby exposing it to the outer environment. PI is a nucleus stain, for which the cells stain positive when their membrane has been completely compromised as in necrosis. Cells were detached using Trypin / EDTA and were then washed twice in PBS followed by centrifugation and resuspension each time. Cells were finally resuspended in 100 μL 1X Binding Buffer per sample. Staining was achieved using 5 μL of Annexin V and 5 μL of PI. Samples were incubated for 15 minutes in darkness before making the final volume up to 500 μL in 1X binding buffer. Analysis was by Flow Cytometry (FACScanTM Becton Dickinson). Settings were adjusted to avoid superimposition between FITC and PE fluorescent signals.

2.11.2 CD surface cell marker analysis

The Attune Acoustic Focusing Cytometer (AppliedBiosystems) was used to study the relative presence of multiple stem cell surface markers, Stro-1 (FITC), CD146 (V450), CD105 (Brilliant violet), CD164 (PE), CD49d (PE-Cy5), Live/Dead (aqua) within MSC populations. The cytometer was equipped with Violet/blue 405 nm (50 mW) and 488 nm (20 mW) lasers. There are three emission channels per laser which allows for six-colour analysis in addition to forward and side scatter data collection. Cells were detatched by Trypsin / EDTA and washed twice in PBS by centrifugation for 5 min at 1300 rpm. Typically, 1 x 10^6 cells were resuspended in 100 μL of Flow Buffer. The minimum volume of antibody required was deduced by titration and then added to each tube. Volumes used were; Stro-1 (20 μL), CD146 (5 μL), CD105 (5 μL), CD164 (20 μL), CD49d (15 μL),

Live/Dead (1 μL). Samples were incubated for 30 mins in the dark then diluted in 1 mL of focusing fluid before being analysed by Attune cytometer.

2.12 Assay analysis

Spectrophotometric measurements of optical densities of samples were conducted in a Tecan M200 (Austria) multi-plate spectrophotometer. This was equipped with a monochromator capable of creating light of a wide range of wavelengths. It was also equipped with a NanoQuant (Tecan) plate for ultra violet spectral quantification of nucleic acid. Fluorometric measurements were conducted in a Fluoroskan (Fischer UK) multi-well fluorometer. This was a filter based instrument; the ones used in this study were 485 nm, 510 nm, 530 nm, and 590 nm.

2.13 Data collection and statistics

2.13.1 Raw data analysis

Raw analytical output from quantitative assays was retrieved with Microsoft Excel. This software was used to organize data as input for statistical analyses with GraphPad Prism v5.

2.13.2 Statistical analysis

The Graphpad Prism version 5.02 statistical package was used for mathematical calculation and statistical analyses of raw data. The calculations included; (i) basic statistics (mean, median, standard deviation, and frequency distribution), (ii) linear regression analysis for standard curves of quantitative colorimetric assays, (iii) interpolation of data sets from standard curves, (iv) statistics for the determination of normality between data sets and (v) evaluation of significance of the difference of means.

Statistical analyses were conducted after generating a data matrix consisting of readings from three donors with three replicates per donor (N = 3; n = 3). Data was first tested for normality with D'Agostino-Pearson normality test. This was followed by repeated measures ANOVA (analysis of variance) with a 2-way repeated measures test utilizing the Bonferonni post test comparing all variables. For samples with lesser replicate numbers or less time points, a 1 way ANOVA was used.

2.14 DFT calculation methods

Density Functional Theory (DFT) calculations were performed using the VASP program (written by G. Kresse and J. Furthmüller, Institute of Material Physics, University of Vienna) and computation time on HECToR. Electronic structure, geometry and total energies were obtained using DFT calculations in the generalised gradient approximation (GGA) with the exchange-correlation functional of (Perdew et al., 1996). In order to improve on the GGA description of the d electrons in TiO_2, we used the GGA + U approach, which acts by adding a positive term (proportional to a parameter, U_{eff}) to the GGA energy. This has the effect of penalising the hybridisation of the specified orbitals of the metal atoms (Ti d orbitals) with the ligands (O atoms) (Anisimov et al., 1991). The introduction of the Hubbard type correction is necessary to overcome the electron self-interaction problem and more accurately reproduces the electronic properties of transition metal oxides within the framework of DFT (Grau-Crespo and Schwingenschlogl, 2011). A value of $U_{eff} = 3$ eV was used as this value provided a good description of the electronic and insulator properties of titanium oxide (Kresse and Joubert, 1999). The interaction between the valence electrons and the core was described with the projected augmented wave (PAW) method in the implementation of Kresse & Joubert (Kresse and Joubert, 1999). The core electrons, up to 3p in Ti and 1s in O were kept frozen in their atomic reference states. The cut-off energy controlling the number of plane wave basis functions was set to $E_{cut} = 400$ eV, and reciprocal space integrations were performed using a mesh of 3 x 3 x 1 points. Relaxations of the ion positions and cell parameters were performed using a conjugate gradient algorithms resulting in a convergence to the equilibrium positions in

the bulk crystal.

The equilibrium shape of the macroscopic crystal surface was constructed using a 4 x 4 x 2 supercell in Materials Studio. The slab model was then generated, to which periodic boundary conditions were applied. An infinite stack of quasi-two dimensional slabs was constructed where each slab is separated from its neighbour by a set vacuum gap. The thickness of the slab was expressed in terms of the number of layers, where a layer is defined as a [110] plane that consists of both Ti and O atoms. The vacuum width was set to 15 Å as this provided sufficient space for the superposition of molecules to the surface. The energetics of the transition metal oxide was found using total-energy calculations, with all the structures considered being relaxed until forces on all atoms were less than 0.01 eV $Å^{-1}$.

Surface energy values gradually converge with increasing slab thickness. We used a 4 layer slab (figure 3.1) as used in previous DFT studies of this surface (Nolan et al., 2008; Tonner, 2010; Hameeuw et al., 2006). The ions in the top two layers were allowed to relax towards their equilibrium positions and the ions in the bottom two layers were fixed in their bulk positions. This is thought to be more representative of the actual structure where the surface effects are only felt by the ions in the uppermost layers. Atomic displacements due to surface relaxation compare well with the experimental data from low energy electron diffraction (LEED) and scattered X-ray diffraction (SXRD) (Lindsay et al., 2005; Charlton et al., 1997).

2.15 Molecular Dynamics

The simulation package was DL_POLY_2 (written by W. Smith and T.R. Forester, Daresbury Laboratory) for running classical MD simulations using the NVT ensemble. The typical cell of the TiO_2 [110] structure was constructed as described above. This set up of the surface was constrained within a x, y periodic box, with slab geometry. A vacuum gap of 15 Å was filled with 150 water molecules with an initial crystal solid structure for simulations involving aqueous solvent. The TIP3P model was used to describe water

molecules and AMBER force fields used to describe pair potentials in organic molecules and TiO_2. The Verlet velocity scheme was employed with Norsé-Hoover thermostat. A timestep Δt of 1 fs was set with relaxation time of 0.5 ps. The total simulation time for each job was 140 ps, including 40 ps of equilibration.

2.16 Raman spectroscopy of Titanium dioxide coated glass

An assessment of the surface composition of the of TiO_2 was performed with Raman spectroscopy. This technique analyses the spectrum of emitted photons generated by incident monochromatic light to obtain the identity of the chemical nature of the target, such as the oxide surface and adsorbed hydrocarbon contaminants.

A Raman spectrum for the Ti discs could not be obtained due to the reflective nature of the surface interfering with the optical receiver of the device. Since any surface effects involve only the initial atomic layers, an analysis of the Ti surface is, in reality, an analysis of TiO_2. The chemical vapour deposition (CVD) technique allows a thin film of TiO_2 to be deposited on glass which could then be used in the analysis of surface effects.

2.16.1 Chemical Vapour Deposition

Thin films of TiO_2 were synthesised using atmospheric pressure (AP)CVD on glass at the department of chemistry, UCL. Titanium tetrachloride ($TiCl_4$) was used as the precursor in ethyl acetate solvent. The $TiCl_4$ bubbler was heated to 68 °C and ethyl acetate heated to 40 °C. All gas lines were heated to over 150 °C. Deposition was carried out on a horizontal bed, CVD reactor at a temperature of 500 °C. The flow rates for the 1 minute deposition were 1.32 litres min^{-1} for $TiCl_4$, 0.3 litres min^{-1} for ethyl acetate. Variations in film thickness were observed by scanning electron microscopy (SEM), indicative of a difference in growth rate between anatase and rutile particles (Cross et al., 2012).

2.16.2 Raman spectroscopy

Raman spectra of TiO_2 films, with and without irradiated UV light, were collected using a LabRam Micro-Raman Spectrometer (Horiba Jobin-Yvon HR300) equipped with an optical microscope and 50x objective lens for total magnification of 500x. A Helium/Neon ion laser (632.8 nm) was used for the excitation of the Raman signal with appropriated notch filters for eliminating the laser line after excitation. The slit width was typically set at 150 μm. A holographic grating having 1800 grooves mm^{-1} was used to collect all Raman spectra. Spectral curve fitting was performed using a mean baseline correction polynomial 6. A multidimensional spectral array was used comprising of a 4 x 4 grid and an accumulation number of 16. In this way multiple spectra were averaged to improve the spectrum quality and to map multiple locations on the sample surface. Integrated peak ratios were then calculated and averaged over three separate samples.

2.16.3 Contact angle measurement

The KSV Cam200 optical contact angle meter was used to measure water contact angles on the TiO_2 surface following UV irradiation. This instrument captures multiple video images (25 frames s^{-1}) of liquid (water) dropped onto the surface of the thin film and analyses the static contact angle based on the droplet shape (figure D.1).

Chapter 3

The effect of van der Waals interactions on the adsorption of organic molecules at the TiO_2 [110] surface

3.1 Introduction

Understanding the interaction of organic adsorbates with the TiO_2 surface is important for research on biological implants (Steinemann, 1998) as well as on many other areas of modern technology (Thompson and Yates, 2006). Titanium and its alloys have long been the material of choice for the repair of damaged or defective bone tissue. Close interactions occur between prototype adhesion proteins on bone cell surfaces and the oxide layer at the surface of the metal implant (Pierschbacher and Ruoslahti, 1984). The important adhesion process is then controlled by the strength of the molecular interactions with the oxide surface.

Rutile TiO_2 [110] has been one of the most widely studied surfaces in surface science

(Diebold, 2003; Schneider and Ciacchi, 2010; Liu et al., 2010). It has the lowest density of exposed bonds of all the low index surfaces of TiO_2 [100, 011 and 001]. This explains it's lowest surface energy of the possible TiO_2 crystal structures and it is the most stable surface in rutile. The structure of its bulk-like (1x1) termination is well known from both experiment and theory (Diebold, 2003). This surface termination exhibits alternating rows of twofold coordinated bridging oxygen atoms and channels that expose fivefold coordinated titanium (Ti_{5f}) atoms with in-plane threefold coordinated O atoms (figure 3.1). In this work, we use the [110] surface as a representative TiO_2 surface, to investigate the role of van der Waals forces in the interaction between oxides surfaces and (small) organic molecules. Establishing the correct theoretical framework for studying these interactions is a necessary first step in order to progress to more complex computer simulations of the adhesion of biological molecules at the TiO_2 surfaces.

Earlier theoretical studies of the interaction of organic molecules with TiO2 surfaces using density functional theory (DFT) have contributed to understanding the main adsorption modes and provided useful estimations of the relative adsorption strengths at different sites (Bates et al., 1997; Sánchez de Armas et al., 2007; Sushko et al., 2006; Tonner, 2010; Charlton et al., 1997) but they suffer from the poor description of van der Waals (vdW) forces within the traditional DFT framework. Both the local density approximation (LDA) and the generalized gradient approximation (GGA) fail to provide the long-range (R^{-6}) attractive dispersion term, which arises from non-local electron-electron correlations. In recent years, several schemes have been proposed to add dispersion corrections to existing DFT formulations (Andersson et al., 1996; Dion et al., 2004; Grimme et al., 2007; Antony and Grimme, 2006; Sato et al., 2007). Among them, the so-called van der Waals density functional (vdW-DF) method, which I focus on in this chapter, is particularly promising because it provides the dispersion correction based directly on the electron density. The vdW-DF method was originally proposed by Dion *et al.* (Dion et al., 2004), and the algorithm was improved by Roman-Perez and Soler to reduce the computational cost (Roman-Perez and Soler, 2009). Klimeš *et al.* also developed a set of modified vdW-DF functionals (optPBE-vdW, optB88-vdW, and optB86b-vdW) where the exchange functionals were optimised for the correlation part (Klimes et al., 2010).

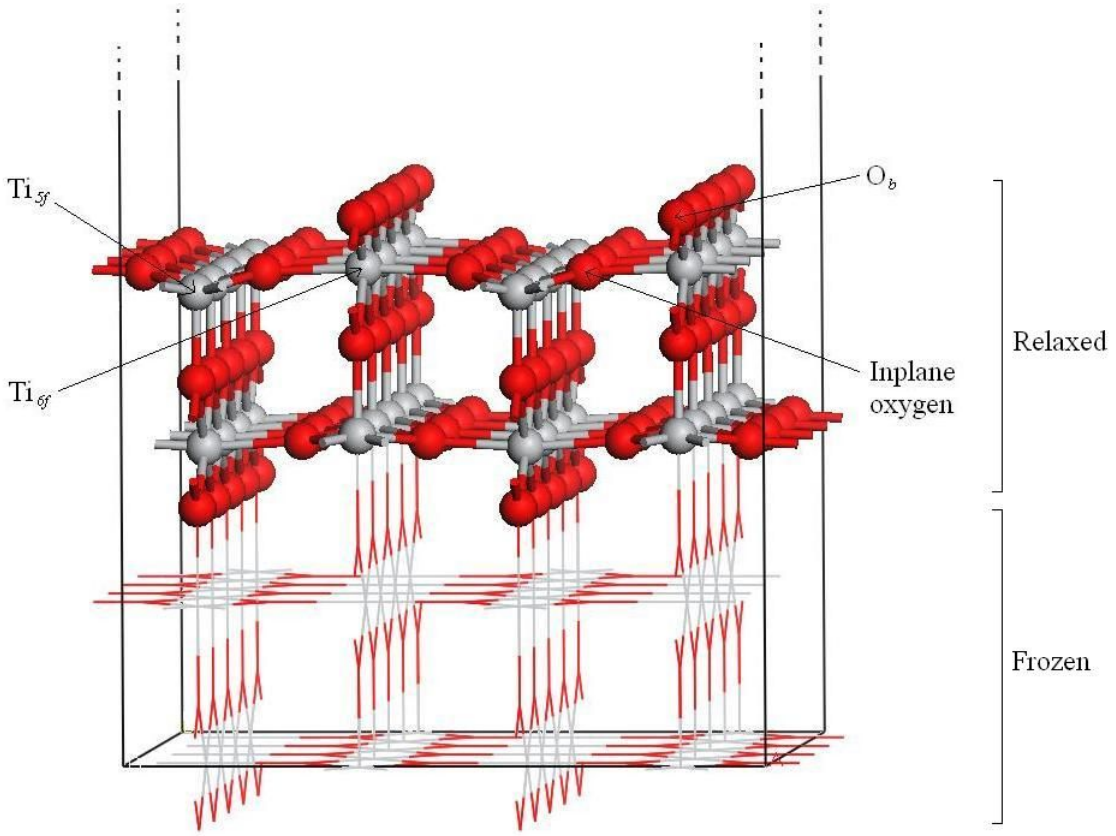

Figure 3.1: $Ti_{64}O_{128}$ slab cell representing the rutile [110] surface used in our calculations. The different Ti and O atomic sites are labelled. The figure represents the frozen-double layer model where the relaxed layers are shown as ball and sticks and the frozen layers are shown in line format.

Capitalising on this recent progress, there has been a number of studies examining the effect of dispersion on oxide surface-adsorbate interactions. For example, Plata *et al.* found that the optB86b-vdW functional computed adsorption energies of acetaldehyde molecules to the TiO_2 solid surface that were larger than those calculated by local GGA functionals (Plata et al., 2013). In addition, it found that the adsorption energy of individual acetaldehyde molecules decreases with increasing surface coverage. This is because the adsorbate-surface bond can be disrupted by the presence of neighbouring species. These adsorbate-adsorbate lateral interactions are involved in the non-ideal behaviour of the adsorption process with increasing surface coverage. It is the dispersion forces that are responsible for the modified description of the lateral interactions. Calculations involving

the optB86b-vdW functional produced a significant reduction in the dipole-dipole and steric repulsion interactions between molecules compared to the GGA functional. Sorescu *et al.* investigated the adsorption of CO_2 on TiO_2[110] and found that adsorption was predicted to be stronger when calculated with several dispersion-corrected functionals as compared with GGA calculations, bringing the theoretical results into closer agreement with experiment (Sorescu et al., 2011). In another recent work by Johnston various vdW functionals were employed to calculate the adsorption energy and geometries of ethanol at the α-Al_2O_3 [0001] surface (Johnston, 2014). This study also found that vdW functionals gave adsorption energies that were significantly larger in absolute value than those from the GGA functional, although both methods predicted dissociative adsorption (with transfer of a proton to the surface) to be more stable than intact molecular adsorption.

It is clear from the results of these studies that DFT calculations including an adequate treatment of vdW interactions can lead to significantly different energies and geometries of adsorbed molecules at oxide surfaces, compared to standard DFT calculations. In the present chapter, my aim is to investigate the effect of vdW forces on the adsorption of small organic molecules at the TiO_2 [110] surface. In order to focus on the direct adsorbate-surface interactions, rather than the lateral interactions, my calculations are undertaken at low coverage. The chapter is organised as follows: I first discuss the equilibrium relaxed structures of TiO_2[110] in comparison with experimental data from low energy electron diffraction (LEED) and surface x-ray diffraction (SXRD). I then discuss the energies and geometries for different adsorption configurations of a number of small organic molecules containing alkyl, hydroxyl, carboxyl and amino groups, as obtained from the simulations with normal GGA calculations and with vdW functionals. I compare my results with those from previous studies, and, whenever possible, with experimental results.

3.2 Calculation methods

The oxide surface was simulated using a periodic stack of quasi-two dimensional slabs, where each slab is separated from the neighbour by a vacuum gap. The gap width was

set to 15 Å to provide sufficient space for the adsorbates, avoiding their interactions with neighbouring (periodic image) slabs. We used slabs with four O-Ti-O tri-layers (figure 3.1), as in several previous theoretical studies of this surface (Tonner, 2010; Hameeuw et al., 2006; Mattsson et al., 2014; Kowalski et al., 2010).

Surface energy is defined as; $E_{surf}(n, L)$ for a system comprising n layers and a vacuum width of L:

$$E_{surf}(n, L) = \frac{E_{tot}(n, L) - E_{tot}(n, 0)}{A} \tag{3.1}$$

where $E_{tot}(n, L)$ and A are the total energy and total surface area per repeating unit, respectively. $L = 0$ corresponds to the bulk crystal. Since each slab has two surfaces, A is twice the area of each surface per repeat unit. Our real interest lies in a semi-infinite material, so we were concerned with the surface energies as both n and L tend to infinity. We eventually used a four-layer slab as this was found to be sufficient for the convergence of the surface formation energy (figure 3.2) and other properties of this surface (Nolan et al., 2008; Tonner, 2010; Hameeuw et al., 2006). Some authors have pointed out that calculated surface energies display significant oscillations with the number of layers and are not well converged for this slab thickness. For example, Kiejna *et al.* reported an increase of 39 % in the surface energy when increasing the slab thickness from 4 to 5 trilayers (Kiejna et al., 2006). The origin of this behaviour is in the relative positions of the ions at each side of the slab, which is different for even and odd numbers of layers. In even-layer slabs the five-fold Ti atom in the top surface is directly above the six-fold Ti atom in the bottom surface, while in odd-layer slabs equivalent Ti atoms at the top and bottom surfaces are exactly opposite each other. Therefore, in even-layer slabs the displacements of Ti atoms at each side of the slab reinforce each other, whereas in odd-layer slabs they oppose each other (Bates et al., 1997). In order to counteract this effect and avoid interactions between the relaxations of the two surfaces, we kept the bottom two layers of our slabs fixed to their bulk positions, while the ions in the top two layers were allowed to relax to their equilibrium positions, as illustrated in figure 3.1. We found that the increase in the GGA

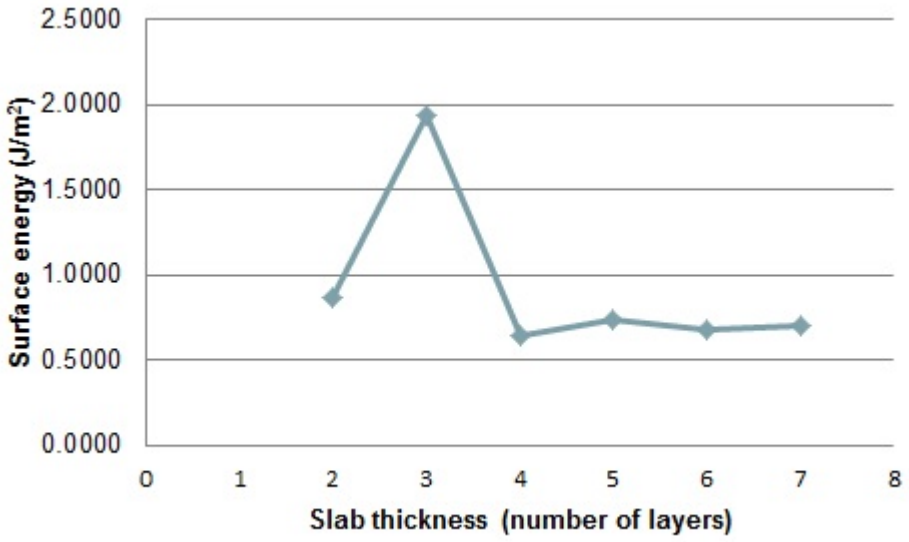

Figure 3.2: Substantial oscillations occur in surface energy as a result of increasing slab thickness and the values converge at around 7 layers. The 4- layer slab provides a reasonable surface energy value whilst providing a structure with a lower total number of atoms.

surface energy from 4- to 5-layer calculations was of 13 % (from 0.65 to 0.73 Jm^{-2}), much less than the increase reported by Kiejna *et al.* Moreover, since the focus of this work is the comparison between van der Waals and local density functional calculations, and both set of calculations are done with the same slab thickness, these relatively small oscillations of the slab properties should not have any significant effect in our conclusions.

In the directions parallel to the surface, the simulation cell contained 42 surface unit cells, which means that the distance from the adsorbed molecule to its periodic images is at least ∼12 Å, and therefore lateral interactions are very small. Adsorption energies E_{ads} were then found using the equation:

$$E_{ads} = E_{slab+molecule} - E_{slab+moleculefar} \tag{3.2}$$

where $E_{slab+molecule}$ is the energy of the molecule / surface complex and $E_{slab+moleculefar}$ is the energy of the same system with the molecule placed in the centre of the vacuum gap, where the interaction with the surface is very small. This approach allows an effective

cancellation of errors from the two terms in the right-hand side of equation 3.2, and also cancels out the small contributions from lateral interactions to E_{ads}. Thus, my results refer to the limit of very low coverage.

3.2.1 Density functional theory calculations

All the calculations were performed using the plane-wave DFT code VASP (Kresse and Furthmüller, 1996). Geometries and total energies were first obtained in the generalised gradient approximation (GGA) with the exchange-correlation functional of Perdew, Burke and Ernzerhof (PBE) (Perdew et al., 1996), and then with the vdW-DF method of Dion *et al.* (Dion et al., 2004), in the opt-B88-vdW formulation implemented in VASP by Klimeš *et al.* (Klimês et al., 2011). In the vdW-DF method, the exchange-correlation term is calculated as:

$$E_{xc} = E_x^{GGA} + E_c^{LDA} + E_c^{nl} \tag{3.3}$$

where E_x^{GGA} is the GGA exchange energy and E_c^{LDA} accounts for the local correlation energy obtained within the local density approximation (LDA). E_c^{nl} is the non-local correlation energy based on electron densities interacting via a model response function (Dion et al., 2004). E_c^{nl} is obtained through a double space integration and provides an improvement to non-local electron correlation effects compared to local or semilocal functionals.

Formally the Ti cations in the TiO_2 bulk and [110] surface are in the 4+ oxidation state, where the d orbitals are empty. In practice, due to covalent effects and, in the case of the surface simulations, to small charge transfer from adsorbates, the occupancy of the Ti 3d levels is not zero. The description of the Ti 3d levels within the DFT framework is problematic, as has been discussed in detail before (Calzado et al., 2008; Morgan and Watson, 2010; Di Valentin et al., 2009). In order to improve the description of the d electrons, we applied a Hubbard-type correction to these orbitals, both in the PBE and in the vdW-DF calculations. This correction, which is proportional to a parameter U_{eff},

has the effect of penalising the hybridisation of the specified orbitals of the metal atoms (Ti d orbitals) with the ligands (O atoms) (Anisimov et al., 1991). A value of $U_{eff} = 3$ eV was used as this value provided a good description of the energetics of adsorption of atoms at TiO_2 surfaces (Nolan et al., 2008; Grau-Crespo and Schwingenschlogl, 2011).

The interaction between the valence electrons and the core was described with the projected augmented wave (PAW) method in the implementation of (Kresse and Joubert, 1999). The core electrons, up to 3p in Ti and 1s in O were kept frozen in their atomic reference states. The cut-off energy controlling the number of plane wave basis functions was set to $E_{cut} = 400$ eV. Due to the size of the simulation cell (12.09 x 13.25 x 27.52), reciprocal space integrations during ion relaxations were performed by sampling only the Γ point of the Brillouin zone. Test calculations confirmed that including more k-points in the integration led to a negligible effect on the relaxed geometries. Final energies were then obtained with a single-point calculation and a finer k-point mesh of 3x3x1 divisions. Relaxations of the ion positions were performed using a conjugate gradient algorithm, until the forces on all atoms were less than 0.01 eV/ Å. The cell parameters in the slab model were kept fixed to the values determined by the bulk relaxation.

3.3 Results and discussion

3.3.1 Hubbard correction

The electronic structure can be deduced from the calculated electronic density of states (DoS) for pure rutile Titanium dioxide. The insulator character of the oxide is accurately reproduced as shown in figure 3.3. This is confirmed by the large band gap seen above the Fermi level. Using the Hubbard correction DFT+$U$3 the band gap is more accurately represented with a value of 2.19 eV. This is in comparison with the experimental band gap of 3.06 eV (Ressler and Walker, 1967). The band gap of the pure oxide is, hence, underestimated here using $U_{eff} = 3$ eV. Using higher values of U provides a more accurate representation of the band gap but also gives less good splitting of orbitals. For our

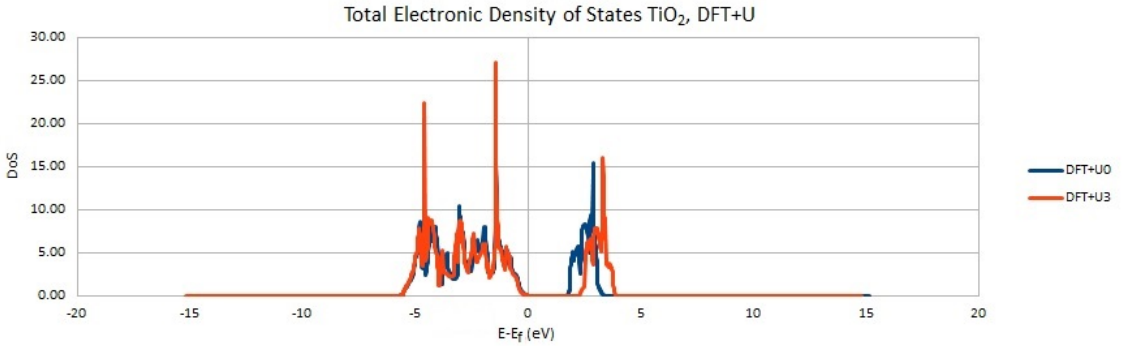

Figure 3.3: Electronic density of states representing the insulator character of TiO_2. The plot in red shows the improvement in band gap width as a result of an increase to the Hubbard correction, DFT+$U$3.

calculations, a value of $U_{eff} = 3$ eV was used as this gave a reasonable separation of oxygen and metal DoS, hence the most accurate description of the electronic and redox properties of the oxide.

3.3.2 Relaxations in the clean surface

We first compare the calculated atomic displacements due to surface relaxations, in the direction perpendicular to the surface, with experimental results. In table 3.1 we list the theoretical displacements obtained with both the PBE functional and the vdW-DF, in comparison with data from quantitative LEED (Cabailh et al., 2007) and SXRD (Kiejna et al., 2006) experiments.

There is good agreement between current SXRD and LEED-IV results. Taking into account the experimental errors, the quantitative difference (Δ) in atomic displacements for the Ti_{5f} and the inplane O were found to be only marginally significant (Ti_{5f}, $\Delta = 0.08 \pm 0.03$ Å), (in plane O, $\Delta = 0.10 \pm 0.09$ Å), whereas the relaxation of the O_b atom was identical using each technique, as reported by Cabailh *et al.* (Cabailh et al., 2007).

This work's displacements of atoms in the surface region are well described by the PBE and vdW-DF approximations for the exchange and correlation functionals. These were in good agreement with the experimental work. The vdW density functional predicts slightly

	This work		Experiment	
Atom	**PBE**	**vdW-DF**	**LEED**[a]	**SXRD**[b]
Ti_{6f}	0.20	0.17	0.25 ± 0.03	0.25 ± 0.01
Ti_{5f}	-0.11	-0.15	-0.19 ± 0.05	-0.11 ± 0.01
O inplane	0.19	0.14	0.27 ± 0.08	0.17 ± 0.03
O_b	0.02	0.01	0.10 ± 0.05	0.10 ± 0.04

[a] **(Lindsay et al., 2005)** [b] **(Sushko et al., 2006)**

Table 3.1: Atomic displacements (Å) along the [110] direction calculated for the relaxed four layer slab model compared with the experimental data. The atoms refer to those shown in the top layer of figure 3.1.

less relaxation of the top Ti and O atoms than that obtained from the PBE functional. However, the inward displacement of the Ti_{5f} atom was larger for the vdW-DF and more similar to the value obtained from LEED ($\Delta = 0.04$ Å). The PBE predicted displacement for the Ti_{6f} was closer, than the vdW-DF result, to both of the experimental measurements ($\Delta = 0.05$ Å). For the in-plane O, the PBE displacement was in between that provided by the LEED and SXRD data whilst the vdW-DF displacement is marginally smaller than the SXRD data ($\Delta = 0.03$ Å). For the O_b displacement, DFT calculations provide the only significant difference with experiment ($\Delta = 0.08$ Å, PBE and $\Delta = 0.09$ Å vdW-DF). Our calculations, using both functionals, gave a small outward shift. This is consistent with previous DFT calculations which conclude that the O_b either maintains its ideal bulk-terminated location, or shifts away from the bulk. For example, ab initio calculations by Hameeuw *et al.* indicate a relaxation of 0.06 Å away from the bulk whereas a study by Kiejna *et al.* reported a zero shift for this atom (Hameeuw et al., 2006; Kiejna et al., 2006). The theoretical-experiment difference has been attributed by Sushko *et al.* to be due to the presence of soft anharmonic surface vibrational modes, which are not fully taken into account in the ab initio calculations (Sushko et al., 2006).

3.3.3 Adsorption of methane

Now considering the interactions of methane with the [110] surface. I used four starting configurations for methane, with either 1, 2, or 3 CH bonds facing the surface. In addition, two CH orientations were used; one with the plane of the CH bonds in parallel with the

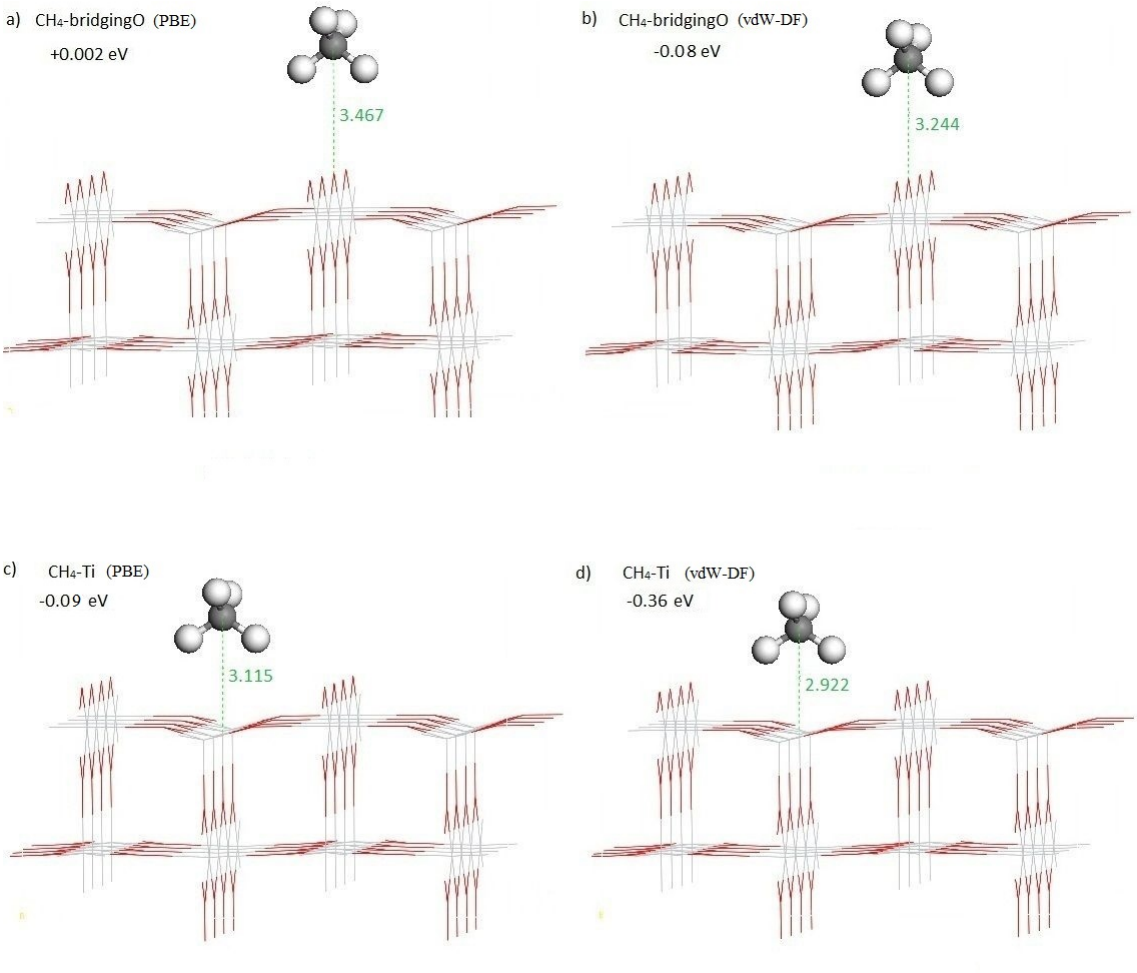

Figure 3.4: Stable adsorption modes of methane at the O_b and the Ti_{5f} sites at the TiO_2 [110] surface. The figures on the left represent calculated values with no vdW forces, those on the right are values calculated using the vdW-DF. Distances are in Å and adsorption energies (E_{ads}) are given in eV.

Ti_{5f} row and the other rotated at 90°, with the CH bonds perpendicular to the Ti_{5f} row. Regardless of the initial configuration and the employed functional, the relaxed adsorbate always has two CH bonds oriented towards the surface perpendicular to the Ti_{5f} row. Other configurations are not minima in the potential energy landscapes.

Two local minima were found in the adsorption landscape for both functionals: one of top of the Ti_{5f} cations and on top of the O_b sites. The stable adsorption configurations are shown in figure 3.4, together with the adsorption energies and geometric details.

In the PBE calculations (no dispersion corrections included), it is found that the interaction between the surface and methane adsorbed on the O_b site was very weak and even slightly positive with respect to the desorbed reference level. A weak adsorption was found at the Ti_{5f} site, with adsorption energy of 85 meV. In all cases, the configuration adopted by the methane molecule exhibits two CH bonds pointing towards the surface, and the plane containing these two bonds is perpendicular to the row of bridging oxygen atoms.

Using the vdW-DF, the adsorption configurations are the same as in the PBE calculation, but the interactions become stronger. The adsorption energy at the O_b site is now slightly negative, while the absolute value of the adsorption energy at the Ti site increases by 0.27 eV. We have not found experimental information on this system to benchmark our calculations against, probably because such experiments would need to be done at very low temperature, considering the weak adsorption behaviour. However, our results clearly illustrate that taking into account the vdW interactions makes a significant difference in the description of the weak adsorption of methane on this surface.

3.3.4 Adsorption of methanol

For methanol (CH_3OH) I considered two starting molecular state orientations and one dissociated ($CH_3O^- + H^+$) state. The starting configurations for molecular adsorption were with the CH_3 group or OH group orientated towards both the in-plane Ti_{5f} and bridging O sites. The dissociated adsorption mode was calculated with the oxygen in the CH_3O^- group interacting directly with the Ti_{5f} site and the proton transferred to a

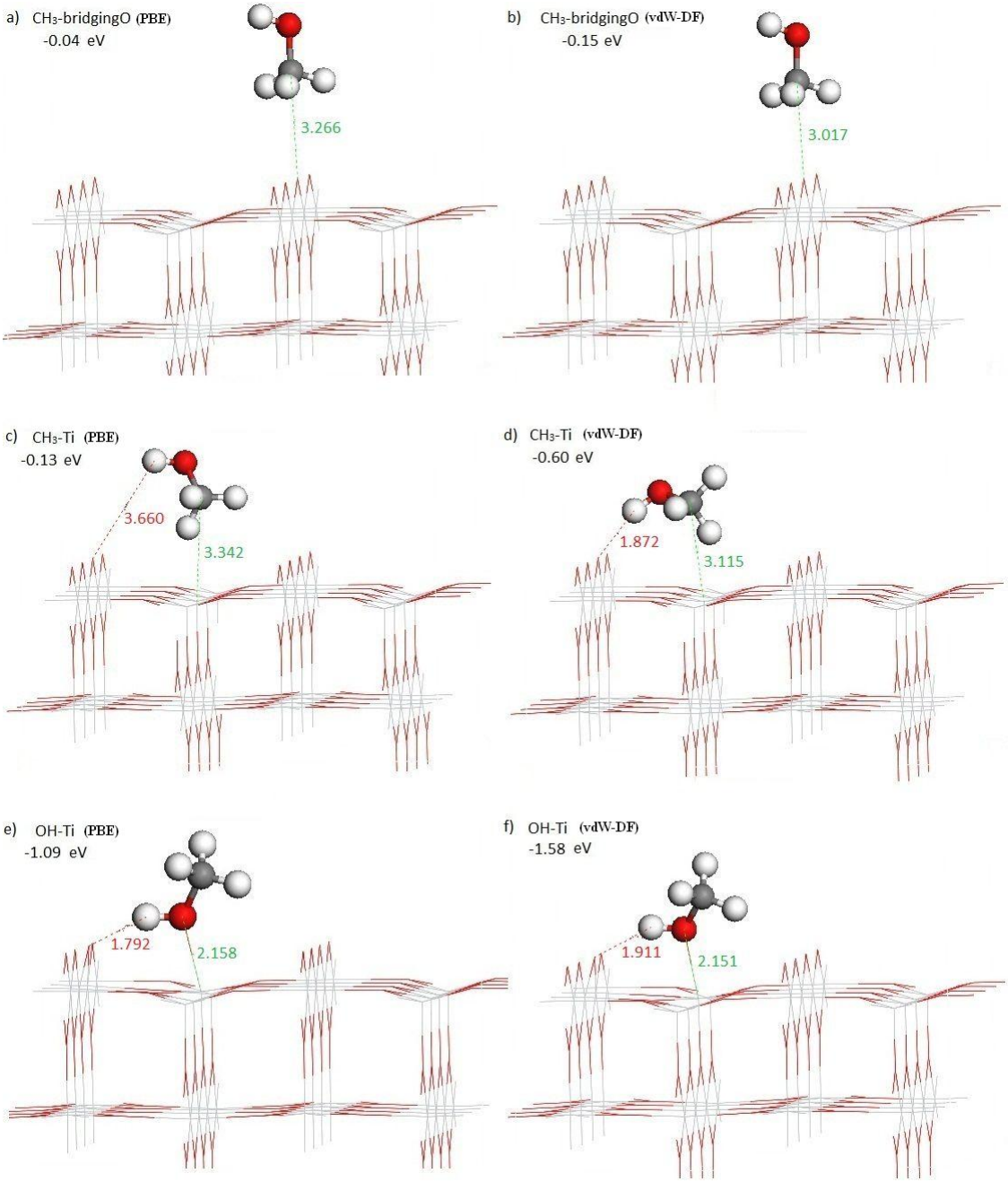

Figure 3.5: Stable adsorption modes of methanol to the TiO_2 [110] surface. OH to bridging O hydrogen bond lengths (Å) are shown in red.

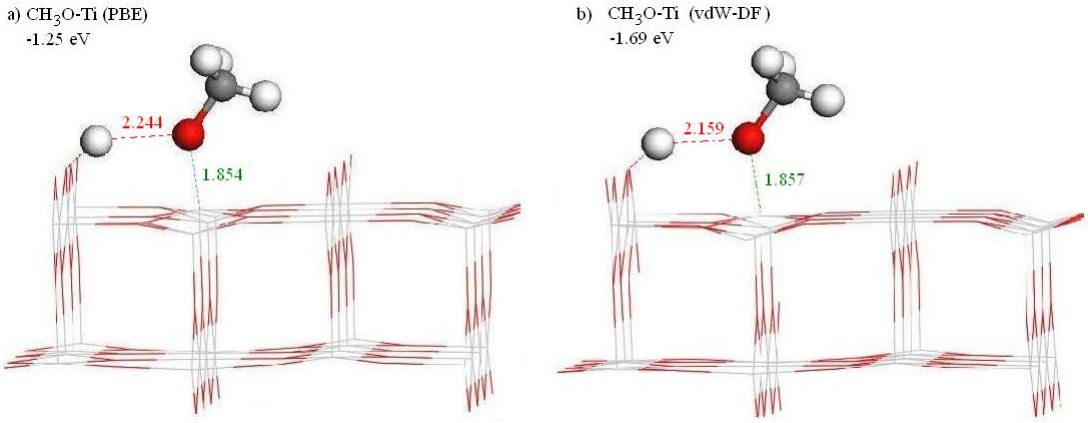

Figure 3.6: Dissociative methanol adsorption modes to the TiO_2 [110] surface.

neighbouring O_b site.

In the least stable of the molecular adsorption configurations found here (figure 3.5a,b), the closest interaction is between the CH_3 group of methanol and the surface O_b site. This interaction mode is very weak (-0.05 eV) when calculated with PBE but it is a stronger (-0.16 eV) when calculated using the vdW-DF.

The CH_3 to Ti_{5f} interaction is stabilised (at least at low surface coverage) with the molecule rotated, at low surface coverage, to form an $OH\cdots O_b$ hydrogen-bond interaction (figure 3.5c, d). This adsorption configuration is stronger by 0.48 eV when using the vdW-DF resulting in an alteration to the binding orientation with a much shorter OH-O bond length, compared to PBE.

The configuration with direct interaction between the OH group and the Ti_{5f} gave the most negative adsorption energy among the non-dissociated configurations (figure 3.5e,f). The geometry was optimised with the proton of the OH group pointing towards the neighbouring O_b site. There was no spontaneous transferring of the proton to the bridging oxygen indicating a meta-stable adsorption mode for the methane molecule. However, the dissociated state has a more negative adsorption energy compared to the molecular state, both with PBE and with the vdW-DF (figure 3.6a, b). This suggests that a transition barrier exists between the molecular and dissociated states at the surface but that the dissociation of methanol is preferred.

The strongest adsorption occurs when methanol dissociates and the negatively charged oxygen atom of the methoxyl (CH_3O) species attaches to the surface Ti_{5f} site. Our results are consistent with temperature programmed desorption (TPD) data by Henderson *et al.*, who found three prominent desorption peaks (at 295 K, 350 K and 480 K) for methanol on the vacuum-annealed surface of TiO2 [110] (Henderson et al., 1998). The 295 K peak was assigned to the molecular adsorption configuration, while the higher temperature peaks were assigned to two dissociative configurations: the 350 K peak corresponds to methoxyls at non-vacancy sites (as calculated here), and the one at 480 K to methoxyls at oxygen vacancy sites. The latter situation, that should corresponds to the most negative adsorption energy, has not been considered here because we only study the stoichiometric surface. This experiment shows that, even at the stoichiometric surface, the dissociative adsorption of methanol is stronger than molecular adsorption.

It is interesting to note here that the DFT calculations from Sánchez de Armas *et al.* found that both the molecular and dissociated states of methanol adsorption are almost degenerate on the TiO_2 [110] surface (Sánchez de Armas et al., 2007). They actually found that the energy difference depend on the thickness of the slab model used to represent the surface, and the average difference from five- and six-layer slabs was only $\sim$0.01 eV (on the stoichiometric surface). The energy difference found in our study was 0.16 eV when using PBE, and 0.10 eV when using the vdW-DF, in both cases favourable to dissociation. As we discussed in the methodology section, by fixing the bottom layers of our slab we can expect our results to converge faster with the thickness of the layer than in symmetric slab calculations. The difference between the results from the two functionals should depend even less on the number of layers included. For the present model, our results are consistent with experimental data, as discussed above, showing that the dissociated form has more negative adsorption energy compared to the molecular form at the TiO2 [110] surface.

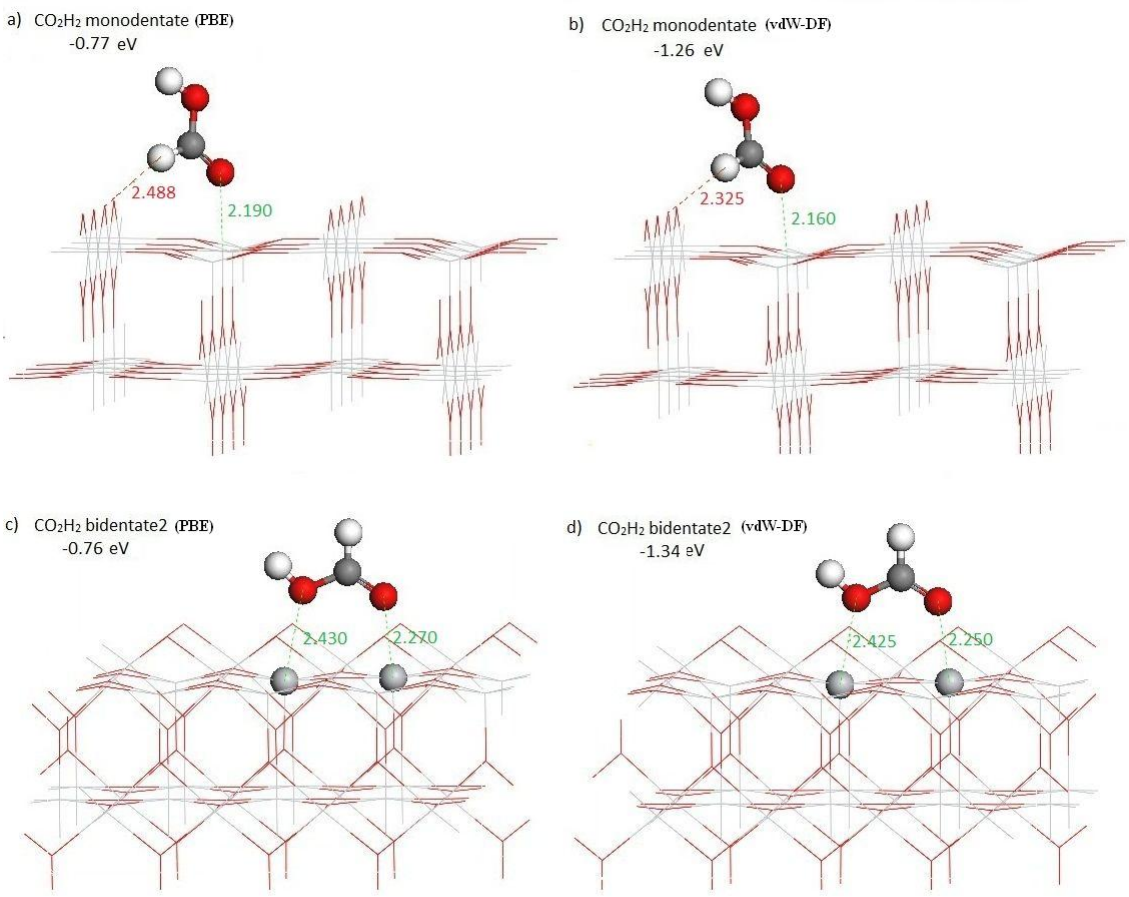

Figure 3.7: Stable adsorption modes of formic acid to the TiO_2 [110] surface. Monodentate views are taken along the xz plane. Bidentate-2 views are taken along the yz plane. Distances are given in Å.

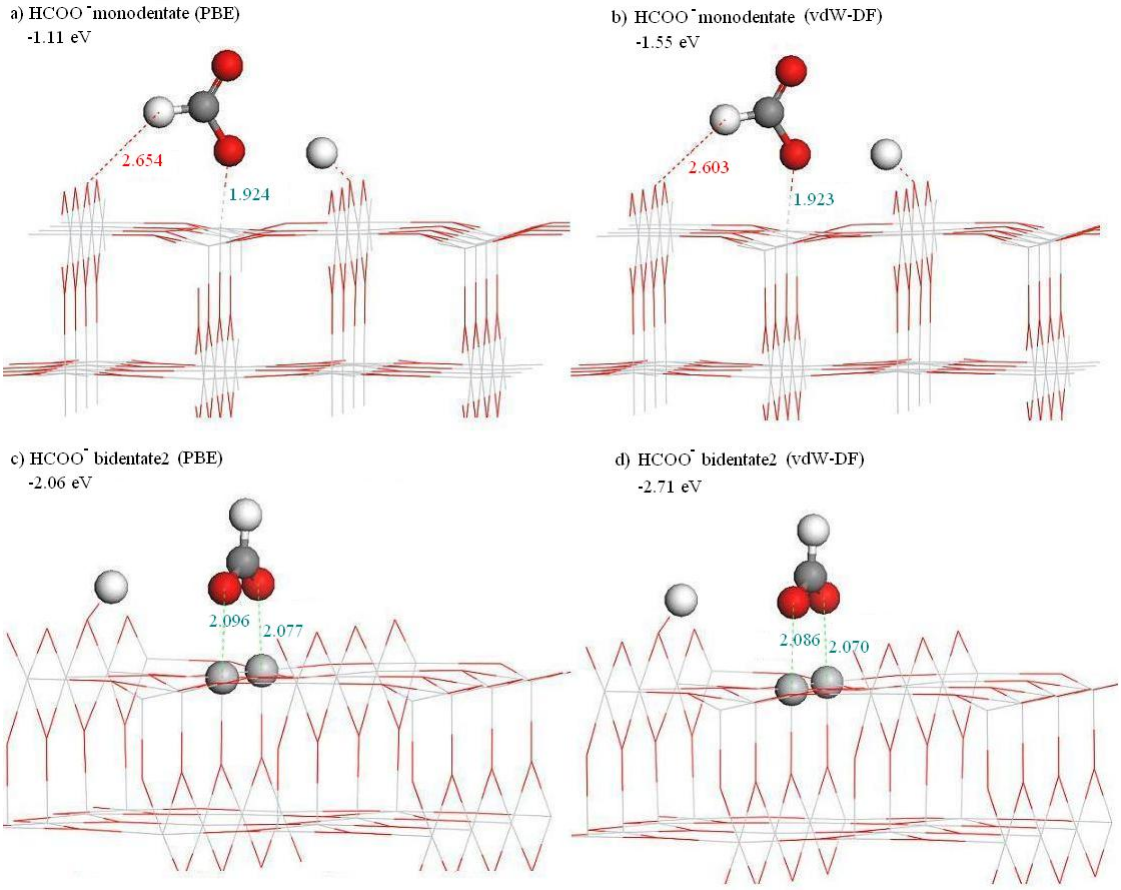

Figure 3.8: Stable adsorption modes of the dissociated formate ion to the TiO_2 [110] surface. Monodentate views are taken along the xz plane. Bidentate-2 views are taken at an angle the xy plane to show the disscoiated proton at the bridging O site. Distances are given in Å.

3.3.5 Adsorption of formic acid

The next adsorbate considered in our study is formic acid (HCOOH). With oxygen atoms in the adsorbate, the dominant interactions are expected to be those between these oxygen atoms and the coordinatively unsaturated Ti atoms at the surface. Following Sushko *et al.*, I consider both monodentate and bidentate adsorption configurations of this molecule, where one or two oxygen atoms of the molecule interact closely with the surface (Sushko et al., 2006). I also compare the stability of molecular versus dissociative adsorption, using the two density functionals.

In principle, for molecular adsorption there are two possible bidentate configurations, with either one or two surface Ti atoms participating in the interaction with the molecule ('bidentate1' and 'bidentate2' respectively). However, in contrast with the work of Sushko *et al.*, where a shallow minimum for the bidentate1 configuration for the formic acid molecule was reported, I found here that for both functionals the bidentate1 adsorption configuration was not a minimum in the energy landscape and converged to a bidentate2 configuration upon relaxation (Sushko et al., 2006). A very recent study using the PBE functional (with Hubbard U but with no dispersion correction) has also found only one bidentate mode for molecular adsorption (Mattsson et al., 2014). My PBE calculations predict the adsorption energy of the formic acid monodentate configuration to be almost exactly equivalent to the bidentate2 at the TiO_2 [110] surface. Sushko *et al.* predicted that the adsorption of formic acid in the bidentate2 configuration has an energy difference of $\sim$0.1 eV compared to the monodentate configuration (Sushko et al., 2006). The relaxation observed in our calculation of the monodentate molecular orientation leads to additional interaction between the central carbons hydrogen atom and the O_b of the surface (figure 3.7a), which results in a monodentate adsorption energy similar to that in the bidentate2 configuration.

However, when the vdW-DF is used to account for the dispersion forces, the adsorption in the monodentate and bidentate2 configurations of (non-dissociated) formic acid is more exothermic by approximately 0.5 eV and 0.6 eV, respectively, than when PBE is used. Thus, whereas the PBE adsorption energy values for monodentate and bidentate2 con-

figurations are essentially the same, the vdW-DF predicts adsorption in the bidentate2 configuration to be stronger (by 0.1 eV) than in the monodentate configuration.

Since there is a considerable body of experimental evidence showing that formic acid dissociates at the TiO_2 [110] surface (Mattsson et al., 2014; Henderson, 1997; Thevuthasan et al., 1998; Hayden et al., 1999; Bennett et al., 2000), we have also considered different modes of dissociative adsorption. The acid dissociation occurs by the transference of the oxygen bound proton to a neighbouring O_b site at the surface. The adsorption of the formate bidentate2 ion was clearly favoured over the monodentate ion using both PBE and the vdW-DF. The bidentate2 ion is bound to the substrate Ti_{5f} cations with the molecule orientated along the [001] direction. The O-C-O intramolecular bond angle was found to be 127.1° using the vdW-DF which represents a widening from 122.2° in the monodentate ion due to the interaction with the two Ti^{4+} surface ions. The value of the bound bidentate2 formate bond angle is within the experimental error of the experimental bond angle of 126 ± 4° as measured by Thevuthasan *et al.* using high-energy photoelectron diffraction (Thevuthasan et al., 1998). These authors also reported a Ti(surface)-O(formate) vertical distance of 2.1 ± 0.1 Å. The DFT calculated data predicts an average vertical separation between the Ti lattice cations and the formate oxygens of 2.09 for PBE and 2.08 Å for the vdW-DF, both in reasonable agreement with experiment.

As expected from experimental information, dissociative adsorption of formic acid is predicted to be more stable than molecular adsorption (figure 3.8). For the most stable adsorption configuration (bidentate), the energy lowering from dissociation at the surface was 1.29 eV using PBE and 1.36 eV using the vdW-DF.

The bridging mode interaction, as seen in the bidentate2 configuration of formic acid, has been reported to be a common orientation for carboxyl group containing species at the TiO_2 surface (Muir and Idriss, 2013; Guo et al., 2011). This orientation was predicted here to be the most stable adsorption mode in both molecular and dissociated formic acid. My results show that when vdW interactions are taken into account, the relative stability of the bidentate configuration with respect to the monodentate mode was increased.

3.3.6 Adsorption of glycine

For glycine I used eight molecular orientations based on the most stable adsorption modes for neutral (N) (H_2N-CH_2-COOH), zwitterionic (ZW) (H_3N-CH_2-COO) and anionic (AN) (H_2N-CH_2-$COO^- + H^+$) forms at the in-plane 5-coordinate Ti^{4+} on the TiO_2 [110] surface.

Glycine shows strong adsorptions to the Ti_{5f} ion with both the amine NH_2 group and the carboxyl group. The strongest adsorption is with the bidentate-2 configuration of the carboxyl group. This mode involving the bridging of two Ti atoms with anionic moieties is similar to the most favourable adsorption behaviour of carboxylic acids on TiO_2 [110]. However, unlike these molecules glycine can form hydrogen bonds via the amino group, thus providing additional stability. Comparison of the AN(OO) adsorption energy of -1.95 eV with the most stable mode of AN_H(OO) E_{ads} = -2.12 eV provides a stabilisation value of 0.17 eV (16 kJ mol^{-1}). Tonner identified a similar value for the stabilisation effect of the surface bound hydrogen atom and the nitrogen atom of the amino group (Tonner, 2010).

In addition to the vdW-DF predicting a stronger adsorption energy with shorter bond lengths, different adsorption modes where identified. Three zwitterionic forms of glycine were adsorbed at the surface when van der Waals forces were not present in the calculation (figures 3.9d, e, f). In contrast, only one stable zwitterionic form was present using the vdW-DF (figure 3.10c). The ZW_H(OO) configuration of glycinate, where the COO^- group is in bidentate-2 coordination and the C-C bond is tilted in the [110] direction to allow a double hydrogen bond system between the NH_3^+ group and the adjacent row of bridging oxygens, was calculated to be the most stable mode in a previous DFT study by Ojamäe *et al.* and co-workers (Ojamae et al., 2006). However, the STM experiments by Barteau and Qiu found no evidence for the zwitterionic structure on the TiO_2 surface (Qiu and Barteau, 2006). If the interaction of the NH_3^+ group of the zwitterions with the surface was sufficiently strong it should prevent free rotation about the C-C bond giving rise to asymmetric features in STM, which were not seen. This is in agreement with more recent findings by Lerotholi *et al.* who used photoelectron diffraction (PhD) to determine that, at low coverage only the deprotonated glycinate species $NH_2CH_2COO^-$ is present (Lerotholi

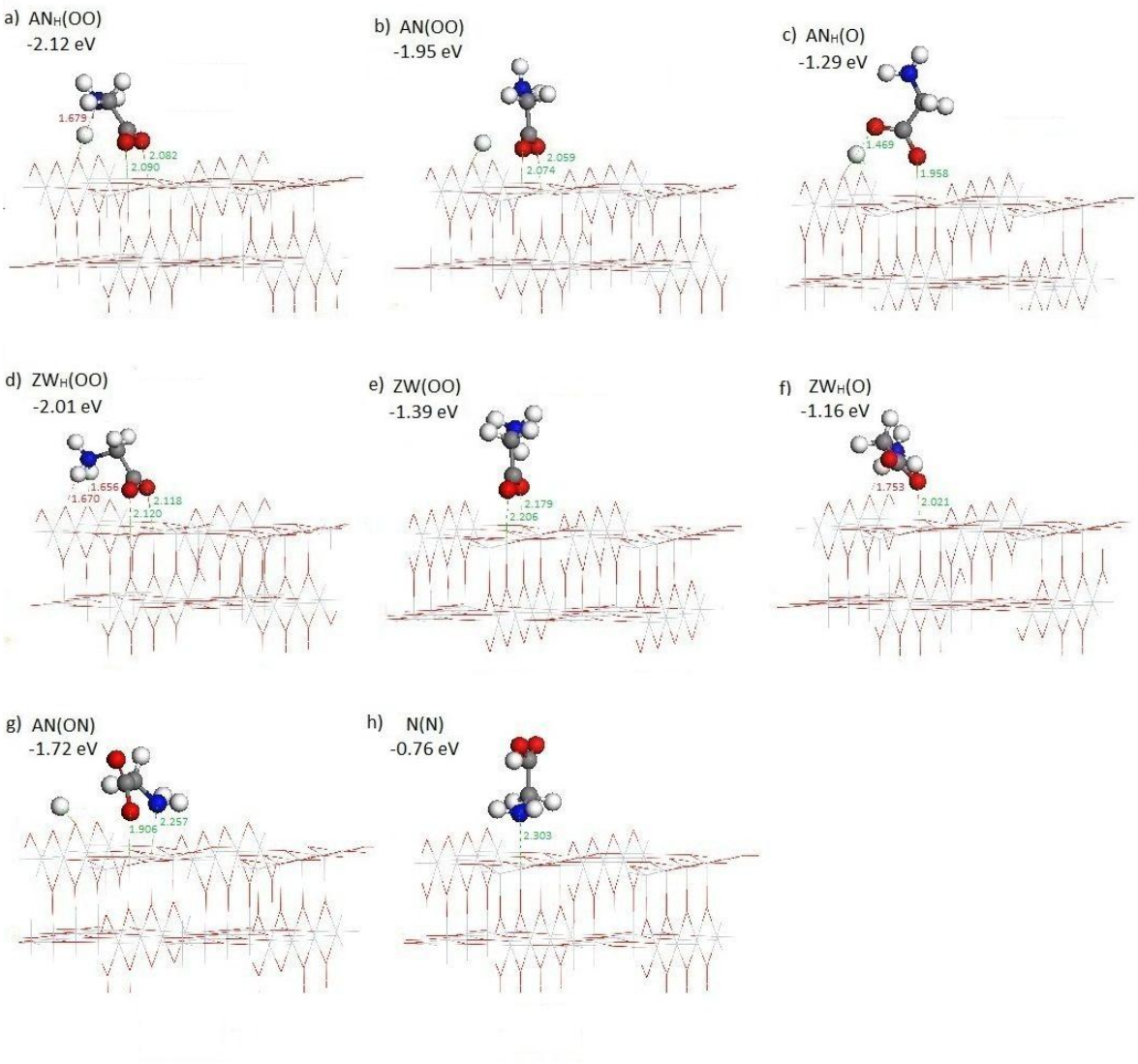

Figure 3.9: Stable adsorption modes without vdW forces for anionic (AN), zwitterionic (ZW) and neutral (N) forms of glycine on the TiO_2 (110) surface, together with adsorption energies and important bonding parameters. NH to O_b hydrogen bond lengths are shown in red. Anionic glycine hydrogen bonding occurs from the transfer of the zwitterionic NH_3^+ proton to the O_b to form a hydroxyl group at the surface. Distances are given in Å.

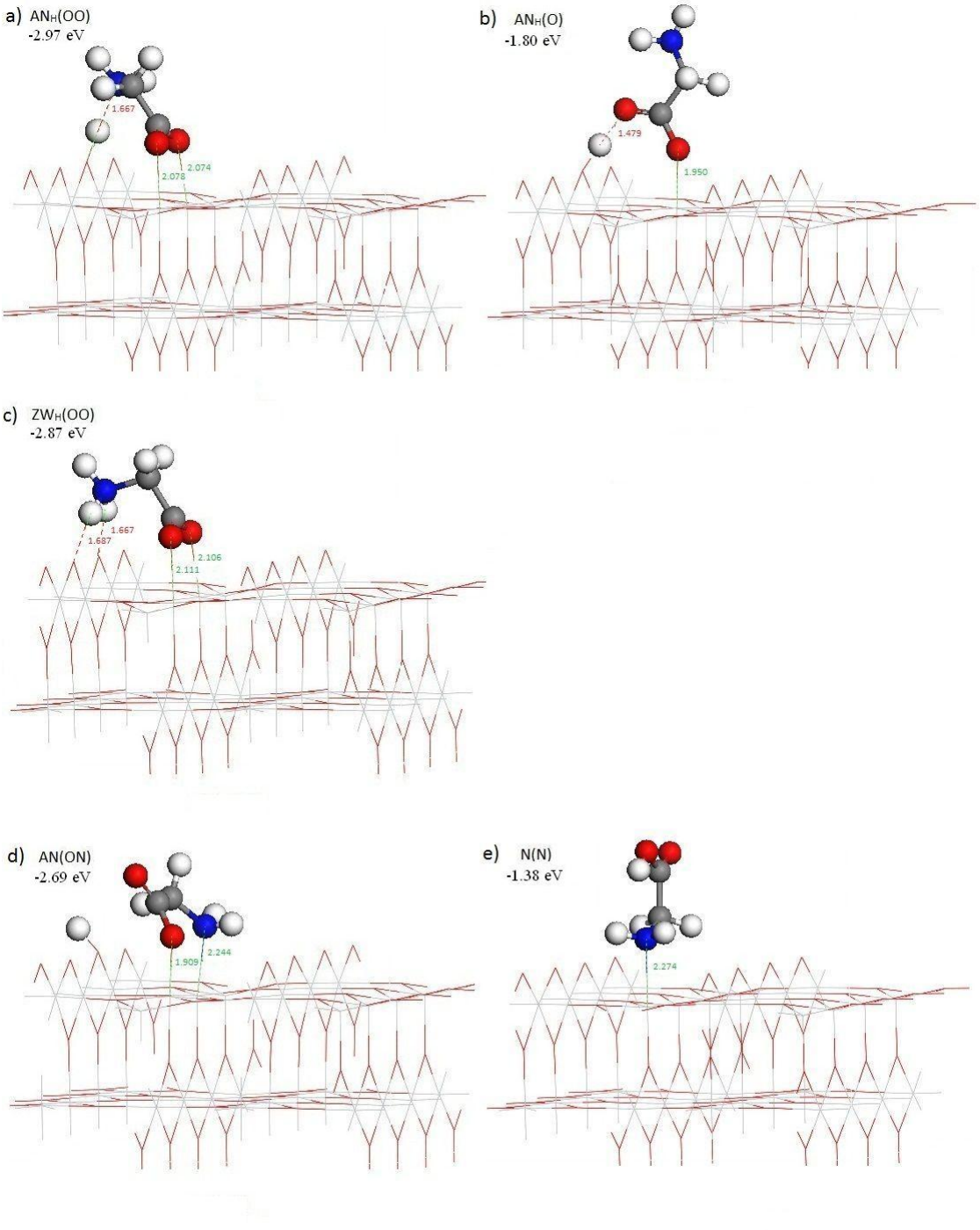

Figure 3.10: Most stable vdW adsorption modes for Anionic (AN), zwitterionic (ZW) and neutral (N) forms of glycine on the TiO_2 [110] surface, together with adsorption energies and important bonding parameters. Distances are given in Å.

et al., 2009). A coadsorbed bridging OH species was also identified by PhD indicating that deprotonation of the chemisorbed species does occur. Our studies also suggest that the anionic form is far more likely to be present at the surface when the vdW-DF is included in DFT calculations, since the larger surface dispersion forces encourage the deprotonation of the zwitterionic amine group to the surface O_b site. This results in the formation of an OH group at the surface and the glycinate anion which interact via the associated OH-amino hydrogen bond (figure 3.10a). This additional contribution from surface protonation makes the anionic form $AN_H(OO)$ more stable than the zwitterionic adsorption mode $ZW_H(OO)$ by 0.10 eV (9.5 kJ mol^{-1}) and explains the disappearance of the weaker zwitterionic modes, ZW(OO) and $ZW_H(O)$, when vdW forces are considered.

Evidence from Raman spectroscopy by Ojamäe *et al.* indicated that in aqueous solution glycine is not adsorbed onto rutile surfaces (Ojamae et al., 2006). This is likely to be due to the presence of partial surface hydroxylation in damp conditions. Glycinate adsorption modes $AN_H(OO)$ are thus not able to form. In addition the amino groups preferentially form hydrogen bonds with the water in solution thus weakening the interaction with TiO_2. Adsorption for organic acids is clearly pH dependant and at pH $\geq$ 7 deprotonation of the carboxyl group together with a reduction in surface hydroxylation provides a mechanism for effective interaction.

3.4 Conclusions

I have presented a DFT investigation of the adsorption of small organic molecules at the TiO2[110] surface, contrasting two different density functionals: the generalized gradient approximation functional PBE, and the non-local correlation functional optB88-vdW, which is capable of correctly describing vdW interactions. Our results show that the inclusion of vdW effects can produce significant differences in both interaction strengths and adsorption geometries of the molecules. As one might expect, the effect of vdW interactions is more important when there are no other strong bonding interactions. In figure 3.11, the variations introduced by vdW-DF (compared to PBE) in the equilibrium

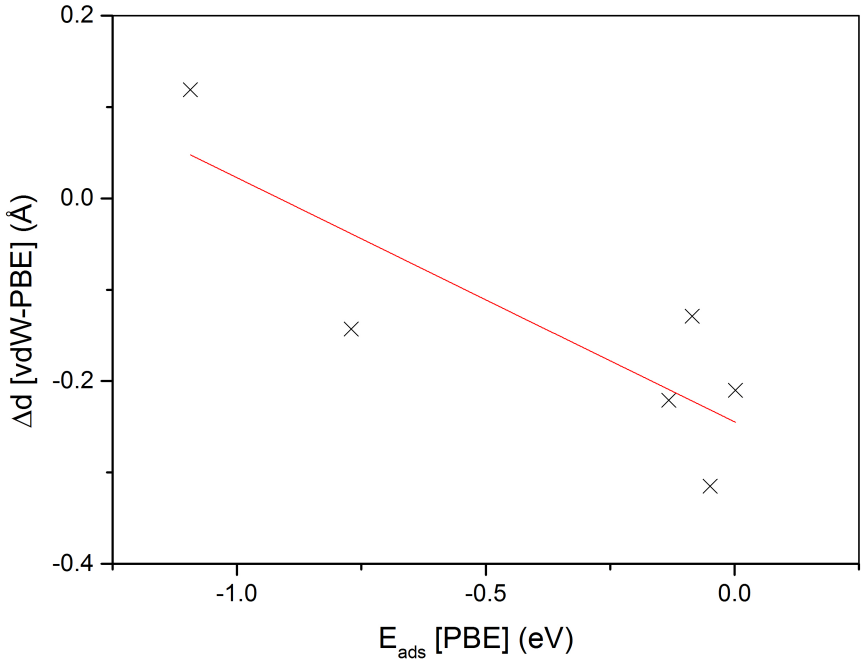

Figure 3.11: The $H_{(molecule)}$-$O_{b(surface)}$ distance difference (Δd) for each adsorption configuration of formic acid, methane and methanol show that vdW forces have a stronger effect on reducing the molecular-surface distances for the lower strength adsorption interactions.

distances between the molecular hydrogen atoms and surface oxygen atoms, are plotted against the adsorption energies (from PBE). The cases of stronger adsorption mediated by carboxylic groups are excluded from the plot. This analysis clearly shows that as the adsorption strength decreases, the effect of the vdW interactions on the adsorption distances becomes larger.

Methane adsorption was found to be much stronger when using the vdW-DF (-0.36 eV) than when using PBE (-0.09 eV) at the most stable configuration. This is as expected, considering that methane is a non-polar molecule for which other interactions, besides dispersion, are very weak. However, although hydroxyl, carboxyl and amino groups all possess a permanent molecular dipole moment, they also showed an increase in the adsorption strength when vdW interactions where included. Methanol adsorption energies were 0.4-0.5 eV (depending on whether dissociation takes place or not) stronger when using

the vdW-DF. But both functional predict that the dissociated state of methanol is more favourable at the surface. The adsorption of formic acid was found to be between 0.4 eV and 0.6 eV (depending on configuration and dissociation) stronger once our calculations fully accounted for dispersion forces. However, the nature of the preferred adsorption configuration of formic acid is also the same for both functionals. The carboxyl group is likely to attach to this surface by binding with each O atom occupying a single Ti_{5f} adsorption site, and dissociation is always favourable over molecular adsorption.

The vdW forces can also have an important effect on the orientation of organic molecules with respect to the surface as seen with the molecular orientations of glycine obtained using the vdW-DF. The experiment analysis using STM and PhD of Barteau and Qiu and Lerotholi *et al.* respectively can be more easily explained once the vdW-DF has been employed (Qiu and Barteau, 2006; Lerotholi et al., 2009). It was observed that although the zwitterion form of glycine does interact with the surface it only occurs in the $ZW_H(OO)$ configuration where two hydrogen atoms on the NH_3^+ group are specifically aligned to interact with two adjacent bridging oxygen atoms. In all other zwitterion configurations the molecule is deprotonated to form the glycinate species $AN_H(OO)$ at the surface. When the glycinate molecule is formed, the acid H is removed to the O_b site thus modifying the structure of TiO_2 [110] surface through the formation of a hydroxyl group.

This study has enabled a better understanding of the effect of dispersion forces on the adsorption geometry and the magnitude of interaction energies of organic molecules at the TiO_2 [110] surface. It is clear from my results that larger scale simulations of the interactions of biomolecules with the TiO_2 layer should also include a proper description of van der Waals forces.

Chapter 4

The impact of ultra violet light on titanium dioxide coated glass

4.1 Introduction

Rough-hydrophilic modified Ti has been shown to promote the adhesion and spreading of a cell (van Kooten et al., 1992) and improves implant osseointegration (Steinemann, 1998). The pre-clinical trials conducted thus far indicate that the SLV surface is capable of inducing significantly more healing than SLA at 2 weeks post implantation (Bornstein et al., 2010). UV irradiation provides an effective means for the hydrophilic conversion of SLA, thus removing a stage from the processing procedure. Possibly, this could provide a simple, quick method for converting native hydrophobic Ti implant surfaces in a clinical setting. The mechanism for the UV induced super-hydrophilic convertion is investigated in this chapter. A novel use of Raman spectroscopy is employed to assess the atomic rearrangements that occur at the TiO_2 surface. In addition, an understanding of the interaction of water with oxide surfaces is investigated using DFT. Water forms an extremely important part of the environment in virtually all biological applications. By studying both theoretically and experimentally how small molecules like H_2O interact with a relatively simple metal crystal surface, we can better understand the elements of

molecular chemistry that occur and how they affect the overall material properties.

4.1.1 Photocatalysis of Titanium dioxide

TiO_2 is well known to be a semiconductor. The value for the band gap energy (E_g) in the rutile form is 3.06 eV (Roessler and Walker, 1967). Irradiation of TiO_2 with UV light, which has an energy greater than the E_g, causes the promotion of an electron from the valance band to the conduction band resulting in the formation of an electron-hole pair. There is now a free electron (e^-) in the conduction band, and a hole (h^+) in the valance band. These are both reactive species which are available to participate in oxidation and reduction processes. These take place either within the TiO_2 itself, through electron and hole recombination, or with adsorbate molecules at the surface (figure 4.1). For example, electron transfer events now occur between the photoexcited TiO_2 and adsorbed H_2O, molecular oxygen and hydroxyl groups that exist at the catalyst surface. This results in the production of superoxide and hydroxyl radicals (scheme 4.1) (Page et al., 2009).

$$TiO_2 + h\nu \longrightarrow e^- + h^+$$

$$h^+ + H_2O_{(ads)} \longrightarrow HO^{\cdot} + H^+$$

$$h^+ + {OH^-}_{(surface)} \longrightarrow HO^{\cdot}$$

$$e^- + O_2 \longrightarrow {O_2}^{\cdot -}$$

$$2{O_2}^{\cdot -} + 2H_2O \longrightarrow 2HO^{\cdot} + 2OH^- + O_2 \tag{4.1}$$

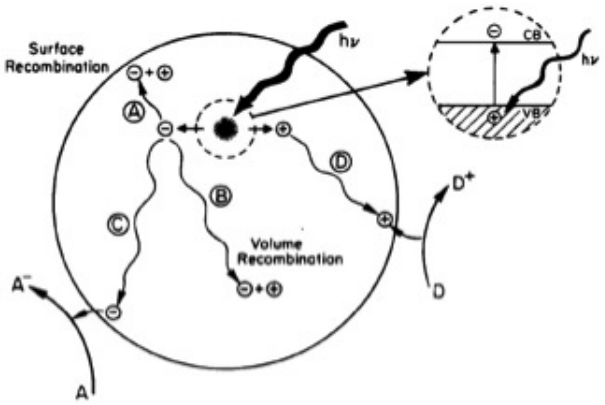

Figure 4.1: Photo-excitation processes in TiO_2, leading to redox behaviour; (A) electron and hole recombination at the surface, (B) electron and hole recombination in the bulk, (C) adsorbate reduction at the surface and (D) adsorbate oxidation at the surface (Linsebigler et al., 1995).

In this way, a key mechanism of TiO_2 photocatalysis is the production of highly reactive oxygen species (radicals). The radicals produced are completely non-selective with the ability to oxidise most organic compounds at the catalyst surface. Thus, one consequence of UV irradiation is the removal of immobilised surface films. Weak UV light is sufficient to decompose adsorbed organic compounds with the evolution of CO_2 as a gas phase product. This is known as photocatalytic decomposition of organic contaminants (PDOC) and means that the TiO_2 surface has the ability to self-regenerate, thus removing surface contaminates as they accumulate in an unobtrusive self-cleaning manner (Fujishima and Zhang, 2006).

4.1.2 Photo-induced super-hydrohilicity

It was found that TiO_2 films acquire super-hydrophilic properties, i.e. a water contact angle of $\sim 0^\circ$ after UV illumination. This is an intrinsic property of the TiO_2 surface. The two proposed mechanisms for the super-hydrophilic conversion are PDOC or the reconstruction of surface hydroxyl groups.

In the case of surface hydroxyl group reconstruction (figure 4.2), the photoexcited e^- are captured by molecular oxygen, while the h^+ diffuse to the TiO_2 surface where they are

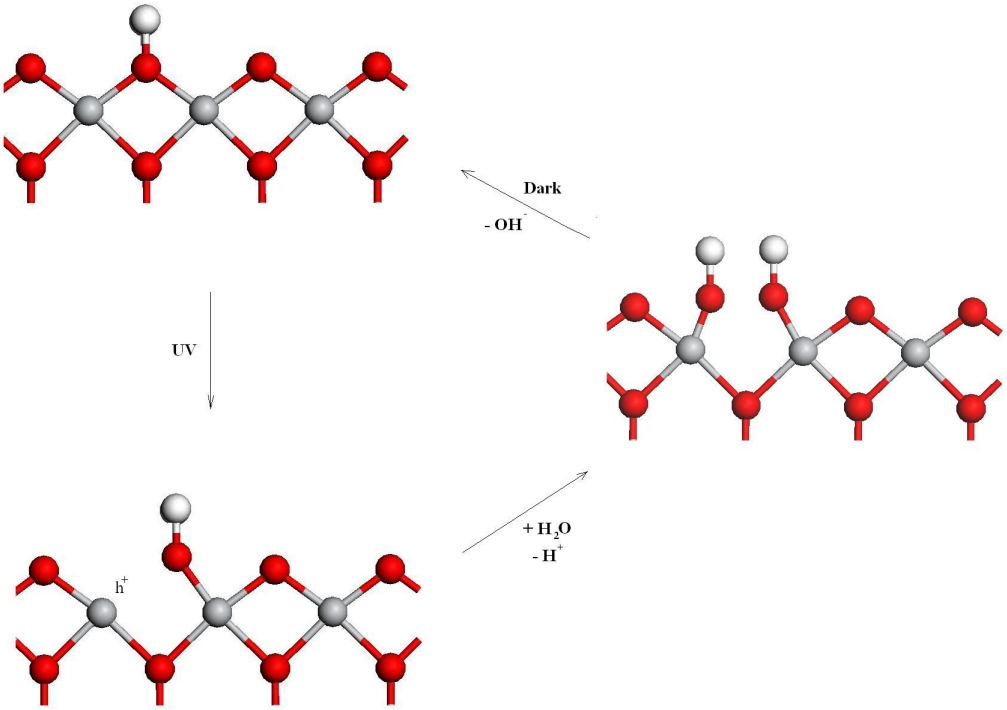

Figure 4.2: Proposed surface hydroxyl reconstruction mechanism of TiO_2 during the reversible hydrophilic change.

trapped by lattice oxygen atoms. Subsequently, the h^+ trapping weakens the binding energy between the Ti atom and the lattice oxygen.

Water is adsorbed molecularly under neutral pH conditions on the stoichiometric [110] surface. The presence of adsorbed water molecules breaks the Ti-O bond, forming a new hydroxyl group at the surface. The introduction of hydroxyl groups would lead to a surface which has a stronger interaction with water. The hydroxyl groups cause the surface to be 'water loving' and any added water droplets will fully wet the surface.

UV induced super-hydrophilicity is a reversible process. In the dark, the hydroxyl groups gradually desorb from the surface in the form of H_2O_2, $H_2O_{(vap)} + O_2$. Ti-O bonds reform and the lattice returns to it's native hydrophobic state.

4.2 Experiment protocols

4.2.1 Raman Spectroscopy

Raman spectra of TiO_2 films were collected using a LabRam Micro-Raman Spectrometer (Horiba Jobin-Yvon HR300) as described in chapter 2, section 15.2.

Thin films of TiO_2 were deposited onto glass microscope slides using CVD techniques as described in chapter 2, section 15.1.

The TiO_2 films exhibited a variation in thickness and crystallinity. Spectral readings were taken in triplicate, using three sample slides of each crystal structure, to ensure consistency was achieved. Analysis was performed at 0, 3, 5, 17 and 24 h of UV irradiation, followed by time points at 48 and 96 h in the dark. A multidimensional spectral array was used on each sample comprising of a 4 x 4 grid. This resulted in the accumulation of 16 separate readings which were averaged to produce a total spectroscopic plot for each sample. In this way, we were able to improve spectrum quality and to map multiple locations on the sample surface. Spectral curve fitting was performed using a mean baseline correction polynomial. Integrated peak ratios were calculated and averaged over the three separate samples.

At each time point the contact angle of liquid (water) dropped onto the surface of the thin film was analysed based on the droplet shape, using the method described in chapter 2, section 15.3. Contact angle measurements at each time point were averaged over the three separate samples.

4.2.2 DFT

The equilibrium bulk geometry was used to construct a slab-gap model with periodic boundary conditions. We used a 4 layer slab in which the ions in the top two layers were allowed to relax towards their equilibrium positions and the ions in the bottom two layers were fixed in their bulk positions (frozen double-layer model, FDL). The vacuum width

was set to 15 Å as this provided sufficient space for the superposition of water molecules avoiding interactions between the molecule and the neighbouring slabs. Initial geometric relaxations were performed for the stoiciometric surface using a single k-point (Γ-point) GGA calculation. Minimisation was deemed to be converged when the forces on each ion were smaller than 0.01 eV $Å^{-1}$. After the stoiciometric surfaces had been relaxed a single oxygen atom was removed from both surfaces of each slab to ensure that an artificial dipole was not created perpendicular to the slab. These reduced surfaces were then relaxed further using the same convergence criteria. Total energy of the TiO_2 rutile + molecule system was computed with a Monkhorst-Pack grid of 3 x 3 x 1 k points. Adsorption energies (E_{ads}) were then found using the equation 3.2.

For the stoiciometric surfaces a Hubbard correction $U(\mathrm{Ti}_d)$ value of 3 eV was used as this gave a good description of the band gap for TiO_2. For the reduced TiO_2 states a $U(\mathrm{Ti}_d)$ value of 4.2 eV was applied. This has previously been shown to provide a good description of O vacancies at the [110] surface and is in good agreement with spectroscopic data (Morgan and Watson, 2007). Dispersion forces arising from non-local electron-electron correlations and have a large impact on the magnitude of adsorption energies for molecules on surfaces. As such, the van der Waals density functional (vdW-DF) of Langreth and Lunqvist (Klimês et al., 2011), employed in the previous chapter to describe non-local interactions at the surface, was used throughout this study to investigate the adsorption of water molecules and their dissociation products at the TiO_2 [110] surface.

4.3 Results and discussion

4.3.1 Raman Spectroscopy

Raman spectra of two types of TiO_2 thin films deposited by CVD are shown in figures 4.3 & 4.4. The TiO_2 film shown in figure 4.3 is the rutile (R) phase which shows major peaks at 238, 446, 612 cm^{-1} and minor peaks at 313 and 818 cm^{-1}. No peaks belonging to the anatase (A) phase were identified in this sample. The broad band observed near 180-240

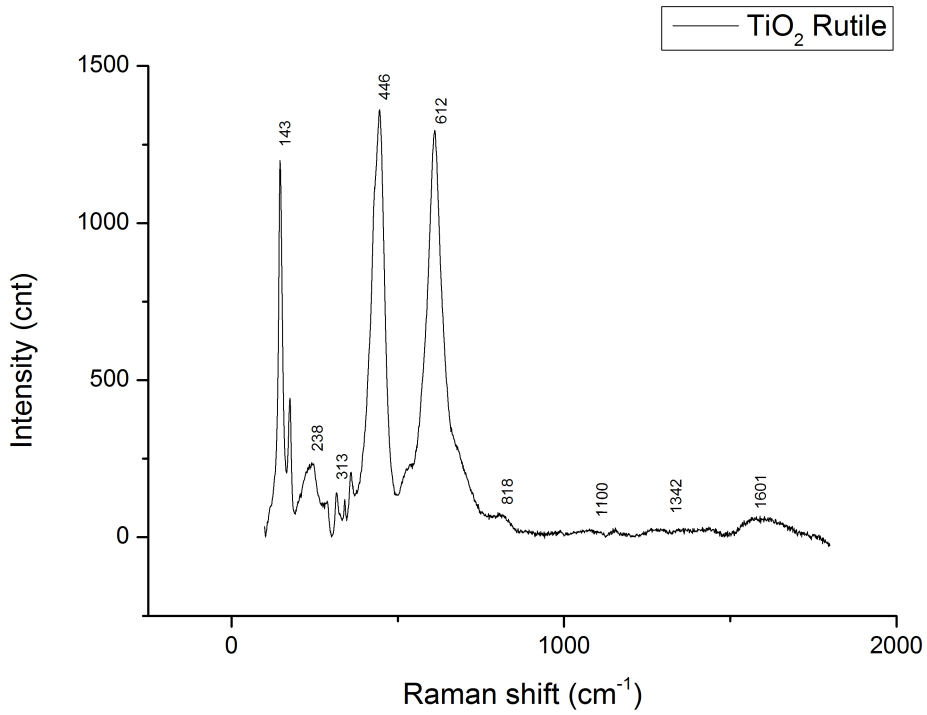

Figure 4.3: Raman spectra of non-UV irradiated CVD thin film coated glass showing characteristic peaks of the rutile (R) phase of TiO_2.

cm^{-1} is assigned to O-O interactions involving three- and four-coordinate oxygen. The Ti-O bond lengths of 4x 1.946 Å and 2x 1.984 Å for rutile are consistent with the observed Ti-O bands at 612 and 446 cm^{-1}. The sharp feature at 143 cm^{-1} is consistent with Ti-Ti covalent interactions (Balachandran and Eror, 1982; Hardcastle et al., 2011).

A second film sample showed that a mixture of rutile and anatase phases of TiO_2 were present (figure 4.4). Anatase exhibits Raman bands at 197, 396, 514 and 635 cm^{-1}, as well as a very sharp, intense peak at 144 cm^{-1}. The peaks at 144 and 197 cm^{-1} are consistent with the Ti-Ti bonding present in octahedral chains of anatase with a bond length of 2.96 Å (Balachandran and Eror, 1982; Hardcastle et al., 2011).

Surface contamination of native TiO_2 is evident from the spectroscopy data due to the appearance of characteristic peaks. The peak at 1100 cm^{-1}, in figures 4.3 & 4.5, indicates the presence of carbonate CO_3^{2-} species. Amorphous carbon is also present, as indicated

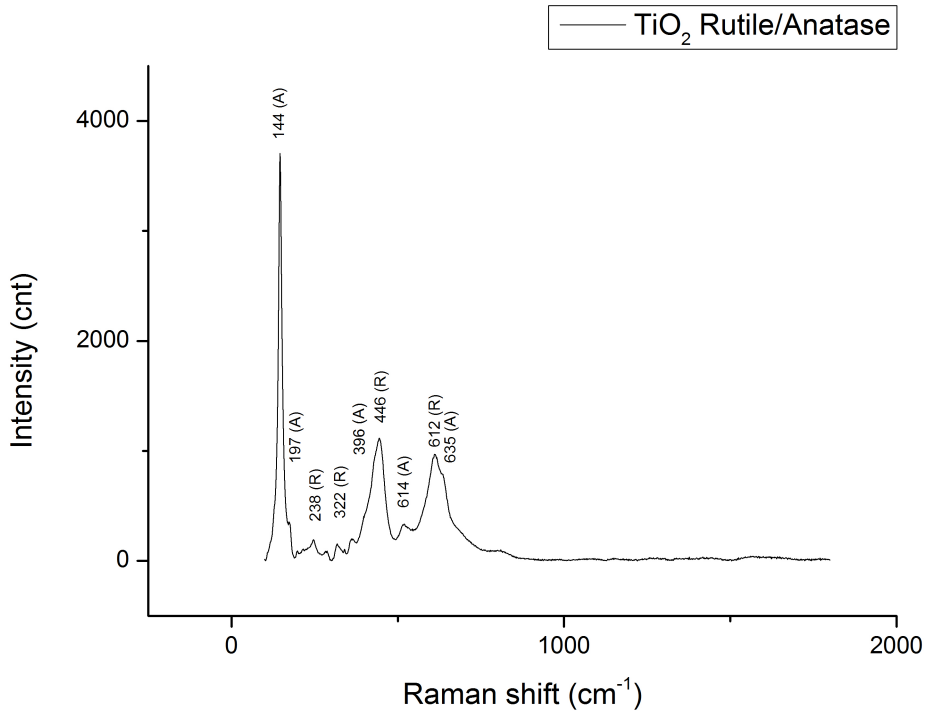

Figure 4.4: Raman spectra of non-UV irradiated CVD thin film coated glass showing a mixed phase rutile and anatase TiO_2 surface.

by bands near 1342 cm^{-1} and 1600 cm^{-1}, indicating and sp^3 and sp^2 hybridised carbon respectively (Hardcastle et al., 2011). These exist from hydrocarbon and carbide adsorption from the atmosphere due to the highly electronegative nature of TiO_2. However, they are only observed here in relatively small amounts.

The intensities, represented by peak heights, of the Raman spectra varied widely with UV irradiation time (figure 4.5). Absolute peak intensity is therefore not a useful indication of any change in surface structure. A better measure of crystal structure is to compare the relative intensities of the Raman peaks (figure 4.6).

As the crystallinity of the rutile phase of TiO_2 increases the Raman bands become sharper (reduction in full width at half maximum (FWHM)) and the relative intensity of the band at 446 cm^{-1} increases relative to the 612 cm^{-1}. Consequently, the ratio of these integrated peaks, I_{446}/I_{610} can provide a measure of the degree of crystallinity for rutile (Hardcastle

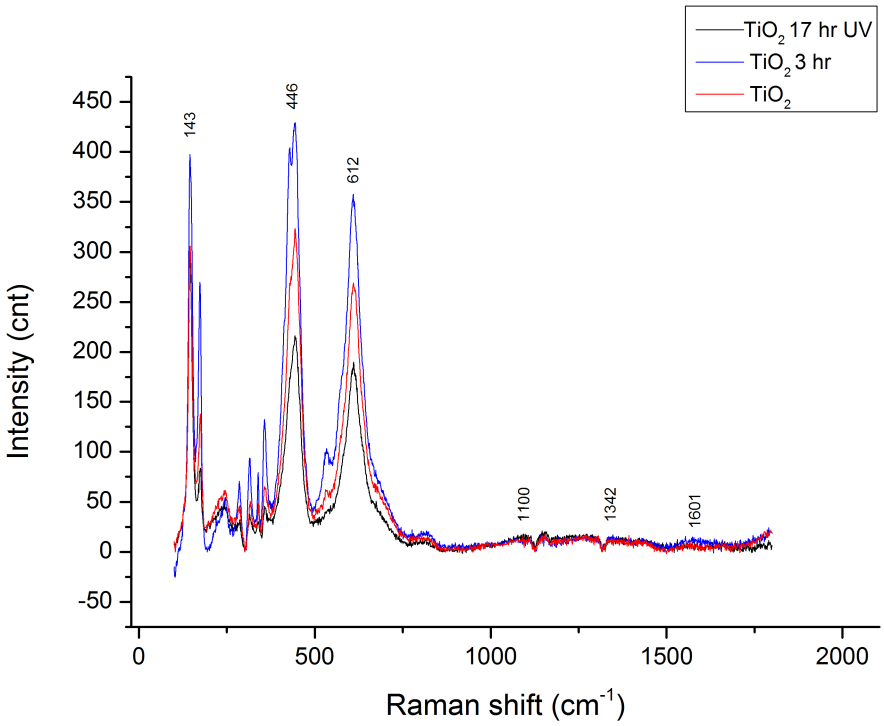

Figure 4.5: Composit plot of Raman spectra TiO_2 (R) coated glass at 0, 3 and 17 h UV illumination time showing that absolute peak height is independent of UV irradiation time.

et al., 2011). The, I_{446}/I_{610} ratio indicates that CVD deposited TiO_2 is highly (∼100 %) crystalline. This crystallinity does not change following irradiation from UV wavelengths of light which suggests little damage is occurring to the crystal lattice. However, with increasing UV irradiation time, there is a steady decrease in the intensity of the Ti-O peak (446 cm^{-1}) relative to the Ti-Ti peak (143 cm^{-1}) (figure 4.6). This was measured from the integrated peak ratio I_{143}/I_{446} and suggests there is a decrease in Ti-O bonding involving the creation of surface hydroxyl groups while the Ti-Ti lattice remains intact. This Raman Spectroscopic analysis provides unique, direct evidence that the UV induced super-hydrophilic conversion of TiO_2 occurs through the mechanism of surface hydroxyl reconstruction.

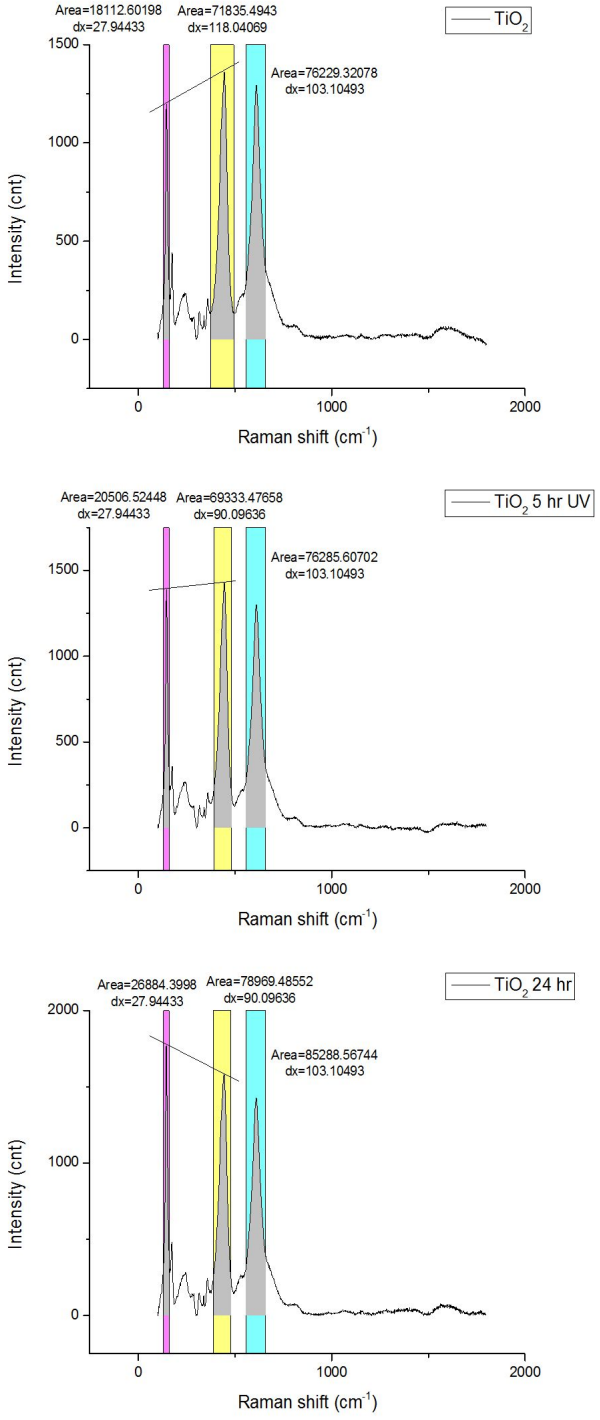

Figure 4.6: Relative peak height provides an indication of structural surface changes due to irradiation. This sequence of Raman spectra TiO_2 (R) shows there is a steady decrease, with increasing UV irradiaiton time (0, 5, 24 h), in the relative intensity of the Ti-O peak (446 cm^{-1}), highlighted in yellow, compared to the Ti-Ti peak (143 cm^{-1}), highlighted in pink.

4.3.2 Contact angles

Contact angle measurements show that the TiO_2 surface becomes super-hydrophilic (completely wetted with contact angle of 0°) after 3 h of UV irradiation time (appendix D.1).

After UV irradiation the surfaces were kept in the dark and showed a steady recovery to the native hydrophobic state. A decrease in the I_{143}/I_{446} ratio indicates the reversible hydrophilic conversion process due to the reforming of Ti-O bonds. Recovery of Ti-O bonding due to hydroxyl group desorption occurs over 72 h after UV irradiation. The surface returned to hydrophobic state contact angle ~ 32 ° in this time (figure 4.7).

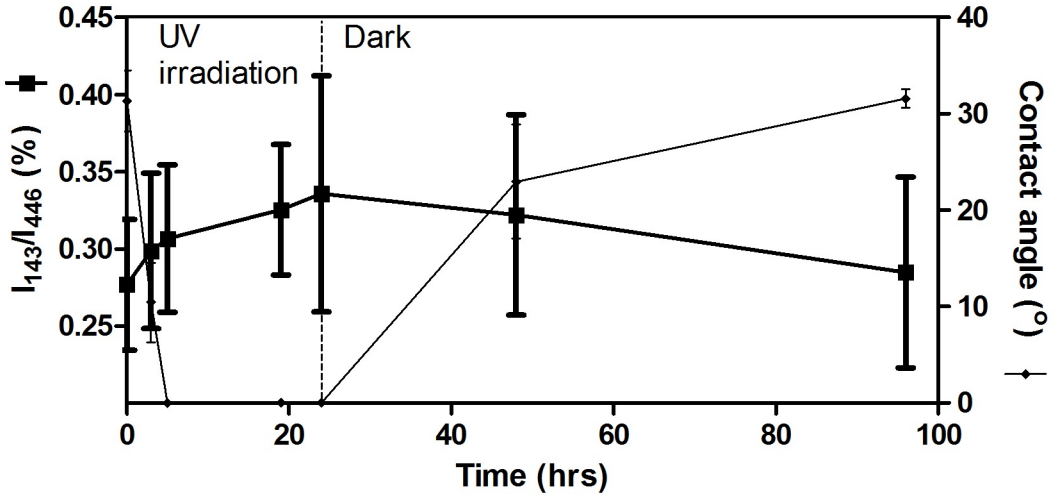

Figure 4.7: The TiO_2 (R) Raman integrated peak ratio I_{143}/I_{446} increases with increased UV irradiaiton time and subsequently recovers it's value after $\sim$ 72 h when the surface is left in the dark. The I_{143}/I_{446} trend reflects a reciprocal trend in contact angle changes. TiO_2 surfaces rapidly show a super-hydrophilic conversion with UV irradiation and a subsequent recovery to the native hydrophobic state in the dark.

4.3.3 Density Functionl Theory (DFT)

A thorough set of DFT calculations were performed involving the interaction of water with the perfect stoiciometric and reduced TiO_2 [110] surfaces. These calculations relate to our

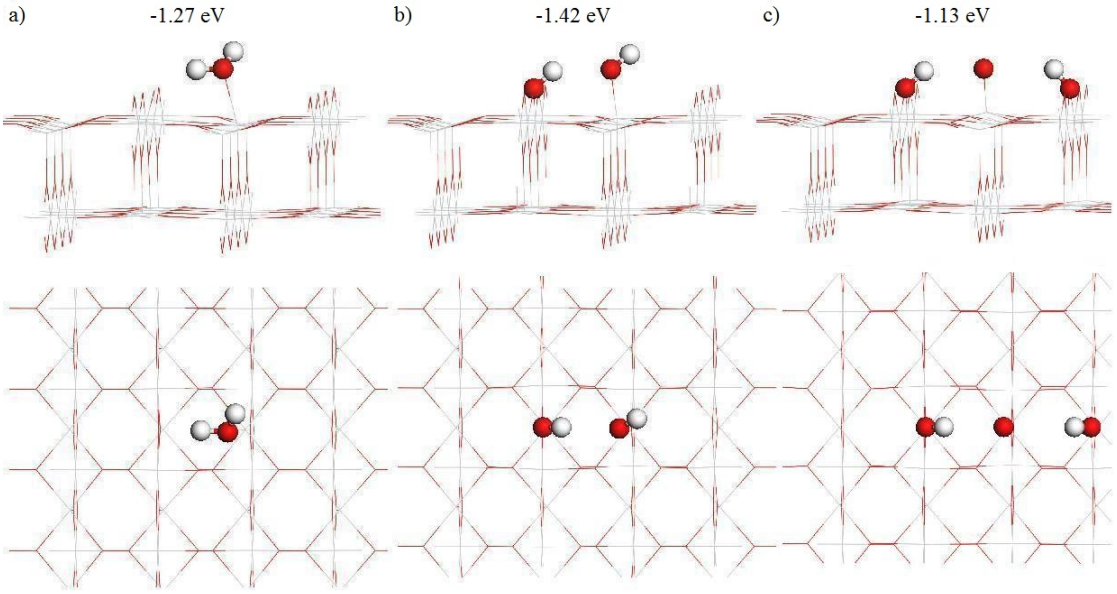

Figure 4.8: Side and the top views for the configurations of a water molecule and two water dissociated states at the perfect stoiciometic TiO_2 [110] surface; a) molecular water at the-Ti_{5f} site, b) proton dissociation to the bridging O site, c) both protons transferred resulting in two single hydroxyls (OH) and an oxygen on top (O_{ot}) of the Ti_{5f}.

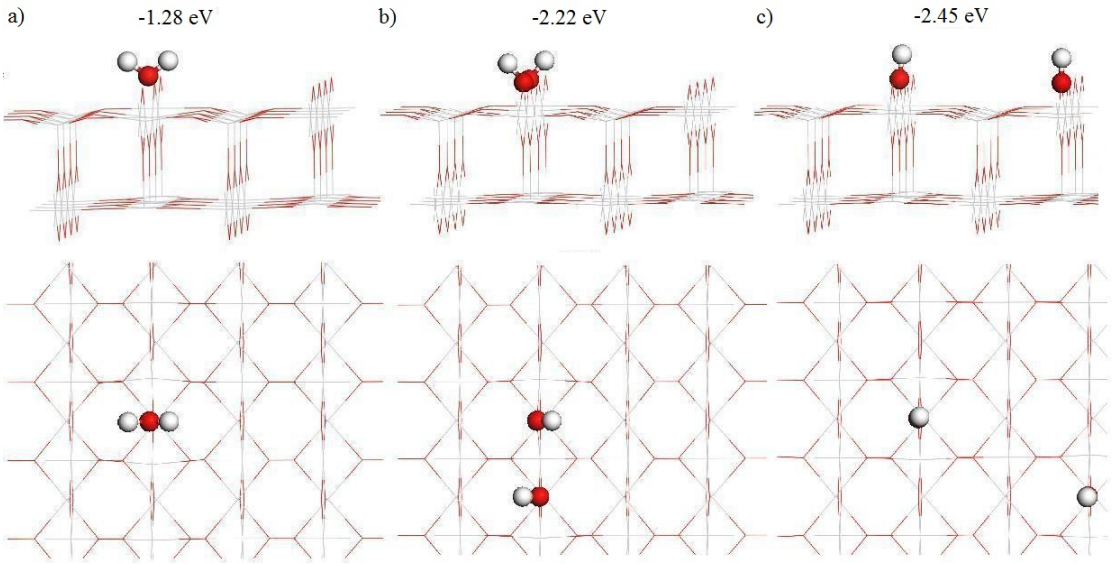

Figure 4.9: Side and top views for the configurations of a single water molecule and two dissociated water states at the reduced TiO_2 [110] surface; a) molecular water at the oxygen vacancy, b) water dissociation leading to paired bridging hydroxyl (2OH) defects, c) paired hydroxyls separate into single hydroxyl (OH) defects at the surface.

observations from Raman spectroscopy, that an increased density of oxygen vacancies is formed in TiO_2 surfaces by UV irradiation. The predominantly stoiciometric surface of native TiO_2 is converted to the reduced surface containing a high density of oxygen defects. The DFT calculations model the underlying atomistic mechanism involved in the reversible hydrophilic conversion of TiO_2 that occurs through the creation of surface hydroxyl groups. We find that H_2O dissociation at oxygen vacancies is energetically more favourable than H_2O adsorption at the Ti_{5f} sites.

For these calculations, a single water molecule was introduced per (4 x 4) surface unit cell to simulate the adsorption at low H_2O partial pressure. On the stoiciometric surface the molecular adsorption on a Ti_{5f} atom is exothermic by 1.27 eV (figure 4.8a). Once adsorbed, the water may dissociate by proton transfer to the adjacent bridging oxygen atom (figure 4.8b). This leads to the formation of two terminal hydroxyl groups with an energy gain of 0.15 eV, which is in good accordance with the value of 0.13 eV, obtained by Wendt *et al.*. In addition, our data compares well with the observation that the transfer of both protons is unfavourable, resulting in the formation of bridging hydroxyl groups with an on-top O atom (O_{ot}) on the Ti row (figure 4.8c) (Wendt et al., 2005).

Adsorption of a water molecule at a bridging oxygen vacancy is energetically comparable to the adsorption at a Ti_{5f} atom on the stoiciometric TiO_2 [110] surface (figure 4.9a). However, 0.94 eV is gained through proton transfer to an adjacent bridging oxygen (figure 4.9b), indicating that the water molecule in the vacancy is thermodynamically unstable. The energy difference of only 0.15 eV is too small to suggest dissociation on the stoiciometric surface. Whereas, an energy gain of 0.94 eV is large enough to reliably predict the formation of a hydroxylated surface following UV generated oxygen vacancy formation. The situation in which paired bridging hydroxyls separate into single hydroxyl groups is even more stable by 0.23 eV (figure 4.9c). As such, DFT predicts water dissociation at bridging oxygen vacancies. This result suggests an energetically feasible mechanism for the observed hydrophobic to hydrophilic conversion.

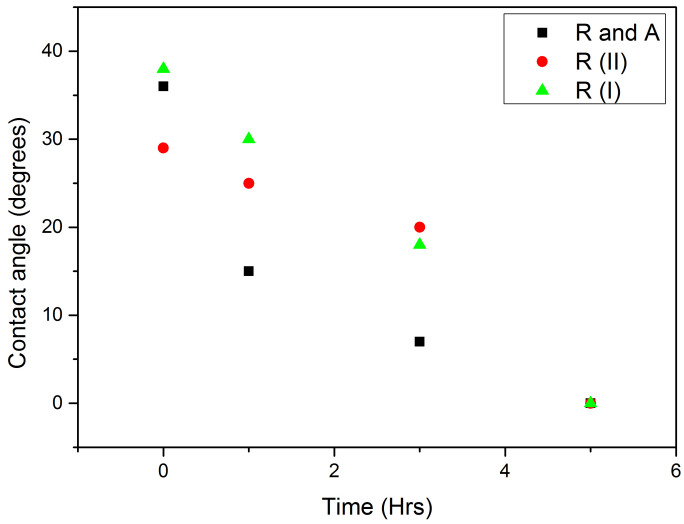

Figure 4.10: Change of contact angle of different TiO_2 thin film compositions over 5 h UV irradiaition time. R and A = mixed rutile / anatase film, R (I) = rutile sample I. R (II) = rutile sample II.

4.4 Quantitative evaluation of the photoinduced hydrophilic conversion

The contact angle on all CVD deposited film types (R, mixed R and A) decreased with UV irradiation time, however, the hydrophilic conversion rate was different for each one (figure 4.10). The rate does not give a constant value even in the same condition of UV irradiation because it depends on the initial value of contact angle which varies between film types. It was necessary to define the hydrophilic conversion rate in a way that is independent of initial contact angle which is determined by the initial oxygen vacancy surface density state.

It was found that the reciprocal of the contact angle plotted against the UV irradiation time gives a straight line in the region before the contact angle reaches a minimum value (Sakai et al., 2003). This provides a value for evaluating the hydrophilic conversion rate (k_f) quantitatively. The k_f values were 6 x 10^4, 2 x 10^4 and 0.9 x 10^4 degree^{-1} min^{-1} for R and A, R (I) and R (II) respectively (figure 4.11). The mixed rutile / anatase TiO_2

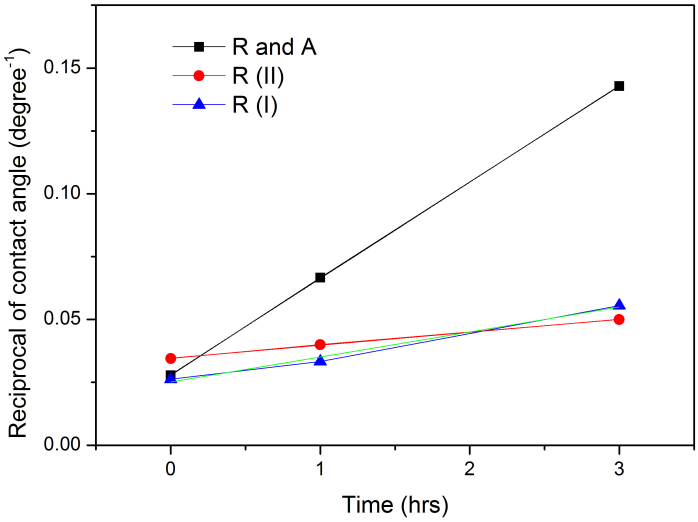

Figure 4.11: Reciprocal of contact angle plotted against UV irradiation time. Each line is a regression straight line plot with correlation coefficient R and A = 1, R (I) = 0.990, R (II) = 0.999. This provides a value for the hydrophilic conversion rate (k_f) which is highest for the mixed R and A phase compared to the R only phase of TiO_2.

sample was seen to have the highest conversion rate which is likely to be due to the higher UV surface activity of the anatase phase.

A subsequent plot of the reciprocal of the contact angle against Raman peak intensity ratio was made for the R only phase. This also produces a linear relationship (figure 4.12) which indicates that the change in the intensity ratio of the Ti-O peak integral strongly correlates with the changes in the hydrophillic conversion of the TiO_2 surface.

As such, there is a strong positive correlation with the increase in surface oxygen vacancies created by UV irradiation and the change of the reciprocal of the contact angle. My DFT calculations demonstrate an increase in UV induced surface oxygen vacancies would lead to an increase in density of surface hydroxyl groups. I can therefore correlate an increase in surface hydroxyl group density with the increase in hydrophilic properties of TiO_2.

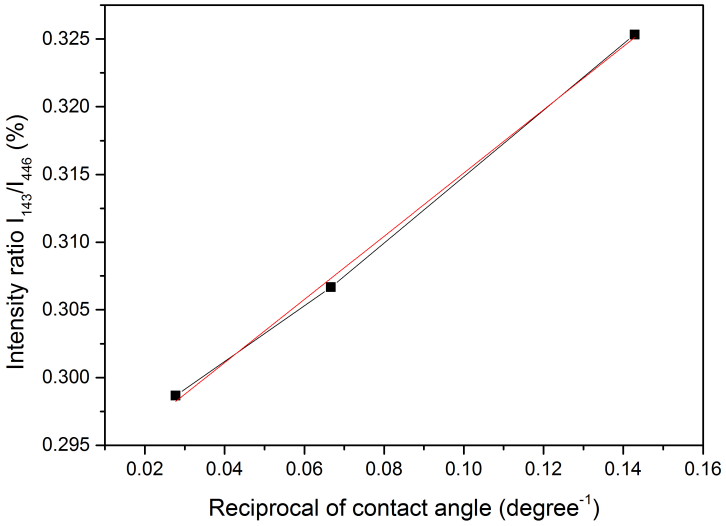

Figure 4.12: Raman integrated peak ratio I_{143}/I_{446} plotted against the reciprocal of the contact angle. The red line is the regression straight line with correlation coefficient of 0.998.

4.5 Conclusions

Variations in crystal phase of the TiO_2 thin films were observed among the CVD samples. Raman peaks showed that some films consisted of both anatase and rutile forms while in others, only the rutile form was seen. The technique used to coat the surfaces in this study, has been reported to produce a predominantly anatase film (Cross et al., 2012), which is the most UV active polymorph owing to its higher surface reactivity compared to rutile. Variations in film thickness were observed across the surface, due to variations in crystal growth between anatase and rutile. A phase transition to rutile, the most thermodynamically stable of the TiO_2 crystal forms, may have occurred through the agglomeration of small rutile particles (Zhang et al., 2006). Additionally, Edusi *et al.* has observed a phase transition to rutile at temperatures of $\geq 550\,^{\circ}C$ during the aerosol assissted (AA)CVD deposition process (Edusi et al., 2011).

The reversible reduction in intensity of the Raman band at 446 cm^{-1} confirms the breaking of Ti-O bonds, creating bridging oxygen vacancies, under UV irradiation of TiO_2. This

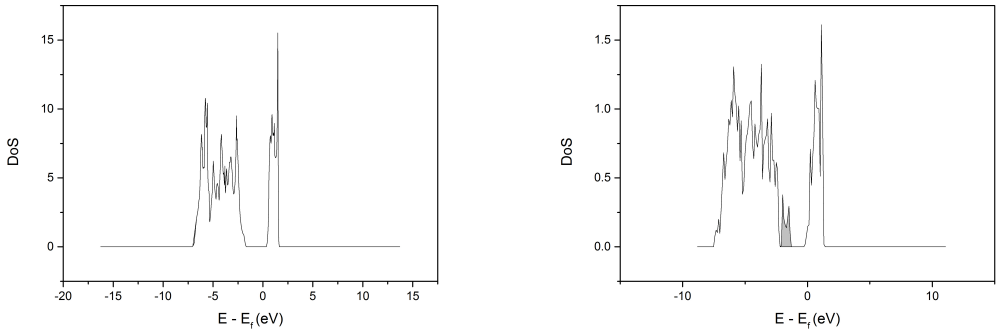

Figure 4.13: Total electronic density of states; a) TiO_2 [110] stoiciometric surface, DFT+U = 3, b) TiO_2 [110] reduced surface, DFT+U = 4.2, showing a gap state appearing between the valance and conduction bands (shaded). The energy scale is zeroed at the fermi level.

points to the mechanism responsible for the photo induced hydrophilic (PIH) effect, namely through the reconstruction of hydroxyl groups at the TiO_2 surface. DFT calculations confirm that paired hydroxyls are a very stable configuration, formed at oxygen vacancies following water dissociation.

The reason for the larger reactivity of the vacancies is associated with the high-energy defects. Oxygen vacancy formation requires the removal of a two coordinate surface oxygen. The excess charge at the surface localises strongly at the two neighbouring Ti sites, reducing these to Ti^{III} and causing a local relaxation of the geometry with increased bond asymmetry between the neighbouring Ti sites. These localised states introduce new bands 1.62 eV below the conduction band minimum. Figure 4.13 shows the total electronic density of states of the TiO_2 stoiciometric and reduced surfaces. Figure 4.13b shows the excess charge associated with the Ti^{III} state (shaded) is localised on the d electrons within Ti atoms adjacent to the O vacancy.

Adsorption of high energy photons of ultra-violet wavelengths is required for the creation of oxygen vacancies. Since the O-defect states constitute frontier orbitals they are likely to be involved in redox reactions involving adsorbed molecules (Morgan and Watson, 2007). When water dissociates, the coordination shell of the Ti underneath the vacancy is refilled, resulting in exothermicity (Schaub et al., 2001).

STM analysis by Wendt *et al* of reduced TiO_2 [110] surfaces found equal values of Type-A (hydroxyl) defects to the original oxygen vacancy concentrations (Wendt et al., 2005). This strongly supports water dissociation at oxygen vacancies being responsible for the transformation of vacancies into paired hydroxyl (2OH) vacancies and finally into twice the number of single hydroxyl (OH) defects.

The effect of enhanced hydrophilicity was found to revert to the normal hydrophobic state during storage of the thin film in the dark.

Photcatalytic decomposition of organic contaminants and UV induced hydrophilicity are two distinct mechanisms that occur at the TiO_2 surface. PDOC may improve hydrophilicity by removing hydrocarbon and carbide contaminants. However, the reduction in hydrocarbon and carbide contamination following UV irradiation was too small to show a noticeable difference by Raman spectroscopy. This suggests that the majority of UV induced hydrophilicity occurs as a result of an alternative mechanism, namely surface reconstruction of hydroxyl groups by means of photo-catalytically created electron holes. Even though there are two intrinsically different photo-induced processes they must be taking place simultaneously. This is one of the unique aspects exhibited by TiO_2 compared to other metal oxides and provides a range of applications for super-hydrophilic technology. For example, in providing self-cleaning and antibacterial surfaces as well as suitable biological cell surface responses in regard to metal implants (Liu et al., 2010).

On the basis of the results, it is concluded that UV irradiation in air causes the reconstruction of surface hydroxyl groups, whose density is strongly correlated with the reciprocal of the contact angle. Photoexcited electrons diffuse to the TiO_2 surface and are captured by lattice oxygen. This weakens the binding energy between Ti and the lattice oxygen. One molecule of water interrupts this bond, forming a new hydroxyl group. The desorption temperature for OH groups produced by UV irradiation is lower than that of OH groups bound to oxygen vacancies, indicating the former is less thermodynamically stable than the latter (Sakai et al., 2003). It is therefore considered that the reconstruction from naturally occurring stable OH groups at oxygen vacancies to thermodynamically metastable UV induced OH groups increases the surface energy of the TiO_2 resulting in

the hydrophilic conversion.

Hydrophilic, roughened surfaces have proven superior properties in regard to TiO_2 implant osseointegration *in vivo* (Steinemann, 1998) and for cell attachment *in vitro* (van Kooten et al., 1992). The use of UV irradiation provides a quick and reliable method of controlling TiO_2 wettability. The hydrophilic effect of UV irradiation is to create extensive hydroxyl groups at the TiO_2 surface which may provide improved protein interactions, through hydrogen bonding. This hypothesis is investigated in the next chapter and these interactions may provide the chemical basis for the improved clinical performance of SLV. UV irradiation has the potential to provide further benefits to the current ultimate standard implant surface material through the mechanism, described here, of additional chemical surface modifications.

Chapter 5

Interaction of the RGD adsorption peptide at the TiO_2 nanotopography surface

5.1 Introduction

The interaction mechanisms that take place during the adsorption of large organic molecules on a surface are complex. All living things rely on the chemical reactions that take place in the presence of water. In order to perform a well-defined investigation of the processes involved in the adsorption of peptides on the implant surface we must focus on TiO_2 in the aqueous system. Water is one of the most important adsorbates, and it's presence can easily affect the adsorption and reaction processes of other molecules at the surface.

Molecular dynamics (MD) is a computer simulation technique where the evolution of set of interacting particles is followed by integrating their equations of motion. The nuclear motion of particles is modelled using classical physics based upon Newton's laws of motion as described in equations 1.8 and 1.9.

5.2 Calculation methods

5.2.1 MD simulation protocol

An explanation of the terms used in this method are given in chapter 1, section 6.2. The simulations were carried out in the DL_POLY package. All the simulations were performed in the canonical (NVT) ensemble using the Norsé-Hoover thermostat with a relaxation constant of 0.5 ps. The equations of motion were solved with the Verlet leapfrog algorithm using a timestep of 0.0001ps. The cutoff distance for van der Waals interactions was set to 5 Å.

In order to test whether specific amino acids could be directly adsorbed onto the TiO_2 surface, each fragment was first placed in a simulation box and surrounded by water molecules in order to find the solvation energy. The TiO_2 surface was hydrated with 150 water molecules to find the energy of hydration. Each fragment was then placed with the carbonyl oxygens at an initial distance of ∼1.4 Å from two adjacent Ti_{5f} sites. The systems were initially minimised to zero K at constant volume in order to remove bad steric contacts over 40 ps of dynamics. This had the effect of randomising the solute positions and then freezing the solute coordinates. Starting from the last equilibrium configuration obtained, the production runs in the NVT ensemble with total simulation time of 100 ps were performed for structural and energetic data collection. The distribution of water molecules over the surface and around the amino acid carbonyl oxygens and amino hydrogens were quantified by radial distribution functions (RDFs). The energy difference between the system and the sum of the hydrated surface and the solvated molecule gives the adsorption interaction energy E_{ads} of the amino acid compared to water:

$$E_{ads} = E_{(system)} - (E_{(hydrated\ surface)} + E_{(solvated\ molecule)}) \tag{5.1}$$

5.2.2 General description of the model

The starting point was the TiO_2 model used in the previous section as this is the most stable crystal face of rutile [110] on which deposition is supposed to occur from an aqueous solution of the peptide. The rutile surface structure was created using Materials Studio software by 4 x 2 periodic replication, in the $x-$ and $y-$directions respectively, of an elementary unit cell of size 3.02 x 1.98 Å. A slab-gap model was created using four atomic layers, each slab containing 64 Ti atoms and 128 O atoms, separated by a vacuum gap of 15 Å. The overall MD simulation box size was 12.88 x 13.25 x 27.53 Å to which periodic boundary conditions were applied in the two dimensions defining the surface. The surface was hydrated by the addition of 150 water molecules to the vacuum gap with the liquid state starting from a configuration that corresponds to a solid lattice. The total number of atoms for the hydrated surface model was 542.

Each individual organic molecule was solvated in a water box containing 552 water molecules with dimensions 30.59 x 30.59 x 30.59 Å in order to calculate the energy of solvation.

To accommodate the large size of the RGD molecule adsorption, a double unit cell of 26.50 x 12.88 x 27.53 Å was employed containing 294 water molecules. The total number of atoms for the RGD-surface model in water was 1311.

The interaction potential parameters necessary to carry out MD simulations of the rutile / peptide / aqueous solution system were taken from published data; water molecules were described by the TIP3P model, and AMBER force fields of Cornell *et al.* and Carravetta and Monti were employed to adequately represent peptide structures (Cornell et al., 1995; Carravetta and Monti, 2006).

There is considerable disagreement on the initial adsorption behaviour of water, especially between theoretical and experimental studies. While most experimental results suggest that water does not dissociate on TiO_2, except at defect sites (as predicted by my own DFT study, chapter 4, section 3.3), some theoretical studies predict dissociative adsorption may occur (Liu et al., 2012). The TIP3P model does not allow for dissociation of water

molecules, so this particular aspect can not be taken into account in this method. The TIP3P model, however, does adequately describe water structural and thermodynamical properties.

Hydroxylated TiO_2 surface model

The fully hydroxylated surface originates from the dissociative adsorption of water on the non-hydroxylated surface. The hydroxyl group binds to the terminal 5-fold coordinated Ti atom (Ti_{5f}) and becomes a terminal hydroxyl. The other proton from the water bonds to a bridging oxygen and forms a bridging hydroxyl (figure 4.8b).

The charges of the surface atoms were taken from (Předota et al., 2004). It was found that only the charges of terminal and bridging O and H atoms had to be modified and the values used are given in table 5.2. Note that the charges have to be balanced across both hydroxylated and nonhydroxylated surfaces.

Due to hydrogen bonding among bridging and terminal hydroxyl groups and water molecules it was necessary to keep the hydroxyl groups rigid during the simulations. Therefore, the bridging and terminal hydroxyl groups at the hydroxylated surface were maintained within fixed Ti-O and O-H bond lengths (table 5.5 (Předota et al., 2004)). Note the length of the bridging Ti-O bond changes on protonation of the bridging oxygen. A bending potential for the Ti-O-H angle, $E_{\angle \text{Ti-O-H}} = (1/2)k_2(\theta - \theta_0)^2$, with k_2 = 59.14 eV mol^{-1} rad^{-2} and θ_0 = 90.85 deg, was applied to both the bridging and terminal hydroxyl groups. All remaining interactions are the same as for the nonhydroxylated surface, including the Lennard-Jones interactions for the bridging and terminal oxygens with solution species as well as Coulombic interactions.

The water model was adjusted for the hydroxylated surface and was represented by the rigid nonpolarisable SPC/E model, with partial charges on the oxygen, q_O = -0.8476e, and two hydrogens, q_H = +0.4238e. The Lennard-Jones (LJ) potential was modified and the value applied to the oxygen site is given in table 5.9. The SPC/E model does not allow for dissociation of water molecules but is known to adequately reproduce the phase envelope

of bulk water, as well as the liquid water structure, diffusivity and dielectric properties over a wide range of temperature and density conditions.

Molecular dynamics simulations were performed for a slab geometry system with two parallel TiO_2 walls and water molecules between them. Therefore, this system had two identical interfaces (i.e. both surfaces hydroxylated or both nonhydroxylated) and the properties reported were averages over both interfaces. For the hydroxylated surface the number of associated water molecules was 294 less the number of dissociatively adsorbed water molecules, which become the terminal hydroxyl and protonated bridging oxygen sites. In this way the number of oxygens and hydrogens is identical for both hydroxylated and nonhydroxylated surfaces.

Atom types

atom	type	description
Titanium	Ti	any 5-fold and 6-fold coordinated titanium
Carbon	CT	any sp^3 carbon
	C	any carbonyl sp^2 carbon
	CA	sp^2 electroneg. carbon C_ϵ of Arg
Nitrogen	N	sp^2 nitrogen in amides
	N2	sp^2 nitrogen in guanidinium ions
Oxygen	O	3-fold coordinated oxygen in Ti layer
	Og	sp^2 oxygen in amides
	O2	sp^2 oxygen in anionic acids
	OW	sp^3 oxygen in TIP3P and SPCE water
	O_b	oxygen of bridging surface hydroxyl group
	O_H	oxygen of terminal surface hydroxyl group
Hydrogen	H	H attached to N
	HC	H attached to aliphatic carbon with no electron-withdrawing substituents
	H1	H attached to aliphatic carbon with one electron-withdrawing substituent
	HW	H in TIP3P and SPCE water
	H_b	hydrogen of bridging surface hydroxyl group
	H_O	hydrogen of terminal surface hydroxyl group

Table 5.1: List of atom types

The peptide atom types employed are given in table 5.1. A significant definition of atom

atom	nonhydroxylated	hydroxylated
Bulk atoms		
Ti	2.196	2.196
O	-1.098	-1.098
O	-1.098	-1.098
sum	0.000	0.000
Terminal group		
terminal Ti	2.196	2.196
3-fold coordinated oxygen in Ti layer	-1.098	-1.098
3-fold coordinated oxygen in Ti layer	-1.098	-1.098
terminal hydroxyl O		-1.008
terminal hydroxyl H		0.459
sum	0.000	-0.549
Bridging group		
bridging Ti	2.196	2.196
3-fold coordinated oxygen under Ti layer	-1.098	-1.098
unprotonated bridging O	-1.098	
protonated bridging O		-1.035
bridging H		0.486
sum	0.000	0.549

Table 5.2: Charges of bulk TiO_2 and surface atoms for the neutral nonhydroxylated and hydroxylated surfaces. All charges are given in the unit of electron charge.

types exists for hydrogens bonded to carbons which are themselves bonded to one or more electronegative atoms and these are labeled H1.

Atomic charges used for arginine (Arg), glycine (Gly) and aspartic acid (Asp) are given in figure 5.1. Charges were modified from (Cornell et al., 1995).

Charges of bulk TiO_2 and surface atoms for the neutral nonhydroxylated and hydroxylated surfaces are given in table 5.2.

Bond and Angle parameters

The bonds and angles in the organic molecules are represented by a simple harmonic expression. The bond potential function as shown in figure 5.2 is described in equation 5.2.

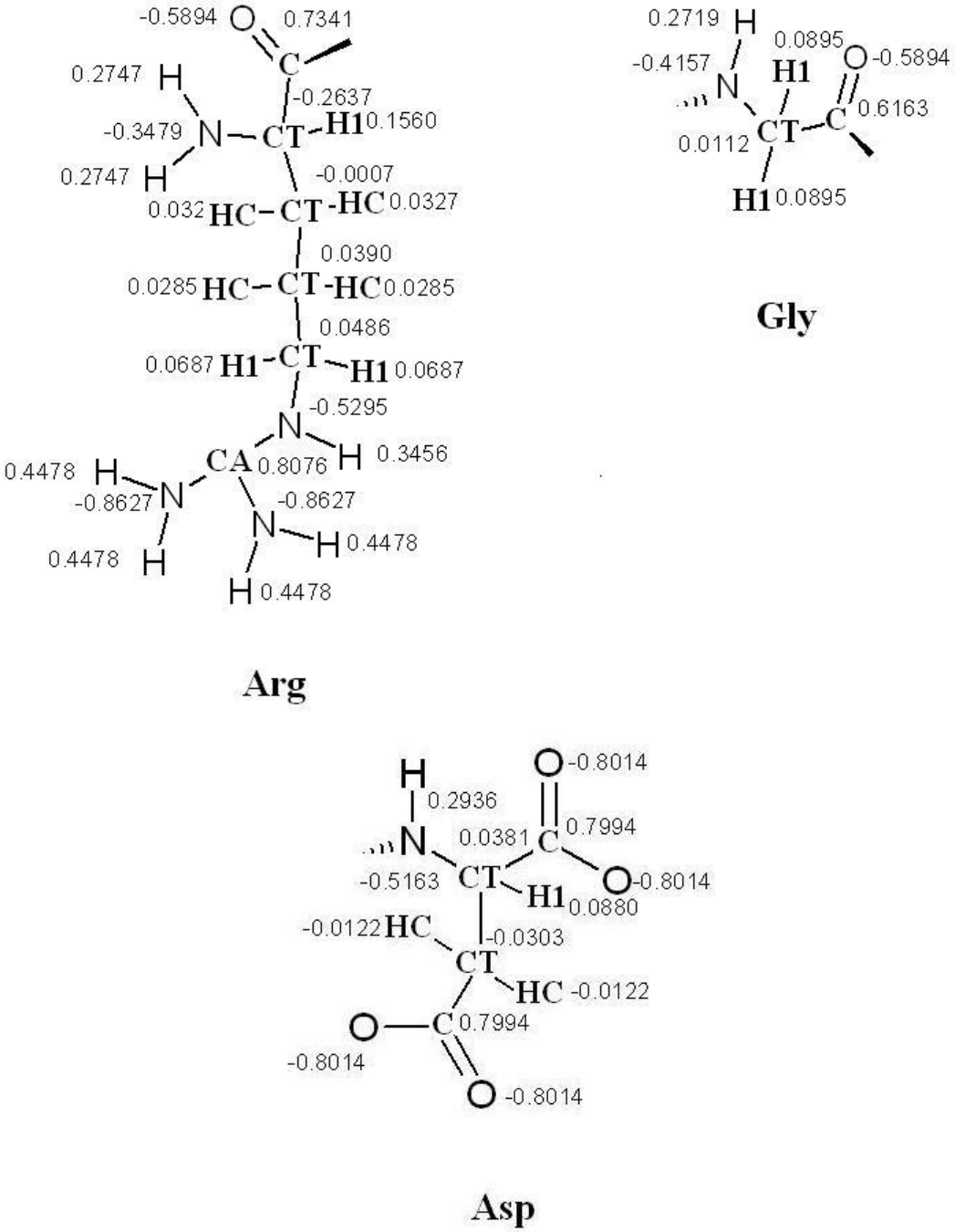

Figure 5.1: Charges for the peptide fragments. All charges for the terminal and non-terminal amino acids of RGD are presented in the unit of electron charge. Individual fragments were used as ionic residues containing NH_2^+ and COO^- terminal groups.

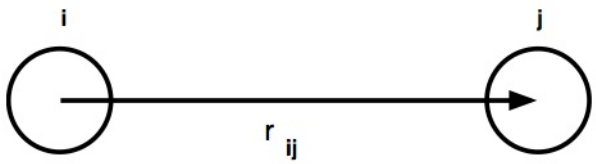

Figure 5.2: The interatomic bond vector. The bond potentials describe *explicit* bonds between specified atoms. They are functions of the interatomic distance only.

$$U(r_{ij}) = \frac{1}{2}k(r_{ij} - r_0)^2 \tag{5.2}$$

The valance angle potential, that describes bond bending between specified atoms, is defined by the equation 5.3 and shown in figure 5.3.

$$U(\theta_{jik}) = \frac{k}{2}(\theta_{jik} - \theta_0)^2 \tag{5.3}$$

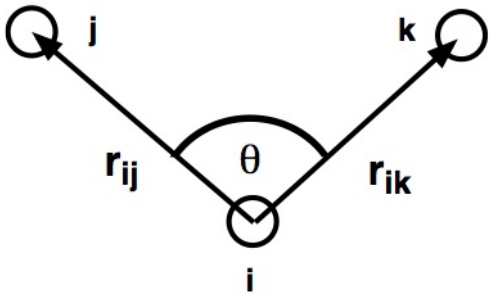

Figure 5.3: The valance angle and associated vectors. The valence angle potentials describe the bond bending terms between the specified atoms.

Bond and angle parameters were taken from Cornell *et al.* and are given in tables 5.3 & 5.4 where k is the force constant at the minimum of the energy well for atoms i and j at interatomic separation of r_{eq} (Cornell et al., 1995). k_θ is the angular force constant between atoms j, i and k at equilibrium angular separation θ_{eq}.

Dihedral angle potentials describe the interaction arising from torsional forces within the molecules and require the specification of four atomic positions as shown in figure 5.4. Cosine potential functions are described in equation 5.4. Parameters in table 5.6.

bond	k_r (eV)	r_{eq} (Å)
C-CT	13.75	1.522
C-N	21.25	1.335
C-O2	28.45	1.250
CA-N2	20.86	1.340
CT-H1	14.74	1.090
CT-HC	14.74	1.090
CT-N	14.61	1.449
CT-N2	14.61	1.463

Table 5.3: Bond Parameters

bond	k_θ (eV)	θ_{eq} (°)
C-CT-CT	2.73	111.10
C-CT-N	2.73	110.10
C-N-CT	2.17	121.90
C-N-H	1.30	120.00
CA-N2-CT	2.17	123.20
CA-N2-H	1.52	120.00
CT-C-N	3.04	116.60
CT-C-O	3.47	120.40
CT-C-O2	3.47	117.00
CT-N2-H	1.52	118.49
H-N2-H	1.52	120.00
H1-CT-N2	2.17	109.50
N-C-O	3.47	122.90
N2-CA-N2	3.04	120.00
O2-C-O2	3.47	126.00
Ti-O-H	59.14	90.85

Table 5.4: Angle Parameters

	terminal		bridging		bridging unprotonated
bonds	Ti-O	O-H	Ti-O	O-H	Ti-O
length (Å)	1.895	0.983	2.022	0.994	1.872

Table 5.5: Hydroxyl group bond constraints

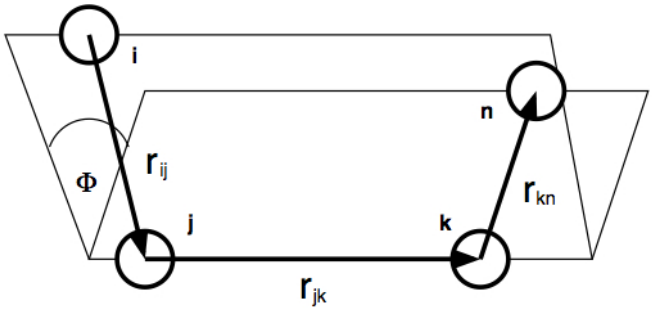

Figure 5.4: The dihedral angle and associated vectors. The dihedral angle potentials describe the interaction arising from torsional forces in molecules. They require the specification of four atomic positions.

torsion	A (eV)	δ (°)	m
X-C-CA-X	0.63	180.0	2.0
X-C-CT-X	0.00	0.0	2.0
X-C-N-X	0.43	180.0	2.0
X-CA-CT-X	0.00	0.0	2.0
X-CA-N2-X	0.42	180.0	2.0
X-CT-CT-X	0.06	0.0	3.0
X-CT-N-X	0.00	0.0	2.0
X-CT-N2-X	0.00	0.0	3.0
C-N-CT-C	0.00	180.0	1.0
CT-CT-C-N	0.00	180.0	1.0
CT-CT-N-C	0.00	180.0	2.0
H-N-C-O	0.11	180.0	2.0
N-CT-C-N	0.00	0.0	3.0

Table 5.6: Torsional Parameters

$$U(\phi_{ijkn}) = A[1 + \cos(m\phi_{ijkn} - \delta)] \tag{5.4}$$

where, A is the magnitude of the torsion in eV, δ is the phase offset in degrees and m is the periodicity of the torsion.

The short range vdW interactions that exist between organic molecules are represented by the 6-12 potential shown in equation 5.5. Values are presented in table 5.7.

atom type	R* (Å)	ϵ (eV)
CT	1.9080	0.00473
C	1.9080	0.03729
CA	1.9080	0.03729
N(sp^2)	1.8240	0.00737
O	1.6612	0.00911
O2	1.6612	0.00911
OW	1.7683	0.00659
H	0.6000	0.00650
HC	1.4870	0.00650
H1	1.3870	0.00650
HW	1.0000	0.00000

Table 5.7: vdW 6-12 parameters

$$U(r_{ij}) = \left(\frac{A}{r_{ij}^{12}}\right) - \left(\frac{B}{r_{ij}^{6}}\right) \tag{5.5}$$

where, $A_{ij} = \epsilon_{ij}^{*}(R_{ij}^{*})^{12}$ and $B_{ij} = 2 * \epsilon_{ij}^{*}(R_{ij}^{*})^{6}$

R^* is the van der Waals radius in Å for an individual atom *i*. The value used in the equation for A and B is R_{ij}^{*}, the interaction of atom i and atom j. $R_{ij}^{*} = R_i^{*} + R_j^{*}$
ϵ is the van der Waals well depth in eV for an individual atom *i*. ϵ_{ij}^{*} is the equilibrium value for the intersection between atoms i and j. $\epsilon_{ij}^{*} = (\epsilon_i \epsilon_j)^{1/2}$.
The distance R_{ij}^{*} is related to σ, the finite distance where the inter-atomic potential is zero, as $R_{ij}^{*} = 2^{1/6}\sigma$.

Additional vdW interactions at the TiO_2 surface were represented by Buckingham potentials and Leonard-Jones potentials of the form of equations 5.6 and 1.15 respectively. Values were taken from Carracetta *et al.*, and are represented in tables 5.8 and 5.9 (Carravetta and Monti, 2006).

$$U(r_{ij}) = A\left(exp - \frac{r}{\rho} - \frac{C}{r^6}\right) \tag{5.6}$$

atom type	atom type	A (eV)	ρ	C
Ti	Ti	31120.1446	0.154	5.2500067
Ti	O_{surf}	16957.49826	0.194	12.58999
Ti	O_H[a]	13680.5458	0.194	12.5899773
Ti	N	5203.694	0.235	19.51
Ti	OW	1239.91102	0.265	6.4178891
O_{surf}	O_{surf}	271716.3	0.234	696.888
O_{surf}	Og	1644.4713	0.2461	8.6053919
O_{surf}	C	26749.2066	0.2796	10.906942
O_{surf}	CA	730.73738	0.2796	10.906942
O_{surf}	H	307.36	0.2563	2.25385
O_{surf}	Ha	307.36	0.2563	2.25385
O_{surf}	HC	307.36	0.2563	2.25385
O_{surf}	O	11782.737	0.234	30.219932
O_{surf}	OW	1644.4713	0.2461	8.6053919
O_{surf}	HW	307.36	0.2563	2.25385

Table 5.8: Buckingham parameters. [a] Modified potential for terminal hydroxyl oxygen atom.

atom type	atom type	ϵ (eV)	σ (Å)
Ti	Og	0.01366013	2.4118
Ti	C	0.018040339	2.4056
Ti	CA	0.018040339	2.4056
Ti	H	0.000062444326	3.7475
Ti	Ha	0.000062444326	3.7475
Ti	HC	0.000062444326	3.7475
O	OW[b]	0.006738785	3.166

Table 5.9: Leonard-Jones parameters. [b] modifed LJ potential for SPCE water used for hydroxylated surface. Oxygen surface atom allowed to have any type.

Hydrogen bonds were defined using the 12-10 H-bond parameters as given in table 5.10:

atom type	atom type	A	B
HW	Og	174.28	61.1
OW	HW	0.00000	0.00000

Table 5.10: H-bond parameters

5.3 Results and discussion

5.3.1 Radial Distribution Function

The radial distribution functions (RDFs) were analysed, at various stages of the modelling process, in order to confirm that the atomic potential parameters used were providing a correct representation of the system.

Hydrated surface

The Ti$\cdots$water oxygen (OW), surface oxygen (O_s)$\cdots$ water hydrogen (HW) and surface oxygen (O_s)$\cdots$ water oxygen (OW) RDFs for the hydrated TiO_2 surface model are shown in figure 5.5. A Ti$\cdots$OW sharp first neighbour peak (r_{fmax}) is centered at 1.86 Å. This corresponds to the first layer of molecularly adsorbed water. A well separated lower and broader second peak is centered at 3.31 Å. This corresponds to the second solvation layer where water molecules are interacting with the first layer of the terminal and bridging oxygens.

The data is in reasonable agreement with x-ray experimental findings of Zhang *et al.* which give average positions of 2.1 and 3.8 Å for the first and second water layers (Zhang et al., 2004). Visualisation of the surface shows that the coverage of the first layer represents exactly one water molecule per terminal Ti. This represents a totally hydrated surface and the presence of a very low amplitude of Ti$\cdots$OW between the first and second peaks indicates that water molecules do not diffuse but are truly adsorbed onto the Ti_{5f} sites.

In the context of the interaction of the surface with an aqueous solution, we can consider that each exposed terminal Ti site is covered by a strongly associated water molecule.

The $O_s\cdots$HW and $O_s\cdots$OW RDFs show a first peak for the first solvation shell at a maximum distance of 1.94 Å and 2.66 Å respectively. A second shoulder appears at 3.17 Å and 3.76 Å respectively. During the whole simulation time water molecules approach the surface oxygen atoms at a H-bonding distance and there is extensive exchange between

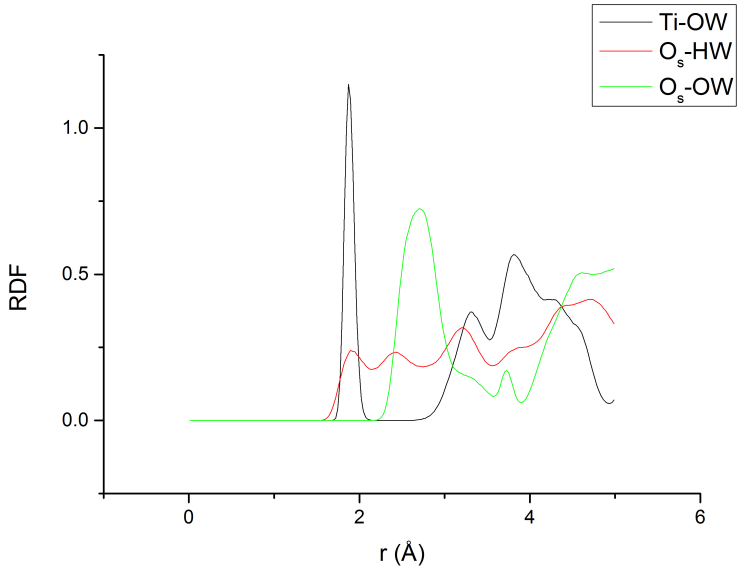

Figure 5.5: RDF of TiO_2 nonhydroxylated surface and water. Water molecules of the first water layer are bound to the surface O_b atoms by H-bonds. Every Ti_{5f} site adsorbs a water molecule. Compared to the water adsorbed on the O_b sites there is no amplitude between the first and second peaks, which indicates that they do not interchange.

the solvation shells. This is indicated by the presence of a significant amplitude between the first two solvation regions and this diffusion is in contrast to where water is almost permanently adsorbed onto the Ti atoms.

Solvated peptide molecules

As shown in Figure 5.6, the RDF of the solvated glycine molecule exhibits a first sharp peak for $O_{COO}\cdots HW$ at a H-bond distance of 1.63 Å. The coordination number $n_{coor} = 2.4$ as shown in figure E.1. A second broader, lower peak centered 2.98 Å is also observed.

The first $H_{NH}\cdots OW$ peak appears at 1.91 Å, also indicating hydrogen bond-like arrangements with water molecules. The second coordination shell of H_{NH} is represented by a diffuse peak centered at 3.39 Å.

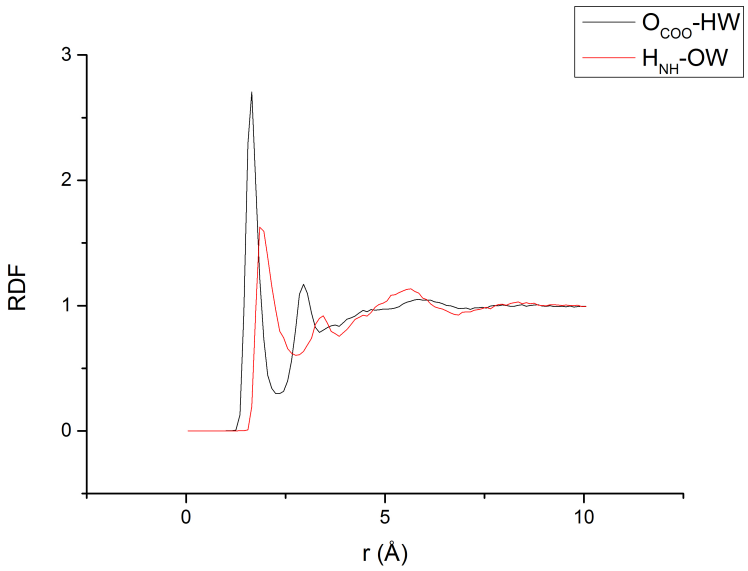

Figure 5.6: RDF of glycine in water. The amino NH_2 and carboxyl COO^- groups are the main groups bound to water molecules via hydrogen bonding.

Adsorption mechanism of RGD

The RDF of amino nitrogen $N_{NH_2}\cdots O_s$ of the arginine side chain of RGD has a first neighbour peak at 2.72Å and the first minima (r_{fmin}) at 3.62 Å (figure 5.7). These results are in good agreement with Carravetta *et al.* which were 2.77 and 3.60 Å for r_{fmax} and r_{fmin} respectively (Carravetta and Monti, 2006). The peak height is low which suggests that there is only a small probability of finding an amino nitrogen atom bound to surface oxygen. Any interaction that does exist between $N_{NH_2}\cdots O_s$ is likely to be extremely weak.

The peptide carboxyl oxygen (O_{COO}) of the RGD C-terminus forms the most stable bond with Ti_{5f} which shows a sharp first neighbour peak at 1.96 Å and a r_{fmin} at 2.72 Å.

These simulation results indicate that among the interactions between the surface Ti and other atoms, the residence time of Ti_{5f}-O_{COO} is maximised and the Ti_{5f}-OW takes second place. i.e. if the RGD molecule is able to displace the water a the Ti_{5f} site it forms the most stable bond and its residence time is effectively infinite. Thus, a favourable RGD interaction on TiO_2 results.

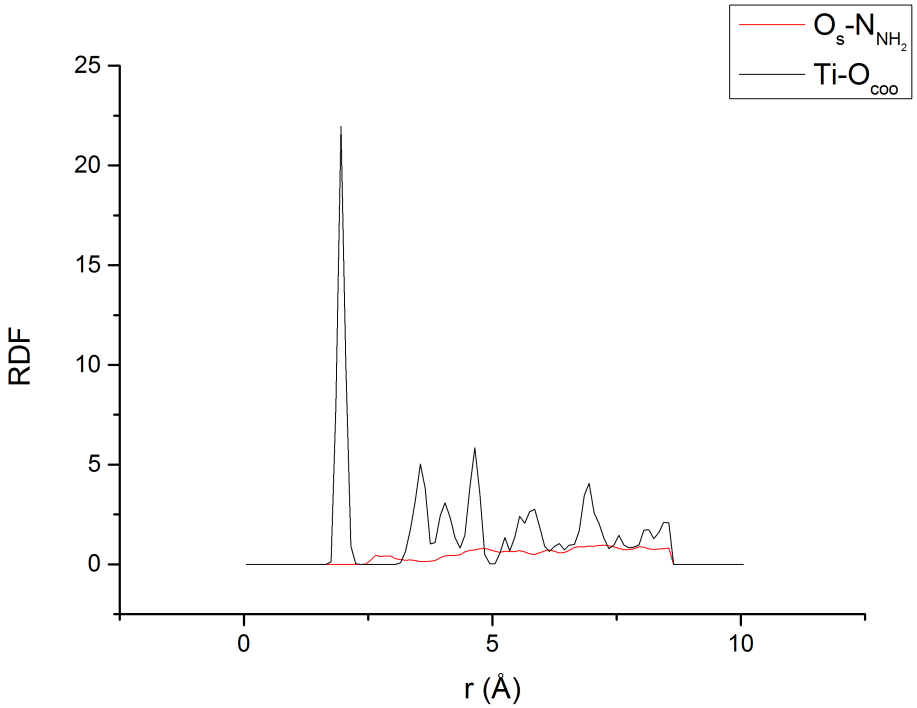

Figure 5.7: RDF of TiO_2 nonhydroxylated surface and RGD in water. The amino NH_2 and carboxyl COO^- groups are the main groups bonding to the TiO_2 surface. In particular, the COO^- group is seen to bind preferentially to a surface Ti_{5f} atoms and may even edge out water molecules from these sites.

5.3.2 Adsorption energies

Our adsorption energies of the molecules at the surface in the aqueous environment, as calculated using MD as the difference in energy between the complete system and the sum of the energies of the hydrated surface and the solvated peptide, is shown in table 5.11. There is generally a good agreement between the DFT calculations and the classical MD simulations. In the MD simulations, the arginine and aspartic acid molecules are less closely bound to the surface, which is reflected in the lower adsorption energies. The differences in the relative adsorptions for the two methods could be due to the approximations inherent and the lack of vibrational properties in the DFT calculations.

The RGD tripeptide and the peptide fragments interact most strongly with the surface *in vacuo*. In an aqueous environment, the strength of the binding of the peptide is af-

Adsorption energies (eV)					
Molecule	DFT vdW-DF *in vacuo* (0 K)	MD *in vacuo* (0 K)	MD *in vacuo* (300 K)	MD in water (300 K)	hydroxylated (300K)
Glycine	-3.0	-3.5	-4.6	-3.6	
Aspartic acid	-2.9	-2.4	-2.5	-1.4	
Arginine	-3.8	-3.5	-2.4	-1.9	
RGD	-4.5	-9.4	-12.0	0.7	-10.5

Table 5.11: Calculated adsorption energies of the peptide molecules at the TiO_2 [110] surface.

fected by the presence, and indeed competition, of the water molecules. In particular, the adsorption energy of RGD at the [110] surface in the aqueous environment is slightly positive indicating a weak minima in the energy landscape. Thus, pre-adsorbed water has destabilised the peptide adsorption. The difference between the adsorbtion energies in a hydrated environment and *in vacuo*, is partly due to the increased stability of the hydrated [110] surface and the solvated peptide molecule. *In vacuo*, the surface and the peptide species can only increase their coordination through interaction with each other. In comparison to the same systems *in aqua*, coordination with water molecules are competitive processes that will reduce configurational and surface energy of the peptide and the surface respectively. There is no overall energy gain from the absorption of RGD at the titania surface due to the loss of surface bound water molecules.

The peptide-surface electrostatic interaction in the hydroxylated system has a higher value than in the nonhydroxylated system. The TiO_2 surface modified with OH groups shows a much greater affinity for RGD through more adsorbed acidic and basic residues leading to a greater molecular-surface electrostatic. In contrast, the first coordination shell of water at the nonhydroxylated surface effectively blocks the reactive Ti_{5f} sites. The peptide molecule can interact directly with OH groups of the hydroxylated surface via hydrogen bonding with it's charged carboxyl and amino groups. In addition, the highly ordered structure of the OH groups on the hydroxylated surface may enhance the number of hydrogen bonds inside this layer and consequently reduce the possibility of H-bond formation between OH atoms and the water layer next to it. This is turn allows the peptide to move more easily into the first solvation layer and associate more closely to the hydrox-

ylated surface i.e. RGD can partially occupy the region of the first solvation layer on the hydroxylated surface, but it is unlikely to break into this region on the nonhydroxylated surface.

5.3.3 Molecular configurations

When adsorbing to a surface, large peptide molecules are able to change their conformation in order to match the surface geometry as closely as possible and to maximise their interactions. It was shown that *in vacuo* the amino (NH_2^+) and the carboxyl COO^- groups of RGD are the main components bonding to the TiO_2 [110] surface through interaction with the Ti^{4+} atoms (figure 5.8). This shows that the peptide has the ability to bridge between two Ti sites, involving a multiple-species interaction with the surface. Incorporating the van der Waals interactions into the DFT calculations, the adsorbtion energy is predicted to be -4.5 eV.

This adsorption energy released was seen to increase to -12.0 eV when using Molecular Dynamics *in vacuo*, where the simulation can incorporate the vibrational properties of the long hydrocarbon backbone. The differences in the energies between the two methods can be considered as an upper limit to the uncertainties in the adsorption energies.

The interfacial water molecules are structured on both hydroxylated and nonhydroxylated surfaces, forming hydrogen-bonded networks. Two solvation shells can be identified from the RDF plots as part of the electrical double layer that forms at the interface. On the TiO_2 [110] hydrated surface, the water molecules adsorb particularly strongly into the parallel gaps between rows of bridging oxygens, shifting the preferred adsorption position of large peptide molecules. The adsorption energy of RGD in water at the TiO_2 [110] surface is predicted to be 0.7 eV. The adsorption energies of small hydrocarbon molecules in water, such as glycine and aspartic acid, are not as greatly reduced since the configurations at the surface are constrained to a few stable orientations.

We can obtain a quantitative measure of configurational change on adsorption from a calculation of the difference in configuration energy of the adsorbed peptide in it's envi-

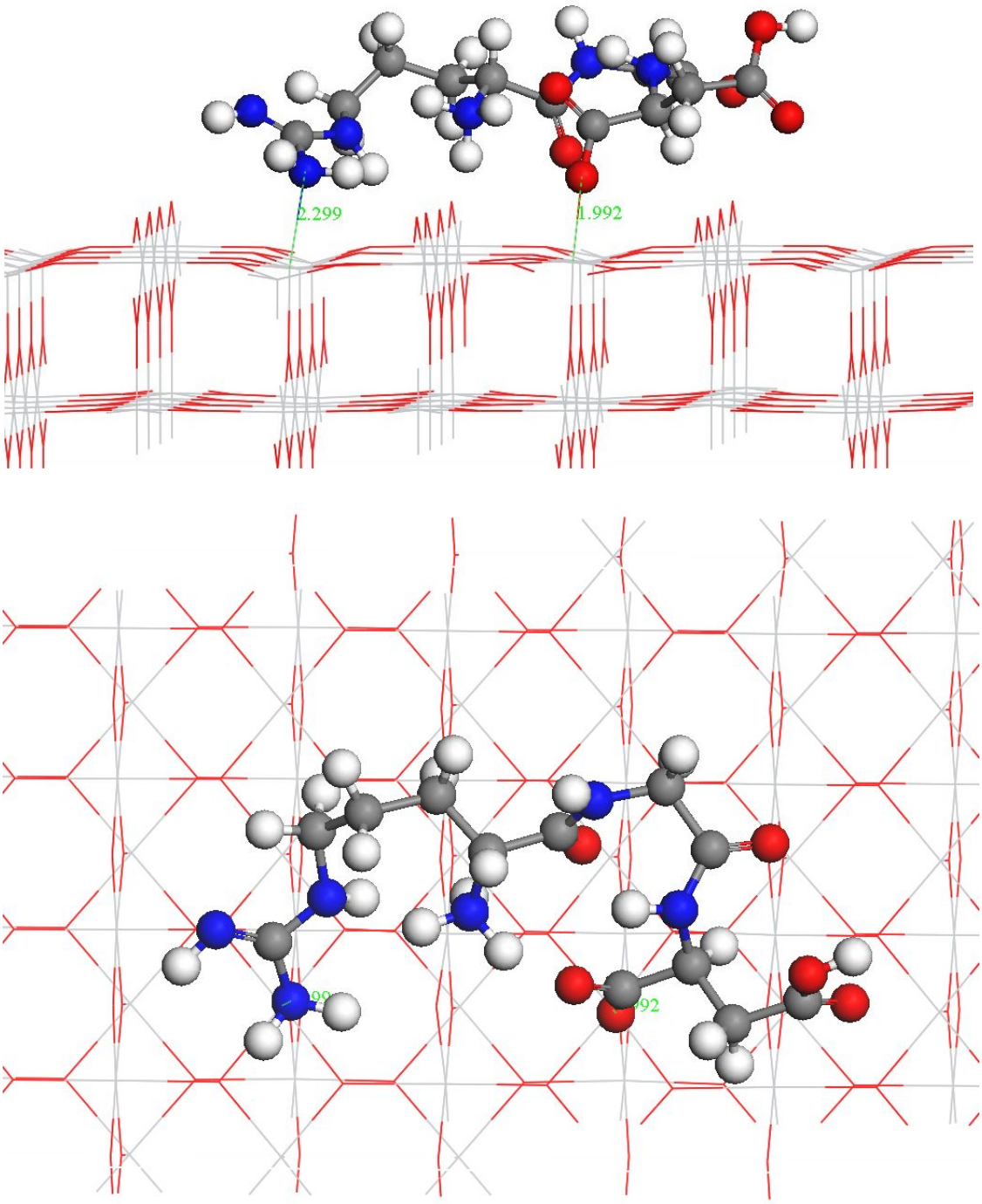

Figure 5.8: vdW adsorption mode for RGD *in vacuo* on the TiO_2 [110] surface. Side and top views. Distances are given in Å. Grey balls represent carbon atoms, white balls hydrogen atoms, red balls oxygen atoms and blue balls nitrogen atoms. The TiO_2 lattice is represented in wire form.

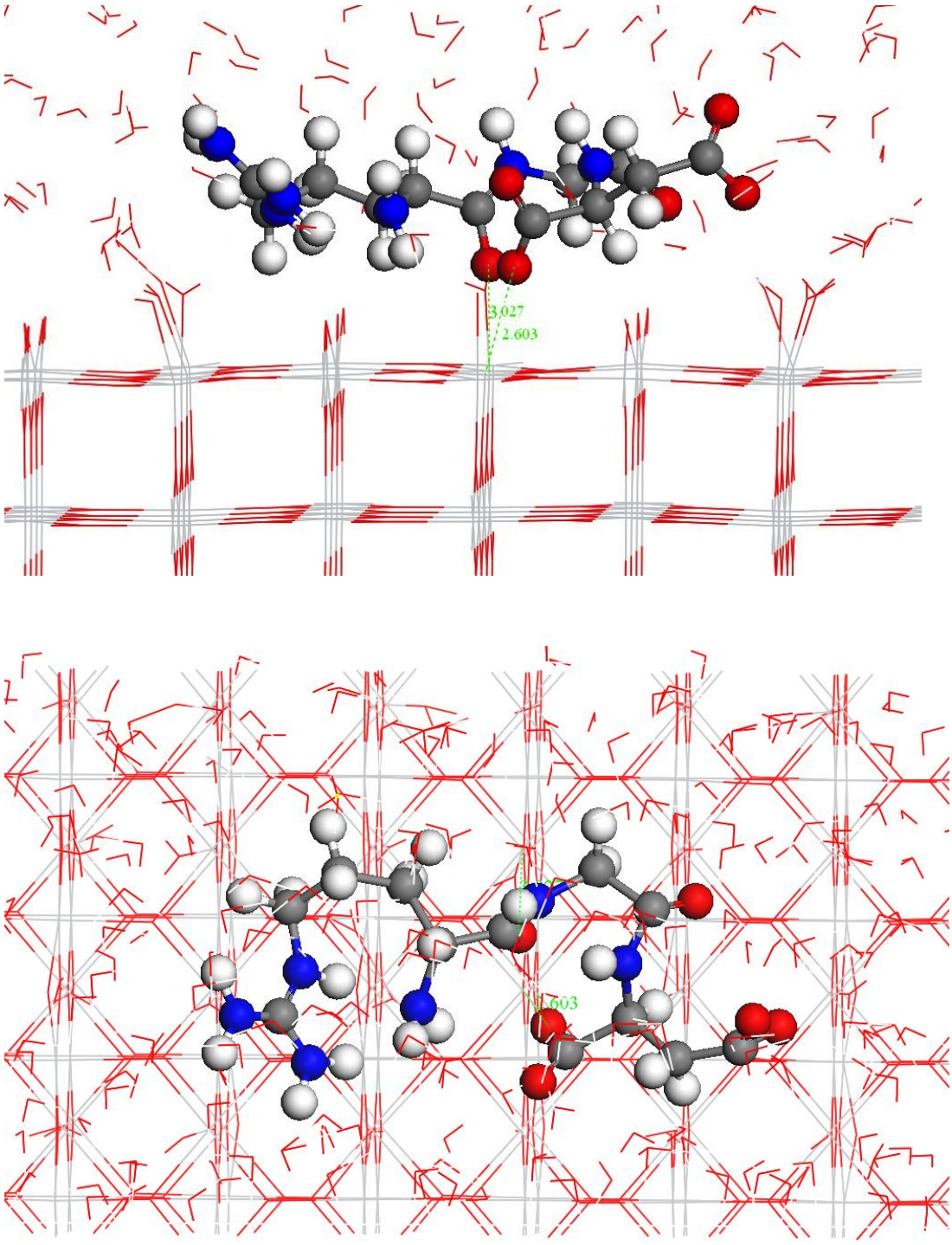

Figure 5.9: Adsorption mode for RGD in water on the TiO_2 [110] surface. Side and top views. Distances are given in Å. Red line 'V's' represent the solvent water molecules. H_2O molecules can be seen to be permanently bound to the Ti_{5f} sites, restricting the approach of terminal amino and carboxyl RGD groups to the surface.

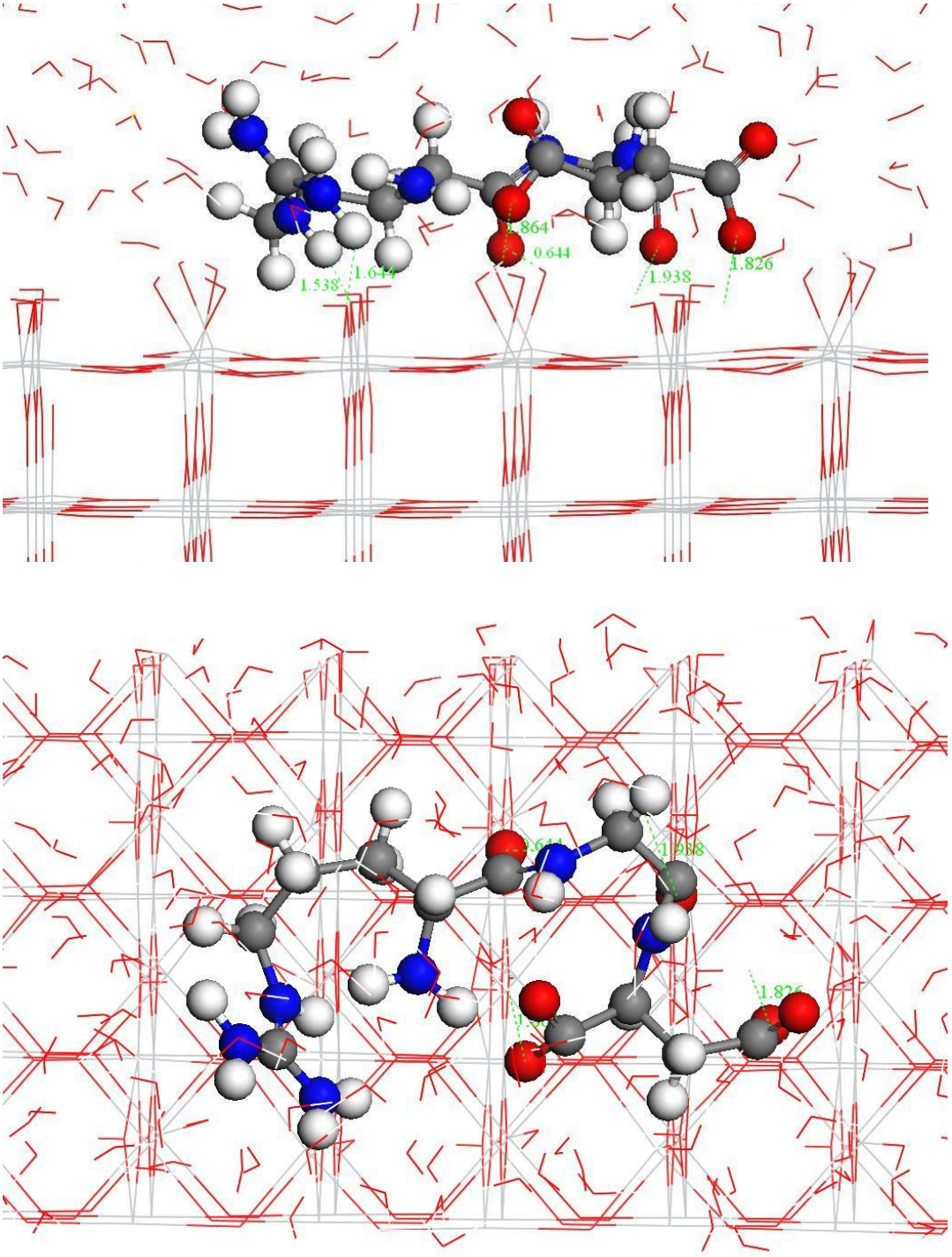

Figure 5.10: Adsorption mode for RGD in water on the hydroxylated TiO_2 [110] surface. Side and top views. Distances are given in Å. The RGD molecule is seen to make more surface interactions in comparison to the nonhydroxylated surface (figure 5.9).

Configuration energies (eV)				
Molecule	*in vacuo* (0 K)	*in vacuo* (300 K)	in water (300 K)	hydroxylated (300 K)
Glycine	-0.5	-3.6	-5.1	
Aspartic acid	0.2	-1.4	1.5	
Arginine	-3.5	-1.9	-2.4	
RGD	-1.6	-9.4	4.8	4.0

Table 5.12: Calculated differences in configurational energies between the peptide molecules at the TiO_2 [110] surface and the unbound molecules. Negative values indicate stable surface configurations.

ronment, compared with the unbound peptide (table 5.12). The configurational energy of the RGD peptide in water in its adsorbed geometry at the [110] surface was found to be 4.8 eV larger, compared to the free solvated peptide conformation. The main difference in adsorption geometry is seen in the interaction with surface species. In an aqueous solvent the NH_2^+ group of RGD is unable to interact with the Ti_{5f} ion. This is presumably due to the presence of adsorbed H_2O molecules and the energy gain from NH_2^+ group interaction is insufficient to displace the water. The RGD molecule is therefore unable to adopt the energetically favourable bridging configuration that is seen at the surface *in vacuo*. In water, RGD is seen to adsorb with one COO^- group and one CO-NH group, interacting at two Ti_{5f} sites within the same row (figure 5.9) at a bond distance of 2.60 and 3.03 Å respectively. The CO-NH group of the peptide bond is a weaker interaction with the surface compared to the charged NH_2^+ group interaction and results in some conformational change in the hydrocarbon backbone leading to the observed larger conformational energy. Because of this higher configurational energy, adsorption at the surface provides a slightly positive value, indicating that the energy from the loss in configurational energy cancels out the close interaction with the surface. In comparison, there is a slight reduction in the configurational energy of RGD on the hydroxylated surface. The OH groups, that extend away from the surface, are seen to draw in the COO^- groups and form close hydrogen bond interactions (figure 5.10).

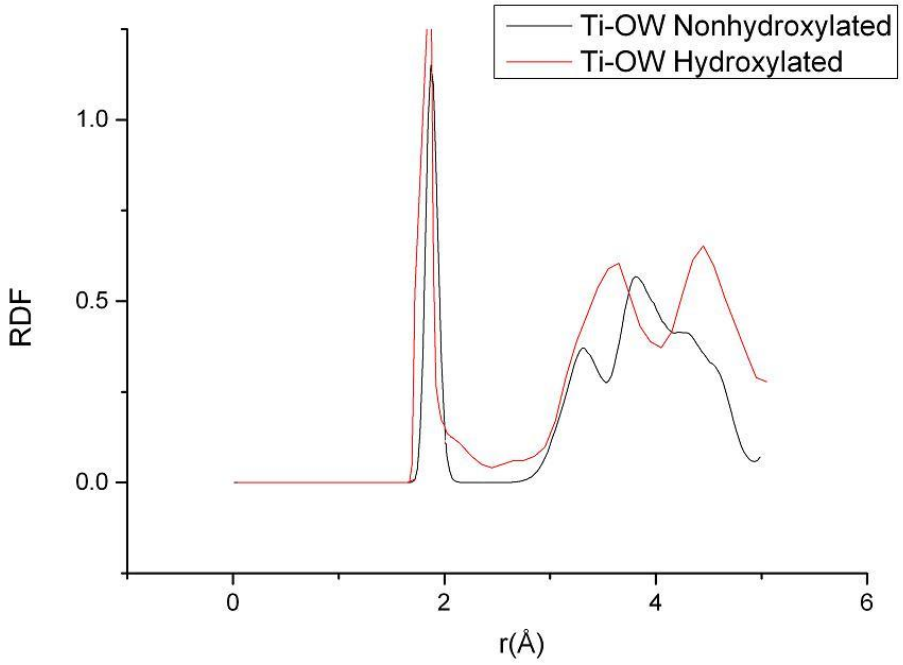

Figure 5.11: Comparison of RDFs of TiO_2 nonhydroxylated surface and hydroxylated surface in water. The sharp peak in red at 1.83 Å corresponds to the oxygen of the terminal hydroxyl group. The sharp peak in black at 1.86 Å corresponds to the first water layer above the nonhydroxylated surface which shows no diffusivity of molecules with the second layer. The amplitude between the first and second-water layers ('camel humps') on the hydroxylated surface show significant interchange of molecules occurs between them.

5.3.4 Hydrophilic surface reconstruction

The first RDF peak of molecularly adsorbed water at the nonhydroxylated surface occurs because the water molecules occupy the terminal Ti_{5f} sites (figure 5.11). The molecules in this layer have demonstrated zero diffusion within the time frame of the simulation. Consequently, this layer can be considered to be truly adsorbed. The Ti_{5f} atom is occupied by a full coverage of terminal oxygens on the hydroxylated surface. The length of the Ti-O bond was fixed at 1.89 Å (see table 5.5), and the peak of terminal hydroxyl oxygens, at 1.83 Å, indicates that the Ti-O bond is almost perpendicular to the surface. The x-ray experiments of Zhang *et al.*, which were unable to distinguish oxygens that are part of the terminal hydroxyl from oxygens of adsorbed water molecules above the Ti_{5f}

site, provided an observed average height of 2.1 Å. This is slightly larger than my MD determined heights for both oxygen species but the second peak around 3.61 Å is in good agreement with the x-ray experiment height of 3.8 Å (Zhang et al., 2004). This second peak corresponds to the first adsorbed layer of water molecules interacting with bridging and terminal hyrdroxyl group oxygens. There is a third peak at 4.45 Å representing the second adsorbed water layer. The amplitude that exists between these two peaks indicates that an interchange of water molecules occurs between the first and second hydration layers on the hydroxylated surface. The diffusivity grows quickly in layers further from the surface until random distribution is achieved in bulk water around 15 Å from the surface. Unlike at the nonhydroxylated surface, where the water molecules point towards the surface to make hydrogen bonds with the adsorbed second-layer water (figure 5.9), the water molecules of the second layer at the hydroxylated surface tend to be orientated away from the surface (figure 5.10). This is because of the electrostatic repulsion between the water molecule oxygens and the negatively charged hydroxyl groups. As a result, the water layers on the nonhydroxylated surface are seen to be less well orientated. Thus, the water diffusivity between the first and second layers is contrasted between the two surface types, where the first-water layer molecules of the nonhydroxylated are relatively immobile compared to the hydroxylated surface. Consequently, any adsorbtion of competing molecules at the hydroxylated surface is much more likely to be an occurrence.

The peptide groups of RGD are able to replace water molecules in the first solvation layer above the hydroxylated surface and form hydrogen bonds with the modified OH groups of the surface. For example, the oxygen atoms of COO^- bind with the hydrogen atoms in both the terminal and bridging OH groups, and the hydrogen atoms of NH_2^+ bind with the oxygen atoms in the bridging hydroxyl groups. In contrast, on the nonhydroxylated surface, the adsorbed groups cannot perturb the water molecules in the first solvation shell as they are bound strongly to the Ti_{5f} atoms.

On adsorption to the hydroxylated surface, the peptide undergoes a conformational change to maximise its affinity and to decrease the free energy of the system. Thus, every residue in the chain can obtain its best binding configuration on the surface. Pining the polymer

to a particle surface clearly reduces the entropy of the chain, but the process is thermodynamically favoured if there is an entropy gain from ejecting the water molecules from the surface. Hydrogen-bonded H_O-O_{COO} and O_H-H_{NH} interactions between the surface and the peptide are energetically more favourable than the H-bond interactions between the surrounding water molecules and the solvated peptide. Thus, if the peptide can form interactions at the surface, the close interaction effect outweighs the increase in configurational energy required to accommodate the peptide to the surface geometry.

5.3.5 Conclusions

In this computer modelling study I have employed molecular dynamics simulations to investigate the interaction of small peptide fragments with the TiO_2 [110] surface. I have used interatomic potential-based models, which agree well with my previous DFT calculations of the same systems as to the mode of bonding and adsorption strength of the peptides at the surface. I have executed a series of molecular dynamics simulations to compare the adsorption of the peptides in an aqueous environment, where my simulations show the strength of the interaction depends on a number of factors:

- The stability of the surface; where the reactive TiO_2 surface interacts strongly with adsorption peptide species at vacuum surfaces, as shown by both DFT and MD calculations.
- The competition from pre-adsorbed water molecules for surface adsorption sites; where it was found that the smaller water molecules effectively block the adsorption of the peptide at the most favourable binding sites on the nonhydroxylated surface. On the nonhydroxylated surface, the residues hardly reach the region that defines the first water layer above the surface due to unfavourable energy effects.
- The surface orientation of the molecule; where the peptide is able to form multiple interactions with the surface species, particularly if it is large enough to bridge between two or more surface Ti^{+4} ions. This is the same as the adsorption of the 10th type III molecules of fibronectin (FN-III10). Shen *et al.* found that the charged COO^- and

NH_3^+ are the strongest groups that interact with the hydroxyapatite (HA) surface, while other groups, such as charged guanido and hydroxyl, have considerable interactions with the surface (Shen et al., 2008). Any conformational change compared to the molecule's optimal geometry can affect the binding strength. In water, the RGD conformation is significantly affected (table 5.12). Adsorption, however, was seen to be feasible in water on the hydroxylated surface where the stronger peptide-surface interactions replace the weaker peptide-water interactions (table 5.11).

As a result of the combination of these factors, the RGD peptide binds far more strongly to the TiO_2 [110] surface *in vacuo* than in an aqueous environment. Indeed, in the presence of bound water at the surface, it is very difficult for organic molecules to bind as the resident time of H_2O at Ti_{5f} sites is very long. Water molecules were seen to be permanently bound for the duration of our simulations and peptide molecules were unable to replace them at the surface. However once peptides were introduced to the surface sites, they bound preferentially. This is even more likely to occur at natural, reactive features on the surface such as oxygen vacancies and step and pit structures. It has been found that modified Ti surfaces that include highly roughened nanotopography are the most favourable for cell interaction (Wall et al., 2009). It is likely that the process of acid etching, such as in the formation of SLA Ti, exposes more terminal and oxygen atoms around the valley rim and surface peak regions. This raises the surface energy further, since atoms must offset their initial positions after relaxation, and creates strong electrostatic interaction regions. Higher surface energy means that RGD can adsorb rapidly on the surface and the carboxyl groups (COO^-) can edge out the adsorbed water molecules in order to bind preferentially to the surface Ti_{5f} atoms.

The effect of UV induced hydrophilicity is to introduce hydroxyl groups at the TiO_2 surface that provide multiple hydrogen bond formation sites. Hydrogen bonding is seen between the OH surface groups and the RGD charged guanido NH_2^+ group and carboxyl COO^- groups. Carboxyl to Ti interaction is no longer possible due to the OH groups blocking access for the large peptide molecule to the surface. However, the OH interactions provides an adsorption energy of $\sim$ -11.25 eV higher than on the hydrophobic, native surface because

of the hydrogen bonding that anchors the molecule at multiple sites. The effect of which is to restrain the movement of RGD and aids further recognition and adhesion of a cell. In this way, a combination of rough hydrophilic properties influences the TiO_2 surface environment which is important for peptide stability.

RGD represents adsorption domains for various biologically important molecules. It is found as an adsorption motif for the fibronectin molecule. Fibronectin binds ECM components such as collagen and binds to membrane spanning receptor proteins called integrins. In addition, osteopontin (OP) and bone sialoprotein (BSP) belong to a group of extracellular matrix proteins in bone. Both contain RGD integrin recognition sequences (Nebe et al., 2008). I can suggest that hydrophilic modified Ti surfaces naturally possess an adhesive environment for extracellular matrix protein interaction, thus effectively combining cells with the underlying nanostructured surface.

Chapter 6

Stem cell selection by modified titanium

6.1 Introduction

Micro structured, high surface energy titanium has been shown to be the most effective substrate for osseointegration of an implant with surrounding bone tissue. The main reason that titanium and titanium based alloys have been used for dental and orthopedic implants is because of their biocompatible nature (Steinemann, 1998; Fukiage et al., 2008; Schuler et al., 2006). The biocompatible nature of Ti can be attributed to the inertness, the potential not to precipitate phosphates and other minerals from bone and favourable interaction energies with cell surface adhesion proteins. Under atmospheric conditions, a thin oxide layer spontaneously forms on Ti and Ti-alloy surfaces. This has a strong, direct effect on the success of the implant. Titanium is a possible material for use in clinical implants because bone regeneration can occur on the surface with no evidence of host rejection. Mesenchymal Stem Cells (MSCs) are present in bone marrow and are the first cells that are recruited an implant placement following a trauma or disease. The initial stage for MSCs producing bone tissue is cell adhesion followed by proliferation and differentiation. It has been shown that osteoblastic cell adhesion, growth and differentiation are

related directly to surface energy and roughness (Wall et al., 2009; Le Guehennec et al., 2008). Osteoblastic bone cells have been shown to respond more favourably to roughened surfaces than smooth (Brett et al., 2004).

Surface roughness has been an important factor for establishing reliable bone-anchored implants. *In vitro* studies have provided a positive correlation between surface roughness and cellular attachment as well as subsequent osteoblast-like cell activity (Rönold et al., 2003). This has been supported using *in vivo* studies, by groups such as Buser *et al.*, who measured the mechanical testing strength of the connection between bone and implant (Buser et al., 1991). Rönold *et al.* suggested that an upper limit exists for the correlation between surface roughness and bone fixation (Rönold et al., 2003).

Wettability and surface energy are key parameters in the performance of various modified implant surfaces. Experimental analyses comparing SLA and SLActive *in vivo* have applied histological and morphometric evaluations to implant integration in various animal subjects, comparing different loading times, assessment of bone implant contact, and interfacial strength between tissue and fixture by removal torques. The examinations indicate a significantly higher bone implant contact % (BIC) and removal torque values in the case of the SLAcitve compared with SLA by as early as two weeks post implantation (Buser et al., 2004). More recent experiments used *in vivo* molecular analyses, using tissue specimen retrieved from subjects at various time intervals for genetic and molecular examinations. One such assessment has indicated more stable hematoma clot formations on the SLActive than SLA; suggestive that the surfaces enhancement effects extend to the spatial orientation of clot constituting elements at the interface (Schwartz et al., 2010). Gene expression analyses of retrieved samples indicate a temporal upregulation in skeletogenesis related genes expression compared to SLA as early as 4 d post implantation (Ivanovski et al., 2011). These studies have suggested that faster healing and greater implant stability was achieved with the SLActive implant surface than around conventional, hydrophobic surfaces. In addition, *in vitro* studies on the biological effects of Ti implant surface characteristics on cellular responses imply these have an intrinsic influence on cellular function. Osteoblastic differentiation, as evaluated by genetic expression of bone physiology related

genes, quantitative assessments of osteoblastic phenotypic protein markers (ALP, OC, OPG and TGF-β1), and functional evaluation of osteogenic phenotypic characteristics, were seen to be enhanced by the most hydrophilic surface (Brett et al., 2004; Wall et al., 2009; Khan et al., 2012). Biomaterials have been shown to provide powerful topographical and chemical cues that can guide cells in the use of regenerative medicine (Dalby et al., 2007; Olivares-Navarrete et al., 2010).

If successfully developed, modified Ti could be applied as a material as part of a bioreactor for the selection and expansion of stem cells that can differentiate to become osteoblasts. The technology could allow medical practitioners to create tailored, homologous replacement bone implants that would result in minimal risk of rejection by the patient's body.

The research described in this chapter, utilises the nanotopography and chemical signals of novel titanium surfaces to provide an exciting approach in the selection of stem cell populations that have an enriched osteogenic potential. This approach has the possibility to be applied to repair and regeneration purposes.

Previous *in vitro* analyses of osteoblastic cells by Dalby *et al.* have suggested that contact with Ti causes an enhancement in cellular phenotypic maturation and function (Dalby et al., 2007). I propose that the effect of Ti is to cause a change in the heterogeneous MSC population through the induction of a selective apoptotic route. I evaluate these population changes by examining phenotypic marker expression and osteogenic mineralisation in MSC populations selected on modified Ti surfaces.

6.2 Methods

6.2.1 Selected population procedure

Mesenchymal Stromal Cells (hMSCs) from three unrelated donors (Caucasian, male: 20-30 year age group) were obtained from the Institute for Regenerative Medicine, Texas A & M Health Science Center, College of Medicine, USA. These cells were isolated from

bone marrow aspirates on their ability to adhere to tissue culture plastic compared to non-adherent hematopoietic adult stem cells. The hMSCs had been pre-characterised for colony forming units, osteogenic, chrondrogenic and adipogenic differentiation and the expression of stromal cell surface markers. The hMSCs were cultured according to the parameters suggested in previous publications (Colter et al., 2001; Sekiya et al., 2002). Cells were expanded at low density (100 cells cm^{-2}) in Growth Medium (GM) comprising Minimal Essential Medium alpha (Gibco) supplemented with 10 % lot selected fetal calf serum (Gibco), 1 % antibiotics(Penicillin / Streptomycin: PAA laboratories) in a 150 cm^2 Tissue Culture (TC) treated flask (Nunc) at 37 °C and 5 % CO_2 with bi-weekly medium changes. On obtaining 80 % confluence, cells were sub-cultured using a solution of 0.05 %/0.002 % Trypsin/EDTA in Ca^{2+}/Mg^{2+} free PBS (PAA laboratories) onto 24 well TC plates containing the following surfaces TCP, SMO, SMOd, SLA and SLV Ti at a density of 40,000 cells / well. The populations of cells exposed to Ti are the selected populations and contain cells that are phenotypically altered. I propose, the population exposed to TCP represent the unchanged parent population (negative control), identical in composition to the original MSC population but having undergone the same manipulations as those selected on the Ti surfaces. Phenotypic analysis experiments were performed on selected populations and the parent population cultures that had undergone a maximum of five passages. An experimental matrix is shown in figure 6.1.

The selected population from SLV Ti was placed back on modified Ti surfaces for 24 hours, harvested and cultured on TCP for proliferation, apoptosis and gene expression assays in comparison to the parent populations responses (figure 6.2). This enabled an analysis to made into the changes that occur within the selected population as a result of contact with SLV.

6.2.2 Cellular viability

Cellular viability of MSC populations that were harvested and expanded from modified Ti surfaces were serially assessed by examining cell number changes and the expression of apoptosis related markers over the course of culture in GM. The different proliferation

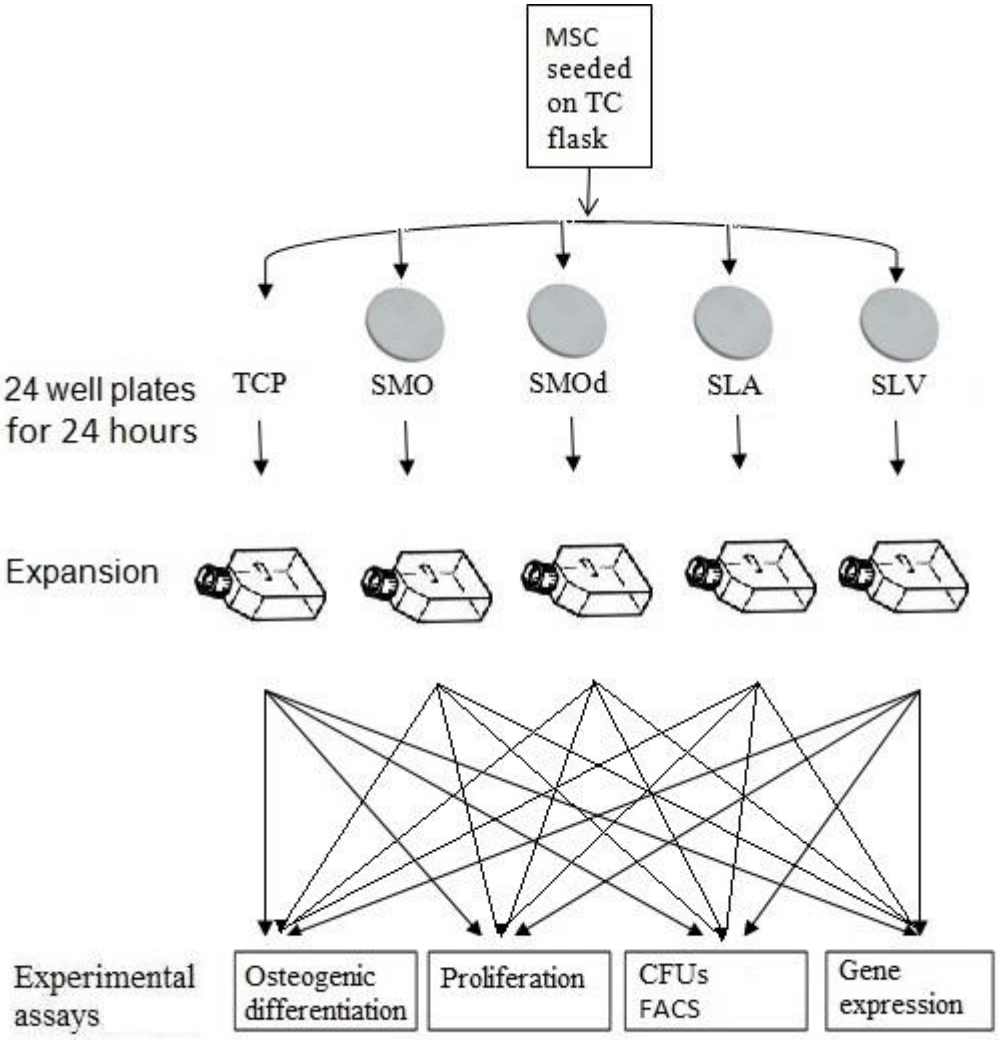

Figure 6.1: Stem cell selection by modified Ti experimental matrix. Variations in osteoblastic differentiation for MSCs selected on Ti surfaces compared to their control, on TCP, were evaluated by genetic expression of bone physiology related genes and functional evaluation of phenotypic characteristics (proliferation, CFU formation, apoptosis effects and quantitative assessment of calcium deposition).

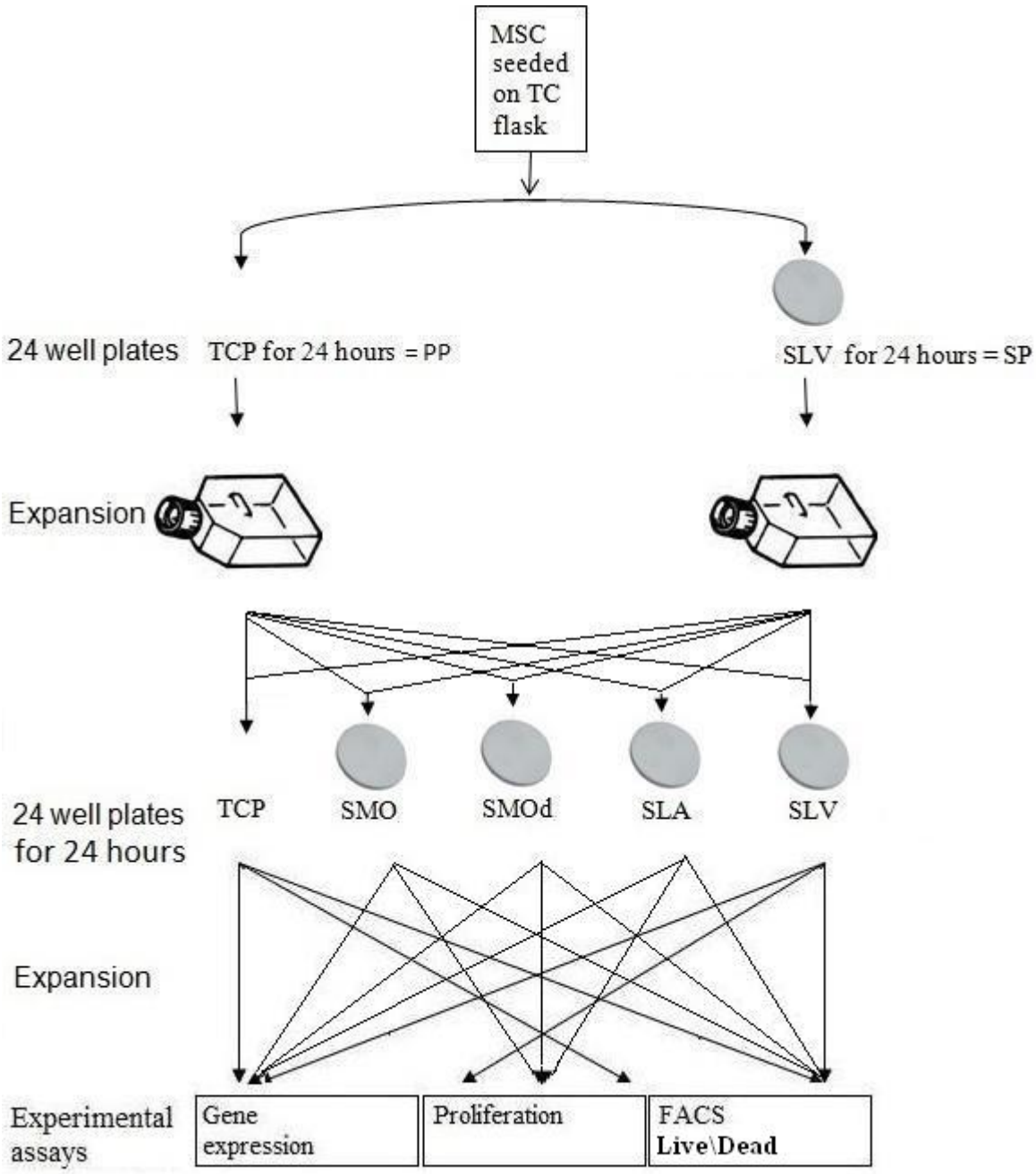

Figure 6.2: Experimental matrix to determine population changes in the SLV selected population (SP) in comparison to the parent population (PP). Cells that were selected on SLV Ti were 'parachuted' back onto Ti surfaces and the variations in osteogenic differentiation were evaluated by genetic expression of bone physiology related genes and functional evaluation of phenotypic characteristics (proliferation, apoptosis effects and quantitative assessment of calcium deposition) using the unaltered parent population as a control.

and apoptosis rates were due to the differential population effects created by the modified Ti surfaces on uncommitted cells. The experiments conducted are detailed below.

The impact of Ti on cell death

The levels of apoptosis and necrosis of cells placed on each modified Ti surface and TCP were analysed by staining with Annexin V-FITC and Propidium Iodide (PI)-PE (BD Biosciences). Cells were detached using Trypsin/EDTA, that was deactivated by culture medium before being washed twice in PBS by centrifugation. Cells were resuspended in 500 μl 1X binding solution / sample (10X binding buffer in 450 μl deionised water). Staining was achieved using 5 μl of Annexin V and 10 μl of PI. Samples were incubated for 10 minutes in darkness before being analysed by Flow Cytometry (FACScanTM Becton Dickinson). Settings were adjusted to avoid superimposition between FITC and PE. The method is detailed in chapter 2, section 10.1.

Cellular proliferation

Cellular proliferation of 2000 cells per disc was serially assessed until confluence was achieved using the AlamarBlue assay (N = 3; n = 3). The method is detailed in chapter 2, section 6.1.

6.2.3 Osteogenic differentiation

The osteogenic mineralisation of MSC populations that were harvested and expanded from modified Ti surfaces was examined using Ca^{2+} and collagen assays by seeding cells on TCP at an initial density of $\sim$ 1.25 x 10^4 cells cm^{-2} in OM. Cultures were maintained with bi-weekly medium changes.

Quantitative assessment of total ECM calcium deposition

A quantitative estimate of ECM deposited calcium was conducted at 7, 14 and 21 days post seeding with the QuantiChrom Calcium assay, according to the method described in chapter 2, section 8.2. Cell numbers were estimated with the AlamarBlue assay described in chapter 2, section 6.1.

Quantification of total ECM collagen

The total ECM collagen formed by cells was measured at 7, 14 and 21 days post seeding according to the Sircol method described in chapter 2, section 9. Total collagen was not measurable within a single well due to small quantities formed by the small number of cells. Hence, collagen isolates from three replicates of a sample were pooled, concentrated with kit reagents and then stained, to obtain a reading. This was normalized to total cell numbers that were estimated with the AlamarBlue assay as in chapter 2, section 6.1.

6.2.4 Quantification of total ECM Ca^{2+} to collagen ratio

A total Ca^{2+} to total collagen ECM ratio was calculated from the Ca^{2+} and collagen data. The total amount of calcium present in the three wells was summed from the values of the three replicates (μg). This value was divided by the total quantity of collagen (μg) assayed in a replica pool of triplicates. This ratio was separately calculated for each of the three donors; their mean later calculated and plotted in a bar chart.

6.2.5 Gene expression analysis of osteogenic genes

Quantitative-polymerase chain reaction (qPCR) was used to evaluate the expression of genes representing different facets of osteogenic differentiation and apoptosis in order to compare the phenotypic changes induced in cell populations from modified Ti. These were:

- the master osteogenic runt-related transcription factor (Runx2) responsible for commitment and initiation of differentiation
- extracellular matrix vesicle associated calcium nucleating proteins Osteopontin (OP / SSP1)
- osteo-specific ECM collagen (COL1A1)
- the pro-apoptotic gene Caspase 3 (Casp3)

MSCs populations that were harvested and expanded from modified Ti surfaces were seeded at a density of $\sim$ 2.0 x 10^4 cells mL^{-1}. Analyses were conducted in GM (N = 3; n = 3) at 24 h post seeding by lysing monolayers, extracting total RNA and converting it to cDNA, followed by PCR with Taqman probes. The methods used in this experiment are detailed in chapter 2, section 7.

6.2.6 Colony Forming Unit (CFU) experiments

Mesenchymal stem cell populations that were harvested and expanded from modified Ti surfaces were seeded at a density of $\sim$ 100 cells in a T-75 flask containing GM for 10 days with bi-weekly media changes. Cultures were fixed and stained in 3 % crystal violet and imaged using Image-Pro Plus software. Comparative parameters used were number and average mean diameter as described in chapter 2, section 5.

6.2.7 CD surface cell marker analysis

Flow cytometry was used to study the relative presence of multiple stem cell surface markers, Stro-1 (FITC), CD146 (V450), CD105 (Brilliant violet), CD164 (PE), CD49d (PE-Cy5), Live/Dead (aqua) within MSCs populations that were harvested and expanded from modified Ti surfaces. Experiment details are provided in chapter 2, section 10.2.

6.3 Results and discussion

6.3.1 Cellular proliferation

The cell numbers increased gradually with a greater initial proliferation rate in the parent population (TCP) compared to the selected populations from the smooth and rough Ti surfaces (figure 6.3). A higher rate of division in the parent population was indicated by roughly a 34 fold increase in cell numbers until a confluent monolayer was reached by day 10. The proliferation of the selected population from SLV was much reduced and showed a cell number increase of roughly half that of the parent population after 10 d in culture.

Analysis of proliferation on SLV shows that the MSC population selected on SLV and the parent population from TCP have similar profiles (figure 6.4). The proliferation profile of the parent population has been reduced on SLV from that of the parent population on TCP (figure 6.3) whereas the selected population proliferation on SLV remains the same as that seen for the selected population proliferation profile on TCP.

6.3.2 The impact of Ti on cell death

There was a greater effect of necrosis and apoptosis in response to MSCs having been exposed to SLV (figure 6.5). There was a significantly higher number of dead cells on SLV than on any other Ti surface and TCP. The latter time point of 24 h showed there was a higher amount of live cells on all surfaces compared to 3 h (figure 6.6). This indicates an event where the population recovers to proliferative capacity. The smallest recovery effect was seen in the cells from SLV.

The selected population from SLV (SLV SP) showed a significantly higher amount of live cells compared to the parent population from SLV (figure 6.7). This indicates that a smaller proportion of cells, within the population, undergo necrosis or apoptosis following the repeated contact with SLV Ti. The SLV selected population contains more the cells that demonstrate the ability to survive a repeated exposure to SLV. Therefore, by taking

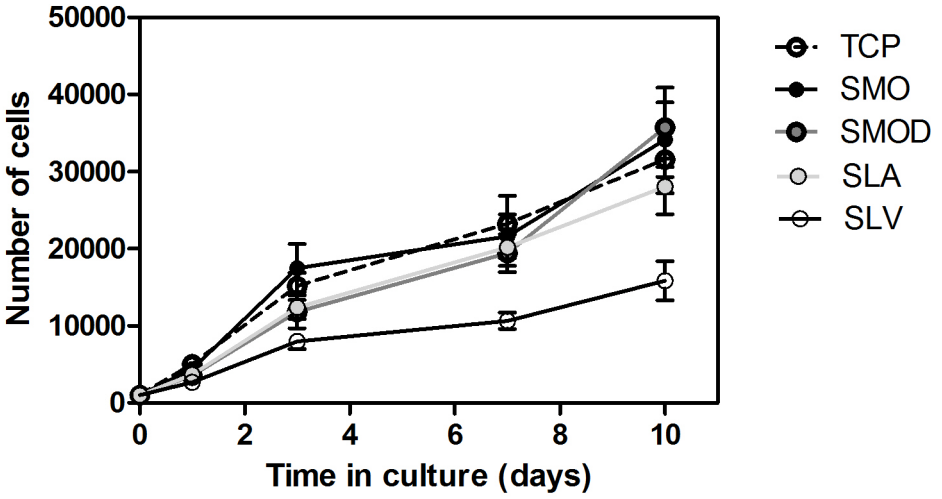

Figure 6.3: MSC selected population proliferation on TCP was serially assessed with AlamarBlue. Cells proliferated at a higher rate in the populations from TCP, smooth Ti (SMO and SMOd) and rough hydrophobic Ti (SLA). Cell proliferation was relatively restricted in the SLV selected cell population. Each bar represents mean ± 1 SD, N = 3, n = 3.

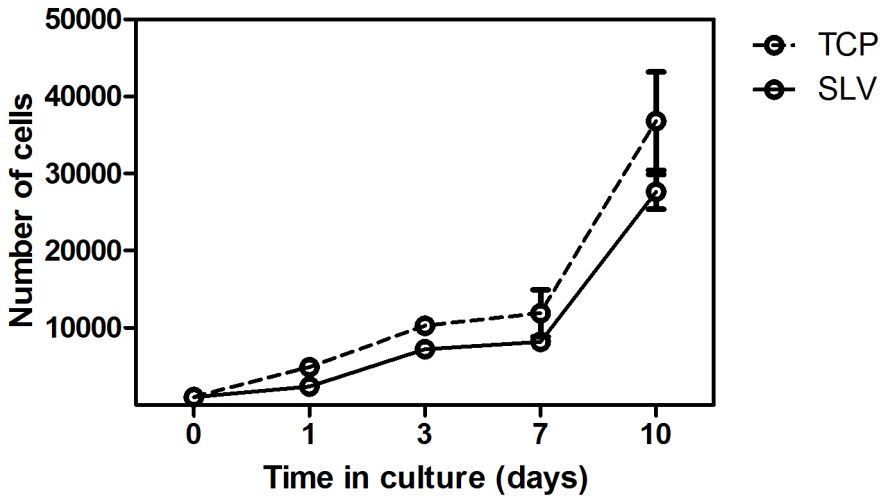

Figure 6.4: MSC proliferation on SLV. The SLV selected population is proliferating at a similar rate to it's proliferation on TCP (figure 6.3). The parent population's proliferation profile (labelled TCP) is reduced compared to that in figure 6.3, indicating a selective process has occurred following 24 hour contact with SLV. Each bar represents mean ± SD, N = 3, n =3.

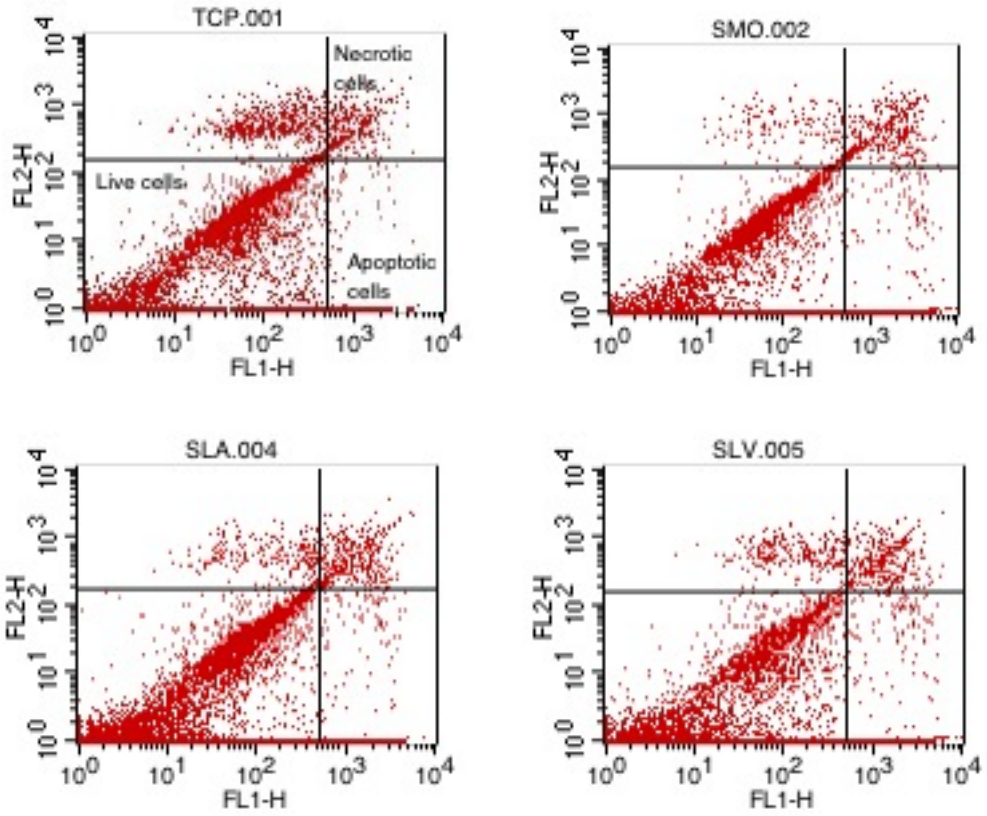

Figure 6.5: Scatter plots of the live/dead composition of MSC selected populations stained with Annexin V-FITC and PI. The proportion of apoptotic cells is significantly higher in the MSC population from SLV.

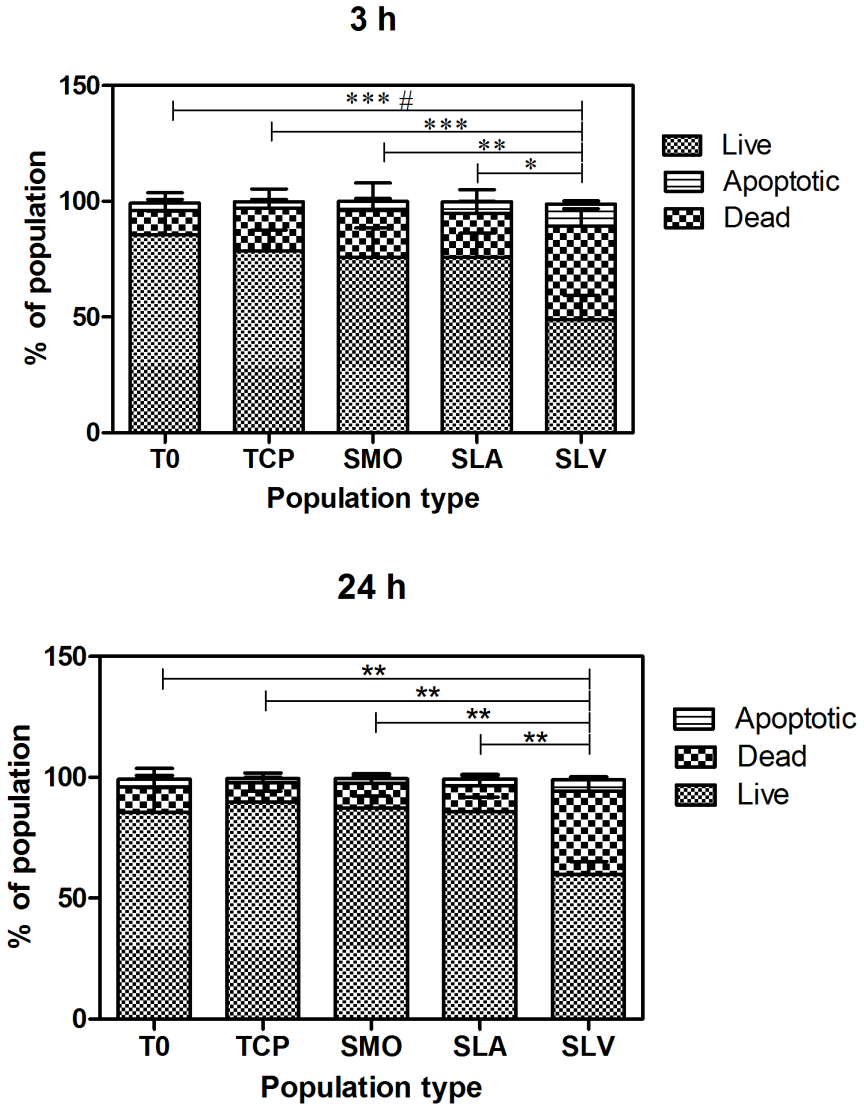

Figure 6.6: The early apoptosis events of MSC selected populations at 3 and 24 h. Measured from FACs analysis using Annexin V / PI staining. Each bar represents mean ± SD, n = 3. *** = $p \leq 0.001$ T0 & TCP vs SLV apoptosis. ** = $p \leq 0.01$ SMO vs SLV apoptosis. * = $p \leq 0.05$ SLA vs SLV apoptosis. # = $P \leq 0.05$ T0 vs SLV Dead. ## = $p \leq 0.01$ T0 & TCP vs SLV Dead. ## = $p \leq 0.01$ SMO vs SLV Dead. ## = $p \leq 0.01$ SLA vs SLV Dead.

a cell population selected on SLV and placing it back on this surface, I can suggest that a permanent change in the cell population composition has occurred due to the differential degree of apoptosis that is observed.

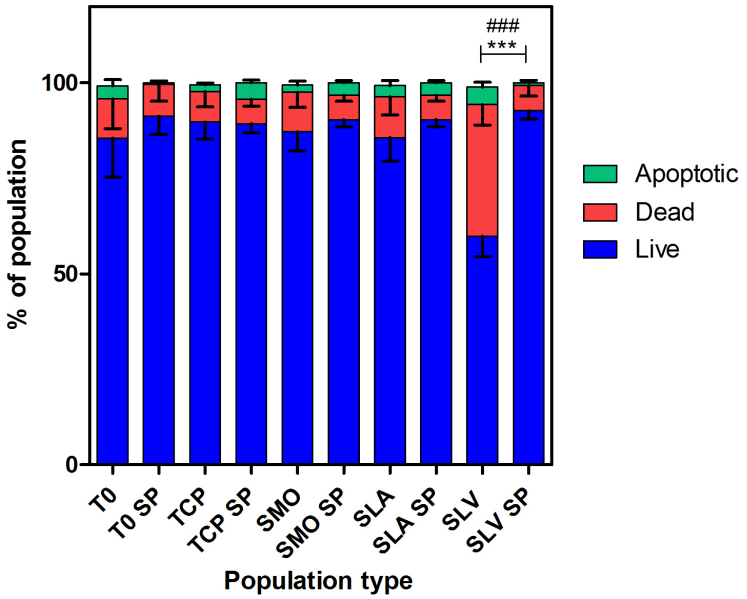

Figure 6.7: Comparison of apoptosis and necrosis in the selected population (SP) and the parent population in response to 24 h on Ti surfaces. The decrease in the amount of dead cells in the SP cultured on SLV compared to the parent population on SLV indicates the removal of a set of cells that are likely to undergo apoptosis has occurred. n = 3, ### = $p \leq 0.001$ apoptotic cells, *** = $p \leq 0.001$ dead.

6.3.3 Assessment of osteogenic mineralisation

The calcium mineralisation per cell was highest in the SLV population by day fourteen. The amount of calcium deposited per cell was significantly higher on days 14 and 21 than in the parent population of cells (figure 6.8).

The amount of collagen formed per cell was lowest in the SLV population at day 21 compared to the other Ti surfaces (figure 6.9). The SMO & SMOd results at day 21 showed the cells on the smooth surfaces were depositing the most collagen. This could result in a less well bonded bone structure to the surface. There was a slight peak in

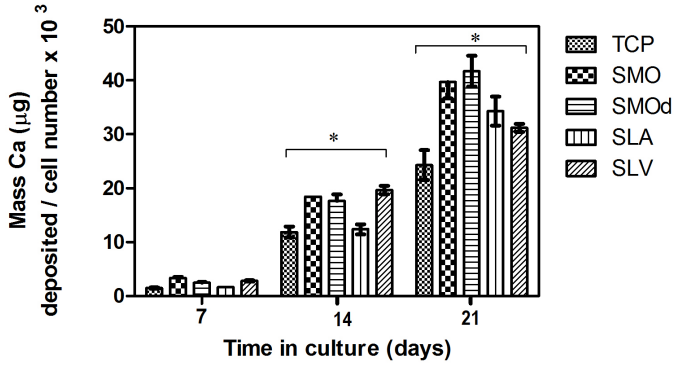

Figure 6.8: Ca^{2+} mineralisation per cell of MSC selected populations cultured in OM. Each bar represents mean ± SD, N = 3, n =3. * = $p \leq 0.05$, TCP 14 vs SLV 14 and TCP 21vs SLV 21.

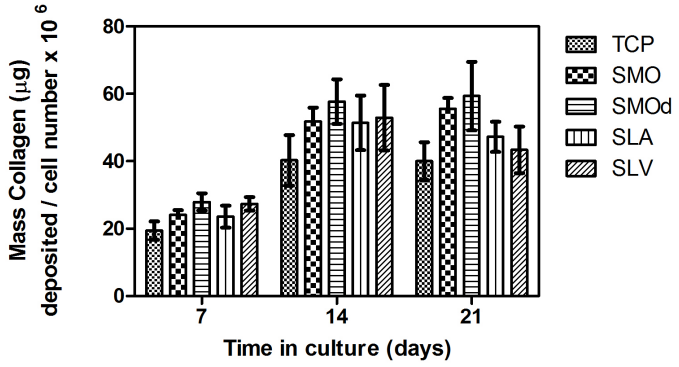

Figure 6.9: Collagen deposition per cell of MSC selected populations cultured in OM. Each bar represents mean ± SD, N = 3, n =3.

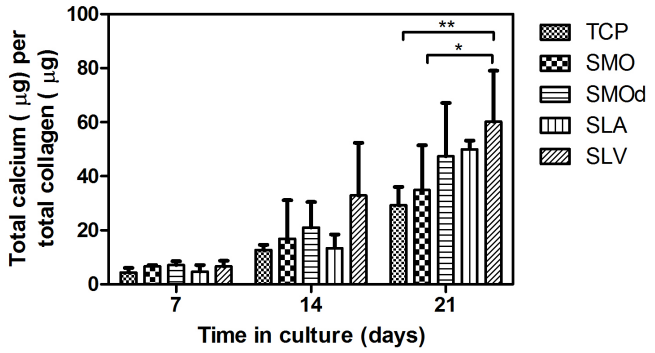

Figure 6.10: Ca^{2+} to collagen ECM ratio formed from each selected population. Each bar represents mean ± SD, N = 3, n =3. * = $p \leq 0.05$ SMO vs SLV 21, ** = $p \leq 0.01$, TCP vs SLV 21.

collagen deposition from the rough surface populations at day 14 which then decreases.

In a comparison between the relative ECM compositions deposited per cell for each selected population, a significantly higher calcium to collagen ratio was seen in the population selected on SLV at day 21 compared to smooth Ti selected populations (SMO) and the parent population from TCP (figure 6.10).

This provides an indication that a more mineralised type of bone likely to be formed from SLV selected populations.

6.3.4 Colony forming units

There were more colonies formed and they were significantly larger in diameter for the selected populations from SLV compared to the parent population (figures 6.11 & 6.12). Of 100 cells seeded per flask, over nine replicates, 19 % of the Parent Population cells formed colony units compared to 34.67 % of the SLV selected population. Colonies in the parent population had a mean surface area of 10.95 mm^2 with an average mean diameter of 3.57 mm. In the SLV population the mean surface area was 12.55 mm^2 with an average mean diameter of 4.04 mm ($p \leq 0.05$ TCP vs SLV).

6.3.5 CD cell surface marker analysis

There was a general trend for cell populations selected on modified Ti to show a reduced number of cells with specific stem cell surface CD markers compared to TCP (figure 6.13). SLV selected populations contained significant lower numbers of cells with CD105 and CD49d surface antigens compared to the parent population and other Ti surfaces.

6.3.6 Gene expression analysis of osteogenic genes

The osteogenic transcription factor Runx2 was significantly upregulated in MSCs that had been plated onto SLV titanium compared to the population that were plated onto

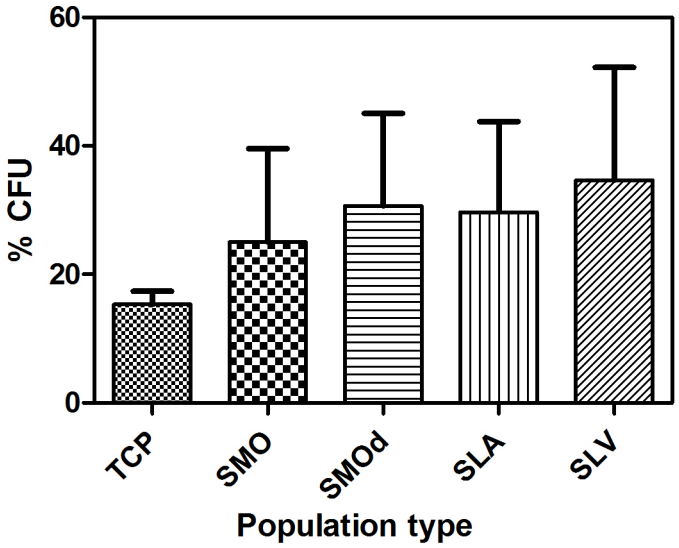

Figure 6.11: Histogram showing the percentage of CFUs for each selected population. There is a higher % of CFUs (ns) in the selected populations in comparison to the parent population from TCP. Each bar represents mean ± SEM, N = 3, n =3.

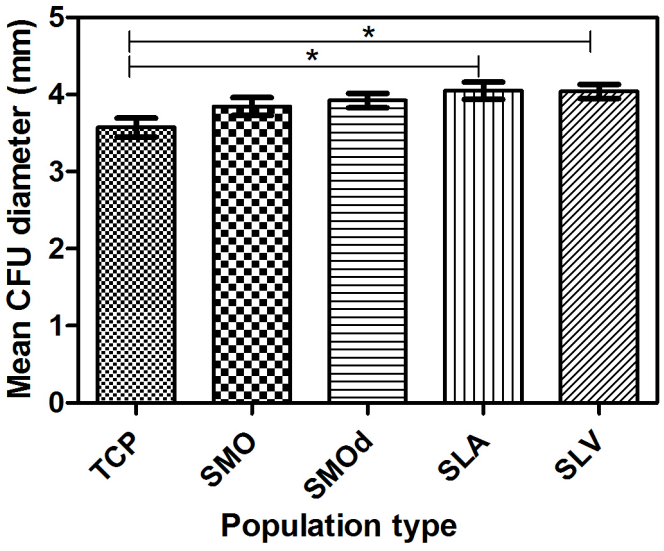

Figure 6.12: CFU mean diameter distribution in the selected populations. Each bar represents mean ± SEM, N = 3, n =3. * = $p \leq 0.05$, TCP vs SLA and TCP vs SLV.

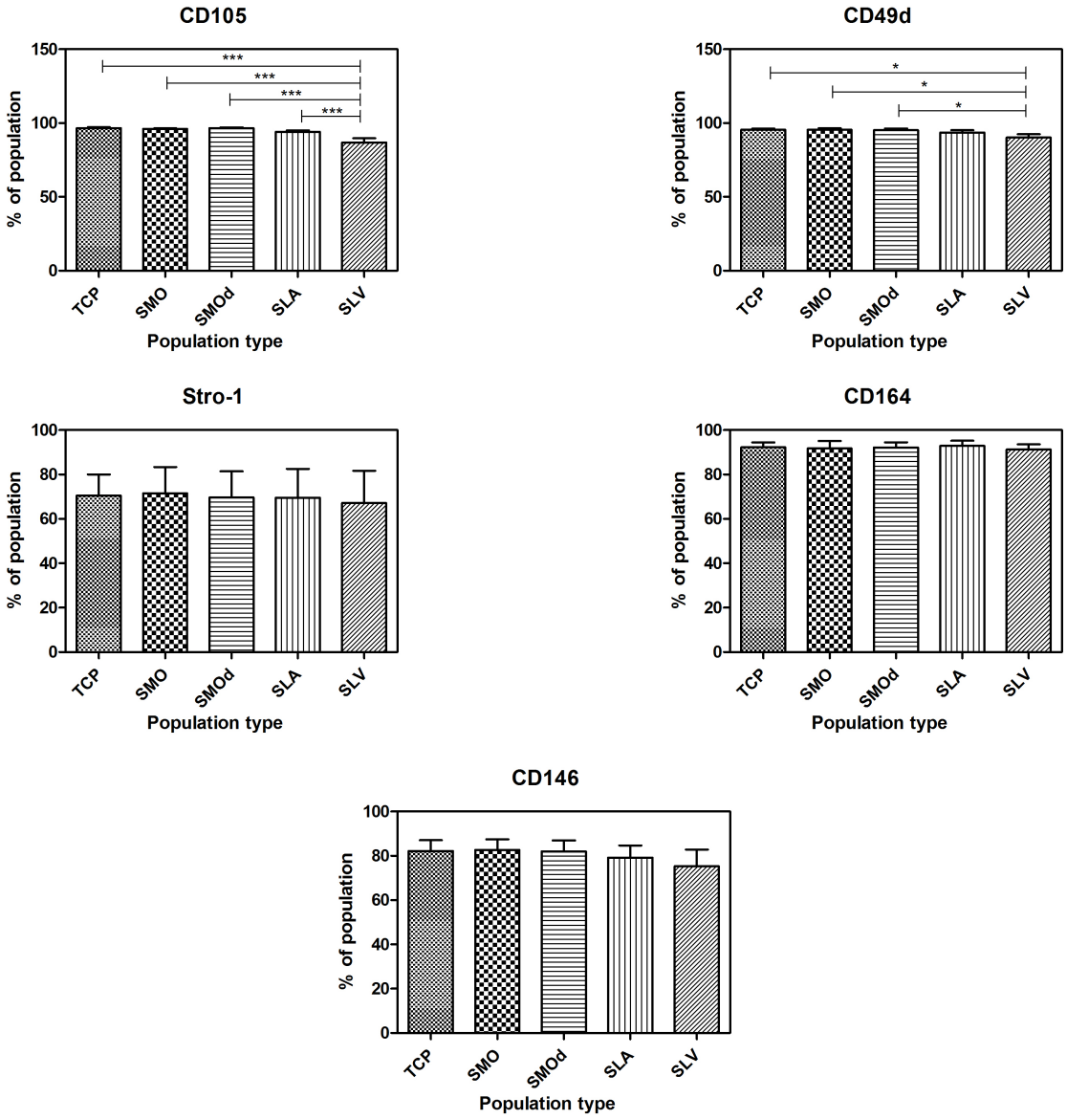

Figure 6.13: Changes to CD surface cell markers within selected populations. Each bar represents mean ± SD, n = 3, *** $p \leq 0.001$ SLV vs SLA, SMOd, SMO and TCP CD105, *$p \leq 0.05$ SLV vs SMOd, SMO, TCP CD49d.

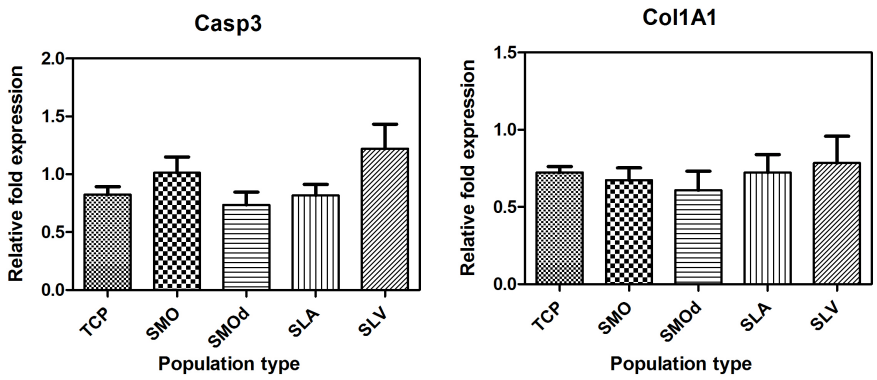

Figure 6.14: Relative fold changes in the expression of Casp3 and Col1A1 in MSC selected populations. Casp3 was transcribed at a higher level on SLV after 24 h exposure to the surface. The level of Col1A1 expression was not significantly different between the surfaces.

plastic, smooth, smooth modified and roughened Ti. OP was also upregulated to a significantly higher extent in the populations from both roughened Ti surfaces (SLA and SLV) compared to the parent population on TCP and the selected populations from smooth Ti (SMO, SMOd) (figure 6.15).

Cells from the SLV selected population had a 2.64 times higher expression value of Runx2 at T0 compared to the non-selected cells (PP T0). This suggests a greater osteogenic commitment potential exists within the SLV selected population. Within this selected population however, there was no significant Runx2 effect in response to subsequent exposure to Ti surfaces (figure 6.16). This suggests, again, that a permanent population change has occurred, rather than it being a simple reactionary response whenever the cells are in contact with the SLV surface.

A significantly higher OP response to Ti surfaces was seen in the SLV selected population, in particular, to SLA and SLV. It is interesting to note that this population responds to TCP, SMO and SMOd Ti in a similar way as the parent population's OP response to SLV (labelled ns, figure 6.17).

Col1A1 and Casp3 showed no significant differences between the selected and parent populations of MSCs (figure 6.18).

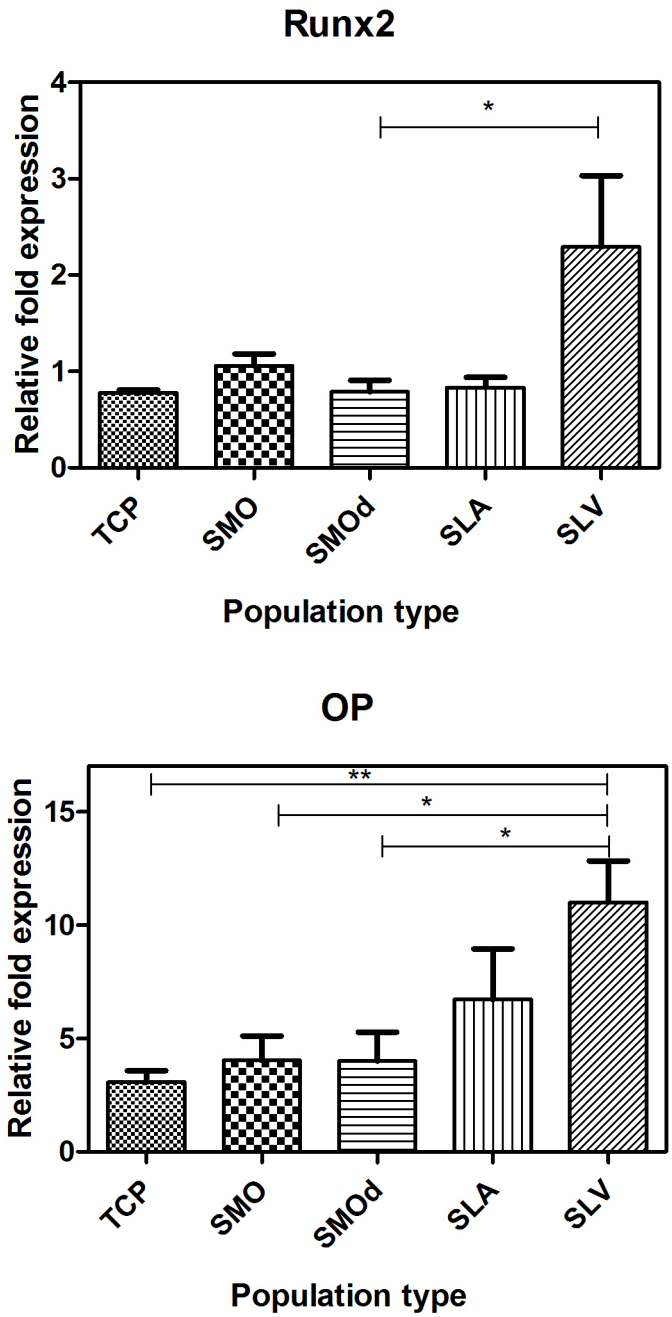

Figure 6.15: Relative fold changes in the expression of Runx2 and OP in MSCs selected populations. Runx2 was significantly up-regulated on rough hydrophilic surfaces (SLV) compared to smooth hydrophilic (SMOd). OP was significantly expressed at a higher fold by cells on SLV than smooth Ti surfaces and TCP. Each bar represents mean ± SEM, N =3, n =3. * = $p \leq 0.05$, SMO & SMOd vs SLV. ** = $p \leq 0.01$, TCP vs SLV.

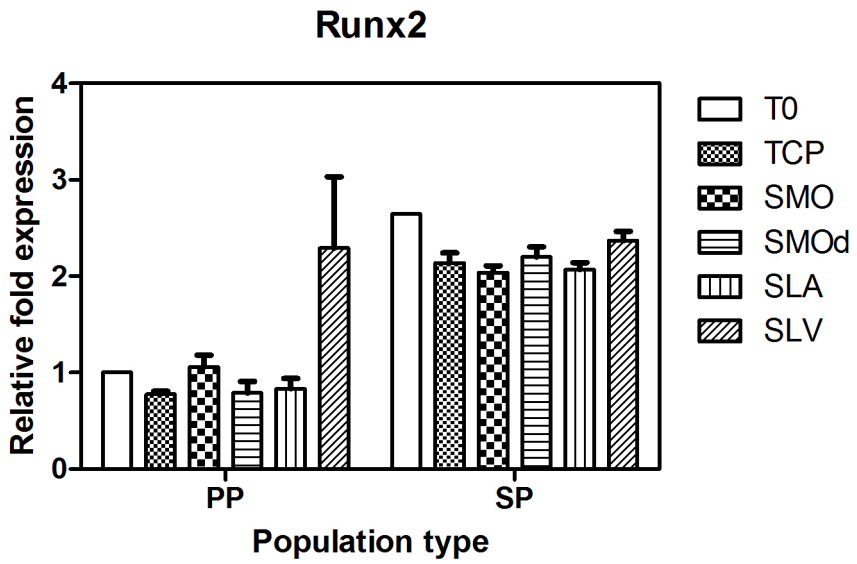

Figure 6.16: Comparison of Runx2 expression changes, in response to Ti surfaces, between the SLV selected and the parent populations. Each bar represents mean ± SEM, N =3, n =3. Expression values are normalised to the parent population T0 = 1.00.

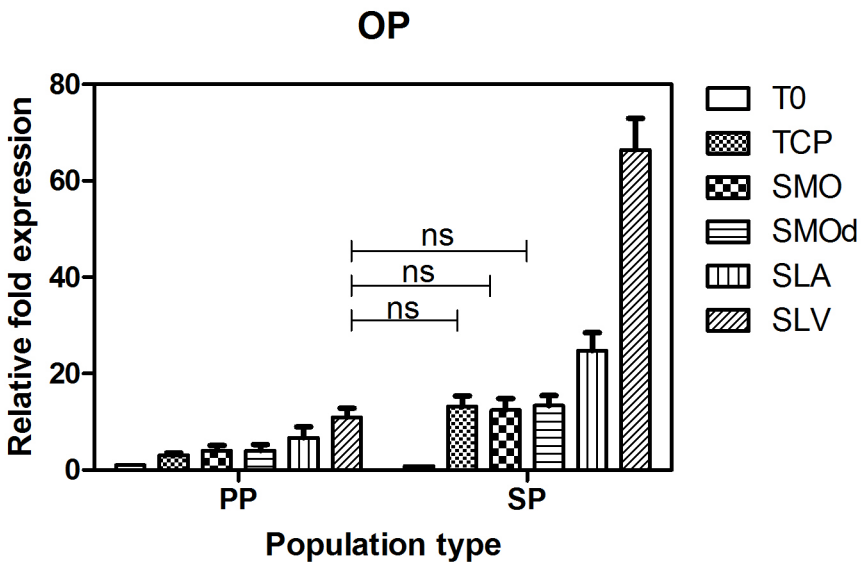

Figure 6.17: Comparison of OP expression changes, in response to Ti surfaces, between the SLV selected and the parent populations. Each bar represents mean ± SEM, N =3, n =3. Expression values are normalised to the parent population T0 = 1.00.

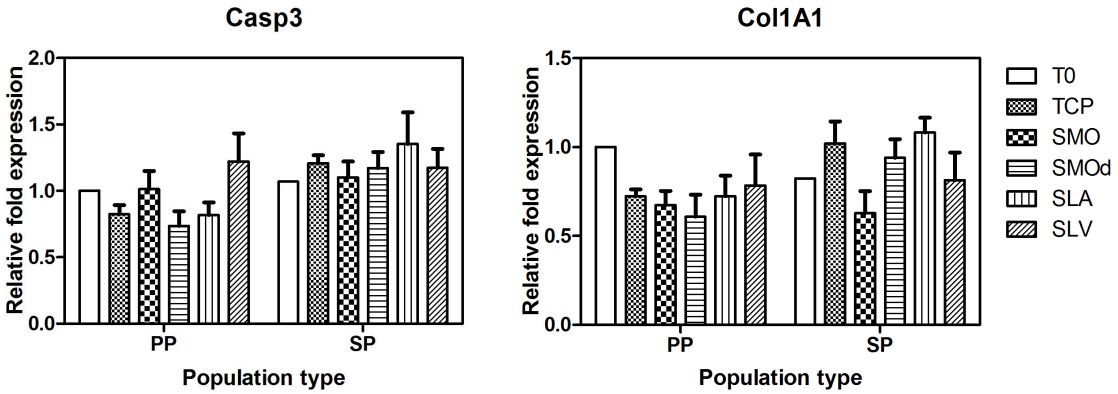

Figure 6.18: Comparison of Casp3 and Col1A1 expression changes, in response to Ti surfaces, between the SLV selected and the parent populations. Expression values are normalised to the parent population T0 = 1.00.

6.4 Conclusions

The properties that characterise stem cells are the ability to self renew and multipotency giving rise to at least three different lineages including osteocytes, adipocytes and chrondrocytes. In this investigation, we have used specific assays that can investigate the stem-like nature of the cells within selected populations from modified Ti surfaces based on these fundamental characteristics.

6.4.1 Cellular proliferation

Proliferation at each cell cycle is coupled to cell growth since mitotic rate is dependent on growth. Analysis on TCP, for cells plated onto modified Ti for 24 hours prior to the growth experiment, showed that the largest drop in proliferative capacity is seen in the selected population exposed to SLV. The proliferation rate was reduced by roughly one half in comparison to the parent population over a ten day period. The decrease in cell growth of the SLV selected population from the first day in culture on TCP suggests that the more proliferative cells, within the heterogeneous parent MSCs, have been selected out through apoptosis and necrosis following exposure to SLV titanium. This indicates a selective process has occurred following 24 h contact with SLV.

When both populations are placed on SLV a similar proliferation profile is seen in the selected and parent population (figure 6.4). There is a selective pressure exerted by the SLV surface acting on the parent population, which reduces its proliferation rate. However, the early proliferation in the selected population is the same as previously seen on TCP. There is no further selective pressure occurring to reduce the proliferation of this population.

It was hypothesised that the initial lag in proliferation detected on SLA and SLV was caused by cell death. In order to investigate this, cells were seeded on Ti discs and analysed for necrosis and apoptosis by flow cytometry after 3 and 24 hours.

6.4.2 The impact of Ti on cell death

The first response, following contact with Ti, is an increased occurrence of apoptosis and necrosis within the cell population. Apoptosis was a particularly significant event on SLV compared to TCP and smooth Ti ($p \leq 0.001$). The number of dead cells on SLV at 3 hours was significantly higher, indicating that the early apoptotic event was more severe with a correspondingly slower return to proliferative capacity. Apoptosis appears to be an initial response that doesn't occur throughout the whole time period that cells spend on the surface. This is deduced from the recovery in the amount of live cells seen on the Ti surfaces from 3 h to 24 h. There was a decrease in the significant difference in apoptotic cells across selected populations from 3 h to 24 h ($p \leq 0.001$ to $p \leq 0.01$ TCP, SMO vs SLV). The dead cells detach from the surface, and surviving cells beginning to proliferate and divide.

6.4.3 Assessment of osteogenic mineralisation

There were increased levels of Ca^{2+} mineralisation and collagen deposition per cell in the SLV selected population compared to the parent population when cultured in osteogenic medium (figure 6.8 & 6.9). This results in a significantly higher ECM calcium to collagen ratio deposited per cell (figure 6.10), indicating that a more mineralised bone structure is likely to be formed. This could lead to greater bone density and strength around the

implant. The cells in this population are more likely to differentiate into osteoblasts that are able to deposit a greater amount of mineral, increasing bone strength and reducing the amount of collagen that can result in unwanted loosening response surrounding the implant.

6.4.4 Colony forming units

The size distribution for the SLV population was skewed towards larger colonies. Colony size is likely to be a function of both cell size and cell spreading. Considering all the populations' CFUs were cultured on TC-treated flasks, the extent of cell spreading should remain identical. This indicates that the SLV population's cells tend to be larger than in the parent population.

6.4.5 CD cell surface marker analysis

The MSCs isolated from bone marrow were tested for a range of cell surface markers (performed by the Institute for Regenerative Medicine, Texas A & M Health Science Center, College of Medicine, USA). They were positive for markers known to be expressed on MSCs i.e $\geq$ 90 % of cells expressed CD29, CD49c. CD59, CD73a, CD90, CD105, CD147, CD166 and HLA-1. However, a distinct MSC-defining surface marker is far from being established (Pilz et al., 2011).

CD49d is known to have a role in cell-cell interactions as well as cell adhesion to the extracellular matrix. CD105 (endoglin) is a regulatory component of the transforming growth factor-β (TGF-β) receptor complex. It has been seen to have an important role in cardiovascular development and vascular remodelling. On a cellular level it mediates the response to TGF-β 1 and it has been proposed that endoglin is involved in the cytoskeletal organization affecting cell morphology and migration (Sanz-Rodriguez et al., 2004). CD146 was found by Pilz *et al.* to be expressed at a low level in placenta-derived MSCs (pMSCs) and that their corresponding osteogenic differentiation potential was weak (Pilz et al., 2011). By comparison, bone marrow derived MSCs expressed CD146 at high levels and

showed pronounced osteogenic differentiation potential. CD164 is known to function as a cell adhesion molecule. CD164 positive cells have been shown by Braun *et al.* to have a strong potential to differentiate into osteoblasts as characterised by von Kossa and Alizarin red S staining (Braun et al., 2010).

Our findings from CD surface markers, although in slight contrast to the CFU results, do not represent a major change in cell population composition. The small, but significant reduction in the number of CD105 and CD49d positive cells in the SLV population suggests that the cells may be different in character but this is not an indication of stem cell or osteogenic relevant changes. This is particularly the case for Stro-1, which was not significantly changed and where osteoprogenitor cells have been shown to have a positive link between surface expression of Stro-1 (Gronthos et al., 1994).

6.4.6 Gene expression analysis of osteogenic genes

The process of adaption begins with the genes. A new surface environment, such as titanium, provides a stimulus that either, turns specific genes on or off, or up or down-regulates genes already being expressed. By altering the expression of genes, the surface environment changes the rates on which the cell makes or breaks down specific proteins. For example, SLV surfaces turn on genes for the production of Casp3 proteins. More Casp3 proteins in the cells leads to programmed cell death (apoptosis). The cells and their transcription systems adapt over days and weeks to the cumulative effects of a new environment.

There was an up-regulation in the cell population from SLV for the transcription factor Runx2 and Casp3 that are responsible for osteogenic differentiation and apoptosis respectively, and OP, that is involved in calcium mineralisation. It appears that cell death plays a role in osseointegration by selecting out cells from a population and the remaining ones express the potential to differentiate into osteogenic cell lines.

Runx2 is a 'point of fate' transcription factor for differentiation which means it plays an important role in osteogenesis. Col1A1 codes for the major component of type 1 collagen,

OP is a protein involved in bone remodelling and Casp3 is involved in cell apoptosis. The upregulation of Runx2 and OP is an indication of commitment to the osteogenic lineage in populations following exposure to roughened, hydrophilic titanium. Col1A1 is a widely expressed gene in the formation of collagen and, although it promotes osteoblast differentiation, its expression is not changed much in any of the selected populations compared to the parent population. The upregulation of Casp3 indicates that higher apoptosis occurred within cells of the SLV compared to the parent population.

The gene expression data confirms the results from the mineralisation and proliferation experiments. It suggests that there are increased levels of cell death in response to SLV and increased differentiation along the osteogenic pathway. It appears that the roughness and hydrophilicity of the surface has an impact on both reducing the cell number and also directing the remaining MSCs towards the osteogenic lineage.

The higher gene expression of Runx2 at T0 within the selected population, indicates either that more cells are expressing this gene or that the same number of cells are expressing but at a higher level (figure 6.16). It is possible that a more concentrated population of osteogenic cells has been formed from exposure to SLV, following cell death of those that are non-osteogenic. This selected population has no further Runx2 response to modified Ti surfaces which indicates that the gene cannot be upregulated further. This provides additional evidence that the population change is permanent. It is possible that the differentiation event has occurred and cannot be repeated by further exposure to SLV. These cells, however, are pre-programmed to respond osteogenically and they produce much higher levels of OP in response to a surface, such as on TCP. OP expression is then further increased in response to Ti surfaces, in particular SLA and SLV, which are known to trigger associated mineralisation (figure 6.17).

It is likely that a sub-population of stem cells which differentiate to form osteogenic cells on SLV has been enriched. This is supported both by the increased amount of osteogenic differentiation seen in the SLV selected population after 14 days in OM and the increase in apoptosis. The stem cells with osteogenic potential survive on rough hydrophilic Ti and the remainder of the stem cells are removed from the population.

6.4.7 Significance of findings

The phenotypic characteristics of hMSCs are affected by substrate material, topography and chemistry. A summary of the significant experimental findings on the surface effects of modified Ti on MSCs is presented here;

- Enrichment of osteoblast-like cells from a heterogeneous population of MSCs can be achieved through adhesion to roughened, hydrophilic titanium and subsequent expansion.
- It was seen that a population expanded following adhesion to SLV is enriched in cells that are capable of differentiation along the osteogenic lineage with some loss in proliferative capacity.
- On contact with the surface MSC numbers are reduced. There are increased levels of necrosis and apoptosis and results in the removal any non-multipotent cells.
- The process leads to the formation of a more concentrated population of cells that possess a natural tendency to differentiate along the osteogenic lineage.
- Cellular mineralisation characteristics are highly altered in cells selected from different Ti surface types. Furthermore, the significant changes to selected cell populations occur from substrate roughened-topography and wettability.
- A greater ECM calcium to collagen ratios is formed from MSCs selected from rough, hydrophilic Ti. These cells are likely to lead to the formation of bone structures that are more mineralised and stronger. In addition, collagen interfaces that are thinner and less likely to cause loosening of the implant. This creates a more reliable implant with a longer life cycle.
- SLV has been shown to provide a way of selecting osteogenic stem cells from a population of mesenchymal origin. This indicates a feasibility of osteogenic enrichment by modified Ti for repair and regeneration.

Rough, hydrophilic SLV Ti is a surface that induces a high amount of cell death and is also a surface that has shown superior osseointegration in bone implants *in vivo* (Rupp et al., 2006). Cell death may play a role in osseointegration by selecting the cells from a heterogeneous population that have the potential to differentiate into osteogenic cell lines.

The differentiation experiments show that there is a significantly increased concentration of cells within the SLV population that are able to mineralise in osteogenic media. Exposure of MSCs to modified Ti surfaces selects cells that are able to differentiate along the osteogenic cell line. The parent population contains a mixture of cell types some of which are more immature 'stem cell' like populations. These are the cells that are more likely to undergo apoptosis on exposure to Ti surfaces and they are less likely to posses the potential to differentiate along the osteogenic pathway. Fukiage *et al.*, found that within a group of 100 MSC clones only five of them showed tri-directional differentiation, 78 clones showed the potential to differentiate into either one or two lineages and 17 clones did not show any differentiation potential (Fukiage et al., 2008). This study has shown that contact with SLV Ti increases apoptosis, possibly among the clones that cannot differentiate along the osteogenic route and any of the other tri-directional routes of differentiation. The resultant progeny of stem cell division may have lost the capacity for self-renewal, but differentiate preferentially yielding osteoblast like cells i.e. more osteogenic cells survive leading to an enriched population. This process is likely to enter into a series of terminal divisions finally yielding an organised tissue such as in bone growth or repair. This presents the possibility of clinical applications for bone regeneration such as scaffold seeding *in vitro* with an osteogenic fraction of MSCs.

When hBMSCs cell are cultured *in vitro*, the adherent population tends to form colonies of spindle-shaped cells, and thus are termed colony-forming units (CFUs). This property can be used for studying the stem-cell like nature of MSCs in culture. The ability of an adherent population to form colonies of spindle-shaped cells is a phenotypic characteristic of MSCs. I would expect a population enriched in stem cells to display an increased ability of forming colonies and this was seen from the higher % of CFUs produced from the populations selected on SLV. It appears that the number of 'stem' like cells has been

increased by contact with the Ti surface.

The selection effect is largely due to the chemistry of the surface since SLA and SLV have identical surface topographies.

SMO and SMOd populations showed no significant differences between them, in gene expression or calcium mineralisation, indicating that hydrophilicity of the surface alone is not responsible for the enrichment effect. SLV surfaces have the biggest effect on the cell population indicating that a combination of both roughness and hydrophilicity is required.

Chapter 7

A comparison of bone marrow-derived and adipose-derived stem cell osteogenesis

7.1 Introduction

The use of bone marrow derived stem cells has already shown promising results in enhancing bone regeneration around Ti implants. The idea of using alternative stem cell sources in bone regeneration applications originates from the discovery that muscle tissue contained cells that could differentiated along the osteogenic lineage (Bosch et al., 2000). There are various advantages with this source of MSCs such as lowered risks associated with bone marrow harvest. Cell harvesting of MSCs from bone marrow is an invasive and painful procedure with significant associated morbidity. The bone marrow aspirates containing MSCs are also comprised of white blood cells, and by removing these suggests that the patient's immune system is decreased. However, the small volumes involved in

removing bone marrow aspirates mean that this effect is not likely to have a considered impact on the patient's health unless in extreme cases. Another potential source of MSCs is adipose tissue, aspirates from which have the advantage of not decreasing the level of the immune system. In addition, adipose tissue is considered to be easily accessible and plentiful.

Two types of stem cells are believed to occur within bone marrow stoma; the hematopoietic and mesenchymal stem cells. The former gives rise to blood progenitor cells while the latter is believed to instigate the lifelong replenishment of mesenchymal tissue precursors.

The osteoblast originates from an adult mesenchymal stem cell through the tightly regulated process of osteogenic differentiation. This is a sequential process, loosely depicted in figure 7.1, in which an MSC initially commits to a pre-osteoblastic progenitor phase that is characterised by the expression of collagen type 1, osteonectin and alkaline phosphatase and exhibiting high proliferation rates. This leads to the pre-mature phase of a functional osteoblast that produces osteoid tissue. Osteoid formation is divisible into two phases; collagen matrix elaboration, and pre-calcification assembly. Initially collagen fibril subunits are translated and secreted by the cells into the ECM where they align and polymerise to form a fibrillar collagenous scaffold. The cells produce alkaline phosphatase and matrix components including bone sialoproteins (BSP types 1 and 2), and osteocalcin amongst the many. In the pre-mineralisation phase of a maturing osteoblast, these components are secreted by means of budding cytoplasmic-membrane vesicles (50-200 nm size) that attach at points in the osteoid to form calcium nucleation sites. In the matrix bound vesicles, Ca^{2+} ions and inorganic phosphate are combined to form octa-calcium phosphate, which then penetrates the vesicle membrane, and combines with the highly osteogenic microenvironment to grow into hydroxylapatite (Anderson et al., 2005; Chen et al., 2008).

Figure 7.1 shows the various stages that an MSC undergoes to transform into a committed osteoblast and later osteocyte as well as indicating the crucial regulatory transcription factors. The process of phenotypic commitment is instigated by the upregulation of Runx2. A number of transcription factors, shown in the top boxes, regulate the effects of Runx2;

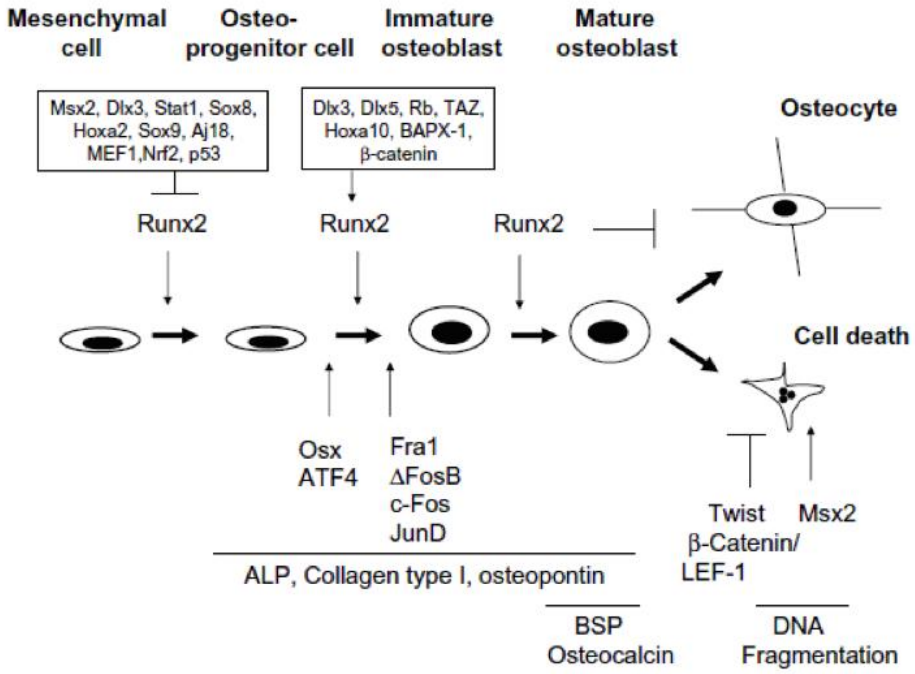

Figure 7.1: Osteogenic differentiation to osteoblast and osteocyte. (Maries, 2008).

inhibitory on left, and stimulatory on right. Runx2 decreases Sox9 (chondrocytic) and PPAR-gamma (adipocytic) differentiation and promotes the expression of Col1A1, ALP, OP, BSP1, BSP2, fibronectin and thrombospondin that form the ECM. Soluble factors that include fibroblast growth factors, transforming growth factor β subtypes; and osteoclastic regulators are also secreted. The MSC transforms from a highly proliferative osteoprogenitor in the beginning to a quiescent state of an osteocyte (Maries, 2008).

There are many genes involved in part of the complex regulatory systems that are essential in osteoblast differentiation. Some of the osteogenesis-related genes that were observed to be significant in this study, and their roles, are described below.

Runx2 is considered to be a central control transcription factor within the osteoblast phenotype. It has a role in the regulation of a broad spectrum of osteoblast specific genes. The Runx2 transcript has the ability to facilitate numerous osteogenic signalling pathways. Factors produced as a consequence of these extracellular signals are recruited by Runx2-specific subnuclear domains, producing a multi-component transcriptional complex. This

multi-component complex interacts with the promotor region of most major osteoblast specific genes (Banerjee et al., 2001; Prince et al., 2001; Sudhakar et al., 2001a,b).

Alkaline phosphatase (ALP) is an ubiquitous cellular protein, although numerous studies have indicated that it may act as an early indicator of cellular activity and differentiation. ALP protein levels have been shown to be upregulated in response to mechanical force application. mRNA levels have been shown to increase post stimulation with steady increases in the progression of osteoblastic differentiation (Shui et al., 2003; Qi et al., 2003).

Osterix (Osx) is an osteoblast specific gene that is thought to act in the regulation of other osteoblast genes such as; OP, BSP and Col1A1. Osx may act downstream or independently of Runx2 (Nakashima et al., 2002; Harada et al., 1999; Komori et al., 1997).

Fibroblast growth factor has been detected in numerous cell types (Carreras et al., 2001). A decrease in the transcription levels encured a significant decrease in bone mass and formation (Coffin et al., 1995). Other osteoblastic genes known to be stimulated by the action of FGF2 include BSP and matrix MMPI (Shimizu-Sasaki et al., 2001).

Collagen 1 is an important component of bone extra-cellular matrix. It forms connections with cell surface integrins and other ECM proteins. The protein is not bone specific as it has been identified in numerous unrelated cell types. The protein has been shown to play a role in cell adhesion, proliferation and differentiation of the osteoblast phenotype. Upregulation has been observed in response to a number of different methods of *in vitro* force applications with mRNA levels increasing after 2 days post stimulation (Jagodzinski et al., 2004; Pavlin and Gluhak-Heinrich, 2001). Therefore, the protein seems to play a key role within the osteoblast phenotype and can be considered as an early indicator of osteoblastic differentiation.

OP is a secreted adhesive glycophosphoprotein and it has been detected in bone, teeth, kidneys, epithelial lining, blood plasma and breast milk. As a consequence, it cannot be considered bone specific but it has a role in important bone related functions. Within bone tissue it functions in cell adhesion, migration and survival (Standal et al., 2004a,b).

Numerous studies have reported the upregulation of OP after the application of *in vitro* artificial mechanical forces (You et al., 2001; Toma et al., 1997).

Bone Sialoprotein (BSP) is a highly sulfated, phosphorylated, and glycosylated protein present within bone matrix. The protein is characterised by an ability to bind to hydroxyapatite through polyglutamic acid sequences and to mediate cell attachment through an RGD sequence (Oldberg et al., 1988; Ogata et al., 1995; Ganss et al., 1999). The presence of BSP within the ECM and its ability to nucleate hydroxyapatite crystal formation, indicates a potential role in the early mineralisation of osteoblasts (Hunter and Goldberg, 1993). In addition, it has been suggested that BSP is mitogenic for pre-osteoblast cells and it can promote their differentiation into mature osteoblasts, ultimately stimulating bone mineralisation (Zhou et al., 1995).

The term MSC (mesenchymal stromal cell) is used throughout this chapter to describe the cell fraction that is derived from bone marrow. Bone marrow-derived stromal cells (hBMSCs) are composed of two types of cell; the hematopoietic cells (HSCs) and the MSCs which are characterised as spindle shaped cells that are adherent to plastic. The MSCs are the bone marrow-derived cell fraction that are compared and contrasted here to adipose-derived stromal cells (ADSCs).

This chapter is presented in two sections. The first section compares the osteogenic differentiation potential between the unaltered, parent populations of MSCs and ADSCs. The osteogenic mineralisation and gene regulation in osteogenic media was assessed using Alizarin Red S staining and analysis using a 46 gene qPCR microarray respectively. An experimental matrix is shown in figure 7.2.

The second section repeats the experimental matrix described in chapter 6 (figure 6.1) to investigate the effect of modified Ti on modulating the osteogenic behaviour of selected ADSC populations. The assays used were those which presented key information on the osteogenic potential of selected cells. These were Ca^{2+} / collagen analysis of osteogenic mineralisation, expression of selected osteogenic genes and the effect of apoptosis using FACs analysis of live / dead cell staining. The results were analysed and graphically

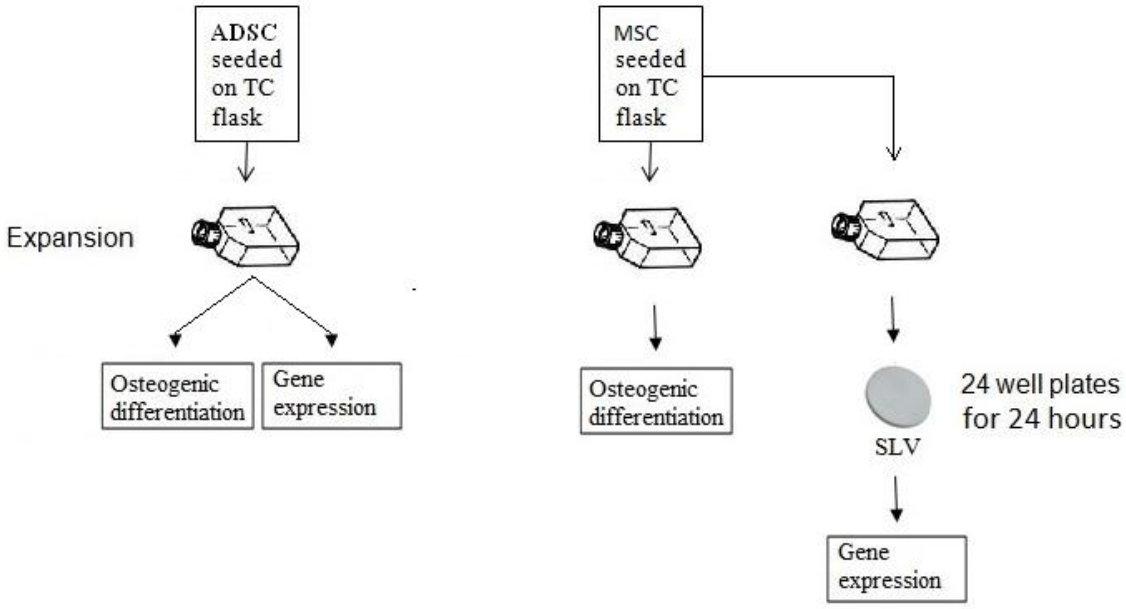

Figure 7.2: Experimental matrix to compare the osteogenic behaviour of MSCs and ADSCs by osteogenic differentiation using Alizarin Red S and gene expression of 46 osteogenic genes.

compered here with those obtained for MSCs in chapter 6, sections 3.3, 3.6 and 3.2.

7.2 Osteogenic differences in MSC and ADSC parent populations

7.2.1 Materials and methods

Osteogenic mineralisation

The semi-quantitative Alizarin Red S dye method was used to assess cellular mineralisation of ADSCs and MSCs parent populations at 7, 14, 21 and 28 d post seeding on TCP. Cells were seeded at a density of $\sim$ 1.25 x 10^4 cells mL^{-1} in 24 well plates and cultured in osteogenic medium using complete growth medium as a control. Cultures were maintained with bi-weekly medium changes. The method for the staining is detailed in chapter 2,

section 8.1.

qPCR array of osteogenic genes

A qPCR array was designed in the format of 2x48 genes in a 96 well plate and procured from AppliedBiosystems (Cat. #1908085). A table of the genes used and their functions is provided in appendix A. Two of the genes were housekeeping genes: GAPDH and 18S ribosomal RNA.

The number of microarray osteogenic plates available for the gene analysis was limited to six. It was therefore decided to analyse the osteogenic effect of ADSCs in OM and MSCs on Ti in GM, in order to maximise the data gathered. This was with the view of providing the most complete picture of the genetic effects caused by both chemical and Ti surface stimulus, rather than providing a direct comparison of ADSC and MSC expression. Genes involved in late osteogenesis were observed in ADSCs in osteogenic media after 14 d in culture, using growth media as a control. For Ti surface effects, genes from MSCs involved in early osteogenesis were observed in response to Ti surfaces after 24 h in growth media using tissue culture plastic (TCP) as a control surface. The gene expression levels were analysed in ADSCs and MSCs from three patients, N=3. The samples were not patient matched and only one replicate per patient was performed. The methods used in this experiment are detailed in chapter 2, section 7.

7.2.2 Results and discussion

Osteogenic mineralisation

Mineralisation was assessed by Alizarin Red S staining and semi-quantification by extraction of the stain and measurement using a spectrophotometer. The results showed that the mineralisation increased over the 4 week time period for both MSCs and ADSCs (Alizarin Red S-Calcium complex staining of ADSCs is shown in figure 7.3). There were higher levels of mineral in all cell types in osteogenic media compared to control media at all

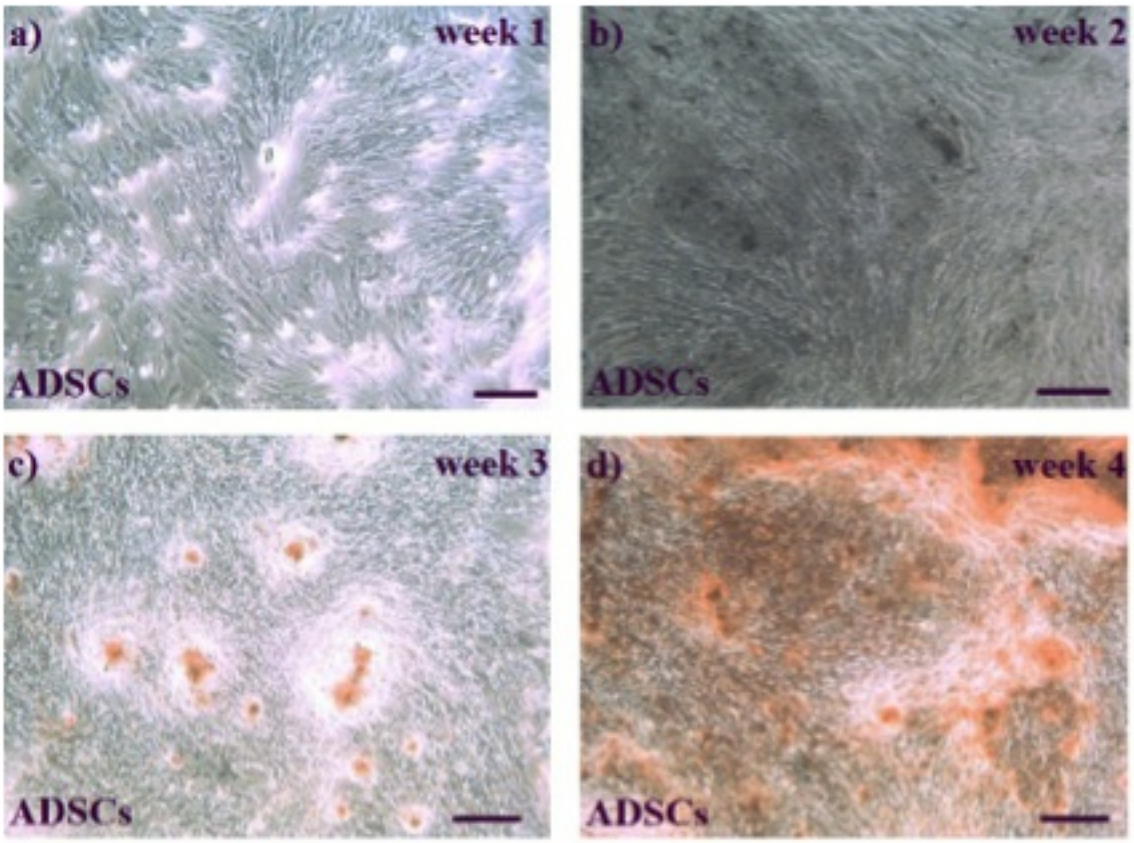

Figure 7.3: Alizarin Red S-Calcium staining of ADSCs over a 4 week assay in OM. ADSCs at a) 1 week b) 2 weeks c) 3 weeks d) 4 weeks. Calcium nodules were visible after 2 weeks in osteogenic media. There was a large increase in mineralisation between weeks 3 and 4. Experiments were performed on three patients in triplicate (N=3, n=3). Magnification x40. Scale bars represent 250 μm.

time points. The highest level of mineralisation was seen in MSCs in osteogenic media. At week 4, the mineralisation of MSCs in osteogenic media was significantly higher than the mineralisation of ADSCs in osteogenic media ($p \leq 0.001$).

Mineralisation showed the largest change induced by osteogenic media occurred between weeks 3 and 4. This was highly significant ($p \leq 0.001$) for MSCs and by ANOVA with Bonferroni adjustments and significant ($p \leq 0.05$) for ADSCs. At every time point for the MSCs there was a significantly higher level of mineralisation in osteogenic media compared to control media ($p \leq 0.05$) by paired t-test. For ADSCs, the level of mineralisation in

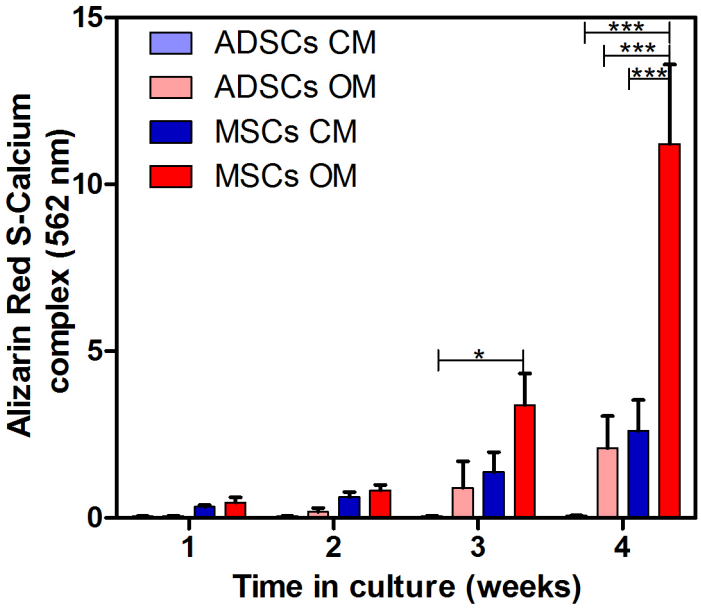

Figure 7.4: Alizarin Red S-Calcium quantification comparison of ADSCs and MSCs in OM and control growth media (CM). Each bar represents mean ± SEM, n = 3, N = 3. *** = P $\leq$ 0.001 MSCs at week 4 in OM vs MSCs in CM and ADSCs in OM and CM. * = P $\leq$ 0.05 MSCs at week 3 in OM vs ADSCs in CM.

osteogenic media compared to control media was not significant at week 1 but significant at weeks 2, 3 and 4 ($p \leq 0.05$) (figure 7.4). For MSCs in control media there was an increase in mineralisation over time. For MSCs this increase was significantly higher for mineralisation in control media between weeks 3 and 4 ($p \leq 0.001$). There was a no significant increase in mineralisation of ADSCs in control media on TCP. Mineralisation appeared to be relatively consistent between MSC donors, with a 2-fold difference between the highest and lowest levels detected at week 4. There was more donor dependent mineralisation activity observed for ADSCs. There was a 3.5-fold difference in the ADSCs from the donor that expressed the most mineralisation and the ADSCs that expressed the least at week 4.

qPCR array of osteogenic genes

Osteogenic gene expression in ADSCs was analysed at 2 weeks in osteogenic media by qPCR array and standardised with the gene expression in growth media as a control.

Gene expression in MSCs in response to modified Ti was analysed after 24 hours on the surface and standardised with the gene expression from cells on TCP as a control.

Up and down regulation

Stem cell types respond to and differentiate into osteoblast precursor cells as a consequence of two main factors: chemical and physical stress application, activating specific signalling pathways.

MSCs on Ti and ADSCs in osteogenic media showed an increased level of Runt-related transcription factor 2 (Runx2). Data from Xiao *et al.* indicated that Runx2 mRNA levels were constitutively expressed, with a lack of correlation between mRNA levels and the acquisition of the osteoblast phenotype (Xiao et al., 2002). However, it should also be noted that the Runx2 gene is not osteoblast specific and its expression has been observed in the early development of numerous cell types such as chrondrocyte differentiation (Lian et al., 1989). The observation that Runx2 is upregulated on Ti surfaces at an early stage in the absence of other osteogenic cues could indicate that modified Ti surfaces provide a powerful stimulus to osteogenesis.

ALP activity of ADSCs in osteogenic media was significantly higher than in control media. ADSCs, in particular, have demonstrated here an upregulation of both Runx2 and ALP in osteogenic media, which could indicate that ALP is directly stimulated by Runx2. MSCs on Ti for 24 hours showed a downregulation of ALP. By acting downstream from Runx2, ALP may not be directly initiated in the early stage of osteogenesis.

A gene that was consistently upregulated across both cell types was PTH1R, which is considered to be an osteoblastic marker since it is expressed in osteoblasts (Ahlstrom

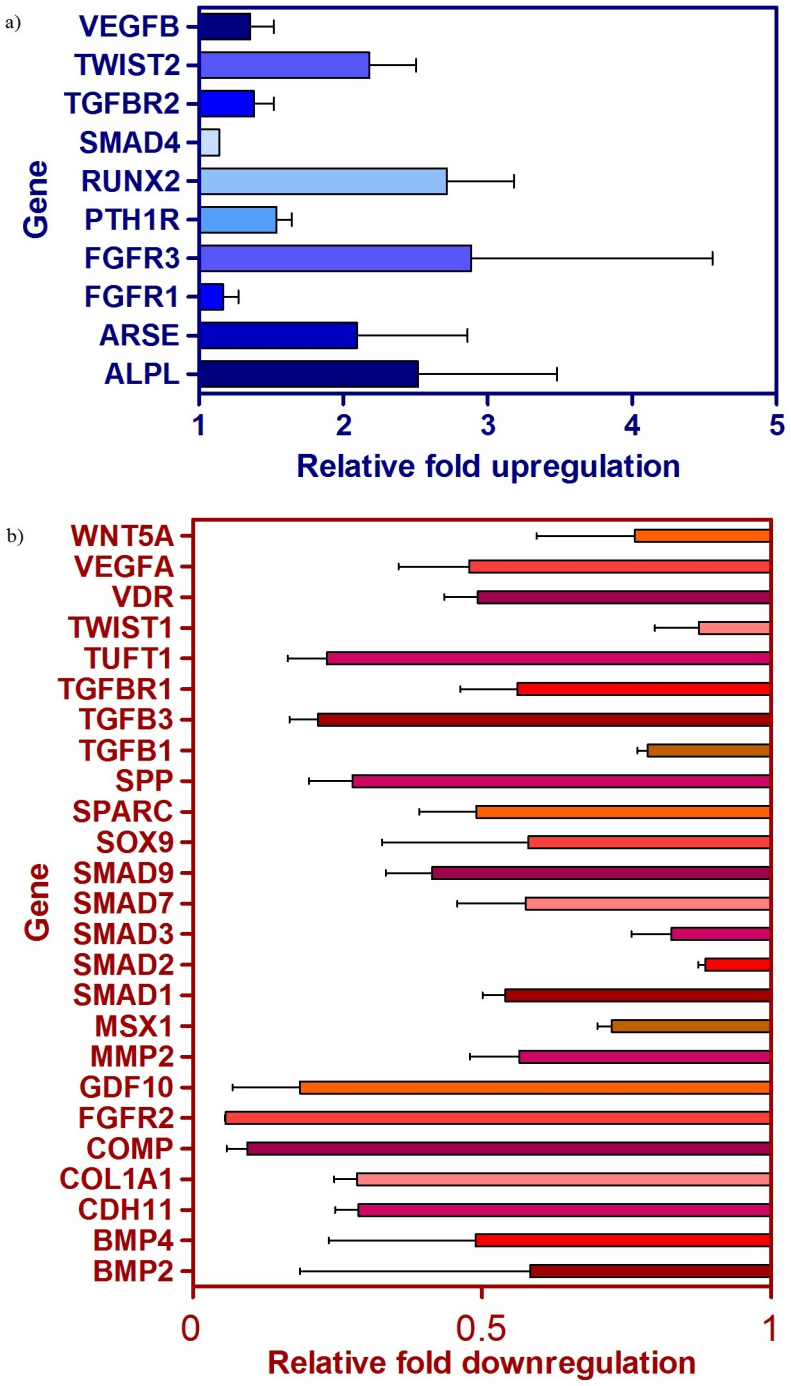

Figure 7.5: Upregulation and downregulation of genes in ADSCs after 2 weeks in OM compared to control growth media (GM). Experiments were performed on three donors (n=3). Each bar represents mean ± SEM.

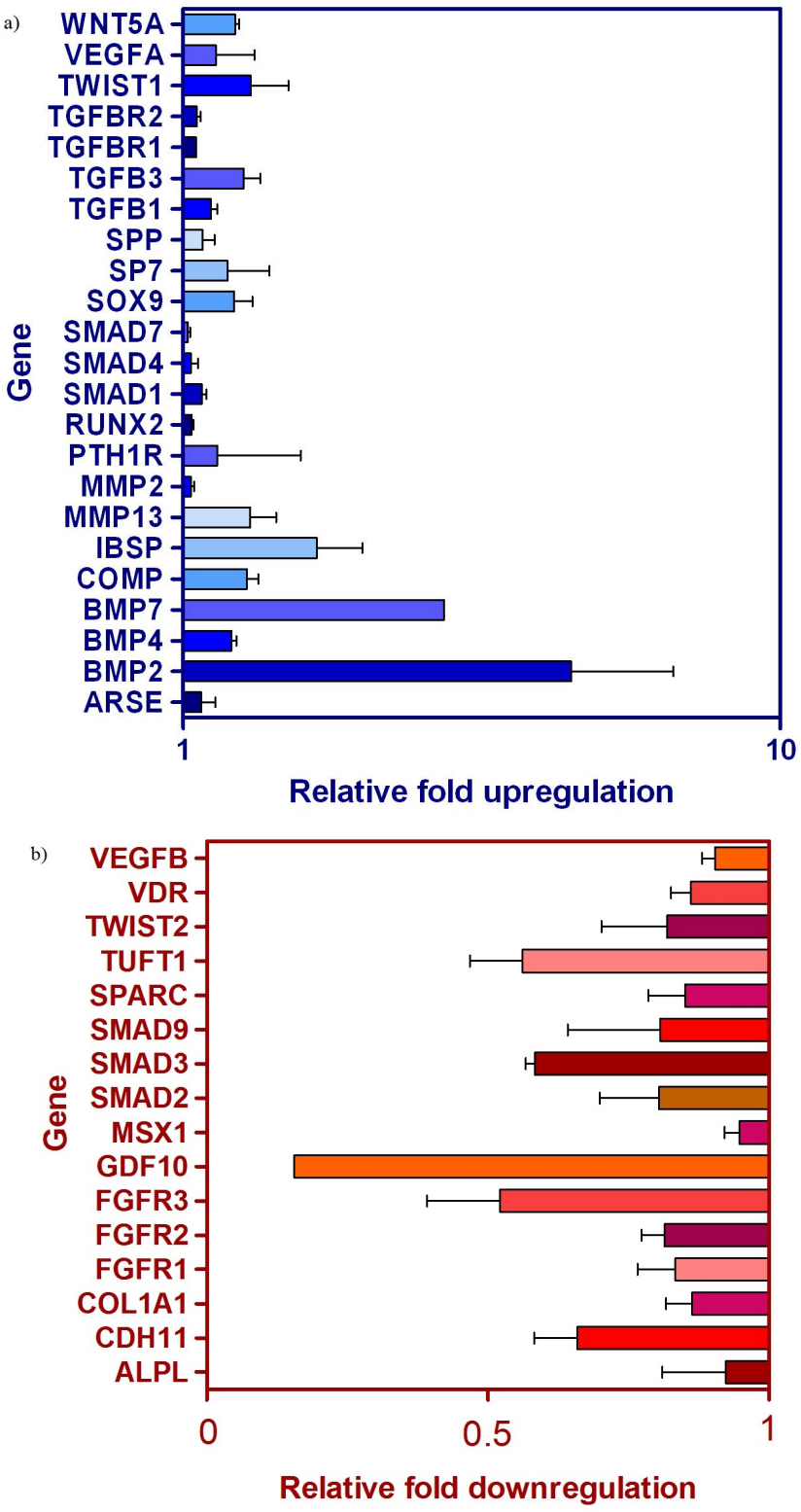

Figure 7.6: Upregulation and downregulation of genes in MSCs after 24 h on SLV Ti in GM compared to cells from TCP. Experiments were performed on three donors (n=3). Each bar represents mean ± SEM.

et al., 2009). It plays an important role in the control of osteoblast intracellular calcium levels (Qi et al., 2003). The upregulation of PTH1R has been described as a combined event with the upregulation of both Runx2 and ALP (Ahlstrom et al., 2009).

The two TWIST factors, 1 and 2, were inconsistent in their expression. It is believed that the expression of TWIST1 and TWIST2 maintains cells in an osteoprogenitor or pre-osteoblast-like state to prevent premature osteoblast development (Lee et al., 2000; Bialek et al., 2004). It has been suggested that the expression must be decreased to allow Runx2 expression to increase. ADSCs at 2 weeks and MSCs on Ti showed a downregulation of at least one TWIST factor, suggesting a more committed osteoblast-like stage. An upregulation of Runx2 is likely to follow.

For ADSCs in osteogenic media, VEGFA and BMP-2 genes were downregulated. The impact of VEGFA on osteogenesis is controversial. Studies by Mayer *et al.* have claimed that VEGFA can enhance osteogenesis whilst studies by Shonmeyer *et al.* suggest it can have a suppressive effect (Mayer et al., 2005; Schonmeyr et al., 2010). In the experiments, VEGFA suppressed the mRNA expression of BMP-2.

For MSCs on Ti, BMP-2 was the most upregulated gene whilst VEGFA was low. This possibly indicates that VEGFA expression was reduced allowing the upregulation of BMP-2 and committing the cells towards the osteogenic phenotype. BMP-2 induces osteogenesis by binding to BMP receptors, which then phosphorylate transcription factors, such as Smad1 that forms a complex with Smad4 in the nucleus. Hence it is logical that when BMP-2 is downregulated Smad1 and Smad4 are also downregulated. Both BMPs, BMP-2 and BMP-4 and the BMP related protein GDF10 were seen to be downregulated in all cell types in osteogenic media as were the cascade of Smad proteins. In the case of MSCs on Ti, a highly upregulated BMP-2 expression should allow the upregulation of Smad1 and Smad4 proteins to follow and this was observed.

VDR is also known to have dual effects: in early osteogenic cultures it can inhibit osteogenic differentiation and in later cultures it can promote osteogenic differentiation. The downregulation of these genes in ADSCs and MSCs could indicate a fully committed

phenotype.

Sox9 was downregulated in ADSCs in OM which indicates that osteogenesis could be ongoing. It is expected that Sox9 is downregulated and Runx2 is upregulated during osteogenesis. Sox9 is mostly known as a marker for chondrogenesis, and research has shown it can suppress bone formation (Hattori et al., 2010). Upregulation of Sox9 was observed, however, in both MSCs and ADSCs on Ti (figure 7.14).

Two genes that encode mineralisation proteins, OP and MSX1 were downregulated in ADSCs in OM (Kazanecki et al., 2007). MSX1 was downregulated in MSCs on Ti. These two proteins are considered markers for terminal differentiation (Blin-Wakkach et al., 2001). The downregulation is not unexpected as at 2 weeks in osteogenic media and 24 h on Ti, ADSCs and MSCs appear to be in a state of early mineralisation only.

Secreted protein acidic cysteine-rich (SPARC) is also a gene that encodes protein that characterises late or terminal differentiation and this was downregulated in ADSCs in OM. MSCs on Ti, however, show slight up and downregulation of OP and MSX1 respectively, indicating a much earlier mineralisation event than ADSCs in response to osteogenic media.

7.2.3 Conclusions

Assessment of osteogenic mineralisation

An increase in mineralisation, primarily by chemical induction of osteogenisis through the presence of dexamethasone in osteogenic media and measured by Alizarin Red S-Calcium assay, could be observed for all cell types tested. The highest degree of mineralisation was seen in MSCs. The highest Alizarin Red S-Calcium complex spectroscopic adsorption value, λ 562 nm, was $\sim$ 12 at week 4. The lowest value of mineralisaion was observed in ADSCs in GM, weeks 1-4 (adsorption, λ 562 nm $\sim$ 2).

Bone marrow-derived MSCs were observed to mineralise in control media on TCP (figure

7.4). This demonstrates a natural tendency towards osteogenic differentiation without any external chemical or physical stimulus. The observation that there was no significant increase in mineralisation of ADSCs in control media on TCP, indicates that there is a lower potential for mineralisation in their natural state. Osteogenic differentiation has been demonstrated here in ADSCs, although it appears chemical or physical induction is strongly required.

Gene expression analysis of osteogenic genes

The gene expression of 46 genes involved in osteogenic differentiation was analysed by qPCR following cells cultured in osteogenic media. Up or down regulation was measured against cells cultured for the same time in control media. Many genes were observed to be downregulated in osteogenic media, especially in ADSCs. At 2 weeks it was not expected that late markers such as BSP or OP to be upregulated, however, early markers such as Cadherin-11 (CDH11) were also downregulated. Liu *et al.* 2008 also found that Runx2 and Col1A1 were not upregulated by 2 weeks in osteogenic media in MSCs (Liu et al., 2008). One explanation could be that the TWIST factors 1 and 2 regulate Runx2 by preventing premature differentiation. The role of CDH11 in human osteogenesis is not clear. In mice it has been proven to promote cancer metastasis in bone (Chu et al., 2008).

The gene effects that govern most cellular processes are highly complex. It is important that throughout osteogenic differentiation there is constant cross talk between signals (Katoh, 2008). The differences observed in stem cell gene expression may be due to different times in the osteogenic differentiation process. It is likely that many of the genes that were downregulated at 2 weeks may already have been upregulated at a prior moment in time or would be upregulated at a later time point in the process. TWIST gene expression has dropped in both ADSCs and MSCs and Runx2 expression is consequently seen to be upregulated.

There was a higher donor variability in gene expression in ADSCs than MSCs. MSCs from different donors showed reasonably consistent gene regulation. This could be due

to the ADSCs being part of a more heterogeneous population, containing fewer cells in terms of their osteogenic capacity than MSCs. This is expected since bone-marrow derived MSCs have their niche in bone and ADSCs have theirs in fatty tissue. It was shown that ADSC gene responses to osteogenesis and mineralisation capacity were similar, despite their anatomical origin. In regard to their relative ease of patient harvesting compared to MSCs, this potential in osteogenic differentiation capacity could lead to a new treatment modes. However, it is clear that MSCs have a higher osteogenic capacity compared to ADSCs in terms of PTH1R and BMP expression and, in particular, the degree of mineralisation observed.

7.3 Stem cell selection of MSCs and ADSCs on modified Ti

7.3.1 Materials and methods

Osteogenic differentiation

A quantitative estimate of ECM deposited calcium for MSC and ADSC selected populations in OM on TCPs was conducted at 7, 14 and 21 days post seeding with the QuantiChrom Calcium assay. MSCs and ADSCs were seeded at a density of $\sim$ 1.25 x 10^4 cells mL^{-1} in OM in 24 well plates on TCP, SMO, SMOd, SLA and SLV. The method is described in chapter 2, section 8.2. Cell numbers were estimated with the AlamarBlue assay described in chapter 2, section 6.1.

The total ECM collagen formed by MSC and ADSC selected populations was measured at 7, 14 and 21 days post seeding using the Sircol method. MSCs and ADSCs were seeded at a density of $\sim$ 1.25 x 10^4 cells mL^{-1} in OM in 24 well plates on TCP, SMO, SMOd, SLA and SLV. Total collagen was not measurable within a single well due to small quantities formed by the small number of cells. Hence, collagen isolates from three replicates of a sample were pooled, concentrated with kit reagents and then stained, to obtain a measure. The method is described in chapter 2, section 9. Cell numbers were estimated with the

AlamarBlue assay as described in chapter 2, section 6.1.

A total Ca^{2+} to total collagen ECM ratio was calculated from the Ca^{2+} and collagen data. The total amount of calcium present in the three wells was summed from the values of the three replicates (μg). This value was divided by the total quantity of collagen (μg) assayed in a replica pool of triplicates. This ratio was separately calculated for each of the three donors; their mean later calculated and plotted in a bar chart.

The impact of Ti on cell death

Flow cytometry was used to evaluate the apoptosis and necrosis rates of MSC and ADSC selected populations. MSCs and ADSCs were seeded at a density of $\sim$ 2 x 10^4 cells mL^{-1} in GM on TCP, SMO, SLA and SLV. The selected populations were harvested from modified Ti surfaces and TCP and then stained with Annexin V and Propidium Iodide (PI) for FACs analysis. The method is detailed in chapter 2, section 10.1.

Gene expression analysis of individual osteogenic genes

Transcriptional changes in MSCs and ADSCs selected populations were analysed from a set of genes associated with different parameters of osteogenic differentiation using qPCR. The set of genes were investigated due to their important roles in osteogenic differentiation and were Runx2, OP, Col1A1, Casp3, Sox9. For this experiment, MSCs and ADSCs were seeded at a density of $\sim$ 2 x 10^4 cells mL^{-1} in GM on TCP, SMO, SMOd SLA and SLV. Analyses were conducted at 24 h post seeding by lysing monolayers, extracting total RNA and converting it to cDNA, followed by qPCR with Taqman probes. The methods used in this experiment are detailed in chapter 2, section 7.

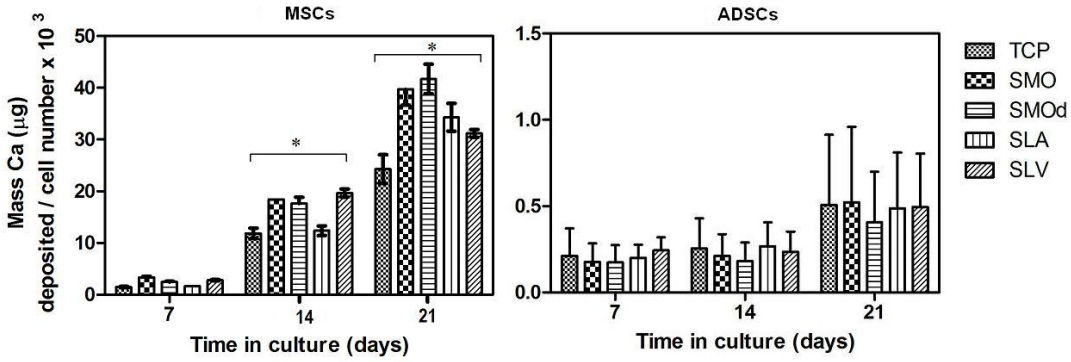

Figure 7.7: Comparison of MSC and ADSC selected population Ca^{2+} mineralisation per cell cultured in OM.

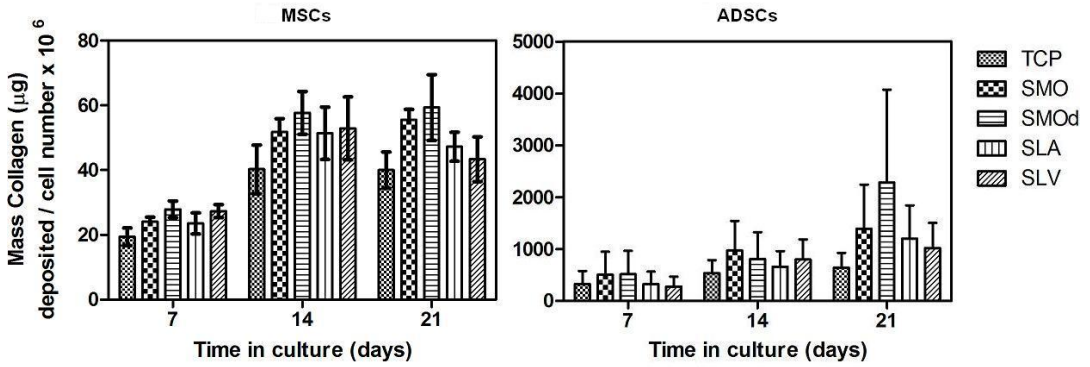

Figure 7.8: Comparison of MSC and ADSC selected population collagen deposition per cell cultured in OM.

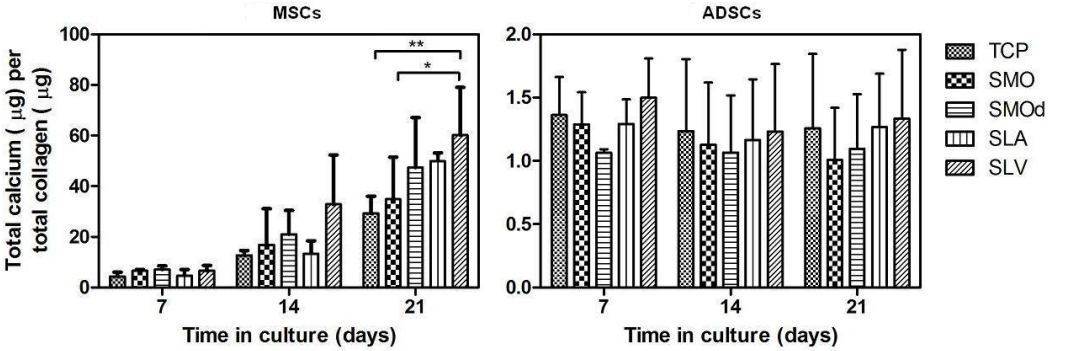

Figure 7.9: Comparison of MSC and ADSC calcium to collagen extra cellular matrix (ECM) ratio formed from each selected population cultured in OM. Each bar represents mean ± SD, N = 3, n =3.

7.3.2 Results and discussion

Osteogenic differentiation

The quantity of calcium deposited per cell number was evaluated at 7, 14 and 21 d post seeding. The results of this analysis are illustrated in figure 7.7. The results show that the amount of Ca^{2+} deposited per cell increases over the 21 day assay by a factor of ~ 20 for MSCs ($p \leq 0.01$ SLV vs TCP at 14 and 21 d). The amount of Ca^{2+} deposited per cell is a magnitude lower for the ADSC selected populations. The ADSC selected cells had deposited an increased amount of Ca^{2+} by 21 d, but there was no significant difference in the levels of Ca^{2+} at 7, 14 or 21 d seen between any of the selected ADSC populations.

The total amount of collagen formed in triplicates was normalized to total cell numbers across three wells to evaluate differences in the synthesis of this ECM component. The results obtained are illustrated in figure 7.8. The analysis indicates that cells harvested from all ADSC surfaces initially formed a significantly higher level of collagen at 7 d compared to MSCs. The amount of collagen deposited by the ADSC parent population (TCP) at 7 d was ~ 15 times greater than that deposited by MSC parent population. The amount of collagen deposited progressively increased through the remainder of the experiment for both MSCs and ADSCs. There was seen to be more collagen deposition from the ADSC SMOd selected population compared to other ADSC Ti selected populations at day 21. There was a high degree of sample variation so any differences between selected populations were not significant.

A ratio of total calcium per collagen was calculated from data collected in figure 7.7 and figure 7.8. The ratio is graphically represented in figure 7.9. ADSCs show that the Ti surfaces have induced a similar amount of calcification per collagen compared to TCP at all time points examined. MSCs show a steady increase in the Ca^{2+} to collagen ECM ratio over 21 d, which was significantly higher in the SLV selected populations compared to SMO and TCP populations ($p \leq 0.01$, $p \leq 0.05$). The Ca^{2+} to collagen ECM ratio in the SLV selected MSC population at 21 d was ~ 40 times higher than in the ADSC populations (figure 7.9). This is attributable to the higher rate of collagen synthesis and

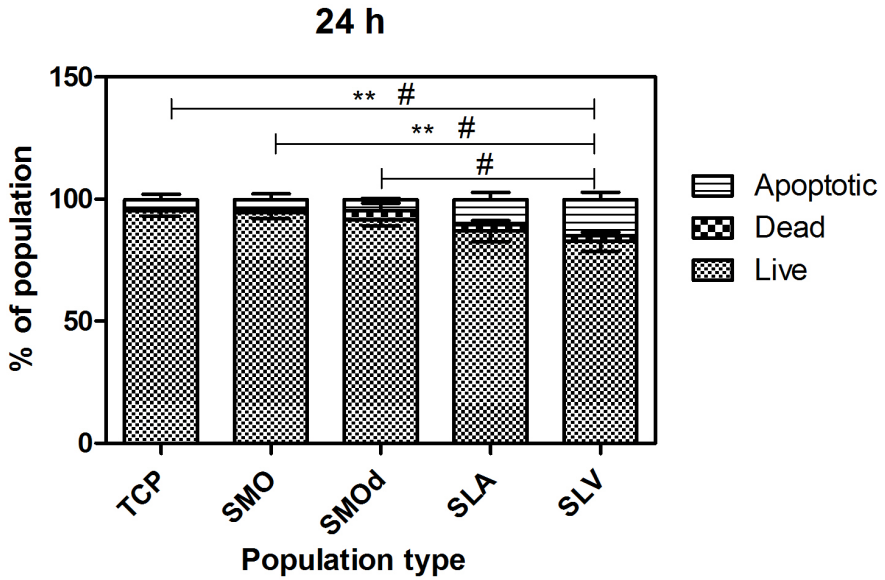

Figure 7.10: The early apoptosis events of ADSCs at 24 h on Ti surfaces in GM, measured from FACs analysis using Annexin V / PI Live/Dead assay. Each bar represents mean ± SD, n = 3.** = P ≤ 0.01 Dead. # = P ≤ 0.05 Apoptosis.

lower rate of calcium deposition from ADSCs.

The impact of Ti on cell death

Cells on SLV underwent significantly more apoptosis and necrosis (# = P ≤ 0.05 Apoptosis. ** = P ≤ 0.01 Dead) compared with other smooth (SMO and SMOd) Ti surfaces and TCP (figure 7.10). There was a clear pattern of the impact of surfaces, where SLA had less apoptosis and necrosis than SLV, but more than SMO and TCP. There was no significant difference between apoptosis and necrosis on TCP and smooth Ti.

Mesenchymal stem cells from TCP, SMO and SLV underwent a significantly higher degree of necrosis (* = p ≤ 0.05. *** = p ≤ 0.001 dead) compared to ADSCs from the same surfaces (figure 7.11). The difference in this apoptosis response to Ti could be due to the difference in cellular origins which reflects the heterogenicity of the populations. Based on the observations that MSCs undergo a greater degree of both apoptosis and mineralisation in response to SLV, I can establish a link between these observations and the osteogenic

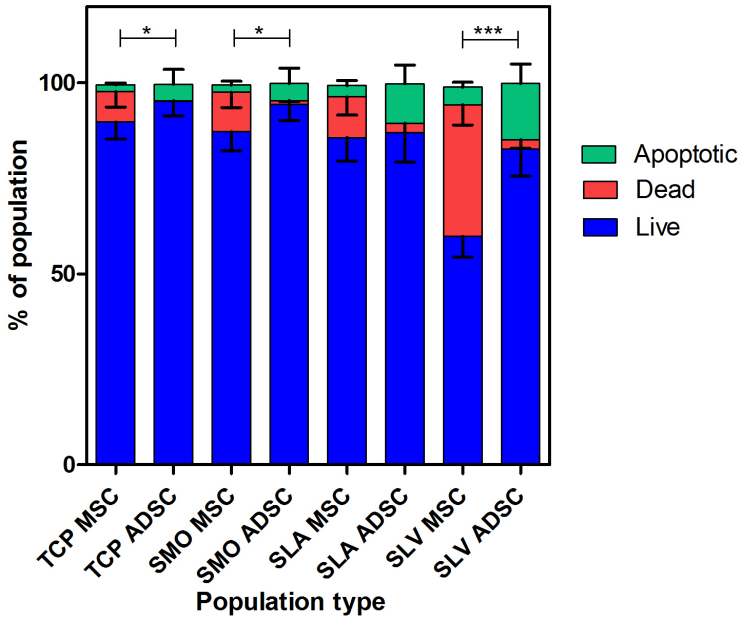

Figure 7.11: Comparison of apoptosis and necrosis in ADSC and MSC selected populations. n = 3, *** = $p \leq 0.001$ dead cells, * = $p \leq 0.05$ dead.

potential of the repective cell types. Since both apoptosis and mineralisation are seen to be higher in the MSC populations, this suggests that hBMSCs may be more heterogeneous and the resulting SLV selected population possesses cells with a greater osteogenic differentiation potential compared to SLV selected ADSCs.

Gene expression analysis of individual osteogenic genes

The expression of Runx2, OP, Col1A1 and Casp3 was not significantly different between the ADSC selected populations (figure 7.12). ADSCs on SLV showed a significantly higher expression of Sox9 compared to TCP ($p \leq 0.05$).

The gene expression at T0 was measured in the unaltered ADSC and MSC populations and can be considered to be a background level of expression of these genes without any surface stimulus. MSCs showed a higher background expression of Runx2, OP and Col1A1 than ADSCs. In addition, MSCs populations selected on SLV Ti showed a significant

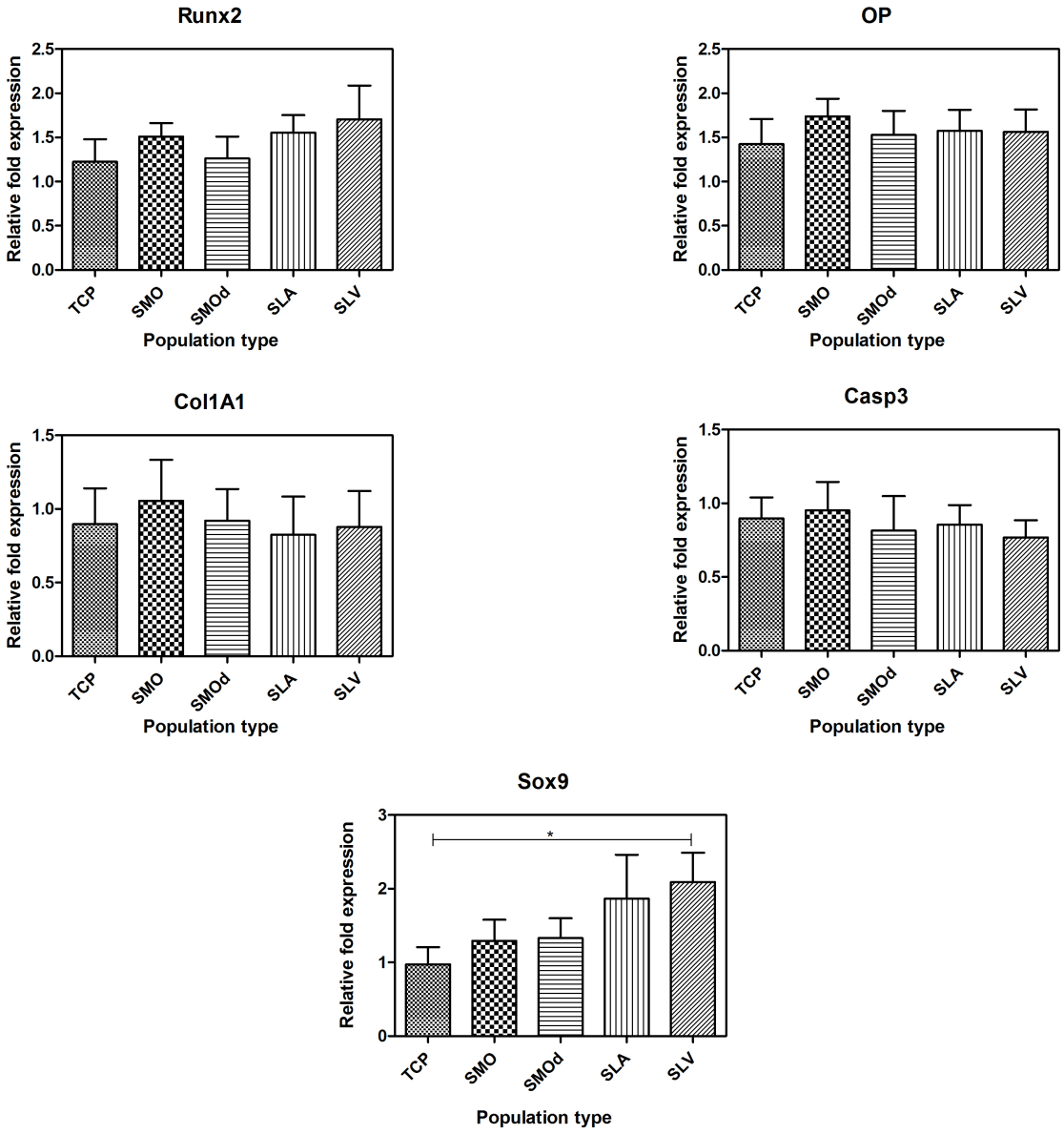

Figure 7.12: Relative fold changes in the expression of Runx2, OP, Col1A1, Casp3 and Sox9 in ADSC selected populations. Each bar represents mean ± SD, N = 3, n =3. Sox9 * = $p \leq 0.05$ SLV vs TCP

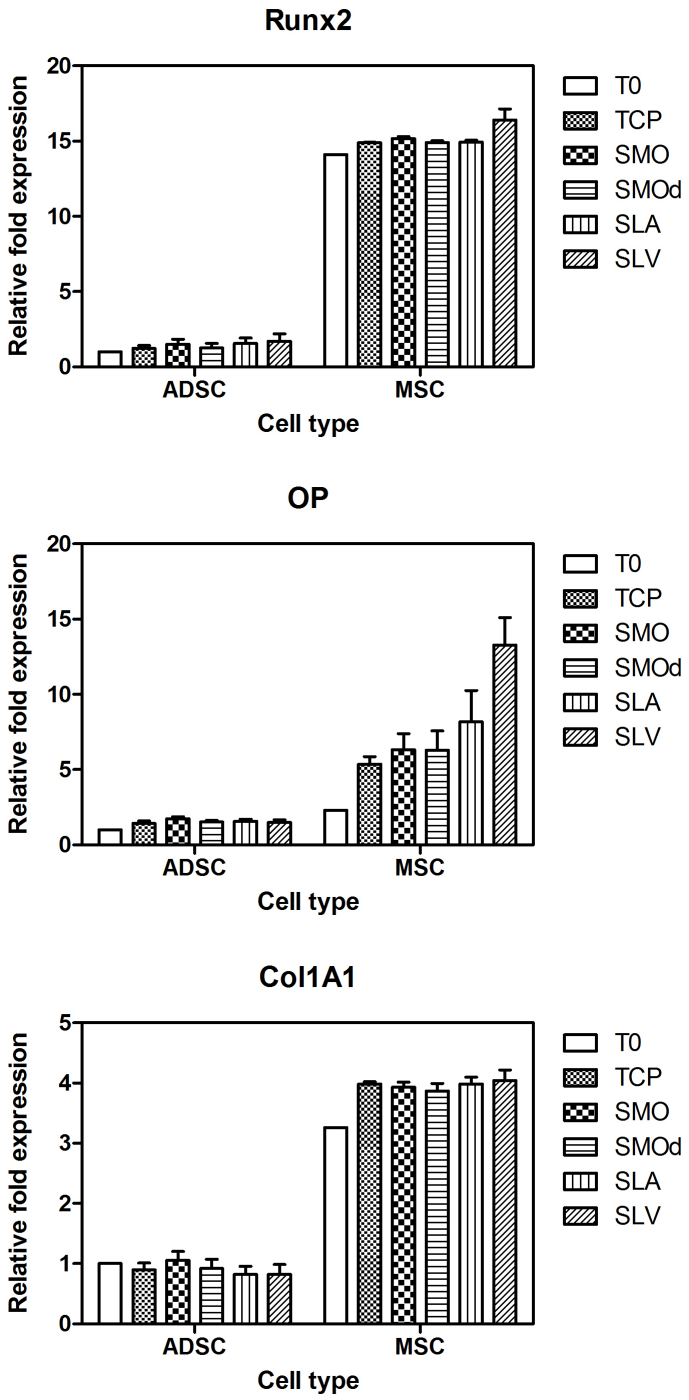

Figure 7.13: Comparison of gene expression of Runx2, OP and Col1A1 in selected MSC and ADSC populations. Expression values are normalised to the parent population T0 = 1.00.

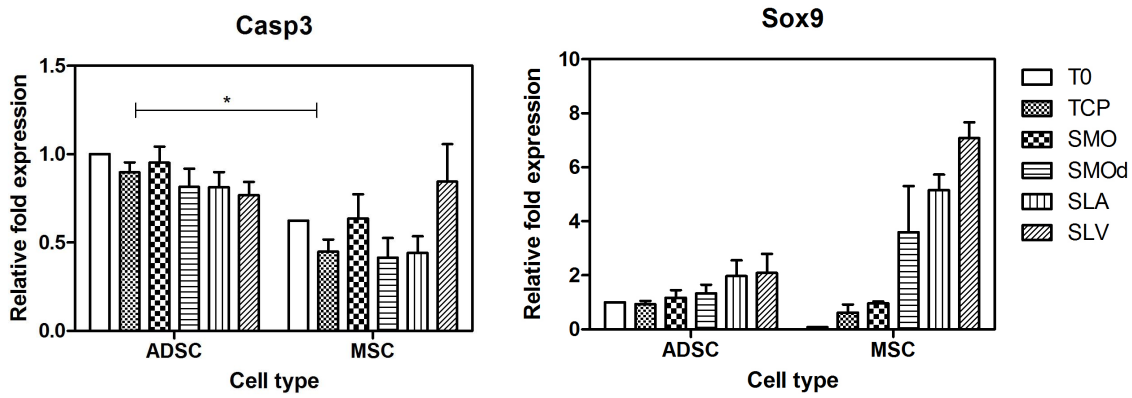

Figure 7.14: Comparison of gene expression of Casp3 and Sox9 in selected MSC and ADSC populations. Expression values are normalised to the parent population T0 = 1.00.

upregulation of Runx2, OP and Col1A1 (figure 7.13).

ADSCs express Casp3 and Sox9 at a significantly higher background level than MSCs (figure 7.14). Despite this, MSC selected populations from SLV showed a significant upregulation of both Casp3 and Sox9 as a result of the surface effect. ADSCs showed a slight upregulation of Runx2, OP, Col1A1 and a significant upregulation of Sox9 in reponse to SLV Ti. A downregulation of Casp3 was observed in ADSC populations selected on SLV.

7.3.3 Conclusions

Osteogenic differentiation

Mesenchymal stromal cells deposit a significantly more mineralised ECM in osteogenic media compared to ADSCs. This is shown in a significantly higher MSC Ca^{2+} to collagen ECM ratio at all times during culture. MSCs were seen to deposit a $\sim$ 15 times greater amount of ECM Ca^{2+} than ADSCs. In contrast, ADSCs deposit a $\sim$ 40 times higher amount of ECM collagen than MSCs. This could be due to differences in their tendency towards osteogenic differentiation in OM. ADSCs have been seen to have a higher expression level of Sox9 in the parent (T0) population which may signify a higher chrondrogenic

potential (figure 7.14). This may be a reason for the high amount of collagen that was seen deposited from ADSCs in OM. Guasti *et al.* has reported that ADSCs had significant plasticity and a high response to chrondrogenic induction resulting in the formation of both cartilage and bone (Guasti et al., 2012).

The impact of cell death on Ti

The results of the analyses conducted into mineralisation and apoptosis effects in response to Ti correlate closely with each other. The effect of modified Ti surfaces on mineralisation creates a magnitudinal enhancement in MSCs compared to ADSCs. The influence of Ti causes cells from MSC populations to commit and transform relatively quicker, and deposit greater amounts of calcified matrix on SLV than ADSC populations. There was a higher incidence of cell death in response to Ti in MSC selected populations compared to ADSCs. The apoptosis effect appears to be linked to the significantly higher degree of mineralisation seen in MSC selected populations from SLV compared to ADSCs. The mechanism of stem cell selection by modified Ti seems, therefore, to occur by removing a subset of cells that are not destined for osteogenic differentiation, thus creating an enriched population of cells that can form osteogenic lineages. As seen in the SLV selected MSCs cultured again on SLV (chapter 6, experiment matrix 6.2), the progeny of cells seem to form a more 'stem cell' like population following a high rate of apoptosis in response to this surface. These cells are more likely to undergo osteogenic differentiation in response to the appropriate stimulus.

It was observed that Casp3 was comparatively upregulated at T0 and on the SLV surfaces at early culture period (24 h) in MSCs compared to ADSCs (figure 7.14). The importance of this molecule in osteogenic differentiation has been highlighted in the absence of Runx2 activity in Casp3 null mice (Miura et al., 2004). Based on this, it was suggested that the Casp3 upregulation in MSCs on SLV may have been due to an osteogenic event in cells resulting from altered attachment and morphology on the rough surfaces. The genetic and phenotypic findings in this section indirectly support this notion of Casp3's association with osteogenesis; as well as strongly indicating the influence of modified Ti surfaces on

MSC fate determination towards an osteogenic lineage.

Gene expression analysis of individual osteogenic genes

The expression of Runx2, OP and Col1A1 was at a higher level in the MSC unaltered population (T0) compared to the ADSCs at T0. Casp3 and Sox9 were expressed at a higher level in ADSCs at T0 compared to MSCs. Runx2 and Sox9 can both be considered 'point of fate' transcription factors in the determination of osteogenic and chrondrogenic differentiation respectively i.e the upregulation of Runx2 is observed during osteogenic differentiation whilst Sox9 is downregulated (Jonason et al., 2009). The opposite is true of chrondrogenic differentiation. The observations here suggest MSCs are more prone towards osteogenic differentiation whilst ADSCs are more likely to form cartilage. The higher expression level of Runx2 and it's further upregulation in response to SLV reflects the bone tissue origin for MSCs. The expression levels of Runx2 and Sox9 may reflect the 'lineage mixed' phenotype of ADSCs which underlies their significant plasticity.

In summary, these results suggest that;

- Genetic expression of key bone physiology related genes is differentially modulated by chemical induction and Ti surface topography.
- ADSCs differentiate along the osteogenic lineage despite their fat tissue origins.
- Multipotent MSCs are highly sensitive to substrate material, topography and chemistry and undergo the most significant population changes.

Obtaining ADSCs does have the advantage over MSCs by reducing morbidity and through their ease of harvest. However, the use of MSCs for expansion and clinical bone regeneration applications has shown significant advantages in terms of their osteogenic differentiation ability over ADSCs.

Chapter 8

Discussion

8.1 Overview of thesis

This thesis' aim has been to combine the knowledge in material science with that of tissue engineering and biology. Knowledge in these areas is important for the design of implant surfaces providing biological signals to cells that favour bone healing and osseointegration. In order to achieve this, it is important to study the interaction of implant surfaces and MSCs, which are precursor cells with bone forming capacity (Schwartz et al., 1999a).

The first part of the study investigated the surface interactions of organic molecules with the TiO_2 [110] surface because, at the heart of all living things are the simple chemical reactions between water, mineral and air. An ubiquitous part of surface interactions results from van der Waals forces. These non-local interactions have, until recently, been difficult to incorporate into computational model systems. As such, it has been important to investigate the effect of their inclusion on biologically important molecular-surface adsorptions. The systems chosen to be studied involved amino acid-surface interactions. The reason these particular molecule-surface interactions were investigated is because, amino acids are the fundamental building blocks of life. All life that we know of is based on these compounds. In particular, current biological implant technology requires chemicals

to combine to metal surfaces, which involves amino acids as a critical first step.

The inclusion of vdW forces was validated in this study by comparison of the results with those from previous studies, and, whenever possible, with experimental results. This was a necessary first step in order to progress to investigate non-local interactions of water and more complex computer simulations involving the adhesion of biological significant molecules at the TiO_2 surfaces. The vdW-DF was used in subsequent calculations and it's inclusion has shown the dissociation of water at oxygen vacancies at the TiO_2 surface, which is a key mechanism in the hydrophilic conversion of TiO_2. The hydrophilic nature of TiO_2 is an important factor in the biocompatibility of Ti implants. As such, it was important to investigate the mechanism of the hydrophilic conversion at a molecular level in order to determine the useful material effects that this conversion has on molecular interactions and ultimately, cell behaviours. The impact of UV light on the hydrophilic conversion was investigated and this surface was utilised in the investigation for stem cell selection of osteogenic MSCs.

The binding of the tripeptide domain RGD to TiO_2 is of importance in this study, as it provides a focal point for the attachment of cells to a surface. Distances between interaction sites on TiO_2 have been seen to match closely with the amino and carboxyl group separation in the RGD molecule. Thus, strong interactions can occur between the RGD tripeptide and the TiO_2 surface. Fibronectin is an important adhesion protein involved in bone cell attachment. Along with osteopontin (OP) and BSP it belongs to non-collagenous extracellular matrix proteins in bone which interact via integrins expressed on the surface of cells (Sodek and Cheietz, 2000). All three molecules contain the RGD integrin recognition sequence, so that any implant surface that interacts well with the RGD motif is likely to improve bone cell contact and adhesion.

The second part examined the phenotypic and osteogenic responses of stem cell populations selected on the modified TiO_2 [110] surfaces. The experiments were conducted on three topographically or chemically different Ti surfaces, using TCP as a control for material based differences. These three Ti surface types are commercially available and we are grateful for the supply of discs to the project by Straumann AG. A fourth surface

modification was developed using UV irradiation to create a smooth hydrophilic surface from the naturally hydrophobic smooth SMO. This relatively simple laboratory procedure has the potential to remove a more expensive, complicated step from the manufacturing process and hence improve efficiency in materials development. The SLV surface has been demonstrated to provide a magnitudinal selection event over SMO, SMOd and SLA, in MSCs that creates a population that is enriched in cells with an osteogenic potential.

Two types of cells were used as biological specimens. The main cell type used for this project were bone marrow-derived hBMSCs, while the type studied to a lesser extent were the hADSCs. The primary difference between these cells is that of lineage; one being from bone marrow and one from fat. Both isolates comprise of a heterogeneous mix of uncommitted cells. While it seems the hMSCs are more capable of differentiating towards the osteoblastic phenotype, both have proven osteogenic potential as well as other plastic nature including adipogenic or chondrogenic capacities.

8.1.1 TiO_2 surface chemistry

A combination of rough, hydrophilic surface modifications have been shown to confer the greatest osteogenic effects in hMSC. One of the key questions is what influence both of these factors have on atomistic surface arrangements, since this ultimately affects stem cell behaviour. Each of the surface properties were considered in turn.

TiO_2 coated glass allowed us to study photo-induced hydrophilicity by Raman spectroscopy. The surface can be deposited by CVD and is identical to the upper oxide layer that forms on native titanium. The coated glass surface is slightly opaque. It does not reflect laser light in the same way as the polished metal surface, thus allowing Raman scattering to be analysed.

I was able to observe a strong positive correlation between the increase in surface oxygen vacancies and the change in the reciprocal of the contact angle. Both effects occur with increasing UV irradiation time.

Water splitting at the TiO_2 surface has long been a matter for debate (Liu et al., 2012). My DFT calculations have shown that this event is unlikely on the perfect stoiciometric surface but can occur at oxygen vacancies on the reduced surface. I am able to correlate the increase in surface hydroxyl groups, from the observation of an increase in oxygen vacancy formation with increased UV irradiation, with an increase in TiO_2 wettability (from contact angle measurements). The OH groups, in the presence of water, create a hydrogen bonded stable wetting layer. This is the origin of the hydrophilic surface property that could cause a cell to spread preferentially and with a higher affinity on an innate object such as Ti metal.

The stable wetting layer that is formed has water molecules bonded tightly to the TiO_2 surface and molecular dynamics (MD) has shown here that H_2O residence times, particularly at Ti_{5f} sites, are high. This effectively seals off the surface and prevents organic molecules from approaching close to and interacting with it. However, our MD simulations have demonstrated that, once introduced, organic amino acid fragments bind stably to the TiO_2 surface. It is proposed that stable adsorption of tripeptide motifs within protein molecules could occur at nanotopography roughened regions (Baier et al., 1984). In this way, the acid etched surfaces (SLA) provide the nanotopography needed for adsorption of cell-surface recognition proteins, such as RGD, leading to cell interaction and adhesion. Since hydrophilic rough Ti (SLV) has improved osseointegration properties over SLA, I have been able to show that this surface improves the binding of RGD further, through the stronger hydrogen bond interactions that result between the tripeptide molecules and surface hydroxyl groups.

I have demonstrated here a mechanism of UV induced hydrophilic conversion in TiO_2. In addition, the combined factors of nano-surface roughness and hydrophilicity (SLV) can vastly alter its physical nature. These factors greatly influence the surface-interactions at the molecular level and the surface-solvation effects in the presence of water.

8.1.2 Stem cell selection response to modified Ti surfaces

Phenotypic and osteogenic mesenchymal stem cell responses to Ti surfaces have been well documented (Wall et al., 2009; Khan et al., 2012). These studies have shown that phenotypic function of the osteogenic differentiation of cells on Ti surfaces is highly enhanced by modified topography and wettability.

This thesis specifically investigated the mechanism of the observed phenotypic response - i.e. is the observation due to individual, internal cellular changes in response to stresses caused by the Ti surface, or is there a cell selection event taking place? We propose that the selection event involves the removal of less 'stem cell' like cells in the heterogeneous population. The cells that do not survive on Ti are the clones identified by, Fukiage *et al.* to represent 17 % of the MSC population, that do not show differentiation potential (Fukiage et al., 2008). The cells that remain demonstrate uni-directional, bi-directional (78 % of clones) or tri-directional differentiation potential, which may include a pre-programmed osteogenic destiny. In this way stem cell selection by Ti creates an enriched osteogenic population of cells, in contrast to an upregulation of the osteogenic phenotype within individual cells.

Cells were cultured on modified Ti discs for 24 hours and, when harvested, were named the selected populations. Phenotypic and osteogenic responses were then compared, using the unaltered parent population of cells (from TCP) as a control.

The phenotype of a mesenchymal tissue derived cell is of an adherent and mitotic type. It is under pressure to attach to a substrate in order to divide to form larger progeny numbers. My experiments suggest that a selective pressure is applied to the parent population of cells in contact with modified Ti. In contrast, a selective population of cells does not 'feel' this selective pressure, when re-plated on Ti, as it has already been applied. The selection event is permanent and the cells have not reverted to their original phenotype during the intermediate period of expansion.

The loss seen in proliferative capacity can be partly attributed to apoptosis and necrosis

events that were observed in response to modified Ti. The selected SLV population of cells, harvested and cultured again on SLV showed a similar live / dead profile to the response of the parent population from TCP. This suggests that no further apoptosis occurs in the SLV selected population in response to SLV. The cells that undergo apoptosis in response to SLV have been removed and a change has occurred in the selected population. This may be due to an epigenetic change that occurs in the cells due to stresses caused by the Ti environment or else there is a clonal expansion which passes on the 'stem cell' like survivability to the resulting progeny.

The function of selected populations extends to increased calcium mineralisation and decreased collagen deposition. If it is the cells from the SLV selected population that are responsible for the better *in vitro* mineralisation performance, they ultimately have the potential for producing better quality bone.

The cell, being a constituent of the organisms anatomy, would bear a memory and is capable of responding to only what it faces within it's microenvironment. The SLV selected MSC populations have a greater proportion of multipotent cells and, therefore, are seen to respond osteogenically, producing higher levels of OP in response to SLV.

A transcriptional upregulation of Casp3 and Runx2 was observed here in the selected SLV population. The function of Runx2 is associated with osteogenic differentiation. Casp3 has an involvement in apoptosis, though it has a reported association with osteogenic differentiation in mice MSCs (Miura et al., 2004). The selected population may contain a higher density of multipotent cells potentially expressing the osteogenic genetic profile, and therefore the triggered osteogenic response to Ti is higher.

Phenotypic surface marker secretion was not seen to be significantly altered in the selected populations of cells, including the absence of changes to the key osteogenic marker Stro-1. Essentially the cells 'look' the same although differences in cellular processes, including tri-directional differentiation potential which is also related to osteogenic activity, suggest an altered population composition has occurred as a result of Ti interaction.

8.2 Correlations and disagreements with other studies

The findings presented in this thesis agree with many of the previous discoveries in TiO_2 surface chemistry and cell-implant interactions concerning the Ti surfaces. Various highlights are listed below.

1. New binding modes were found for glycine once van der Waals interactions were included in DFT calculations. These were found to agree better with experimental proposals compared to previous theoretical work (Tonner, 2010). The predicted anionic binding modes have been supported by STM experimental observation (Ojamae et al., 2006). However, the new bridging interaction found with the amino $N\cdots O_b$ coordination prevents free rotation around the central bond which is in contrast with STM observations (Qiu and Barteau, 2006).

2. Raman spectroscopy has been used previously to characterise TiO_2 structure; (Hardcastle et al., 2011; Balachandran and Eror, 1982). It's use here in the analysis of UV effects represents a novel and powerful ultilisation of this technique.

3. Water splitting has been proven not to occur on the TiO_2 defect-free hydrophilic surface (Liu et al., 2012). DFT studies here have identified proton exchange events from water molecules at oxygen vacancies. Surface hydroxyl group formation at oxygen vacancies has been previously observed using STM analysis (Wendt et al., 2005) which helps to confirm this proposed theoretical mechanism.

4. Brett *et al.* reported differences in cells of a mesenchymal lineage spreading on modified Ti (Brett et al., 2004). It was shown that cells spread highly on the rough SLA and were stretched on the smooth surfaces (figure 1.3). Osteoblastic cell adhesion and differentiation have been shown to be more favourable responses to roughened surfaces than smooth (Wall et al., 2009).

5. The reduction in cellular viability on SLA and SLV has been reported previously; (Olivares-Navarrete et al., 2010; Wall et al., 2009; Rausch-Fan et al., 2007). This occurrence is related to increased apoptosis as suggested by transcriptional upregu-

lation of Casp3 and related factors (Miura et al., 2004). The results here from both FACs and qPCR support the notion of surface induced apoptosis.

6. Results from Miron *et al.*, Wall *et al.* and Khan *et al.* have reported that calcium deposition is higher on the rough than smooth Ti (Miron et al., 2010; Wall et al., 2009; Khan et al., 2012). These studies provide an observation of a phenotypic response caused within MSCs placed directly on Ti. The results here, however, provide a quantitative assessment of increased ECM mineralisation within cells harvested from Ti and grown subsequently on TCP.

7. Wall *et al.* suggested the event of cellular enrichment occurring on the rough Ti surfaces, in particular SLV, leads to a comparative increase in the number of Stro-1 positive cells (Wall et al., 2009). It was suggested this could manifest in the form of Stro-1 negative cell elimination and/or the premature commitment of Stro-1 positive cells by substrate topography. An enriched population of Stro-1 positive cells was not observed here by FACs, although it is thought that cell selection may underpin the increased osteogenic differentiation observed on these surfaces even though a marker for this has not been shown.

8.3 Significance of findings and future directions

The adsorption of oxygen-containing organic molecules has shown significant interference with H_2O and thus can best be understood in aqueous solutions. The opening of Ti-O bonds was induced by UV irradiation. This was seen to be reversible by Raman spectroscopic and contact angle observations. The mechanism of 'healing' of oxygen vacancies was not investigated fully but is likely occur via hydroxyl group desorption as a first step. This can be confirmed by thermal desorption spectra (TDS) observations by Lausmaa et al. (1999). The feasibility of O_2 splitting, initiated at surface vacancies, as a final step may help to confirm the reversible nature of the hydrophilic conversion.

The present study, like any form of research, has several implications. Biological implant materials are designed to repair and improve worn out or damaged body parts, but they

present a 'foreign' object to biological systems. The understanding of materials and how surfaces interact at the molecular level is vitally important for future, improved implant design. The 'regenerative system' is one that has not been well characterised but has immense importance considering the continual drive for ever newer therapeutic developments. It can be loosely seen to consist of cells of an uncommitted / plastic nature, sequestered in tightly regulated pockets within various forms of tissue (mostly highlighted in blood, bone, muscle); which are mobilized by cytokines to reparative regions.

The present theoretical implication of MSCs considers them as active participants in tissue repair and their ability to regenerate may be enhanced with human intervention in the form of biomaterials. Ti has been long known as a biocompatible material. The exact biological mechanisms that achieve osseointegration are largely unknown. However, *in vitro* studies have demonstrated cell phenotypic responses to modified surfaces. These responses appear permanent and are retained in daughter cells following the differentiation event. Further studies will produce much useful information to help dissect the important events in osteogenesis leading to the design of novel molecular therapies.

Stem cell changes in response to an implant that are of interest include epigenetic changes and nemosis. It is possible that changes in DNA methylation patterns may be responsible for cell differentiation behaviour in response to a stressful environment such as Ti. It has been reported by Obokata *et al.* that acid environments can provide a shock to stem cells that induces pluipotent differentiation potential (Obokata et al., 2014). Nemosis involves cell death in fibroblasts through cell-to-cell contact and is associated with inflammation. If MSCs are transplanted to wound sites, none are found after a period of around three months and also there are no progeny, but there is an observed improvement in wound healing. It is possible that nemosis is an important process that creates inflammation responses that results in more rapid healing. Alternatively, the high rate of apoptosis of MSCs on Ti may reduce the inflammation associated with the programmed cell death processes of necrosis and nemosis.

Titanium continues to be the implant material of choice. It has been successfully developed from the early multi-stage techniques of Warnke *et al.* to more recent 3D print

designs using laser melting of Ti powder, such as the technique used by Kroonenburgh *et al.* to make a custom design for a whole mandible replacement (Warnke et al., 2004; Kroonenburgh et al., 2012). The future therapeutic implications of Ti could include; (i) its use as an *in vitro* substrate for the evaluation of osteogenic events and (ii) for biomaterial design of bone related tissue engineering purposes. The long term implications involve identifying relevant sub-cellular target pathways, which may be manipulated in order to gain the desired osteogenic outcome with a high degree of specificity and efficiency.

It would be interesting to compare the quantitative and qualitative state of key osteogenesis associated proteins such as Runx2, OP and BMP receptors, BSP subtypes, etc at the protein level. Gene expression is difficult to interpret as it does not provide information at the protein level. Protein levels in some instances may present more accurate information of an actual phenotypic change as increased mRNA levels do not always lead to an increase in the effector molecules (proteins). The accurate identification of the effector molecules actually participating in the difference could help identify upstream molecular systems and lead to new therapeutic interventions.

A main aim for this thesis was to investigate the potential for the selection of an osteogenic subpopulation of hMSCs which might be used for regenerative or bone engineering applications. It can be concluded that the fraction of MSCs obtained through the adherence to modified Ti, could be used in bone regeneration applications due to their enhanced osteogenic behaviour. The hADSCs consist of cells with lower osteogenic potential compared to MSCs, however, it should be remembered that obtaining ADSCs has the advantage of reducing morbidity. The selected cells have the potential to be expanded and seeded onto Ti implants to enhance osseointegration. This study has been performed using MSCs attached to Ti surfaces in monolayer. It is not clear how well this monolayer represents the *in vivo* 3D network of ECM and various cell types in bone. For bone engineering applications, it is considered that a scaffold of some sort will be needed to provide the desired 3D structure of the bone tissue. In order to regenerate new bone an anatomical mesh will most likely be needed, such as the calcium-phosphate coated porous Ti alloy proposed by García-Gareta et al. (2014). Adequate perfusion in a bioreactor is considered essential

since the diffusional limitations of mass transport can severely affect cell survival, differentiation and proliferation within the scaffold. To minimise diffusional gradients within engineered constructs, two systems involving flow and mixing of culture medium can be used. These are typically, spinner flasks and perfusion cartridges. Convective mixing in a spinner flask bioreactor or convective flow in a perfusion bioreactor improves cell seeding density and homogeneity, thereby improving the tissue architecture of the construct. High initial cell densities have also been associated with enhanced tissue formation features, including bone mineralisation (Martin et al., 2004).

8.4 Limitations

Although there has been significant progress in the theoretical study of surface science, there are important limitations in modelling complex molecular systems. The approximations that are necessary to make DFT a workable method that accurately calculates the properties of a system at the electronic level are discussed in chapter 1, section 6. An important modification towards an improved description of non-local interactions is thoroughly investigated in chapter 3. However, the main limitation being the size of the system that can be realistically calculated. The studies described here have demonstrated the use of DFT and atomistic MD to obtain information on the structure and kinetics of organic molecules interacting with the TiO_2 surface, including within a water solution. Investigations of the same computational approaches involving larger peptides and, possibly, protein structures could be made possible with ever increasing advances in computational capacity.

The observation of Casp3 activity at the genetic level is attributed to increased levels of apoptosis and necrosis seen on the rough surfaces (Wall et al., 2009). This situation is also accompanied by the increased Runx2 activity which has an associated role in the osteogenic differentiation of bone marrow stromal cells. Decreased bone mineral density is reported to be due to decreased Runx2 expression in Casp3 null mice (Miura et al., 2004). Since the gene expression signature of these key factors has been shown to hold true they can be

considered to predict osteogenic behaviour. To this end, the differences in expression levels of 46 genes, distinguished for their role in osteogenesis, were analysed here in micro-array experiments. The gene expression signatures suggest a stronger osteogenic response in MSCs due to Ti than with chemical induction from surrounding media. Although single genes themselves have tiny effects, the interactions of a small sub-set of 46 genes represents findings that are too complex to interpret. The reality is of hundreds of genes involved in each cell's response to modified Ti. Because of the complexity of genetics, results should be interpreted cautiously. Nonetheless, the studies present a stride toward understanding the genomic scaffolding of stem cell osteogenic differentiation.

8.5 Conclusion

In conclusion, I have used a combination of quantum chemistry calculation techniques and novel cell assays to establish the influence of the TiO_2 surface on the selection of an osteogenic population of stem cells from MSCs.

The findings here implicate the differences in molecular adsorption as a result of the hydrophilic conversion in substrate chemistry of TiO_2 and nano-roughened topography. It is considered that the differential adsorption of organic molecules is a reflection on variations in intermolecular forces, surface energy and interactions involving liquid water. This study proposes that UV irradiation produces a reversible hydrophilic conversion in TiO_2 through the creation of electron-hole pairs which react with lattice oxygens forming surface oxygen vacancies. Water splitting at oxygen vacancies creates a hydroxylated surface (figure 4.9). In combination, surface topography and wettability enhance the interaction of carboxyl and amino groups found within biologically important molecules. This in turn has selective effects on cells coming into contact with the Ti surfaces and underpins the differences seen in clinical performances and stem cell selection.

Previous studies propose that surface topography of SLV 'accelerates the osteogenic differentiation of MSCs'. This study, by suggesting an alternative mechanism to the phenotypic induction differentiation by Ti, proposes that a selection event of a fraction of cells occurs

following apoptosis on SLV, and leads to an expansion of the enriched osteogenic sub-set following rounds of cell replication.

The key processes involved in this thesis can be summarised here:
Mesenchymal stem cell contact with modified Ti creates a population that expresses higher levels of Runx2 and Sox9 (figure 7.12). These 'point of fate' transcription factors for osteogenic and chrondrogenic destinations, indicate that there is a clonal selection event for cells that posses the potential to differentiate.

Along the osteogenic pathway, OP acts downstream from Runx2 (figure 7.1). OP was seen to be highly upregulated in MSC cell populations selected from rough, hydrophilic Ti (figure 6.15). This indicates that a surface effect of SLV Ti is to induce osteogenic differentiation which is also observed by the increased levels of Ca^{2+} mineralisation (figure 6.8). The OP gene encodes an ECM protein in bone which, in common with the other ECM components, fibronectin and BSP (also upregulated on SLV (figure 7.6)), contain the Arg-Gly-Asp (RGD) adsorption domain.

The RGD tripeptide conformation provides amino and carboxyl groups at separation distances that fit into adjacent active Ti_{5f} adsorption sites on the TiO_2 surface via a bridging mechanism (figure 5.8). This provides a strong adsorption mode that is unique to Ti. Nano-surface roughness enhances the adsorption effect in water, through step and pit structures where RGD can adhere. Hydrophilic Ti, containing surface OH groups, enhances the adsorption effect of RGD further via hydrogen bonding with dangling amino groups (figure 5.9). Rough hydrophilic properties combined, provide the ideal surface environment for TiO_2 that establishes a tightly bound ECM. This effectively 'walls off' the surface to incoming cells that no-longer encounter a foreign material. Bone cells bind to the ECM fibronectin, OP and BSP components via integrin recognition sequences. In addition to the formation of an increased calcified, collagen matrix, this provides a strong, flexible bond between the implant and surrounding bone that is observed in the *in vivo* osseointegration of Ti.

Appendix A

Microarray osteogenic genes

Forty eight genes were represented on a customised qPCR microarray from AppliedBiosystems. The details of the genes and their functions are tabulated here. This table consists of five columns entitled; gene symbol, description, molecule type, process and gene function. The first and second columns indicate gene identity. The third is the designate of molecule type. The processes represent the significance of gene function in the context of stem cell osteogenic differentiation. The final column represents the possible functions that are significant to stem cell biology. Biological descriptions are derived from the PANTHER (Protein ANalysis Through Evolutionary Relationships; (Gene Ontology Reference Genome Project 2011)) classification system and were accessed on March, 2014.

Gene	Description	Molecular type	Process	Function
18S	Eukaryotic 18S rRNA	ribozyme	translation	Part of the small ribosomal subunit. Aides in catalyzing amino acid transfer from tRNAs
GAPDH	glyceraldehyde-3-phosphate dehydrogenase	dehydrogenase	carbohydrate metabolism	catalyzes the reversible oxidative phosphorylation of glyceraldehyde-3-phosphate in the presence of inorganic phosphate and nicotinamide adenine dinucleotide
ALPL	alkaline phosphatase	enzyme	hydrolase	responsible for removing phosphate groups from other types of molecules, including nucleotides, proteins, and alkaloids. Bone ALP is used as an osteogenic marker
AMBN	ameloblastin	enamel matrix glycoprotein	ECM structure	secreted by ameloblasts and is involved in the mineralisation of enamel
AMELY	amelogenin, Y-linked	enamel matrix protein	ECM structural	involved in biomineralisation during tooth enamel development
ARSE	arylsulfatase E (chondrodysplasia punctata 1)	enzyme	hydrolysis	catalyses the hydrolysis of sulphate ester bonds
BMP2	bone morphogenetic protein 2	growth factor of the TGF-β family	cytokine	acts as a disulfide-linked homodimer and induces bone and cartilage formation. Has a key role in osteoblast differentiation
BMP4	bone morphogenetic protein 4	growth factor of the TGF-β family	cytokine	induces bone formation

BMP7	bone morphogenetic protein 7	growth factor of the TGF-β family	cytokine	has a key role in osteoblast differentiation. It also induces the production of SMAD1
CALCR	calcitonin receptor	G-protein coupled receptor	calcium homostasis	binds to peptide hormone calcitonin for regulation of bone formation and metabolism
CASR	calcium-sensing receptor	G-protein coupled receptor	expressed on parathyroid glands	regulates PTH on the basis of Ca^{2+}
CDH11	cadherin 11, type 2, OB-cadherin (osteoblast)	Cell surface	Cell adhesion molecule; negative regulation of cell proliferation	encoded protein is a calcium-dependent cell-cell adhesion glycoprotein comprised of five extracellular cadherin repeats, a transmembrane region and a highly conserved cytoplasmic tail. Functioning as cadherin by imparting to cells homophilic bindings, may play an important role in endothelial cell biology through control of the cohesion and organization of the intercellular junctions
COL1A1	collagen, type I, α 1	Extracellular matrix structural protein	skeletal development; blood vessel development; osteoblast differentiation	type I is a fibril-forming collagen found in most connective tissues and is abundant in bone
COMP	cartilage oligomeric matrix protein	member of thrombospondin gene family	noncollagenous ECM protein, secreted by chondrocytes. A marker of cartilage turnover	

DMP1	dentin matrix acidic phosphoprotein 1	acidic phosphoprotein	ECM protein expressed by osteocytes	involved in mineralisation by binding to Ca^{2+} and apatite
FGFR1	fibroblast growth factor receptor 1	tyrosin kinase receptor	interacts with fibroblast growth factors	invloved in the growth of the long bones
FGFR2	fibroblast growth factor receptor 2	tyrosin kinase receptor	interacts with fibroblast growth factors	invloved in the growth of the long bones. It is regulated by TWIST1
FGFR3	fibroblast growth factor receptor 3	tyrosin kinase receptor	interacts with fibroblast growth factors	Functions as a negative regulator in the growth of the long bones
FLT1	fms-related tyrosine kinase 1 (vascular endothelial growth factor/vascular permeability factor receptor)	protein kinase receptor	sprouting angiogenesis ; development ; pregnancy ; cell differentiation	gene encodes a member of the vascular endothelial growth factor receptor (VEGFR) family. This protein binds to VEGFR-A, VEGFR-B and placental growth factor and plays an important role in angiogenesis and vasculogenesis. Expression of this receptor is found in vascular endothelial cells, placental trophoblast cells and peripheral blood monocytes

GDF10	growth differentiation factor 10	belongs to the TGF-β family	closely related to BMP3	has a role in endochondral bone formation
IBSP	integrin-binding sialoprotein	glycoprotein	bone ECM	expressed by fully differentiated osteoblast and acts as a structural protein in bone matrix by binding to hydroxyapatite
MMP13	matrix metallopeptidase 13 (collagenase 3)	enzyme	expressed by hypertrophic chrondrocytes or osteoblasts	catalyses the degradation of ECM and release factors stored in ECM such as VEGFA. Inactivation in osteoblasts leads to increased spongy bone
MMP2	matrix metallopeptidase 2	enzyme	expressed by MSCs	involved in the breakdown of ECM and the degradation of type IV collagen, a major structural component of basement membranes
MSX1	msh homeobox 1	homobox gene	downregulates RUNX2	involved in the terminal differentiation of tooth and craniofacial skeleton
DSPP	dentin sialophosphoprotein	dentin ECM protein of the tooth	odontoblastspecific expression	involved in the biomineralisation process of dentin
RUNX2	runt-related transcription factor 2	Transcription factor	skeletal development	gene is a member of the RUNX family of transcription factors and encodes a nuclear protein; protein is essential for osteoblastic differentiation

SMAD1	SMAD family member 1	glycoprotein	immediate downstream molecule of BMP receptors and signalled through SMAD4	activates downstream gene transcription
SMAD2	SMAD family member 2	glycoprotein	complexes with SMAD4 that regulates transcription of target genes	TGF-β stimulation leads to activation
SMAD3	SMAD family member 3	glycoprotein	complexes with SMAD4 that regulates transcription of target genes	responsible for TGF-β1-induced migration of MSCs
SMAD4	SMAD family member 4 glycoprotein	SMAD2 and SMAD3 complexes with SMAD4	regulates target genes	
SMAD7	SMAD family member 7	glycoprotein	regulates TGF-β and BMPs	inhibits SMAD pathways in chrondrocytes
SMAD9	SMAD family member 9	glycoprotein	immediate downstream molecule of BMP receptors	part of BMP signalling
SOX9	SRY (sex determining region Y)-box 9	Transcription factor & cardiac cell fate determination	involved in the regulation of embryonic development and in the determination of the cell fate. Required for chrondrocyte differentiation and cartilage formation	

SPARC	secreted protein, acidic, cysteine-rich (osteonectin)	bone tissue specific protein	binds to both hydroxyapatite and collagen	initiates mineralisation process in skeletal tissue
SPP1	secreted phosphoprotein 1	matrix protein	attachment protein linking cells to the bone mineral	involved in bone remodelling
TGFB1	transforming growth factor, beta 1	cytokine	TGF-β super family	recruits MSCs to bone remodelling *in vitro*. Stimulates proliferation of progenitors and initiates osteoblastic differentiation
TGFB3	transforming growth factor, beta 3	cytokine	TGF-β super family	inhibits osteogenesis of MSCs
TGFBR1	transforming growth factor, beta receptor 1	receptor	recruited by TGF-βR2 and activates SMAD	transduces the TGF-beta signal from the cell surface to the cytoplasm
TGFBR2	transforming growth factor, beta receptor II (70/80kDa)	receptor	phosphorylates proteins which enter the nucleus and regulate the transcription of a subset of genes related to cell proliferation	activates TGF-βR2
TUFT1	tuftelin 1	phosporylated glycoprotein	enamelin group of proteins	codes the enamel protein tuftelin

TWIST1	twist homolog 1 (Drosophila)	transcription factor	regulates bone remodelling by decreasing RUNX2 and OP	involved in osteogenic cell lineage determination and differentiation
TWIST2	twist homolog 2 (Drosophila)	transcription factor	regulates bone remodelling by decreasing RUNX2 and OP	involved in osteogenic cell lineage determination and differentiation
VDR	vitamin D (1,25-dihydroxyvitamin D3) receptor	receptor	binds to 1,25-dihydroxyvitamin D	regulates mineral ion homeostasis
VEGFA	vascular endothelial growth factor A	growth factor	inhibits BMP2 mRNA expression	increases vascular permeability, inducing angiogenesis, endothelial cell growth, promotes cell migration, and inhibiting apoptosis
VEGFB	vascular endothelial growth factor B	growth factor	coupled with the FLT1 receptor	plays a role in the maintenance of blood vessels and neurons
SP7	Osterix	Zinc finger transcription factor	member of the SP family	master regulator of bone cell differentiation, only detected in embryonic human tissue not in adult tissue
WNT5A	wingless-type MMTV integration site family, member 5A	glycoprotein	encodes secreted signalling proteins	promotes osteogenesis in adult MSCs
PTH1R	parathyroid hormone 1 receptor	G protein-coupled receptor	activation of adenylate cyclase and phospholipase C	expressed on the surface of osteocytes and is involved in calcium ion homeostasis

Table A.1: Description of genes

Appendix B

EDAX characterisation of Ti

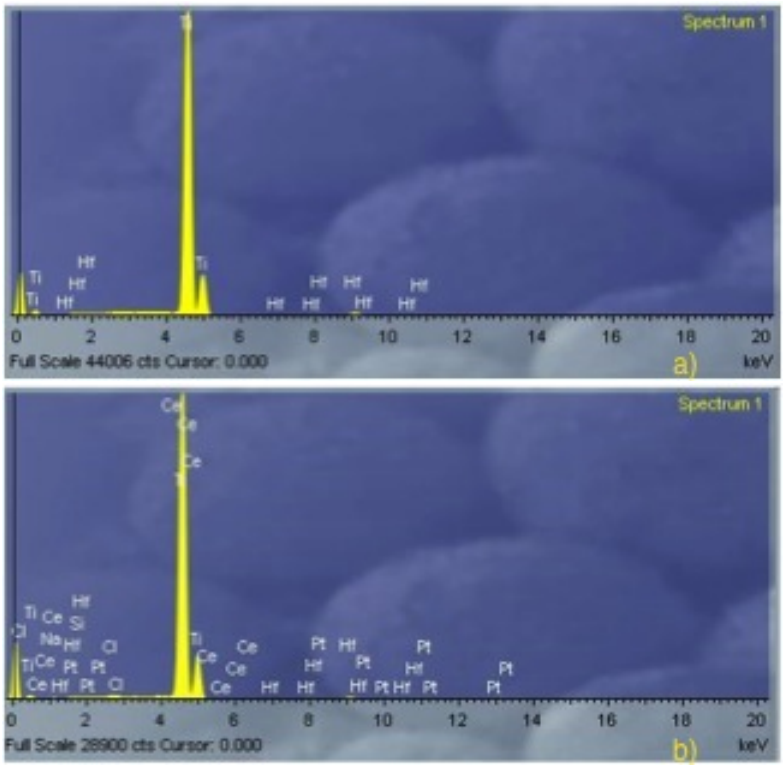

Figure B.1: EDAX analysis showing the chemical composition of the titanium discs used in this study; a) smooth polished Ti (SMO), b) roughened, hydrophilic Ti (SLV). They consist of high purity titanium with traces of Hafnium and Cerium. Some sodium impurities were found on the surface of SLV due to its storage in saline solution after roughening. Images taken at the Eastman Dental Institute.

Appendix C

Standard curves

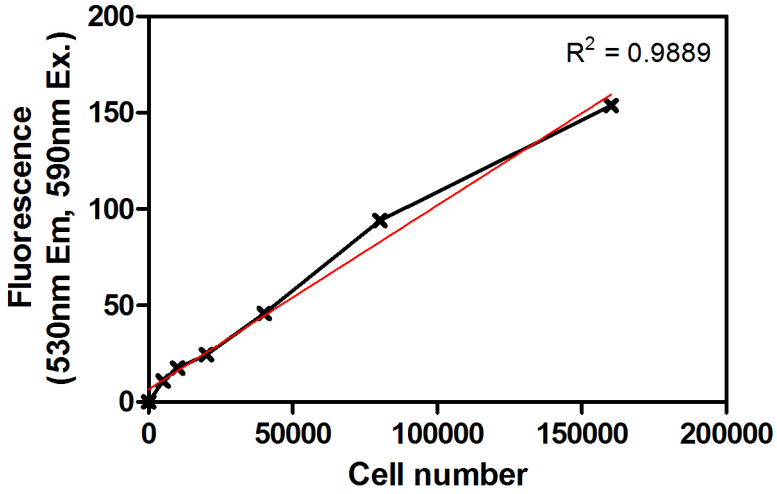

Figure C.1: Standard curve of fluorescence vs cell number after 4 h incubation with AlamarBlue. Graph is a seven point standard curve as a result of 160,000, 80,000, 40,000, 20,000, 10,000, 5,000 and 0 seeding densities of MSCs in a 24-well plate. Curve drawn from zero-subtracted readings and using linear regression analysis.

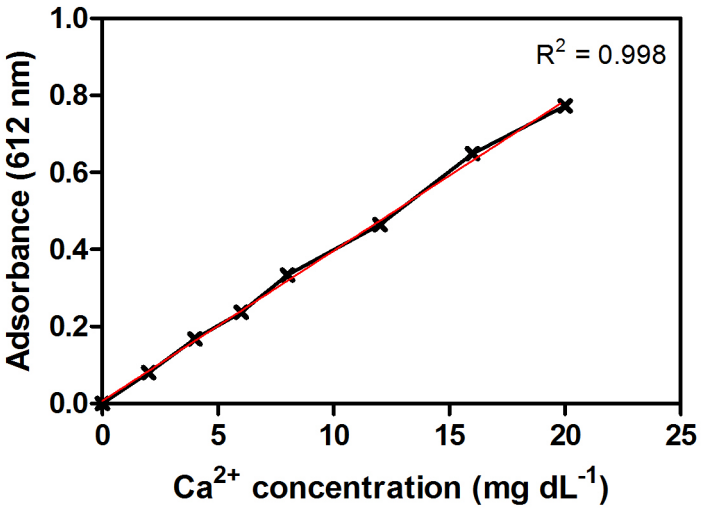

Figure C.2: Standard curve of absorbance at 612nm vs Ca^{2+} concentration. An eight point standard curve consisting of 20, 16, 12, 8, 6, 4, 2 and 0 mg dL^{-1} of calcium salt was formed in 96-well plates. Samples were processed and stained as described in chapter 2, section 9.2. Curve drawn from zero-subtracted readings using linear regression analysis.

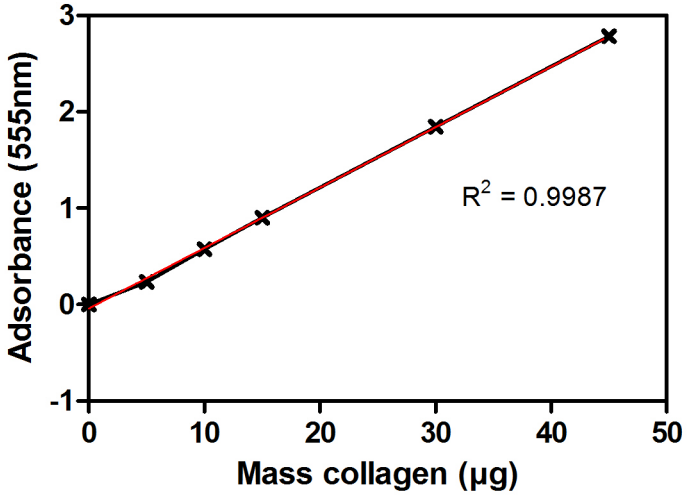

Figure C.3: Standard curve of absorbance at 555 nm vs mass of collagen. A six point standard curve of 0, 5, 10, 15, 30 and 45 μg of collagen was generated from a stock (1 mg mL^{-1}) in 1.5 mL tubes and stained with Sircol Red as described in chapter 2, section 10. Curve drawn from zero-subtracted readings using linear regression analysis.

Appendix D

Contact angle images

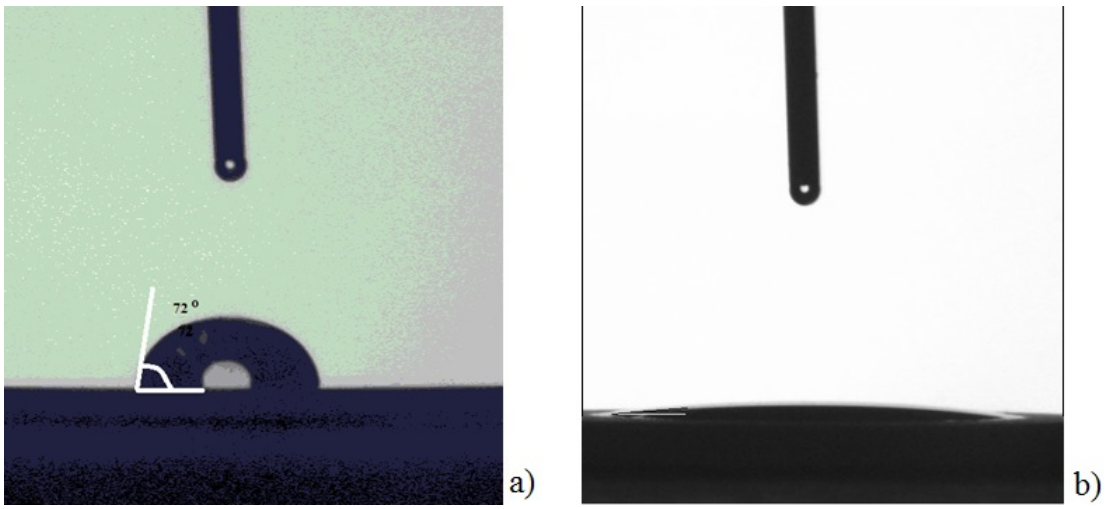

Figure D.1: Examples of contact angle measurement images. The contact angle of water on smooth hydrophobic (SMO) Ti is reduced from a) $\sim$ 72 $^\circ$ to b) completely wetted $\sim$ 0° following 3 h UV irradiation.

Appendix E

Coordination number of molecular-solvent interactions

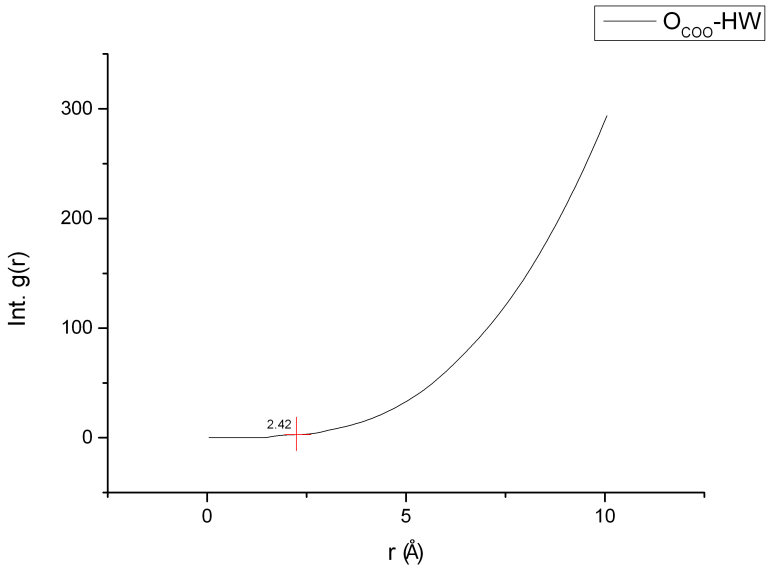

Figure E.1: The integration of the RDF gO_{COO}HW(r) provides the coordination number of glycine in water which is found from the intersection with the first plateau. $n_{\text{coor}} = 2.4$

Appendix F

Academic activities

Publications

Book chapter in Biomaterials and Stem Cells in Regenerative Medicine.
Publisher; Taylor and Francis group. Feb. 2012.
Title - Osteogenic adult stem cells and titanium constructs for repair and regeneration.

Tillotson, M.J. Brett, P.M. Bennett, R.A. Grau-Crespo, R. The effect of van der Waals interactions on the adsorption of organic molecules at the TiO2 [110] surface. *Submitted to Surface Science.*

Tillotson, M.J. Logan, N. Donos, N. Brett, P.M. Osteogenic stem cell selection for repair and regeneration. *Submitted to the Journal of Tissue Engineering and Regenerative Medicine.*

Presentations

Oral; UCL M.Phil upgrade, Oct. 2011 - Osteogenic adult stem cells and Titanium constructs for repair and regeneration.

Poster; World Regenerative Medicine conference, Leipzig, Germany Nov. 2011 - Potential of Titanium surfaces to select osteogenic stem cells for repair and regeneration.

Poster; The Thomas Young Centre - 2nd Energy Materials workshop and tutorial, King's College London June 2012 - The effect of the van der Waals interactions on the adsorption energies of organic molecules with the TiO_2 [110] surface.

Poster; UCL Industrial Training Center IDT, industry day June 2013 - The impact of ultraviolet (UV) light on TiO_2 coated glass.

Poster; European Society of Biomaterials, Madrid, Spain Sept. 2013 - Material Based Stem Cell Selection for Bone Repair and Regeneration.

Conference attendance

Discussion workshop: Stem cells. Institute of Biomedical Science. June 2011.

Thomas Young Centre - Thermodynamics and Kinetics of Surfaces and Interfaces from Simulations, Imperial Collage London June 2011.

Surface Science of Biologically Important Interfaces 14th annual meeting: University of Manchester Nov. 2012.

Awards

UCL Graduate School Conference fund; 2012 & 2013 total = £550.00.

The UK's HPC Materials Chemistry Consortium awarded computational resource time on HECToR, the UK's national high performance computing service. Sept. 2011 & March 2012. Project title: Interaction of organic molecules with Titanium dioxide. Total time allocation = 1.35 M Au.

Bibliography

Ahlstrom, M., Pekkinen, M., and Lamberg-Allardt, C. (2009). Dexamethasone downregulates the expression of parathyroid hormone-related protein (PTHrP) in mesenchymal stem cells. *Steroids*, 74(2):277–82.

Alhadlaq, A. and Mao, J. (2005). Tissue-engineered osteochrondral constructs in the shape of an articular condyle. *J. Bone Joint Surg. Am.*, 87(5):936–44.

Almora-Barrios, N. and de Leeuw, N. (2010). Modelling the interaction of a Hyp-Pro-Gly peptide with hydroxyapatite surfaces in aqueous environment. *Crystengcomm*, 12(3):960–967.

Anderson, H., Garimella, R., and Tague, S. (2005). The role of matrix vesicles in growth plate development and biomineralization. *Front Biosci*, 10(822-37).

Andersson, Y., Langreth, D., and Lundqvist, B. (1996). van der Waals interactions in density-functional theory. *Phys Rev Lett*, 76(1):102–105.

Anisimov, V., Zaanen, J., and Andersen, O. (1991). Band theory and mott insulators: Hubbard U instead of Stoner I. *Phys Rev B Condens Matter*, 44(3):943–954.

Antony, J. and Grimme, S. (2006). Density functional theory including dispersion corrections for intermolecular interactions in a large benchmark set of biologically relevant molecules. *Physical Chemistry Chemical Physics*, 8(45):5287–5293.

Baier, R. E., Meyer, A. E., Natiella, J. R., Natiella, R. R., and Carter, J. M. (1984). Surface-properties determine bioadhesive outcomes - methods and results. *Journal of Biomedical Materials Research*, 18(4):337–355.

Balachandran, U. and Eror, N. (1982). Raman-spectra of Titanium-dioxide. *Journal of Solid State Chemistry*, 42(3):276–282.

Banerjee, C., Javed, A., Choi, J. Y., Green, J., Rosen, V., van Wijnen, A. J., Stein, J. L., Lian, J. B., and Stein, G. S. (2001). Differential regulation of the two principal Runx2/Cbfa1 n-terminal isoforms in response to bone morphogenetic protein-2 during development of the osteoblast phenotype. *Endocrinology*, 142(9):4026–39.

Bates, S., Kresse, G., and Gillan, M. (1997). A systematic study of the surface energetics and structure of TiO_2 (110) by first-principles calculations. *Surface Science*, 385(2-3):386–394.

Benayahu, D. (2007). Differentiation of bone marrow stroma derived mesenchymal cells. *Current Medicinal Chemistry*, 14:173–179.

Bennett, R., Stone, P., Smith, R., and Bowker, M. (2000). Formic acid adsorption and decomposition on non-stoichiometric TiO_2(110). *Surface Science*, 454-456:390–395.

Bialek, P., Kern, B., Yang, X., Schrock, M., Sosic, D., Hong, N., Wu, H., Yu, K., Ornitz, D. M., Olson, E. N., Justice, M. J., and Karsenty, G. (2004). A twist code determines the onset of osteoblast differentiation. *Dev Cell*, 6(3):423–35.

Blin-Wakkach, C., Lezot, F., Ghoul-Mazgar, S., Hotton, D., Monteiro, S., Teillaud, C., Pibouin, L., Orestes-Cardoso, S., Papagerakis, P., Macdougall, M., Robert, B., and Berdal, A. (2001). Endogenous Msx1 antisense transcript: in vivo and in vitro evidences, structure, and potential involvement in skeleton development in mammals. *Proc Natl Acad Sci U S A*, 98(13):7336–41.

Boehm, H. (1971). Acidic and basic properties of hydroxylated metal-oxide surfaces. *Discussions of the Faraday Society*, 52:264.

Bornstein, M., Wittneben, J., Bragger, U., and Buser, D. (2010). Early loding at 21 days of non-submerged titanium implamts with a chemically modified sandblasted and acid-etched surface: 3-year results of a prospective study in the posterior mandible. *J Periodontal*, 81(6):809–818.

Bosch, P., Musgrave, D. S., Lee, J. Y., Cummins, J., Shuler, F., Ghivizzani, S. C., Evans, C., Robbins, P. D., and Huard, J. (2000). Osteoprogenitor cells within skeletal muscle. *Journal of Orthopaedic Research*, 18(6):933–944.

Branemark, P. (2005). *The osseointegration book*, volume 1st ed. Quintessence books.

Braun, J., Hack, A., Weis-Klemm, M., Conrad, S., Treml, S., Kohler, K., Walliser, U., Skutella, T., and Aicher, W. K. (2010). Evaluation of the osteogenic and chondrogenic differentiation capacities of equine adipose tissue-derived mesenchymal stem cells. *Am J Vet Res*, 71(10):1228–36.

Brett, P. M., Harle, J., Salih, V., Mihoc, R., Olsen, I., Jones, F. H., and Tonetti, M. (2004). Roughness response genes in osteoblasts. *Bone*, 35(1):124–33.

Brzoska, M., Geiger, H., Gauer, S., and Baer, P. (2005). Epithelial differentiation of human adipose tissue-derived adult stem cells. *Biochemical and Biophysical Research Communications*, 330(1):142–150.

Buser, D., Broggini, Wieland, Schenk, Denzer, Cochra, Hoffmann, Lussi, and Steinemann (2004). Enhanced bone apposition to a chemically modified (sla) titanium surface. *Journal of Dental Research*, 83(7):529–533.

Buser, D., Schenk, R. K., Steinemann, S., Fiorellini, J. P., Fox, C. H., and Stich, H. (1991). Influence of surface characteristics on bone integration of Titanium implants - a histomorphometric study in miniature pigs. *J Biomed Mater Res*, 25(7):889–902.

Cabailh, G., Torrelles, X., Lindsay, R., Bikondoa, O., Joumard, I., Zegenhagen, J., and Thornton, G. (2007). Geometric structure of TiO_2 (110): Achieving experimental consensus. *Physical Review B*, 75(24):241–403.

Calzado, C., Hernandez, N., and Sanz, J. (2008). Effect of on-site coulomb repulsion term u on the band-gap states of the reduced rutile (110) TiO_2 surface. *Physical Review B*, 77(4):045118.

Caplin, A. (2008). All MSCs are preicytes? *Cell Stem Cell*, (229-30).

Carravetta, V. and Monti, S. (2006). Peptide-TiO_2 surface interaction in solution by ab initio and molecular dynamics simulations. *Journal of Physical Chemistry B*, 110(12):6160–6169.

Carreras, I., Rich, C. B., Jaworski, J. A., Dicamillo, S. J., Panchenko, M. P., Goldstein, R., and Foster, J. A. (2001). Functional components of basic fibroblast growth factor signaling that inhibit lung elastin gene expression. *Am J Physiol Lung Cell Mol Physiol*, 281(4):766–75.

Charlton, G., Howes, P. B., Nicklin, C. L., Steadman, P., Taylor, J. S. G., Muryn, C. A., Harte, S. P., Mercer, J., McGrath, R., Norman, D., Turner, T. S., and Thornton, G. (1997). Relaxation of TiO_2 (110)-(1x1) using surface x-ray diffraction. *Phys Rev Lett*, 78(3):495–498.

Chen, N. X., O'Neill, K. D., Chen, X., and Moe, S. M. (2008.). Annexin-mediated matrix vesicle calcification in vascular smooth muscle cells. *J Bone Miner Res*, 23(11):1798–805.

Chu, K., Cheng, C. J., Ye, X., Lee, Y. C., Zurita, A. J., Chen, D. T., Yu-Lee, L. Y., Zhang, S., Yeh, E. T., Hu, M. C., Logothetis, C. J., and Lin, S. H. (2008). Cadherin-11 promotes the metastasis of prostate cancer cells to bone. *Mol Cancer Res*, 6(8):1259–67.

Coffin, J. D., Florkiewicz, R. Z., Neumann, J., Mort-Hopkins, T., Dorn, G. W., Lightfoot, P., German, R., Howles, P. N., Kier, A., and O'Toole, B. A. (1995). Abnormal bone growth and selective translational regulation in basic fibroblast growth factor (FGF-2) transgenic mice. *Mol Biol Cell*, 6(12):1861–73.

Colter, D., Sekiya, I., and Prockop, D. (2001). Identification of a subpopulation of rapidly self-renewing and multipotential adult stem cells in colonies of human marrow stromal cells. *Proc Natl Acad Sci U S A*, 98(14):7841–5.

Colter, D.C., e. a. (2000). Rapid expansion of recycling stem cells in cultures of plastic-adherent cells from human bone marrow. *Proc Natl Acad Sci U S A*, 97(7):3213–8.

Cornell, W. D., Cieplak, P., Bayly, C. I., Gould, I. R., Merz, K. M., Ferguson, D. M., Spellmeyer, D. C., Fox, T., Caldwell, J. W., and Kollman, P. A. (1995). A 2nd generation

force-field for the simulation of proteins, nucleic-acids, and organic-molecules. *Journal of the American Chemical Society*, 117(19):5179–5197.

Crisan, M. (2008). A perivascular origin for mesenchymal stem cells in multiple human organs. *Cell Stem Cell*, 3:301–313.

Cross, A. J., Dunnill, C. W., and Parkin, I. P. (2012). Production of predominantly anatase thin films on various grades of steel and other metallic substrates from $TiCl_4$ and ethyl acetate by atmospheric pressure CVD. *Chemical Vapor Deposition*, 18(4-6):133–139.

Cuomo, A., Virk, M., Petrigliano, F., Morgan, E., and Lierberman, J. (2009). Mesenchymal stem cell concentration and bone repair: Potential pitfalls from bench to bedside. *J Bone Joint Surg Am*, 91:1073–83.

Dalby, M. J., Gadegaard, N., Tare, R., Andar, A., Riehle, M. O., Herzyk, P., Wilkinson, C. D. W., and Oreffo, R. O. C. (2007). The control of human mesenchymal cell differentiation using nanoscale symmetry and disorder. *Nat Mater*, 6(12):997–1003.

Davies, J. (1998). Mechanisms of endosseous integration. *Int J Prosthodont*, 11(5):391–401.

Davies, J. (2003). Understanding peri-implant endosseous healing. *Journal of dental education*, 67(8):932–49.

Davies, L. C., Locke, M., Webb, R. D., Roberts, J. T., Langley, M., Thomas, D. W., Archer, C. W., and Stephens, P. (2010). A multipotent neural crest-derived progenitor cell population is resident within the oral mucosa lamina propria. *Stem Cells Dev*, 19(6):819–30.

Di Valentin, C., Pacchioni, G., and Selloni, A. (2009). Reduced and n-type doped TiO_2: Nature of Ti^{3+} species. *Journal of Physical Chemistry C*, 113(48):20543–20552.

Diebold, U. (2003). The surface science of Titanium dioxide. *Surface Science Reports*, 48(5-8):53–229.

Dion, M., Rydberg, H., Schroder, E., Langreth, D. C., and Lundqvist, B. I. (2004). van der Waals density functional for general geometries. *Phys Rev Lett*, 92(24).

Dowthwaite, G. P., Bishop, J. C., Redman, S. N., Khan, I. M., Rooney, P., Evans, D. J. R., Haughton, L., Bayram, Z., Boyer, S., Thomson, B., Wolfe, M. S., and Archer, C. W. (2004). The surface of articular cartilage contains a progenitor cell population. *J. Cell Sci*, 117:889–897.

Dudarev, S. L., Botton, G. A., Savrasov, S. Y., Humphreys, C. J., and Sutton, A. P. (1998). Electron-energy-loss spectra and the structural stability of nickel oxide: An LSDA+U study. *Physical Review B*, 57(3):1505–1509.

Edusi, C., Hyett, G., Sankar, G., and Parkin, I. P. (2011). Aerosol-assisted CVD of titanium dioxide thin films from methanolic solutions of titanium tetraisopropoxide; substrate and aerosol-selective deposition of rutile or anatase. *Chemical Vapor Deposition*, 17(1-3):30–36.

Eremia, S. and Newman, N. (2000). Long-term follow-up after autologous fat grafting: analysis of results from 116 patients followed up at least 12 months after receiving the last of a minimum of two treatments. *Dermatol Surg*, 26:1050–8.

Esposito, M., Hirsch, J. M., Lekholm, U., and Thomsen, P. (1998). Biological factors contributing to failures of osseointegrated oral implants. (I) Success criteria and epidemiology. *Eur J Oral Sci*, 106(1):527–51.

Fujishima, A. and Zhang, X. (2006). Titanium dioxide photocatalysis: present situation and future approaches. *Comptes Rendus Chimie*, 9(5-6):750–760.

Fukiage, K., Aoyama, T., Shibata, K. R., Otsuka, S., Furu, M., Kohno, Y., Ito, K., Jin, Y., Fujita, S., Fujibayashi, S., Neo, M., Nakayama, T., Nakamura, T., and Toguchida, J. (2008). Expression of vascular cell adhesion molecule-1 indicates the differentiation potential of human bone marrow stromal cells. *Biochem Biophys Res Commun*, 365(3):406–12.

Ganss, B., Kim, R., and Sodek, J. (1999). Bone sialoprotein. *Crit Rev Oral Biol Med*, 10(1):79–98.

García-Gareta, E., Hua, J., Rayan, F., and Blunn, G. (2014). Stem cell engineered bone

with calcium-phosphate coated porous titanium scaffold or silicon hydroxyapatite granules for revision total joint arthroplasty. *J Mater Sci Mater Med*, pages 1–10.

Grau-Crespo, R. and Schwingenschlogl, U. (2011). The interplay between dopants and oxygen vacancies in the magnetism of v-doped TiO_2. *J Phys Condens Matter*, 23(33):334216.

Grimme, S., Antony, J., Schwabe, T., and Muck-Lichtenfeld, C. (2007). Density functional theory with dispersion corrections for supramolecular structures, aggregates, and complexes of (bio)organic molecules. *Org Biomol Chem*, 5(5):741–58.

Gronthos, S., Graves, S., Ohta, S., and Simmons, P. (1994). The Stro-1+ fraction of adult human bone marrow contains the osteogenic precursors. *Blood*, 84(12):4164–73.

Guasti, L., Prasongchean, W., Kleftouris, G., Mukherjee, S., Thrasher, A. J., Bulstrode, N. W., and Ferretti, P. (2012). High plasticity of pediatric adipose tissue-derived stem cells: Too much for selective skeletogenic differentiation? *Stem Cells Translational Medicine*, 1(5):384–395.

Guo, Y. N., Lu, X., Zhang, H. P., Weng, J., Watari, F., and Leng, Y. (2011). DFT study of the adsorption of aspartic acid on pure, N-doped, and Ca-doped rutile (110) surfaces. *Journal of Physical Chemistry C*, 115(38):18572–18581.

Hameeuw, K. J., Cantele, G., Ninno, D., Trani, F., and Iadonisi, G. (2006). The rutile TiO_2 (110) surface: Obtaining converged structural properties from first-principles calculations. *Journal of Chemical Physics*, 124(2).

Harada, H., Tagashira, S., Fujiwara, M., Ogawa, S., Katsumata, T., Yamaguchi, A., Komori, T., and Nakatsuka, M. (1999). Cbfa1 isoforms exert functional differences in osteoblast differentiation. *Journal of Biological Chemistry*, 274(11):6972–6978.

Hardcastle, F. D., Ishihara, H., Sharma, R., and Biris, A. S. (2011). Photoelectroactivity and raman spectroscopy of anodized titania (TiO_2) photoactive water-splitting catalysts as a function of oxygen-annealing temperature. *Journal of Materials Chemistry*, 21(17):6337–6345.

Hattori, T., Muller, C., Gebhard, S., Bauer, E., Pausch, F., Schlund, B., Bosl, M. R., Hess, A., Surmann-Schmitt, C., von der Mark, H., de Crombrugghe, B., and von der Mark, K. (2010). SOX9 is a major negative regulator of cartilage vascularization, bone marrow formation and endochondral ossification. *Development*, 137(6):901–11.

Hayden, B., King, A., and Newton, M. (1999). Fourier transform reflection absorption IR spectroscopy study of formate adsorption on TiO_2 (110). *Journal of Physical Chemistry B*, 103:203–208.

Henderson, M. (1997). Complexity in the decomposition of formic acid on the TiO_2(110) surface. *Physical Chemistry B*, 101:221–229.

Henderson, M., Otero-Tapia, S., and Castro, M. (1998). Electron-induced decomposition of methanol on the vacuum-annealed surface of TiO_2 (110). *Surface Science*, 412-13:252–272.

Higuchi, A., Chuang, C.-W., Ling, Q.-D., Huang, S.-C., Wang, L.-M., Chen, H., Chang, Y., Wang, H.-C., Bing, J.-T., Chang, Y., and Hsu, S.-T. (2011). Differentiation ability of adipose-derived stem cells separated from adipose tissue by a membrane filtration method. *J Memb Sci*, 366(1-2):286–94.

Hohenberg, P. and Kohn, W. (1964). Inhomogeneous electron gas. *Phys. Rev.*, 136.

Hubbard, J. (1963). Electron correlations in narrow energy bands. *Proceedings of the Royal Society of London Series a-Mathematical and Physical Sciences*, 276(1364):238–+.

Hunter, G. and Goldberg, H. (1993). Nucleation of hydroxyapatite by bone sialoprotein. *Proc Natl Acad Sci U S A*, 90(18):8562–5.

Ivanovski, S., Hamlet, S., Salvi, G., Huynh-Ba, G., Bosshardt, D., Lang, N., and Donos, N. (2011). Transcriptional profiling of osseointegration in humans. *Clin Oral Implants Res*, 22(373-381).

Jagodzinski, M., Drescher, M., Zeichen, J., Hankemeier, S., Krettek, C., Bosch, U., and van Griensven, M. (2004). Effects of cyclic longitudinal mechanical strain and dexamethasone on osteogenic differentiation of human bone marrow stromal cells. *Eur Cell Mater*, 7:35–41.

Jang, S., Cho, H., Cho, Y., Park, J., and Jeong, H. (2010). Functional neural differentiation of human adipose tissue-derived stem cells using bfgf and forskolin. *BMC Cell Biol*, 11(25).

Johnston, K. (2014). A van der waals density functional study of the adsorption of ethanol on the α-alumina (0001) surface. *Surface Science*, 621:16–22.

Jonason, J. H., Xiao, G., Zhang, M., Xing, L., and Chen, D. (2009). Post-translational regulation of Runx2 in bone and cartilage. *Journal of Dental Research*, 88(8):693–703.

Jones, P. and Watt (1993). Separation of human epidermal stem cells from transit amplifying cells on the basis of differences in integrin function and expression. *Cell*, 73:713–724.

Katoh, M. (2008). Cancer genomics and genetics of FGFR2 (review). *Int J Oncol*, 33(2):233–7.

Kazanecki, C., Uzwiak, D., and Denhardt, D. (2007). Control of osteopontin signaling and function by post-translational phosphorylation and protein folding. *J Cell Biochem*, 102(4):912–24.

Khan, M. R., Donos, N., Salih, V., and Brett, P. M. (2012). The enhanced modulation of key bone matrix components by modified Titanium implant surfaces. *Bone*, 50(1):1–8.

Kiejna, A., Pabisiak, T., and Gao, S. (2006). The energetics and structure of rutile TiO_2 (110). *J Phys Condens Matter*, 18(17):4207–17.

Kim, M., Kim, I., Lee, S. K., Bang, S. I., and Lim, S. Y. (2011). Clinical trial of autologous differentiated adipocytes from stem cells derived from human adipose tissue. *Dermatol Surg*, 37(6):750–9.

Klimes, J., Bowler, D., and Michaelides, A. (2010). A critical assessment of theoretical methods for finding reaction pathways and transition states of surface processes. *Journal of Physics-Condensed Matter*, 22(7).

Klimês, J., Bowler, D., and Michaelides, A. (2011). van der Waals density functionals applied to solids. *Physical Review B*, 83(19).

Kohn, W. and Sham, L. J. (1965). Self-consistent equations including exchange and correlation effects. *Phys. Rev.*, 240.

Komori, T. andYagi, H., Nomura, S., Yamaguchi, A., Sasaki, K., Deguchi, K., Shimizu, Y., Bronson, R. T., Gao, Y. H., Inada, M., Sato, M., , Okamoto, R., Kitamura, Y., Yoshiki, S., and Kishimoto, T. (1997). Targeted disruption of Cbfa1 results in a complete lack of bone formation owing to maturational arrest of osteoblasts. *Cell*, 89(5):755–64.

Kowalski, P., Camellone, M., Nair, N., Meyer, B., and Marx, D. (2010). Charge localization dynamics induced by oxygen vacancies on the TiO_2 surface. *Phys Rev Lett*, 105(034705).

Kresse, G. and Furthmüller, J. (1996). Efficient iterative schemes for ab initio total-energy calculations using a plane-wave basis set. *Physical Review B*, 54(16):11169–11186.

Kresse, G. and Joubert, D. (1999). From ultrasoft pseudopotentials to the projector augmented-wave method. *Physical Review B*, 59(3):1758–1775.

Kroonenburgh, I., Beerens, M., Engel, C., Mercelis, I. P., Lambrichts, I., and Poukens, J. (2012). Doctor and engineer creating the future for 3D printed custom made implants. *Digital Dental News*, 6:60–65.

Lausmaa, J., Lofgren, P., and Kasemo, B. (1999). Adsorption and coadsorption of water and glycine on TiO_2. *J Biomed Mater Res*, 44(3):227–242.

Lazennec, G. and Jorgensen, C. (2008). Adult multipotent stromal cells and cancer: risk or benefit? *Stem Cells*, 26(6):1387–1394.

Le Guehennec, L., Lopez-Heredia, M. A., Enkel, B., Weiss, P., Amouriq, Y., and Layrolle, P. (2008). Osteoblastic cell behaviour on different titanium implant surfaces. *Acta Biomaterialia*, 4(3):535–43.

Lee, M. S., Lowe, G., Flanagan, S., Kuchler, K., and Glackin, C. A. (2000). Human Dermo-1 has attributes similar to twist in early bone development. *Bone*, 27(5):591–602.

Lendeckel, S., Jodicke, A., Christophis, P., Heidinger, K., Wolff, J., Fraser, J. K., Hedrick, M. H., Berthold, L., and Howaldt, H. P. (2004). Autologous stem cells (adipose) and

fibrin glue used to treat widespread traumatic calvarial defects: case report. *J Craniomaxillofac Surg*, 32(6):370–3.

Lerotholi, T. J., Kroger, E. A., Knight, M. J., Unterberger, W., Hogan, K., Jackson, D. C., Lamont, C. L. A., and Woodruff, D. P. (2009). Adsorption structure of glycine on TiO_2 (110): A photoelectron diffraction determination. *Surface Science*, 603(15):2305–2311.

Li, P., Ohtsuki, C., Kokubo, T., Nakanishi, K., Soga, N., and de Groot, K. (1994). The role of hydrated silica, titania, and alumina in inducing apatite on implants. *Journal of Biomedical Materials Research*, 28(1):7–15.

Lian, J. and Stein, G. (1993). The developmental stages of osteoblast growth and differentiation exhibit selective responses of genes to growth factors (TGF beta 1) and hormones (vitamin D and glucocorticoids). *J Oral Implantol*, 19(2):95–105.

Lian, J., Stewart, C., Puchacz, E., Mackowiak, S., Shalhoub, V., Collart, D., Zambetti, G., and Stein, G. (1989). Structure of the rat osteocalcin gene and regulation of vitamin D-dependent expression. *Proc Natl Acad Sci U S A*, 86(4):1143–7.

Lindsay, R., Wander, A., Ernst, A., Montanari, B., Thornton, G., and Harrison, N. M. (2005). Revisiting the surface structure of TiO_2 (110): A quantitative low-energy electron diffraction study. *Phys Rev Lett*, 94(24).

Linsebigler, A., Lu, G., and Yates, J. (1995). Photocatalysis on TiO_2 surfaces - principles, mechanisms, and selected results. *Chemical Reviews*, 95(3):735–758.

Liu, F., Akiyama, Y., Tai, S., Maruyama, K., Kawaguchi, Y., Muramatsu, K., and Yamaguchi, K. (2008). Changes in the expression of CD106, osteogenic genes, and transcription factors involved in the osteogenic differentiation of human bone marrow mesenchymal stem cells. *J Bone Miner Metab*, 26(4):312–20.

Liu, L., Zhang, C., Thornton, G., and Michaelides, A. (2010). Structure and Dynamics of liquid water on rutile TiO_2 (110). *Physical Review B*, 82(16):161415.

Liu, L.-M., Zhang, C., Thornton, G., and Michaelides, A. (2012). Reply to comment on "Structure and Dynamics of liquid water on rutile TiO_2 (110)". *Phys. Rev. B*, 85:167402.

Liu, X., Chu, P., and Ding, C. (2004). Surface modifications of titanium, titanium alloys and related materials for biomedical applications. *Materials Science & Engineering*, 47:49–121.

Loeffler, M. and Roeder, I. (2002). Tisasue stem cells: definition, plasticity, heterogeneity, self-organisation and models- a conceptual approach. *Cells Tissues Organs*, 171:8–26.

Mackey, A., Kjaer, M., Charifi, N., Henriksson, J., Bojsen-Moller, J., Holm, L., and Kadi, F. (2009). Assessment of satellite cell number and activity status in human skeletal muscle biopsies. *Muscle and Nerve*, 40(3):455–465.

Marie, P. and Fromigue, O. (2006). Osteogenic differentiation of human marrow-derived mesenchymal stem cells. *Regenerative Medicine*, 1(4):539–548.

Maries, J. (2008). Transcription factors controlling osteoblastogenesis. *Archives of Biochemistry and Biophysics*, 473:93–105.

Martin, I., Wendt, D., and Heberer, M. (2004). The role of bioreactors in tissue engineering. *Trends in Biotechnology*, 22(2):80–86.

Mattsson, A., Hu, S., Hermansson, K., and Österlund, L. (2014). Adsorption of formic acid on rutile TiO_2 revisited: An infrared reflection-absorption spectroscopy and density functional theory study. *The Journal of chemical physics*, 140(034705).

Mayer, H., Bertram, H., Lindenmaier, W., Korff, T., Weber, H., and Weich, H. (2005). Vascular endothelial growth factor (VEGF-A) expression in human mesenchymal stem cells: autocrine and paracrine role on osteoblastic and endothelial differentiation. *J Cell Biochem*, 95(4):827–39.

Meinel, L., Karageorgiou, V., Fajardo, R., Snyder, B., Shinde-Patil, V., Zichner, L., Kaplan, D., Langer, R., and Vunjak-Novakovic, G. (2004). Bone tissue engineering using human mesenchymal stem cells: effects of scaffold material and medium flow. *Annals of Biomedical Engineering*, 32(1):112–22.

Mendonca, G., Mendonca, D., Aragao, F., and Cooper, L. (2008). Advancing dental implant surface topography - from micron to nanotopography. *Biomaterials*, 29:3822–3835.

Miron, R., Oates, C., Molenberg, A., Dard, M., and Hamilton, D. (2010). The effect of enamel matrix proteins on the spreading, proliferation and differentiation of osteoblasts cultured on titanium surfaces. *Biomaterials*, 31:449–460.

Miura, M., Chen, X., Allen, M., Bi, Y., Gronthos, S., Seo, B., Lakhani, S., Flavell, R., Feng, X., Roey, P., Young, M., and Shi, S. (2004). A crucial role of caspase-3 in osteogenic differentiation of bone marrow stromal stem cells. *Jounal of clinical investigation*, 114(12):1704–1713.

Morgan, B. and Watson, G. (2007). A DFT+U description of oxygen vacancies at the TiO_2 rutile (110) surface. *Surface Science*, 601(21):5034–5041.

Morgan, B. and Watson, G. (2010). Intrinsic n-type defect formation in TiO_2: A comparison of rutile and anatase from GGA+ U calculations. *The Journal of Physical Chemistry C*, 114(5):2321–2328.

Muir, J. M. R. and Idriss, H. (2013). Computational study of cysteine interaction with the rutile computational study of cysteine interaction with the rutile TiO_2 (110) surface. *Surface Science*, 617:60–67.

Muraglia, A., Cancedda, R., and Quarto, R. (2000). Clonal mesenchymal progenitors from human bone marrow differentiate in vitro according to a hierarchical model. *Journal of Cell Science*, 113(7):1161–1166.

Nakashima, K., Zhou, X., Kunkel, G., Zhang, Z. P., Deng, J. M., Behringer, R. R., and de Crombrugghe, B. (2002). The novel zinc finger-containing transcription factor Osterix is required for osteoblast differentiation and bone formation. *Cell*, 108(1):17–29.

Nebe, J. B., Muller, L., Luthen, F., Ewald, A., Bergemann, C., Conforto, E., and Muller, F. A. (2008). Osteoblast response to biomimetically altered titanium surfaces. *Acta Biomaterialia*, 4:1985–1995.

Nolan, M., Elliott, S. D., Mulley, J. S., Bennett, R. A., Basham, M., and Mulheran, P. (2008). Electronic structure of point defects in controlled self-doping of the TiO_2 (110) surface: Combined photoemission spectroscopy and density functional theory study. *Physical Review B*, 77(23).

Obokata, H., Wakayama, T., Sasai, Y., Kojima, K., Vacanti, M. P., Niwa, H., M., Y., and Vacanti, C. A. (2014). Stimulus-triggered fate conversion of somatic cells into pluripotency. *Nature*, 505:641–647.

Ogata, Y., Yamauchi, M., Kim, R. H., Li, J. J., Freedman, L. P., and Sodek, J. (1995). Glucocorticoid regulation of bone sialoprotein (BSP) gene expression. identification of a glucocorticoid response element in the bone sialoprotein gene promoter. *Eur J Biochem*, 230(1):183–92.

Ojamae, L., Aulin, C., Pedersen, H., and Kall, P. O. (2006). IR and quantum-chemical studies of carboxylic acid and glycine adsorption on rutile TiO_2 nanoparticles. *J Colloid Interface Sci*, 296(1):71–78.

Oldberg, A., Franzen, A., and Heinegard, D. (1988). The primary structure of a cell-binding bone sialoprotein. *J Biol Chem*, 263(36):19430–2.

Olivares-Navarrete, R., Hyzy, S. L., Hutton, D. L., Erdman, C. P., Wieland, M., Boyan, B. D., and Schwartz, Z. (2010). Direct and indirect effects of microstructured titanium substrates on the induction of mesenchymal stem cell differentiation towards the osteoblast lineage. *Biomaterials*, 31(10):2728–35.

Ozeki, N., Lim, M., Yao, C.-C., Tolar, M., and Kramer, R. (2006). $\alpha 7$ integrin expressing human fetal myogenic progenitors have stem cell-like properties and are capable of osteogenic differentiation. *Experimental Cell Research*, 312(20):4162–80.

Page, K., Wilson, M., and Parkin, I. (2009). Antimicrobial surfaces and their potential in reducing the role of the inanimate environment in the incidence of hospital-acquired infections. *Journal of Materials Chemistry*, 19(23):3819–383.

Park, P., Selvarajah, S., Bayani, J., Zielenska, M., and Squire, J. A. (2007). Stem cell enrichment approaches. *Seminars in cancer biology*, 17:257–264.

Pavlin, D. and Gluhak-Heinrich, J. (2001). Effect of mechanical loading on periodontal cells. *Crit Rev Oral Biol Med*, 12(5):414–24.

Perdew, J., Burke, K., and Ernzerhof, M. (1996). Generalized Gradient Approximation made simple. *Phys Rev Lett*, 77(18):3865–3868.

Pierschbacher, M. and Ruoslahti, E. (1984). Cell attachment activity of fibronectin can be duplicated by small synthetic fragments of the molecule. *Nature*, 309(5963):30–33.

Pilz, G. A., Ulrich, C., Ruh, M., Abele, H., Schäfer, R., Kluba, T., Bühring, H., Rolauffs, B., and Aicher, W. K. (2011). Human term placenta-derived mesenchymal stromal cells are less prone to osteogenic differentiation than bone marrow-derived mesenchymal stromal cells. *Stem Cells Dev*, 20(4):635–46.

Pittenger, M., Mackay, A., Beck, S., Jaiswal, R., Douglas, R., Mosca, J., Moorman, M., Simonetti, D., Craig, S., and Marshak, D. (1999). Multilineage potential of adult human mesenchymal stem cells. *Science*, 284(5411):143–147.

Plata, J. J., Collico, V., Marquez, A. M., and Sanz, J. F. (2013). Analysis of the origin of lateral interactions in the adsorption of small organic molecules on oxide surfaces. *Theoretical Chemistry Accounts*, 132(2).

Prince, M., Banerjee, C., Javed, A., Green, J., Lian, J. B., Stein, G. S., Bodine, P. V., and Komm, B. S. (2001). Expression and regulation of Runx2/Cbfa1 and osteoblast phenotypic markers during the growth and differentiation of human osteoblasts. *J Cell Biochem*, 80(3):424–40.

Předota, M., Bandura, A. V., Cummings, P. T., Kubicki, J. D., Wesolowski, D. J., Chialvo, A. A., and Machesky, M. L. (2004). Electric double layer at the rutile (110) surface. 1. structure of surfaces and interfacial water from molecular dynamics by use of ab initio potentials. *J. Phys. Chem. B*, 108(32):12049–12060.

Qi, H., Aguiar, D. J., Williams, S. M., La Pean, A., Pan, W., and Verfaillie, C. M. (2003). Identification of genes responsible for osteoblast differentiation from human mesodermal progenitor cells. *Proc Natl Acad Sci U S A*, 100(6):3305–10.

Qiu, T. and Barteau, M. (2006). STM study of glycine on TiO_2(110) single crystal surfaces. *J Colloid Interface Sci*, 303(1):229–35.

Qu-Petersen, Z., Deasy, B., Jankowski, R., Ikezawa, M., Cummins, J., Pruchnic, R., Mytinger, J., Cao, B., Gates, C., Wernig, A., and Huard, J. (2002). Identification of a

novel population of muscle stem cells in mice: potential for muscle regeneration. *JCR*, 157(5):851–64.

Rausch-Fan, X., Qu, Z., Wieland, M., Matejka, M., and Schedle, A. (2007). Differentiation and cytokine synthesis of human alveolar osteoblasts compared to osteoblast like cells in response to titanium surfaces. *Dental Materials*, 24(2):102–110.

Ressler, D. M. and Walker, W. (1967). Electronic spectrum and ultraviolet optical properties of crystalline Mg—textscO. *Phys. Rev.*, 159:733.

Rodriguez, L., Alfonso, Z., Zhang, R., Leung, J., Wu, B., and Ignarro, L. (2006). Clonogenic multipotent stem cells in human adipose tissue differentiate into functional smooth muscle cells. *Proc Natl Acad Sci U S A*, 103(32):12167–12172.

Roessler, D. and Walker, W. (1967). Electronic spectrum and ultraviolet optical properties of crystalline MgO. *Physical Review*, 159(3):733–&.

Roman-Perez, G. and Soler, J. (2009). Efficient implementation of a van der waals density functional: Application to double-wall carbon nanotubes. *Phys Rev Lett*, 103(9).

Rönold, H., Lyngstadaas, S., and Ellingsen, J. (2003). Analysing the optimal value for titanium implant roughness in bone attachment using a tensile test. *Biomaterials*, 24(25):4559–64.

Rupp, F., Scheideler, L., Olshanska, N., de Wild, M., Wieland, M., and Geis-Gerstorfer, J. (2006). Enhancing surface free energy and hydrophilicity through chemical modification of microstructured titanium implant surfaces. *J Biomed Mater Res A*, 76(2):323–34.

Sakai, N., Fujishima, A., Watanabe, T., and Hashimoto, K. (2003). Quantitative evaluation of the photoinduced hydrophilic conversion properties of TiO_2 thin film surfaces by the reciprocal of contact angle. *Journal of Physical Chemistry B*, 107(4):1028–1035.

Salgado, A., Reis, R., Sousa, N., and Gimble, J. (2010). Adipose tissue derived stem cells secretome: Soluble factors and their roles in regenerative medicine. *Curr Stem Cell Res Ther*, 5(2):103–10.

Sánchez de Armas, R., Oviedo, J., San Miguel, M., and Sanz, J. (2007). Methanol adsorption and dissociation on TiO_2(110) from first principles calculations. *J Phys Chem C*, 111:10023–10028.

Sandor, G. K., Tuovinen, V. J., Wolff, J., Patrikoski, M., Jokinen, J., Nieminen, E., Mannerstrom, B., Lappalainen, O. P., Seppanen, R., and Miettinen, S. (2013). Adipose stem cell tissue-engineered construct used to treat large anterior mandibular defect: A case report and review of the clinical application of good manufacturing practice-level adipose stem cells for bone regeneration. *Journal of Oral and Maxillofacial Surgery*, 71(5):938–950.

Sanz-Rodriguez, F., Guerrero-Esteo, M., Botella, L. M., Banville, D., Vary, C. P., and Bernabeu, C. (2004). Endoglin regulates cytoskeletal organization through binding to ZRP-1, a member of the Lim family of proteins. *J Biol Chem*, 279(31):32858–68.

Sato, T., Tsuneda, T., and Hirao, K. (2007). Long-range corrected density functional study on weakly bound systems: Balanced descriptions of various types of molecular interactions. *Journal of Chemical Physics*, 126(23).

Schaub, R., Thostrup, P., Lopez, N., Laegsgaard, E., Stensgaard, I., Norskov, J. K., and Besenbacher, F. (2001). Oxygen vacancies as active sites for water dissociation on rutile TiO_2(110). *Physical Review Letters*, 87(26).

Schneider, J. and Ciacchi, L. (2010). First principles and classical modeling of the oxidized titanium (0001) surface. *Surface Science*, 604(13-14):1105–1115.

Schonmeyr, B. H., Soares, M., Avraham, T., Clavin, N. W., Gewalli, F., and Mehrara, B. J. (2010). Vascular endothelial growth factor inhibits bone morphogenetic protein 2 expression in rat mesenchymal stem cells. *Tissue Eng Part A*, 16(2):653–62.

Schuler, M., Trentin, D., Textor, M., and Tosatti, S. G. (2006). Biomedical interfaces: titanium surface technology for implants and cell carriers. *Nanomedicine (Lond)*, 1(4):449–63.

Schwartz, F., Sager, M., Kadeka, I., Ferrari, D., and Becker, J. (2010). Influence of

titanium implant surface characteristics on bone regeneration in dehiscence type defects: an experimental study in dogs. *J Clin Periodontol*, 37:466–473.

Schwartz, Z., Lohmann, C., Oefinger, J., Bonewald, L., Dead, D., and Boyan, B. (1999a). Implant surface characteristics modulate differentiation behavior of cells in the osteoblastic lineage. *Adv. Dent. Res.*, 13:38–48.

Schwartz, Z., Lohmann, C., Oefinger, J., Bonewald, L., Dean, D., and Boyan, B. (1999b). Implant surface characteristics modulate differentiation behaviour of cells in the osteogenic lineage. *Adv. Dent. Res.*, 13:38–48.

Sekiya, I., Larson, B. L., Smith, J. R., Pochampally, R., Cui, J. G., and Prockop, D. J. (2002). Expansion of human adult stem cells from bone marrow stroma: conditions that maximize the yields of early progenitors and evaluate their quality. *Stem Cells*, 20(6):530–41.

Shen, J., Wu, T., Wang, Q., and Pan, H. (2008). Molecular simulation of protein adsorption and desorption on hydroxyapatite surfaces. *Biomaterials*, 29:513–32.

Shimizu-Sasaki, E., Yamazaki, M., Furuyama, S., Sugiya, H., Sodek, J., and Ogata, Y. (2001). Identification of a novel response element in the rat bone sialoprotein (BSP) gene promoter that mediates constitutive and fibroblast growth factor 2-induced expression of BSP. *J Biol Chem*, 276(8):5459–66.

Shui, C., Spelsberg, T. C., Riggs, B. L., and Khosla, S. (2003). Changes in Runx2/Cbfa1 expression and activity during osteoblastic differentiation of human bone marrow stromal cells. *J Bone Miner Res*, 18(2):213–21.

Sloan, A. and Waddington, R. (2009). Dental pulp stem cells: what, where, how? *International Journal of Paediatric Dentistry*, 19(1):61–70.

Sodek, J. and Cheietz, S. (2000). *Molecular regulation of osteogenesis.*, pages 31–43. Number ISBN 0-9686980-0-X. Em Squared Inc, Toronto.

Somasundaran P, W. (1984). Surface chemical characteristics and adsorption properties of apatite. *New York: Plenum Press*, (129-149).

Sommerfeldt, D. and Rubin, C. (2001). Biology of bone and how it orchestrates the form and function of the skeleton. *Eur. Spine. J.*, 10:86–95.

Sorescu, D., Lee, J., Al-Saidi, W., and Jordan, K. (2011). CO_2 adsorption on TiO_2(110) rutile: Insight from dispersion-corrected density functional theory calculations and scanning tunneling microscopy experiments. *The Journal of chemical physics*, 134(104707).

Standal, T., Borset, M., and Sundan, A. (2004a). Role of osteopontin in adhesion, migration, cell survival and bone remodeling. *Exp Oncol*, 26(3):179–84.

Standal, T., Hjorth-Hansen, H., Rasmussen, T., Dahl, I. M., Lenhoff, S., Brenne, A. T., Seidel, C., Baykov, V., Waage, A., Borset, M., Sundan, A., and Hjertner, O. (2004b). Osteopontin is an adhesive factor for myeloma cells and is found in increased levels in plasma from patients with multiple myeloma. *Haematologica*, 89(2):174–82.

Steinemann, S. (1998). Titanium–the material of choice? *Periodontol 2000*, 17:7–21.

Sudhakar, S., Katz, M., and Elango, N. (2001a). Analysis of type-I and type-II Runx2 protein expression in osteoblasts. *Biochem Biophys Res Commun*, 286(1):74–9.

Sudhakar, S., Li, Y., Katz, M. S., and Elango, N. (2001b). Translational regulation is a control point in Runx2/Cbfa1 gene expression. *Biochem Biophys Res Commun*, 289(2):616–22.

Sullivan, R. (2001). Implant dentistry and the concept of osseointegration: a historical perspective. *J Calif Dent Assoc*, 29(11):737–45.

Sushko, M., Gal, A., and Shluger, A. (2006). Interaction of organic molecules with the TiO_2 (110) surface: ab inito calculations and classical force fields. *J Phys Chem B*, 110(10):4853–62.

Tapp, H., Hanley, E., Patt, J., and Gruber, H. (2009). Adipose-derived stem cells: Characterization and current application in orthopaedic tissue repair. *Exp Biol Med*, 234(1):1–9.

Thesleff, T., Lehtimaki, K., Niskakangas, T., Mannerstrom, B., Miettinen, S., Suuronen, R., and Ohman, J. (2011). Cranioplasty with adipose-derived stem cells and biomaterial: a novel method for cranial reconstruction. *Neurosurgery*, 68:1535–40.

Thevuthasan, S., Herman, G., Kim, Y., Chambers, S., Peden, C., Wang, Z., Ynzunza, R., Tober, E., Morais, J., and Fadley, C. (1998). The structure of formate on TiO_2(110) by scanned-energy and scanned-angle photoelectron diffraction. *Surface Science*, 401:261–268.

Thibodeau, G. and Patton, K. (2007). *Anatomy and Physiology*. Mosby Elsevier, 6th edition.

Thompson, T. and Yates, J. (2006). Surface science studies of the photoactivation of TiO_2-new photochemical processes. *Chemical Reviews*, 106(10):4428–4453.

Toma, C. D., Ashkar, S., Gray, M. L., Schaffer, J. L., and Gerstenfeld, L. C. (1997). Signal transduction of mechanical stimuli is dependent on microfilament integrity: identification of osteopontin as a mechanically induced gene in osteoblasts. *J Bone Miner Res*, 12(10):1626–36.

Tomasi, J., Mennucci, B., and Cammi, R. (2005). Quantum mechanical continuum solvation models. *Chem. Rev.*, 105(8):2999–3094.

Tonner, R. (2010). Adsorption of proline and glycine on the TiO_2(110) surface: a density functional theory study. *Chemphyschem*, 11(5):1053–61.

Tortora, G. and Derrickson, B. (2009). *Principles of anatomy and physiology*, chapter The skeletal system: bone tissue, pages 176–1991. John Wiley & Sons. Inc, 12 edition.

Van der Dolder, J. and Jansen, J. (2007). Enrichment of osteogenic cell populations from rat bone marrow stroma. *Biomaterials*, 28(2):249–55.

van Kooten, T. G., Schakenraad, J. M., van der Mei, H. C., and Busscher, H. J. (1992). Influence of substratum wettability on the strength of adhesion of human fibroblasts. *Biomaterials*, 13(13):897–904.

Vassilios, I., Temenoff, J., and Mikos, A. (2001). Biomaterials and mechanotransduction. *Biomaterials*, 22:2581–2593.

Wall, I., Donos, N., Carlqvist, K., Jones, F., and Brett, P. (2009). Modified titanium surfaces promote accelerated osteogenic differentiation of mesenchymal stromal cells in vitro. *Bone*, 45(1):17–26.

Warnke, P. H., Springer, I. N. G., Wiltfang, J., Acil, Y., Eufinger, H., Wehmoller, M., Russo, P. A. J., Bolte, H., Sherry, E., Behrens, E., and Terheyden, H. (2004). Growth and transplantation of a custom vascularised bone graft in a man. *Lancet*, 364(9436):766–770.

Weiss, M. J., Lafferty, M. A., Slaughter, C., Raducha, M., and Harris, H. (1986). Isolation and characterization of a cDNA encoding a human liver/bone/kidney-type alkaline phosphatase. *Proc. Natl. Acad. Sci. U.S.A.*, 87(2220-4).

Wendt, S., Schaub, R., Matthiesen, J., Vestergaard, E. K., Wahlstrom, E., Rasmussen, M. D., Thostrup, P., Molina, L. M., Laegsgaard, E., Stensgaard, I., Hammer, B., and Besenbacher, F. (2005). Oxygen vacancies on TiO_2(110) and their interaction with H_2O and O_2: A combined high-resolution STM and DFT study. *Surface Science*, 598(1-3):226–245.

Xiao, G., Gopalakrishnan, R., Jiang, D., Reith, E., Benson, M. D., and Franceschi, R. T. (2002). Bone morphogenetic proteins, extracellular matrix, and mitogen-activated protein kinase signaling pathways are required for osteoblast-specific gene expression and differentiation in MC3T3-E1 cells. *J Bone Miner Res*, 17(1):101–10.

You, J., Reilly, G. C., Zhen, X., Yellowley, C. E., Chen, Q., Donahue, H. J., and Jacobs, C. R. (2001). Osteopontin gene regulation by oscillatory fluid flow via intracellular calcium mobilization and activation of mitogen-activated protein kinase in MC3T3-E1 osteoblasts. *J Biol Chem*, 276(16):13365–71.

Zhang, J., Li, M., Feng, Z., Chen, J., and Li, C. (2006). UV raman spectroscopic study on TiO_2. I. phase transformation at the surface and in the bulk. *J Phys Chem B*, 110(2):927–935.

Zhang, Z., Fenter, P., Cheng, L., Sturchio, N. C., Bedzyk, M. J., Predota, M., Bandura, A., Kubicki, J. D., Lvov, S. N., Cummings, P. T., Chialvo, A. A., Ridley, M. K., Benezeth,

P., Anovitz, L., Palmer, D. A., Machesky, M. L., and Wesolowski, D. J. (2004). Ion adsorption at the rutile-water interface: Linking molecular and macroscopic properties. *Lanqmuir*, 20(12):4954–4969.

Zhou, H. Y., Takita, H., Fujisawa, R., Mizuno, M., and Kuboki, Y. (1995). Stimulation by bone sialoprotein of calcification in osteoblast-like MC3T3-E1 cells. *Calcif Tissue Int*, 56(5):403–7.